

SMALL-ANGLE X-RAY SCATTERING ANALYSIS OF  
NANOMATERIALS

A STRUCTURAL STUDY OF DNA ORIGAMI, PEROVSKITE NANOPARTICLES, AND  
PHOTO-SWITCHABLE BIOMOLECULES

STEFAN FISCHER



MÜNCHEN 2017



SMALL-ANGLE X-RAY SCATTERING ANALYSIS OF  
NANOMATERIALS

A STRUCTURAL STUDY OF DNA ORIGAMI, PEROVSKITE NANOPARTICLES, AND  
PHOTO-SWITCHABLE BIOMOLECULES

STEFAN FISCHER



Dissertation  
Fakultät für Physik  
Ludwig-Maximilians-Universität

vorgelegt von  
Stefan Fischer  
aus Rotenburg (Wümme)

München, den 20. September 2017

Stefan Fischer: *Small-angle X-ray scattering analysis of nanomaterials*, A structural study of DNA origami, perovskite nanoparticles, and photo-switchable biomolecules, © 20. September 2017

ERSTGUTACHTER: PD Dr. Bert Nickel

ZWEITGUTACHTER: Prof. Jan Lipfert

TAG DER MÜNDLICHEN PRÜFUNG: 14. November 2017

# ZUSAMMENFASSUNG

---

In den letzten drei Jahrzehnten ist das Feld der Nanotechnologie durch die Entwicklung neuer Methoden schnell gewachsen. Diese eröffnen die Möglichkeit Strukturen im Nanometerbereich anzuordnen. Die Einsatzgebiete sind immens und reichen von elektronischen Bauteilen bis hin zu Anwendungen im medizinischen Bereich. Darüber hinaus befinden sich viele biologische Prozesse sowie die Bausteine des Lebens auf der Nanometerskala. Jedoch stellt die Kontrolle des geplanten Designs und die Abbildung von Strukturen eine große Herausforderung dar.

In dieser Arbeit wurde ein Kleinwinkelröntgenaufbau errichtet, mit dem Ziel Strukturen im Nanometerbereich zu messen. Dabei werden wichtige Fragestellungen, wie z. B. die Wahl der geeigneten Röntgenenergie, ausführlich erläutert. Die Röntgenanlage wurde anhand von Standardproben wie Silberbehenat, glasartigem Kohlenstoff und dem Protein Cytochrom *c* charakterisiert. Im nächsten Schritt wurden drei unterschiedliche wissenschaftliche Fragestellungen adressiert, welche die Vorteile von Röntgenstreuung an Nanoobjekten zeigen. Als Erstes wurden zweidimensionale Perovskit Nanoplättchen aus Methylammonium Bleitribromid ( $\text{MAPbBr}_3$ ) in Kooperation mit der Gruppe von Dr. Alexander Urban untersucht. Diese Plättchen zeigen den Effekt von Quanten-Confinement in optischen Experimenten. In dieser Arbeit wurde die Kristallstruktur für verschiedene Synthesebedingungen bestimmt und es wurde festgestellt, dass die Perovskit Kristallstruktur für alle Bedingungen erhalten bleibt. Als Zweites wurden Nanoobjekte aus DNA gemessen, die durch geplante Selbstorganisation entstehen und als DNA Origami bezeichnet werden. Dies geschah in Kooperation mit der Gruppe von Prof. Tim Liedl. Dabei wurden sowohl einzelne Objekte als auch zu einem 3D Gitter angeordnete DNA Origami studiert. Für einzelne Strukturen konnte die Größe der Objekte sowie der mittlere interhelikale Abstand bis zu Ångström Auflösung identifiziert werden. Außerdem wurde die Stabilität mit verschiedenen Salzkonzentrationen und Temperaturen im physiologisch relevanten Bereich bestimmt. Mit geringer werdender  $\text{Mg}^{2+}$  Konzentration schwillt die Struktur bis zu 10 % an, bevor sie aufgrund von elektrostatischer Abstoßung der negativ geladenen DNA zerstört wird. Im Gegensatz dazu schmilzt die Struktur abrupt bei einem Temperaturanstieg ab  $53.5^\circ\text{C}$  beziehungsweise ab  $57.5^\circ\text{C}$  für hexagonale und rechteckige Gitteranordnungen im DNA Origami. Für das 3D Gitter konnte eine rhomboedrische Kristallstruktur mit einer Gitterkonstante von etwa 65 nm bestimmt werden. Darüber hinaus ist es gelungen die erfolgreiche Anbindung von Goldnanopartikeln im Gitter zu zeigen. Als Drittes wurde die strukturelle Veränderung von photoschaltbaren Lipiden und Fettsäuren für Doppelschichten und Multilagenn mit Ångström Auflösung bestimmt.

Röntgenmessungen ermöglichen in-situ Experimente mit unterschiedlichen

Umgebungsbedingungen. Dabei können die Proben ohne zusätzliche Präparation verwendet werden. So ist es zum Beispiel möglich Zwischenzustände bei der Faltung von DNA Origami zu beobachten. Sogar komplexe 3D Strukturen können charakterisiert werden, wenn die Objekte klar definiert sind. Bezüglich der DNA Kristalle scheint es in naher Zukunft realistisch zu sein Proteine in DNA Gittern anzuordnen und somit eine Vision aus den 80er Jahren zu erfüllen.

## ABSTRACT

---

In the last three decades, the field of nanotechnology grew rapidly due to the development of new techniques, which can assemble structures on the nanoscale. The field of application of nanostructures is wide and reaches from electronic devices to medical treatment. Moreover, many biological processes and the building blocks of life are on the nanoscale. However, the control of the planned design and the imaging of structures remain challenging. In this thesis, a small-angle X-ray scattering setup was built in order to study structures on the nanoscale. The choice of the X-ray energy was evaluated and an X-ray energy of 17.4 keV was chosen. The setup was characterized with established test samples as silver behenate, glassy carbon, and the protein cytochrome *c*. In the next step, three diverse scientific questions were addressed and highlight the application of X-ray scattering for nanoobjects. First, two-dimensional perovskite nanoplatelets of methylammonium lead tribromide (MAPbBr<sub>3</sub>) were studied in cooperation with the group of Dr. Alexander Urban. The platelets show the effect of quantum confinement in optical experiments. In this thesis, the crystal structure was determined for different synthesis compositions and it was found that the perovskite crystal structure is preserved for all syntheses. Secondly, nanostructures of DNA, which are built via self-assembly, so-called DNA origami, were studied as single objects as well as assembled 3D lattices in cooperation with the group of Prof. Tim Liedl. For the single objects, the overall sizes in the nanometer regime, as well as the mean inter-helical distance, could be determined down to Ångström resolution. The stability with salt concentration and the temperature was tested in the physiological interesting region. A decreasing Mg<sup>2+</sup> concentration leads to a swelling of up to 10 % before the whole object disassembled due to electrostatic repulsion of the negatively charged DNA. In contrast, with a temperature increase an abrupt melting was found at about 53.5 °C and 57.5 °C for hexagonal and square lattice structures respectively. For the 3D lattice a rhombohedral crystal structure with a lattice constant of about 65 nm could be determined. Furthermore, the successful incorporation of gold nanoparticles into the lattice could be shown. Thirdly, the structural behavior of photo-switchable lipids and fatty acids could be determined on the Ångström scale for bilayers as well as multilayers. X-ray measurements enable experiments with nanoobjects under different physiologically relevant in-situ conditions using samples without additional preparation. Such experiments allow for example for resolving of intermediate states during the folding of DNA origami; here even rather complex 3D structures can be characterized. In the context of DNA lattices, it seems now quite feasible that in the near future it will be possible to place proteins in artificial DNA crystals for X-ray analysis, a vision first formulated in the 80s.



# CONTENTS

---

<b>I</b>	<b>INTRODUCTION, STRUCTURE RESOLVING TECHNIQUES AND BASIC THEORY</b>	<b>1</b>
1	INTRODUCTION	3
2	MICROSCOPY AND SCATTERING TECHNIQUES	7
2.1	Super-Resolution Microscopy . . . . .	7
2.2	Atomic Force Microscopy . . . . .	8
2.3	Electron Microscopy . . . . .	9
2.4	X-ray . . . . .	10
2.4.1	History of X-ray Scattering . . . . .	10
2.4.2	Evolution of X-ray Sources . . . . .	12
3	X-RAY SCATTERING THEORY FOR SAXS AND DIFFRACTION	15
3.1	X-ray Generation . . . . .	15
3.2	Basic Scattering by Particles . . . . .	18
3.3	Small-Angle X-ray Scattering . . . . .	19
3.3.1	Guinier and Porod Regime . . . . .	19
3.3.2	Pair Distance Distribution Function . . . . .	21
3.3.3	Absolute Intensity . . . . .	22
3.4	Diffraction by Crystals . . . . .	23
<b>II</b>	<b>CONSTRUCTION OF A SMALL-ANGLE X-RAY SCATTERING SETUP AND APPLICATIONS</b>	<b>27</b>
4	BUILDING A SMALL-ANGLE X-RAY SCATTERING SETUP	29
4.1	Requirements . . . . .	30
4.2	q-Range . . . . .	31
4.3	q-Resolution . . . . .	34
4.4	Signal-to-Background . . . . .	36
4.4.1	Parameters of Scattering Intensity . . . . .	36
4.4.2	Background . . . . .	40
4.4.3	Radiation Damage . . . . .	43
4.4.4	Conclusion . . . . .	45
4.5	Detailed Description of Components . . . . .	45
4.5.1	Hardware . . . . .	46
4.5.2	Software . . . . .	54
5	PEROVSKITE NANOPATELETS	57
5.1	Perovskite Powder . . . . .	59
5.2	Crystal Size Evaluation by X-ray Bragg Peak Analysis . . . . .	61
6	DNA ORIGAMI	65
6.1	Single DNA Origami Objects . . . . .	68
6.1.1	Scattering of Different Shapes . . . . .	68
6.1.2	Influence of Ionic Strength . . . . .	81
6.1.3	Influence of Temperature . . . . .	83

6.1.4	Conclusion and Outlook . . . . .	88
6.2	DNA Origami Lattice with Guest Particles . . . . .	89
6.2.1	Scattering of Monomers . . . . .	89
6.2.2	Scattering of Gold Nanoparticle Lattice . . . . .	90
6.2.3	Scattering of DNA Lattice . . . . .	94
7	PHOTO-SWITCHABLE LIPIDS AND FATTY ACIDS . . . . .	97
7.1	Preparation and Characterization Methods . . . . .	98
7.2	Study of Lipid Phases . . . . .	99
7.3	Ratio of Switched Molecules . . . . .	100
7.4	X-ray Reflectometry of Bilayers . . . . .	103
7.5	Azo-PC Multilayer . . . . .	105
7.5.1	Multilayer Thickness . . . . .	106
7.5.2	Time-resolved X-ray Measurements . . . . .	108
<b>III</b>	<b>CONCLUSION</b> . . . . .	<b>111</b>
<b>8</b>	<b>SUMMARY</b> . . . . .	<b>113</b>
<b>9</b>	<b>CONCLUSION AND OUTLOOK</b> . . . . .	<b>115</b>
<b>A</b>	<b>APPENDIX</b> . . . . .	<b>119</b>
A.1	Full Text of Manuscript 1 . . . . .	119
A.1.1	Supplementary Information for Manuscript 1 . . . . .	127
	<b>BIBLIOGRAPHY</b> . . . . .	<b>143</b>

## ACRONYMS

---

1-LS	one layer sheet
14HB	14 helix bundle
24HB	24 helix bundle
3-LS	three layer sheet
AFM	atomic force microscopy
Ag	silver
AgBE	silver behenate
AuNP	gold nanoparticle
bp	base pair
cryo-EM	cryo-electron microscopy
Cu	copper
DESY	Deutsches Elektronen-Synchrotron
DHPE	1,2-dihexadecanoyl-sn-glycero-3-phosphoethanolamine
DNA	deoxyribonucleic acid
DOPC	1,2-dioleoyl-sn-glycero-3-phosphocholine
DOPE	1,2-dioleoyl-sn-glycero-3-phosphoethanolamine
DREAM	DiffeREntial Evolution Adaptive Metropolis
DSPC	1,2-distearoyl-sn-glycero-3-phosphocholine
EM	electron microscopy
ESRF	European Synchrotron Radiation Facility
FA	fatty acid
FCC	face centered cubic
FEL	free electron laser
FWHM	full-width half-maximum
GISAXS	grazing incidence small-angle X-ray scattering
GIXD	grazing incidence X-ray diffraction

GPU	graphics processing unit
GUI	graphical user interface
HWHM	half-width half-maximum
LaB <sub>6</sub>	lanthanum hexaboride
laser	light amplification by stimulated emission of radiation
LED	light emitting diode
MA	methylammonium
MD	molecular dynamics
Mo	molybdenum
NIST	National Institute of Standards and Technology
OA	octylammonium
Pb	lead
PBS	phosphate-buffered saline
PC	phosphocholine
PCR	polymerase chain reaction
pdb	protein data bank
PDDF	pair distance distribution function
PL	photoluminescence
PSE	photostationary equilibrium
PSF	point spread function
RH	relative humidity
RNA	ribonucleic acid
ROI	region of interest
SAXS	small-angle X-ray scattering
S/B	signal-to-background
SC	simple cubic
SCP	secure copy
SDD	sample-to-detector distance
SEM	scanning electron microscopy

SLD	scattering length density
SOP	stack of plates
TEM	transmission electron microscopy
TTL	transistor–transistor logic
USB	universal serial bus
UV	ultraviolet
Vis	visible
VMD	visual molecular dynamics
XRD	X-ray diffraction
XRR	X-ray reflectometry
WAXS	wide angle X-ray scattering



Part I

INTRODUCTION, STRUCTURE RESOLVING  
TECHNIQUES AND BASIC THEORY



## INTRODUCTION

---

The human understanding of the world changed over time by the invention of revolutionary scientific techniques. A groundbreaking example is the development of the telescope which allowed humans to discover the universe for the first time. Furthermore, the invention of the microscope created a similarly significant impact by opening up a world which has not been accessible to the human eye before: the micro-scale. Finally, the application of this tool enabled scientists to observe cells. Over time, more and more new techniques like X-ray or electron microscopy were discovered and by now it is possible to resolve structures in the nanometer regime. However, current technical opportunities are no longer limited to observations. Various techniques have been developed to even build structures down to the nanoscale, either by top down or bottom up approaches via self-assembly. Figure 1.1 depicts a few of the biological and technical examples on the different length scales.

These discoveries and the ability to build structures on the nanoscale had a strong bearing on contemporary life. Modern computer technology, for instance, could not have transformed today's society without the fabrication of small transistors. More recent discoveries are graphene or quantum dots, which exhibit completely new properties and can only be explained by quantum mechanics. However, a breakthrough application does not exist yet. In the realm of biology, modern techniques were able to sequence the genome and to understand the functions within living organism down to the molecule. Of course, the knowledge is still incomplete, but the possibility to assemble structures in the same size as nature does enables a new way of thinking about medication and medical treatment. Naturally, progressions in science like these result in new risks and must always be weighed up against the benefits at hand.

Despite potential hazards, however, the nanoworld is in the focus of research nowadays. This interest is mirrored in the appearance of the "nano" topic in scientific journals, which increased since 2000 dramatically, see Figure 1.2. In 1990, only 15 publications had covered the nano topic, and it rose to 1180 in 2000 already. In 2016, the publication number reached over 19000 and therefore had risen by 1600% in merely 16 years. This publication number ranges significantly above the general growth rate in scientific publications which usually only doubles in number every 15 years [1]. An additional indication for the relevance of nano related topics is the recent Nobel Prize for super-resolution microscopy awarded in 2014 [2].

A key parameter for nanotechnology is the control of the structure, for medical application as well as for technology. However, the control of nanometer size objects can be a significant challenge as classical microscopy fails.

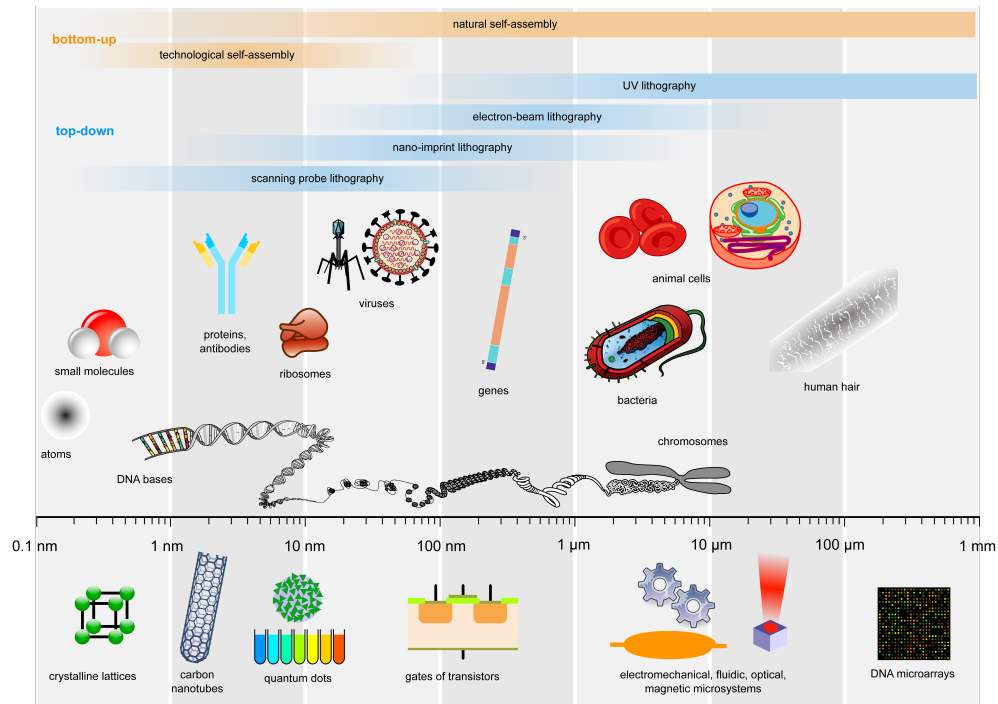


Figure 1.1: Visualization of length scales of biological assemblies and technological devices. On top the bottom-up and top-down techniques are shown, which are used for assembly of the structures. [source: Guillaume Paumier et al. is licensed under CC BY SA 2.5]

As mentioned above, several new techniques for structural control evolved and the most important ones will shortly be introduced in chapter 2; some amongst them are using X-rays. In contrast to the other techniques, X-rays have the major advantage of not needing any labels like fluorophores or staining to enhance the contrast for biological samples, which are studied with electron microscopy (EM). The first application of X-rays was imaging of the human body and it is still widely utilized for medical diagnosis. The development in nanofabrication, with Fresnel lenses, for example, enabled X-ray microscopy. Besides imaging, X-rays allow for scattering and diffraction. First, the high intensity of the diffraction of lattices was used to solve the structure of matter. With the development of sources and equipment, the application field broadened and the study of non-crystalline samples could be realized, with e. g. small-angle X-ray scattering (SAXS). With the ultra high brilliance of a new generation of free electron lasers (FELs) the study of single molecules might become feasible. More details about the history and application of X-rays can be found in section 2.4.

The advancement of the brilliance of synchrotrons, but also of in-house X-ray tubes was tremendous over the last decade. Furthermore, a new generation of detectors with single photon counting evolved. Especially these two advances made in-house SAXS become an interesting alternative to synchrotron beamtimes. Another significant factor for the growing field of SAXS is the increasing computing power, which makes more and more complex

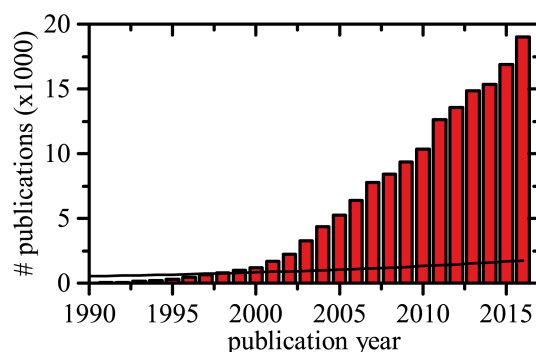


Figure 1.2: Number of publications per year with topic 'nano' starting from 1990. The solid black line indicates the general growth of scientific publications. [source: Thomas Reuters (Web of Science)].

models possible and therefore further information can be extracted.

One goal of this thesis was to build a state of the art SAXS setup, which due to its flexibility and can be used for a variety of applications. A detailed description of the setup with the reasoning behind the design is given in chapter 4. In the next step, the new setup was used to study several different nanomaterials. Three highlights of these samples are presented in the chapters 5 to 7. First, nanoplatelets of organometal halide perovskite were investigated by X-ray diffraction (XRD) in order to control the crystal structure of the nanoparticles and to estimate their size. A study with additional photoluminescence (PL), transmission electron microscopy (TEM) measurements and theoretical calculations was published [3] and is highly cited<sup>1</sup>. The second investigation on so-called deoxyribonucleic acid (DNA) origami was conducted. The SAXS measurements were evaluated in great detail and structural behavior of temperature as well as ionic strength change was analyzed. This work was also successfully published [5]. The third project deals with photo-switchable molecules, which mimic fatty acids (FAs) and lipids. The structural response upon illumination of bilayers, multilayers, and mixtures with natural lipids was measured and analyzed.

The quality of the built SAXS setup was verified with examples mentioned above and test measurements of common proteins [6]. Critical parameters of the setup such as resolution, signal-to-background (S/B) and radiation damage are addressed in chapter 4. Furthermore, the setup enables the study of many different nanomaterials, only three highlights are presented here. These examples profit from the unique properties of X-ray scattering in contrast to other common techniques which are introduced in the next chapter and therefore, prove the importance of X-ray scattering in the nanotechnology.

<sup>1</sup> As of January/February 2017, this highly cited paper received enough citations to place it in the top 1% of the academic field of Physics based on a highly cited threshold for the field and publication year. [4]



## MICROSCOPY AND SCATTERING TECHNIQUES

---

Understanding the structure of objects on the nanoscale is challenging because conventional light microscopes fail to resolve it as a consequence of Abbe's Law [7]:

$$d \geq \frac{\lambda}{NA} \quad (2.1)$$

where  $d$  is the minimal resolvable spacing,  $\lambda$  the wavelength of light and  $NA$  the numerical aperture of the lens of the microscope. Hence, it follows that typically the shortest resolvable distance is about  $\lambda/2$ , which is for green light about 250 nm. However, there are several approaches to overcome this diffraction limit.

### 2.1 SUPER-RESOLUTION MICROSCOPY

One approach is super-resolution microscopy, for which the Nobel Prize in Chemistry was awarded in 2014 [2]. This technique can resolve distances in the nanometer regime exploiting visible light. The super-resolution microscopy utilizes fluorophores for imaging and is, therefore, a fluorescence microscopy technique.

The image of a fluorophore is convoluted with a so-called point spread function (PSF). The full-width half-maximum (FWHM) of a PSF has the width of the resolution limit following Abbe's Law (Equation 2.1). There are two ways to overcome this resolution limit. The first one involves stochastic techniques which rely on switchable fluorophores. In this way the fluorophores can be isolated over time. The center of a single PSF of a fluorophore can be determined more precisely by fitting the intensity. The minimal resolvable distance  $\Delta r_s$  decreases with the number of photons  $N$  as shown in Equation 2.2.  $\Delta$  describes the FWHM of the PSF of a fluorophore, which is the resolution limited width.

$$\Delta r_s \approx \frac{\Delta}{\sqrt{N}} \quad (2.2)$$

There are several different techniques, which rely on the same principle. They differ in the mechanism, which turns the fluorophore on and off and the type of fluorophore used.

The second method consists of deterministic techniques. The stimulated emission depletion (STED) technique is the most prominent one belonging to this category. A diffraction limited excitation laser excites the fluorophore

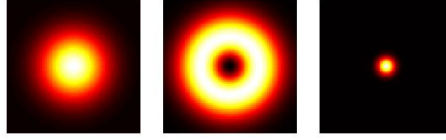


Figure 2.1: Display of excitation focus (left), de-excitation focus (center) and remaining fluorescence distribution in a STED microscope by Marcel Lauterbach is licensed under CC BY SA 3.

and a second light amplification by stimulated emission of radiation (laser) with a donut shape in the focus de-excites the fluorophores due to stimulated emission. In this way, the resulting fluorescence is smaller than the diffraction limited excitation like sketched in Figure 2.1. The resolvable distance  $r_d$  of a STED microscope can be estimated by Equation 2.3.

$$\Delta r_d \approx \frac{\Delta}{\sqrt{1 + I_{max}/I_T}} \quad (2.3)$$

$\Delta$  is the FWHM of the diffraction limited beam and  $I_{max}$  describes the maximal intensity of the second laser, which introduces the stimulated emission.  $I_T$  represents the threshold intensity, which is needed to achieve saturated emission depletion of the fluorophore.

In conclusion, all super-resolution microscopy techniques rely on fluorescence. On the one hand, this has the advantage that the fluorophores can be targeted and therefore selective visualization is possible. On the other hand, the effect of the fluorophore on the structure is not clear. Techniques with labels can potentially introduce artifacts. As for standard fluorescence microscopy, several other considerations like bleaching have to be taken into account [8].

## 2.2 ATOMIC FORCE MICROSCOPY

Atomic force microscopy (AFM) belongs to the scanning probe microscopy techniques. A tip probes the surface and the position of the tip is measured by a reflected laser beam with a photodiode. The sample is scanned with a piezoelectric motor in x-y direction. An AFM can be used in different operation modes, e. g. tapping or constant height, which depends on the nature of the sample. Besides imaging the topography of the surface, an AFM can be used for force measurements [9] and as a manipulation tool, e. g. for placing molecules in a desired position on the surface [10].

For imaging, the attainable resolution is determined by the tip size. Depending on the examined sample, a typical AFM can achieve a lateral resolution down to 10 nm. For example, deep holes or edges lead to tip artifacts. The vertical resolution is higher and is about 1 Å. The lateral resolution can be further increased by using smaller tips, e. g. for imaging of DNA with a tip size of 3 nm [11]. Under extreme conditions with ultrahigh vacuum at a

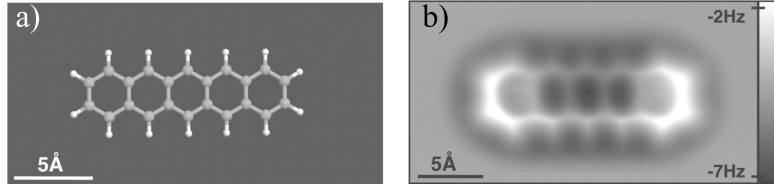


Figure 2.2: a) Chemical structure of pentacene b) high-resolution AFM image of pentacene with a CO-terminated tip. Reprinted with permission from AAAS [12].

temperature of 5 K and specialized tips, it is even possible to image single molecules (Figure 2.2).

However, the technique has some disadvantages. It is a surface based technique and hence the sample has to be bound or at least stick to a surface. Furthermore, the tip can introduce image artifacts due to the finite tip size. As a consequence of the piezo driven scanning process, the AFM technique is slow compared to e.g. EM. The slow speed can also lead to a drift of the sample during the measurement, which results in artifacts of the image. Since the tip contacts with the sample directly, it can also damage it and must frequently be exchanged due to degradation.

### 2.3 ELECTRON MICROSCOPY

Abbe's Law in Equation 2.1 shows that decreasing the wavelength may lead to an increase in the resolution. This idea is used for EM. Every particle has an associated wavelength, which is named De-Broglie wavelength. The Nobel Prize was awarded in 1929 "for his discovery of the wave nature of electrons" [13]. The wavelength of a particle is found by the momentum of the particle with Planck's constant  $h$ , shown in Equation 2.4.

$$\lambda = \frac{h}{p} = \frac{h}{\sqrt{2meV}} \quad (2.4)$$

Using the momentum of the electron with mass  $m$  and the elementary charge  $e$ , the wavelength of an electron is determined by the acceleration voltage  $V$ . Since electrons are considered as relativistic particles with a typical acceleration voltage  $V$  of 100 keV, the formula in Equation 2.4 has to be modified by a relativistic correction. Even with this correction, the wavelength of an electron with an acceleration voltage of 100 keV is 3.7 pm and appears much smaller than the atomic radius of hydrogen. Therefore, EM is not limited by the wavelength.

A variety of techniques exist for EM, but only the most common ones for imaging will be introduced in this thesis: scanning electron microscopy (SEM), TEM and nowadays cryo-electron microscopy (cryo-EM). SEM counts as a raster scanning technique. The electron beam is focused on the surface and secondary electrons, which get excited from the primary beam and leave the sample, are detected. The energy of the secondary electrons depends on the type of material. Hence, with an energy sensitive detector the material can

be identified. The measurements are fast and have a high field of view in the order of square millimeters. In contrast to the AFM, the image is only a 2-dimensional projection. Furthermore, the high energy electrons destroy the sample, which is especially the case for biological specimens. Another drawback is that this technique is only feasible in a high vacuum environment and that the sample needs to be dry. Samples are often prepared with a thin gold layer which increases the number of secondary electrons.

A TEM has the same working principle like a conventional light microscope but uses electrons instead of photons for imaging. Due to the high interaction of the electrons with the sample, the absorption is high and samples have to be extremely thin (10 - 100 nm). However, small biological samples are often stained with heavy elements like uranyl acetate since otherwise, the contrast would be too low. Moreover, it helps to fix the sample on a grid. The uranyl acetate is imaged because it has a high electron density. Hence, the cover of the actual sample is visualized, which can introduce artifacts.

The cryo-EM technique has the same working principle like a TEM, but the sample is shock frozen before the measurement. Low temperatures increase the resolution because the thermal movement of the sample is minimized. If the sample is distributed randomly in different orientations, even a 3-dimensional reconstruction with about nanometer resolution is possible, for example of DNA objects [14].

## 2.4 X-RAY

Another way to study nanomaterials is to use the wavelength of an electromagnetic wave, which is short enough to decrease the resolution limit. X-rays, for instance, fulfill this requirement. However, microscopy is difficult with X-rays because the refraction index of most media is almost one,  $n \approx 1 - 10^{-5}$ , and therefore X-ray optics are more complicated to manufacture and need more space than for visible light. X-ray microscopy started in the 1970s with soft X-rays below 1 keV, but recent technology advances like nanofabrication and 3rd and 4th generation X-ray sources improved the quality of images significantly, also for hard X-rays [15].

In order to understand ordered or crystalline structures, X-ray diffraction is a well established technique for more than 100 years. With the advancement of technology and theory, X-ray scattering on less ordered or unordered systems became possible. The disadvantage of X-ray scattering is that it is an indirect measurement technique, which relies on models. Therefore, often data of imaging techniques, e. g. EM, function as verification for the results of X-ray scattering measurements.

### 2.4.1 *History of X-ray Scattering*

X-ray radiation was discovered by Wilhelm C. Röntgen in 1895 and is therefore called "Röntgenstrahlung" in German. He was awarded the first Nobel Prize in Physics in 1901 [16]. The discovery of the X-ray radiation had a

enormous impact on the scientific society and was followed by many applications and discoveries, which earned succeeding Nobel Prizes in the 1910s. First, Max von Laue was awarded "for his discovery of the diffraction of X-rays by crystals" in 1914 [17]. One year later, Sir William Henry Bragg and his son were honored with the Nobel Prize "for their services in the analysis of crystal structure by means of X-rays" [18]. In 1917, Charles Glover Barkla received the prize "for his discovery of the characteristic Röntgen radiation of the elements"[19]. His discovery took already place before von Laue's and Bragg's observation. The benefit of the discovery of X-ray radiation was immense as, for example, the structure of DNA could be determined [20, 21]. The original X-ray diffraction image is shown in Figure 6.1.

One sub-field was small-angle X-ray scattering (SAXS), which emerged in the late 1930s. It provides information in the size regime of a few nanometers up to hundreds of nanometers. Therefore, it is well suited for the study of macromolecules or nanoparticles.

#### *History of Small-Angle X-ray Scattering*

The Debye equation was described in 1915 and expresses the scattering intensity of a collection of atoms as the sum of the interactions between single atoms. Due to the extremely large sum, the lack of computing power depicted an unsurmountable obstacle at that time. Instead, research concentrated on the scattering of crystals [22]. With increasing computing power, it moved more and more into the foreground and stipulated the cornerstone for example for pair distance distribution function (PDDF) analysis described in section 3.3.2. In 1939 André Guinier introduced an approximation for low scattering angles with the radius of gyration as a measure of the size of a particle [23]. Results could already be obtained with a linear fit and therefore no computing power was necessary declaring it as a standard analysis technique in SAXS. More details are presented in section 3.3.1. The next milestone in the history of SAXS was the publication of Debye and Bueche in 1949. They established the analysis of scattering by inhomogeneities and introduced the current method for displaying scattering intensities using the scattering vector [24]. Between 1949 and 1957, SAXS was formally developed with many contributions from Porod, Debye, and Kratky. The advent of synchrotron radiation in the 1970s was a substantial next step for SAXS because high-intensity sources were needed due to the low scattering intensity of disordered objects compared to crystals. A new analysis tool using indirect Fourier transform, introduced by Otto Glatter in 1977 [25], enabled a routine usage of the PDDF. The new computing power starting in the 1980s fostered the application of numerous software applications to analyze SAXS data with increased detail. The GNOM software was launched, which can efficiently calculate the PDDF [26]. The software CRY SOL can simulate scattering intensities of atomistic models with protein data bank (pdb) files [27]. Between 1998 and 2001 many *ab initio* model methods were established, which, for example, apply beads to determine the envelope of molecules [28–31].

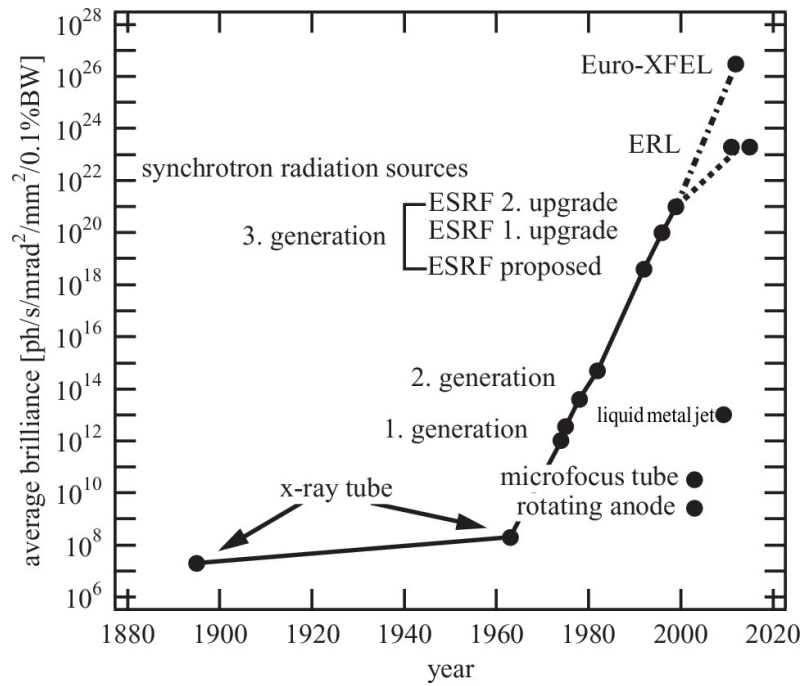


Figure 2.3: The evolution of brilliance of synchrotrons and laboratory X-ray sources. Reprinted from [33], with the permission of AIP Publishing.

#### 2.4.2 Evolution of X-ray Sources

Although the first results of X-ray scattering on DNA or crystals were remarkable, the applications of X-ray tubes were limited due to their rather low intensity. An alternative source grew out of the work on particle accelerators. In 1947, the first synchrotron radiation was observed, but only in the visible and ultraviolet (UV) region due to the low energy of the storage ring [32]. It was first considered a nuisance because the particles lose energy in the process, but it was then recognized in the 1960s for the special properties of the light that overcame the shortcomings of common X-ray tubes. In the mid- to late 1970s, the idea arose to exploit synchrotrons to produce extremely bright X-rays. These discussions led to the construction of the first dedicated synchrotron sources. In the late 1980s and early 1990s, the European Synchrotron Radiation Facility (ESRF) and shortly after that two other “third-generation” synchrotrons (Advanced Photon Source (APS) in the USA and SPring-8 in Japan) were built. Fourth-generation X-ray sources are the so called free electron lasers (FELs). How the brilliance evolved from first X-ray tubes to state of the art synchrotron sources is sketched in Figure 2.3. The brilliance also considers the divergence and the size of the beam and spectral width besides the intensity. Not only the brilliance of the synchrotrons sources evolved but also the lab sources experienced a remarkable improvement. The brilliance of different in-house X-ray sources is given in Table 2.1. The technique of the rotating anode reduced the power load per area on the anode and led to a six times increased intensity. The next step was the development of microfocus tubes, which focus the electrons on the

System	Brilliance $\times 10^9$ (photons/(s mm <sup>2</sup> mrad))
Standard sealed tube	0.1
Standard rotating-anode generator	0.6
Microfocus sealed tube	2.0
Microfocus rotating-anode generator	6.0
State-of-the-art microfocus rotating-anode generator	12
Excillum JXS-D1-200 (liquid metal source)	26

Table 2.1: Brilliance of laboratory X-ray sources [36].

anode material. In this way, the collimation of the beam in both directions is possible, which decreases the divergence significantly. The brilliance is increased in spite of fewer photons produced due to a lower power because otherwise, the anode material would melt. Again the brilliance can be increased with a rotating anode. Recently, the liquid metal source was introduced. A proof of principle of this technique was shown in 2003 [34] and a first prototype was shipped in 2010 [35]. The principle is similar to a microfocus tube: An electron beam is focused on a small spot on the anode. The difference is that instead of a solid anode material, a liquid metal is used. Therefore, the power load can be increased significantly, which leads to a five to ten times higher generation of photons compared to microfocus tubes. Gallium and indium alloys are commercially used as anode materials. The corresponding  $K_{\alpha}$  lines are 9.2 keV and 24.2 keV, respectively.



## X-RAY SCATTERING THEORY FOR SAXS AND DIFFRACTION

---

The books of Als-Nielsen and MacMorrow [37], de Jeu [38], and Guinier [39] provide the main basis for this chapter. For more details on X-ray diffraction, the book of Warren is suggested [40] and for more details on SAXS it is referred to the book of Guinier and Fournet [41]. A quick guide for beginners in SAXS is the SAXS Guide [42].

### 3.1 X-RAY GENERATION

All conventional X-ray sources like sealed, microfocus or liquid metal tubes are based on the same working principle. Electrons are accelerated with a high voltage of up to 160 kV on the anode. The decelerated electrons produce a continuous broad spectrum, also called Bremsstrahlung, because the lost kinetic energy is converted into photons. However, most of the energy is transferred to heat. Additionally, characteristic radiation of the target material is emitted because some of the accelerated electrons excite inner shell electrons of the anode material. Electrons of other shells fall back to the ground state and emit photons with the corresponding energy. The transition from L to K shell is called  $K_\alpha$  radiation and from M to K shell is the  $K_\beta$  radiation. Both split due to the spin in  $K_{\alpha_{1,2}}$  and  $K_{\beta_{1,2'}}$ , respectively. The intensity of the  $K_\alpha$ -line is higher than the  $K_\beta$ . The behavior of the intensity of the K-line can be estimated with Equation 3.1.

$$I_K(V) = ci(V - V_K)^n \quad (3.1)$$

$I_K$  is the intensity of the  $K_\alpha$ -line and  $V_K$  the corresponding energy of the  $K_\alpha$ -line. The factor  $c$  is a constant proportionality factor and  $i$  is the electron beam current. The exponent is  $n \approx 1.5$  for  $V < 2V_K$  and goes to 1 for  $V > 2V_K$ . For the same power of the tube, first, the voltage should be increased and then the current because of the nonlinear behavior.

For monochromatic radiation, an optic is necessary to separate one energy from Bremsstrahlung and the different K-lines. Usually, the Bragg condition (Equation 3.31) is used either by a multilayer mirror or a single crystal like silicon to obtain monochromatic radiation.

Synchrotron radiation is achieved by accelerating electrons on a ring at relativistic speeds. The radiation cone has an opening angle of  $1/\gamma$  like sketched in Figure 3.1. The characteristic features of synchrotron radiation are given by the cyclic frequency  $\omega_0$  and  $\gamma = E_e/mc^2$ , which is the electron energy in units of the rest mass. The radius of the synchrotron is determined

*For a detailed mathematical description: Classical Electrodynamics from Jackson [43]*

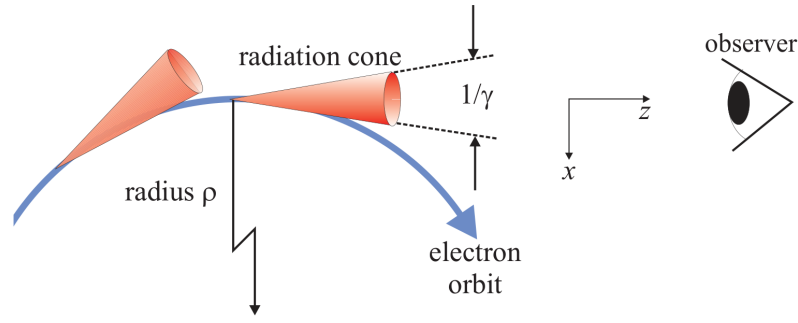


Figure 3.1: The trajectory of an electron is approximated by a circle of radius  $\rho$ . The radiation is confined to a narrow cone with an opening angle of  $1/\gamma$  around the instantaneous velocity. Reused with permission from [37].

by the electron energy and the magnetic field  $B$  of the bending magnets and can be written in practical units as:

$$\rho[m] = 3.3 \frac{E_e[\text{GeV}]}{B[\text{T}]} \quad (3.2)$$

This leads for the ESRF to a radius of 24.8 m with its electron energy  $E_e$  of 6 GeV and a magnetic field of 0.8 T. The characteristic frequency of a synchrotron is  $\omega_c = 3/2\gamma^3\omega_0$ , which depends on the cyclic frequency and must be corrected due to the relativistic speed of the electron. The critical energy of the storage ring results in:

$$E_c = \hbar\omega_c = 0.665 \cdot E_e[\text{GeV}]^2 \cdot B[\text{T}] \quad (3.3)$$

The brilliance spectrum of bending magnets is a universal function of the photon energy and the critical energy of the ring and is given in Figure 3.2. It scales with the square of the electron energy and linearly with the current in the storage ring. In the example of the ESRF, the critical energy is 19.2 keV. The opening angle is  $1/\gamma = 5.11 \cdot 10^5 / 6 \cdot 10^9 = 0.08 \text{ mrad}$ . The peak flux of these values is

$$\text{Flux} = B \cdot \Delta\theta^2 \cdot E_c^2 \cdot I_e \text{ Ph/s/}0.1\% \text{ BW} = 9 \cdot 10^{12} \text{ Ph/s/}0.1\% \text{ BW} \quad (3.4)$$

with the peak brilliance  $B$  shown in Figure 3.2 at about  $0.835 \cdot E_c$ , which is in the example of the ESRF about 16 keV.  $\Delta\theta$  is the divergence of the beam and  $I_e$  is the electron current in the ring.

Modern synchrotron sources utilize insertion devices, wiggler or undulator. A wiggler can be seen as a series of bending magnets, which leads to an enhancement in the intensity of the observed radiation by a factor  $2N$ , where  $N$  is the number of periods in the wiggler. An undulator has also alternating magnets and forces the electrons to oscillate. In contrast to the wiggler, the amplitude of these oscillations is small and the emitted radiation from one oscillation is in phase with the next one. The coherent addition of the amplitudes is only valid at one particular wavelength (and its harmonics) and the

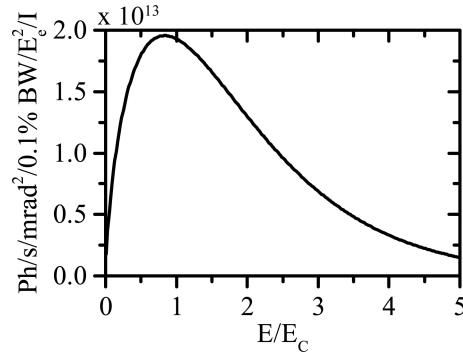


Figure 3.2: Energy dependency of the brilliance of synchrotron radiation of a bending magnet. The values are given in terms of the critical energy of storage ring  $E_c$ .

intensity is increased by  $N^2$ . An important parameter, which describes the undulator, is  $K$ , which is defined in Equation 3.5.

$$K = 0.934\lambda_u[cm]B_0[T] \quad (3.5)$$

It depends on the magnetic field  $B_0$  of the undulator and the spatial period  $\lambda_u$ , which is of the order of 1 cm. The photon wavelength of the first harmonic can be calculated with Equation 3.6.

$$\lambda_1 \approx \frac{\lambda_u}{2\gamma^2} \left(1 + \frac{K^2}{2}\right) \quad (3.6)$$

For this approximation, it was assumed that the observation is on the same axis as the undulator axis. Since  $\gamma \propto E_e$ , a higher ring energy leads to shorter wavelengths of photons. Furthermore, the energy of the harmonics can be tuned with the magnetic field  $B_0$ . For an undulator, the divergence of the X-ray beam is also lower than for a bending magnet or wiggler. It is proportional to  $1/\sqrt{N}\gamma$ . This dependency also leads to a highly increased brilliance compared to bending magnets and wigglers.

Beside the brilliance, the coherence length is another defining parameter of an X-ray source. It is a measure for a distance, for which two electrons or particles can interfere constructively. The transverse coherence length is limited by the divergence  $\Delta 2\theta$  of the X-ray beam.

$$L_T = \frac{\lambda}{2 \tan \Delta 2\theta} \approx \frac{\lambda}{2\Delta 2\theta} \quad (3.7)$$

The longitudinal coherence length is limited by energy resolution of the source.

$$L_L = \frac{\lambda^2}{2\Delta\lambda} \quad (3.8)$$

$\Delta\lambda$  is the resolution in X-ray wavelength of the source. In the case of X-ray tubes the resolution is limited by the splitting of the  $K_\alpha$ -lines.

## 3.2 BASIC SCATTERING BY PARTICLES

In X-ray scattering the data is often shown with the momentum transfer vector  $\vec{q}$  given by the incident  $\vec{k}_i$  and final wave vector  $\vec{k}_f$ .  
*Books describe  $q$  also as  $Q$ ,  $s$ ,  $h$  or  $k$ .*

$$\begin{aligned}\vec{q} &= \vec{k}_f - \vec{k}_i \\ q &= \frac{4\pi}{\lambda} \sin\left(\frac{2\theta}{2}\right)\end{aligned}\quad (3.9)$$

For elastic scattering with  $|k_i| = |k_f|$ , the simple description for the absolute value of  $\vec{q}$  in Equation 3.9 holds for the scattering angle  $2\theta$  and wavelength  $\lambda$  of the X-rays.

The scattering intensity of particles with the experimental parameters of the incident intensity  $I_0 = \Phi_0 A$  in photons/s with the flux per area  $\Phi_0$  in photons/s/cm<sup>2</sup>, the cross section of the beam  $A$ , the sample volume  $V_S = At$  with sample thickness  $t$ , the sample transmission  $T$ , the detector efficiency  $\epsilon$  and solid angle covered by the detector  $\Omega$  is given in Equation 3.10.

$$I(\vec{q}) = I_0 t T \epsilon \Omega \frac{d\Sigma}{d\Omega}(\vec{q}) \quad (3.10)$$

The experimental parameters are basically scaling factors of the intensity, see section 3.3.3. The differential cross section  $\frac{d\Sigma}{d\Omega}(\vec{q})$  is the only  $q$ -dependent factor in Equation 3.10 and is given in Equation 3.11.

$$\frac{d\Sigma}{d\Omega}(\vec{q}) = V_s^{-1} \left| \int_{V_s} \rho(\vec{r}) e^{i\vec{q}\cdot\vec{r}} d\vec{r} \right|^2 \quad (3.11)$$

$\rho(\vec{r})$  is proportional to the electron density of the sample and is integrated over the whole sample taking the phase into account. It has the form of a Fourier transform of the electron distribution and is used in the same form for atoms as well as for particles. Often the integral is described by a single particle form factor  $F(\vec{q})$  like shown in Equation 3.12 and 3.13.

$$\frac{d\Sigma}{d\Omega}(\vec{q}) = V_s^{-1} |\Delta\rho V_p F(\vec{q})|^2 \quad (3.12)$$

In the definition of the form factor in Equation 3.12, the scattering contrast  $\Delta\rho = \rho_p - \rho_M$  is introduced. Therefore, a uniform electron density within the particle  $\rho_p$  and the medium  $\rho_M$  is assumed. The integration takes place over the particle volume  $V_p$  and is normalized.

$$F(\vec{q}) = \frac{1}{V_p} \int_{V_p} e^{i\vec{q}\cdot\vec{r}} d\vec{r} \quad (3.13)$$

The intensity of a single particle can be expressed without experimental parameters of the setup and is typically shown as given in Equation 3.14 in the literature. The intensity is proportional to  $V_p^2$  and  $\Delta\rho^2$ . Therefore, samples with high electron density or large particles have a high scattering intensity.

$$I_p(\vec{q}) = V_p^2 \Delta\rho^2 |F(\vec{q})|^2 \quad (3.14)$$

If the particles are in solution, they are freely distributed and all orientations of the particle contribute to the scattering. Therefore, the radial averaged form factor  $P(q)$  is used.

$$\begin{aligned} P(q) &= \langle |F(\vec{q})|^2 \rangle \\ &= \int_{\phi=0}^{2\pi} \int_{\theta=0}^{\pi} |F(q \sin \theta \cos \phi, q \sin \theta \sin \phi, q \cos \theta)|^2 \cdot \sin \theta d\theta d\phi \end{aligned} \quad (3.15)$$

The brackets  $\langle \dots \rangle$  indicate the isotropic orientational average and the integration is typically carried out in spherical coordinates.

Normally the sample is not monodisperse. The polydispersity is modeled with a particle size distribution function  $D(R)$  with the radius  $R$  of the particle.

$$I(q) = \Delta\rho^2 \int_0^{\infty} D(R) V_P(R)^2 P(q, R) dR \quad (3.16)$$

The particle size distribution is normalized  $\int_0^{\infty} D(R) dR = 1$ .

### 3.3 SMALL-ANGLE X-RAY SCATTERING

Due to the orientational average in SAXS measurements, detailed information gets lost and therefore it can be of great advantage to order the sample, for instance, by binding it to a surface. However, still much information can be gained from the averaged data with rather simple methods shown in the next sections.

#### 3.3.1 Guinier and Porod Regime

The simplest case for a geometric form factor is a sphere, which is shown in Equation 3.17. It is one of the few cases for which it can be calculated analytically.

*This section is summarized from Elements of Modern X-ray Physics, Second Edition [37].*

$$\begin{aligned} F(q) &= \frac{1}{V_P} \int_0^{2R} \int_0^{2\pi} \int_0^{\pi} e^{iqr \cos \theta} r^2 \sin \theta d\theta d\phi dr = \frac{1}{V_P} \int_0^R 4\pi \frac{\sin(qr)}{qr} r^2 dr \\ &= 3 \left[ \frac{\sin(qR) - qR \cos(qR)}{(qR)^3} \right] = \frac{3J_1(qR)}{qR} \end{aligned} \quad (3.17)$$

$J_1(x)$  is the Bessel function of the first kind. In the limit for  $qR \rightarrow 0$ , the Taylor expansion of the form factor of a sphere yields

$$\begin{aligned} F(q) &\approx \frac{3}{(qR)^3} \left[ qR - \frac{(qR)^3}{6} + \frac{(qR)^5}{120} - \dots - qR \left( 1 - \frac{(qR)^2}{2} + \frac{(qR)^4}{24} - \dots \right) \right] \\ &\approx 1 - \frac{(qR)^2}{10} \approx e^{-(qR)^2/10} \end{aligned} \quad (3.18)$$

For the scattering intensity follows in the exponential form

$$I(q) \approx V_P^2 \Delta\rho^2 e^{-(qR)^2/5} \quad (3.19)$$

Dimension (shape)	Radius of gyration $R_G$	Porod exponent $n$
d=3 (sphere)	$\sqrt{\frac{3}{5}}R$	-4
d=2 (disc)	$\sqrt{\frac{1}{2}}R$	-2
d=1 (rod)	$\sqrt{\frac{1}{12}}L$	-1

Table 3.1: Radius of gyration and Porod exponent for objects of different dimensionality.

Higher orders than  $(qR)^2$  can be neglected and  $qR \ll 1$ . Thus, for a sphere the radius can already be determined by low  $q$ -values by the slope of a plot of  $\ln[I(q)]$  vs.  $q^2$ , which is called a Guinier plot.

The so-called Guinier analysis can be applied not only to spheres but to any dilute system containing particles of arbitrary shape. In this case, the radius of the sphere has to be replaced by a more general measure of the particle size, known as the radius of gyration. The radius of gyration  $R_G$  of a particle is defined as the root-mean-squared distance from the particle's center of mass:

$$R_G^2 = \frac{\int_{V_p} \rho(\vec{r}) r^2 d\vec{r}}{\int_{V_p} \rho(\vec{r}) d\vec{r}} \quad (3.20)$$

These integrals have to be evaluated first and then an orientational average has to be performed. Usually, numerical methods allow for this, but one exception is the sphere with the result  $R_G^2 = \frac{3}{5}R^2$ . Other exceptions are shown in Table 3.1 with the corresponding dependencies of the radius of gyration. By using Equation 3.19, the typical expression for the Guinier analysis results in

$$I(q) = V_p^2 \Delta\rho^2 e^{-(qR_G)^2/3} \quad (3.21)$$

Since the small angle approximation is only valid if  $qR_G$  is small, typically a  $q$  range threshold of  $qR_G$  smaller than 1 or 1.3 is used [44, 45].

The second approximation is for  $qR \gg 1$ , but the  $q$ -range is still lower than the inter-atomic spacings. It is known as Porod analysis. In this case the expansion of the form factor is

$$F(q) = 3 \left[ \frac{\sin qR}{(qR)^3} - \frac{\cos qR}{(qR)^2} \right] \approx 3 \left[ -\frac{\cos qR}{(qR)^2} \right] \quad (3.22)$$

Since the first term has a  $1/(qR)^3$  and the second term a  $1/(qR)^2$  dependency, only the second term remains in the limit for  $qR \gg 1$ . For  $qR \gg 1$ ,  $\cos^2 qR$  oscillates as function of  $q$  with an average value of 1/2 and therefore the intensity can be written as

$$I(q) = 9V_p^2 \Delta\rho^2 \frac{1}{2} \frac{1}{(qR)^4} \quad (3.23)$$

which can also be expressed in terms of the surface  $S_P = 4\pi R^2$  of a sphere by using  $V_P^2 = [(4\pi/3)R^3]^2 = (4\pi/9)R^4 S_P$ :

$$I(q) = \frac{2\pi\Delta\rho^2}{q^4} S_P \quad (3.24)$$

Therefore, it is proportional to the surface of the sphere, but it has always a  $q^{-4}$  behavior. In fact, the variation of intensity with  $q$  in the Porod regime turns out to depend on the shape of the particle, including its dimensionality. This is already notable in the form factor in Equation 3.13 because the integral is over the particle volume. For the sphere, this is  $dV_P = 4\pi r^2 dr$  as used in Equation 3.17. In a infinitesimal thin disc, it is already reduced to  $dA_P = 2\pi r dr$ . These differences in the form factor lead to a different behavior in the Porod regime. The asymptotic  $q$  dependence of the form factor is such that  $|F(q)|^2 \propto q^{-n}$  and  $n$  is called Porod exponent. The behavior for different dimensions is summarized in Table 3.1.

### 3.3.2 Pair Distance Distribution Function

The Debye Equation was introduced by Debye in 1915.

$$I(q) = \sum_i^n \sum_j^n f_i f_j \frac{\sin qr_{ij}}{qr_{ij}} \quad (3.25)$$

The atomic form factors  $f_{i,j}$  are calculated the same way as the form factor introduced in Equation 3.13 using the electron distribution of an atom for the calculation. The sums are taken over all atoms in the particle and  $r_{ij} = |\vec{r}_i - \vec{r}_j|$ . The number of atoms is usually too high to calculate the whole sum and the SAXS data quality is not high enough to extract all atomic spacings due to orientational averaging. Nowadays with increased computing power, the Debye Equation is used in software [46].

Another approach is to apply the correlation function  $\gamma$  of the particle, which was first introduced by Debye and Bueche in 1949 [24]. It describes the distances within the particle and the scattering intensity can be calculated in the following way:

$$I(q) = 4\pi \int_0^\infty \gamma(r) \frac{\sin qr}{qr} r^2 dr \quad (3.26)$$

$$\gamma(r) = \langle \rho(\vec{r}) * \rho(-\vec{r}) \rangle$$

$*$  is a convolution and  $\langle \dots \rangle$  is the average. The self-convolution of the electron density distribution  $\gamma(r)$  for a distance higher than the maximal distance  $D_{max}$  within the particle is zero and therefore the intensity results in:

$$I(q) = 4\pi \int_0^{D_{max}} \gamma(r) r^2 \frac{\sin qr}{qr} dr \quad (3.27)$$

Beside the correlation function, the pair distance distribution function  $p(r) = \gamma(r)r^2$  is widely used for the analysis of particles with SAXS. By using Equation 3.27 the scattering intensity can be fitted by varying the correlation function or the pair distance distribution function. It can provide information

*This part is summarized from Structure Analysis By Small-Angle X-ray and Neutron Scattering [44].*

about the shape of the particle, e. g. spherical against elongated. Furthermore, distances can be measured, e. g. the distance between two linked gold nanoparticles (AuNPs) [47].

### 3.3.3 Absolute Intensity

For the absolute intensity, the data must be normalized by characteristics of the setup like beam size or incident flux. So far, the scattering length density (SLD) was only introduced as a measure of the electron density. For the absolute intensity a precise definition is required:

$$\rho = \sum_i f_i \cdot r_0 / V_P \quad (3.28)$$

All atomic form factor  $f_i$  within the particle are summed and normalized by the volume of the particle  $V_P$ . The atomic form factor is thus proportional to the number of the electrons and  $r_0$  is the Thomson scattering length, which is a measure for the scattering of a single electron. It is also referred to as the classical electron radius and  $r_0 = e^2 / 4\pi\epsilon_0 m_e c^2 \approx 2.82 \cdot 10^{-13} \text{ cm}$  with the elementary charge  $e$ , mass of the electron  $m_e$ , the vacuum permittivity  $\epsilon_0$  and the speed of light  $c$ . The unit of the SLD is  $1/\text{cm}^2$  or  $1/\text{\AA}^2$  and the  $\Delta\rho$  used above is the difference in SLD between medium and particle. Note that the SLD of X-rays is defined by multiplying the electron density in electrons/ $\text{\AA}^3$  of the material by  $2.82 \cdot 10^{-5} \text{ \AA}$ .

In Equation 3.14, the intensity is given per unit volume and for the experimental intensity, the cross section is normalized by the illuminated volume  $V_S$ . Therefore, the unit of the intensity on the absolute scale is  $1/\text{cm}$ . The measured intensity is given in Equation 3.10 for a given measurement time. The unit of the intensity depends on the detector type. In the case of a single photon detector, it is photons/s. The measured data must, therefore, be divided by the factor

$$f = I_0 t T \epsilon \Omega t_m \quad (3.29)$$

with the same definitions as in Equation 3.10 and  $t_m$  the measurement time. Usually the intensity is evaluated per pixel and this results in  $\Omega = A_{\text{pixel}} / D^2$  for the solid angle with the pixel size  $A_{\text{pixel}}$  and the sample-to-detector distance (SDD)  $D$ . If the detector can measure the direct beam because the intensity is below the nonlinear regime of the detector, the other factor  $I_0 T \epsilon$  can directly be determined by measuring the direct beam with the sample in the beam. Consequently, the absolute intensity can be calculated with this information if the sample thickness  $t$  is also known. Instead of measuring the direct beam, calibration standards with known intensity are often used for calibration. Many different calibration standards exist, amongst them glassy carbon or water [48].

If the intensity is calibrated to the absolute intensity  $I_{\text{absolute}}$ , the molecular

weight  $M$  or the concentration  $c$  of the particle can be extracted like shown in Equation 3.30.

$$I_{absolute}(q) = \frac{d\Sigma}{d\Omega}(q) = c(\Delta\rho)^2(M/N_A)P(q) \quad (3.30)$$

$N_A$  is the Avogadro constant. A detailed derivation with other applications can be found in literature [49].

### 3.4 DIFFRACTION BY CRYSTALS

Crystals have an important role in the history of X-ray diffraction because crystals exhibit high-intensity peaks in the scattering pattern. Therefore, they have been studied for a long time and it was discovered that a lot of materials have a crystalline structure. There are many types of lattices, which can be categorized by the so-called Bravais lattices. The simplest form is the cubic structure. A crystal can always be described by a unit cell and basis vectors, which already can define the whole crystal. The lattice vectors define the crystal in real space. In a crystal several different lattice planes exist, which can be described by the Miller indices  $h, k$  and  $l$ . A lattice can also be described by the reciprocal lattice.

*A detailed description of lattices and Miller indices can be found in various textbooks, e. g. [37, 50].*

The Bragg condition determines the occurrence of peaks according to the lattice structure.

$$n\lambda = 2d \sin \theta \quad (3.31)$$

with the X-ray wavelength  $\lambda$ , order of diffraction  $n$ , scattering angle  $\theta$ , and distance  $d$ .

In the following a detailed description of scattering of lattices is presented, which takes care of the form factor of single particles within the lattice and makes some corrections, e. g. diffuse scattering. The following theory was described by Yager et al. [51].

The most basic description of the scattering of a crystal is the lattice sum (Equation 3.32), which adds the contributions of all electrons taking the phase into account.

$$I(\vec{q}) = \left| \sum_{n=1}^{N_n} \sum_{j=1}^{N_j} \sum_{p=1}^{N_p} \rho_{njp} e^{i\vec{q} \cdot \vec{r}_{njp}} \right|^2 = \left| \sum_{n=1}^{N_n} e^{i\vec{q} \cdot \vec{r}_n} \sum_{j=1}^{N_j} e^{i\vec{q} \cdot \vec{r}_j} \sum_{p=1}^{N_p} \rho_p e^{i\vec{q} \cdot \vec{r}_p} \right|^2 \quad (3.32)$$

The vector  $\vec{r}_{njp} = \vec{r}_n + \vec{r}_j + \vec{r}_p$  points to all electrons and is split in three parts. The first vector  $\vec{r}_n$  points to the unit cell, the second  $\vec{r}_j$  to the atom or particle within the cell and  $\vec{r}_p$  to all electrons within the atom or particle. The last sum is the atomic form factor, or just form factor written as sum and not as integral like in Equation 3.13. So far in section 3.2 and 3.3, this was the only part which was considered because for SAXS often the assumption of isolated particles can be made. Within lattices this is not possible anymore

and a structure factor is introduced. One possible representation for the scattering intensity of a lattice is shown in Equation 3.33.

$$I(q) = \frac{N_n}{\Omega q^{d-1}} \sum_{\{hkl\}} m_{hkl} \left| \sum_{j=1}^{N_j} F_j(M_j \cdot \vec{q}_{hkl}) e^{i\vec{q} \cdot \vec{r}_j} \right|^2 L(q - q_{hkl}) = cZ_0(q) \quad (3.33)$$

$$Z_0(q) = 1/q^2 \sum_{\{hkl\}} m_{hkl} \left| \sum_{j=1}^{N_j} F_j(M_j \cdot \vec{q}_{hkl}) e^{2\pi i(x_j h + y_j k + z_j l)} \right|^2 L(q - q_{hkl})$$

The function  $L$  represents a Bragg peak and can be, for example, a Gauss or Lorentz function. The peak positions are evaluated assuming a certain lattice type and are represented by  $q_{hkl}$ . The multiplicity  $m_{hkl}$  is also taken into account. The orientation of the particle is included, which is done with a corresponding rotation matrix  $M_j$ . The phase within the unit cell is respected, which can lead to systematic vanishing of peaks, and the sum is over all  $N_j$  atoms/particles in the unit cell. The prefactor consists of the number of unit cells  $N_n$  and the Lorentz factor  $\Omega q^{d-1}$  for  $d$ -dimensional lattice with the solid angle  $\Omega$ . The Lorentz factor considers geometrical factors related to the orientation of crystal planes.  $Z_0$  is shown for a 3-dimensional lattice and the prefactor  $\frac{N_n}{\Omega}$  is represented by a constant  $c$ . In practice, the factor  $c$  is used as scaling factor for a variety of effects, e. g. concentration of scattering objects for solution scattering.

The peak positions of a rhombohedral lattice with the Miller indices  $h, k$  and  $l$  are

$$q_{hkl} = 2\pi a / \sqrt{\frac{1 - 3 \cos^2 \alpha + 2 \cos^3 \alpha}{(h^2 + k^2 + l^2) \sin^2 \alpha + 2(hk + kl + hl)(\cos^2 \alpha - \cos \alpha)}} \quad (3.34)$$

All peaks can be determined by the lattice constant  $a$  and the inclination angle  $\alpha$  of the unit cell.

Typically, the form factor is not included in the structure factor because the orientation plays no role for an isotropic atom for instance. Therefore, the scattered intensity can be written as a product of the radial averaged form factor  $P(q)$  and the structure factor  $S_0(q)$  like shown in Equation 3.35.

$$I_0(q) = P(q)S_0(q) \quad (3.35)$$

With the definition of the structure factor like shown in Equation 3.36, the orientation of the particles in the unit cell is included and the scattering intensity is the same as described in Equation 3.33.

$$S_0(q) = \frac{cZ_0(q)}{P(q)} \quad (3.36)$$

The intensity can be corrected for diffuse scattering and polydispersity of the particles. These two effects are included in Equation 3.37.

$$I(q) = P(q) \left[ \frac{cZ_0(q)}{P(q)} G(q) + 1 - \beta(q)G(q) \right] \quad (3.37)$$

Fluctuations (e. g. thermal) of the particle positions within the unit cell lead to lattice disorder. This disorder causes a lowering of intensity of structural peaks (especially for higher orders) and is defined as  $G(q) = \exp(-\sigma_D^2 a^2 q^2)$  with  $\sigma_D = \sigma_{rms}/a$  is the relative root-mean-square displacement for a unit cell size  $a$ . It is called Debye-Waller factor. The particle distribution is called  $\beta(q)$ . For the limit of monodisperse particles  $\beta(q) = 1$ . For a particle size distribution with a finite width of  $\sigma_R$ , it can be approximated with  $\beta(q) \approx \exp(-\sigma_R^2 R^2 q^2)$  with radius of particles  $R$  [52]. The term  $1 - \beta(q)G(q)$  in Equation 3.37 is the diffuse scattering and appears as a broad baseline in the data.

In general, crystals have a finite size. Some crystals like silicon wafers of the semiconductor industry can be almost considered as infinite crystals. However, some crystals are also restricted deliberately in size like perovskite nanoplatelets introduced in chapter 5. Finite crystal size causes a decrease in intensity and additionally, Bragg peaks appear broader. For the relation between peak broadening and crystal size usually the Scherrer equation is used.

$$L = \frac{K\lambda}{\Delta(2\theta) \cos \theta_0} = \frac{2\pi K}{\Delta q} \quad (3.38)$$

The average domain size along the axis of a peak  $L$  is inversely proportional to FWHM of the peak  $\Delta q$  in  $q$ . The Scherrer factor  $K$  is an empirical factor, which takes the shape of the lattice into account and is approximately one. The classical description is in angles with the FWHM  $\Delta(2\theta)$  of a peak at a peak position  $\theta_0$  and a wavelength  $\lambda$  of the X-ray.



## Part II

### CONSTRUCTION OF A SMALL-ANGLE X-RAY SCATTERING SETUP AND APPLICATIONS

First, considerations about the design of a SAXS setup are discussed in detail. This includes considerations of the energy dependency of X-ray scattering and a detailed description of the built setup [6]. Secondly, wide angle X-ray scattering (WAXS) and XRD measurements are presented with the example of Perovskite nanoplatelets [3]. Thirdly, the results of SAXS measurements on DNA origami for single objects [5] as well as for polymerized crystals are presented (Appendix A.1). Fourthly, an example of photo-switchable lipid bilayers as well as multilayers is shown.



## BUILDING A SMALL-ANGLE X-RAY SCATTERING SETUP

---

*The work described in this section has been partly published [6].*

The development of SAXS equipment has made significant progress in recent years and facilitate experiments at in-house setups [36]. Microfocus X-ray sources with a 2D multilayer mirror became available and provided in-house SAXS setups with a point shaped X-ray beams with comparably high brilliance to previous sources. The next level of improvement in X-ray sources were liquid metal sources, which enable even higher flux. Not only the quality of X-ray sources developed. The collimation of the X-ray beam reduced dramatically parasitic scattering with the invention of the so-called scatterless slits, which use single crystals of silicon or germanium [53]. The detection was also enhanced due to advancements in the semiconductor industry bringing forward 2D solid state detectors. They provide single photon counting without dark noise and can cover a wide area, which collects sufficient scattering intensity for SAXS analysis within one measurement. Some applications still need the high brilliance of state of the art synchrotron sources, but with a well equipped SAXS setup in the laboratory, various significant observations can be made without having beamtime at synchrotrons. The choice of the X-ray energy is one of the crucial parameters for the experimentalist and is explained in detail in the following sections. With synchrotron sources, especially at third generation ones, the X-ray energy can be selected with insertion devices and monochromators made of single crystals. For an in-house setup, the target material in the X-ray tube and thus the X-ray energy has to be chosen carefully. However, systems with dual or even triple sources are already commercially available, for example, the system Xeuss 2.0 from Xenocs [54].

Since there is no "perfect system", compromises always have to be made. For this reason, the desired application of the experimental setup must be determined from the beginning. First, the requirements for SAXS setups and the decisions to be made are pointed out in the sections 4.1-4.3. Secondly, the consequences associated with the choice of a specific anode material are explained using the example of copper (Cu) and molybdenum (Mo) anode based setups. Finally, the section 4.5 concludes with a detailed description of the in-house SAXS setup which was built within this thesis.

## 4.1 REQUIREMENTS

The dimensions of typical samples which are studied by X-rays are on the nanoscale and characteristic distances within the sample or particle sizes reach from a few Å to several 100 nm. This length scale corresponds to  $q$ -values of  $10^{-3} - 6 \text{ \AA}^{-1}$ , which is for an X-ray wavelength of  $1 \text{ \AA}$  an angular range of  $0.01^\circ$  to about  $60^\circ$ . Therefore, it is hardly feasible to measure the entire  $q$ -range in one measurement. Even at state of the art synchrotron beamlines like ID02 (ESRF, Grenoble), such a large  $q$ -range can only be measured with at least two different sample-to-detector positions. Therefore, the first important choice is the necessary  $q$ -range which needs to be covered.

**Q-RANGE** If the attention is focused on proteins and macromolecules in solution, a range up to  $0.15 \text{ \AA}^{-1}$  will be sufficient. A long sample-to-detector distance (SDD) is required in order to obtain a sufficiently low minimal  $q$ -value ( $q_{min}$ ). In order to cover also lipid multilayers or even powder samples of atomic lattices, the  $q$ -range must be extended to at least  $2 \text{ \AA}^{-1}$ .

Sometimes a high  $q$ -range alone will prove to be insufficient if the  $q$ -resolution is too low. Thus, the second crucial parameter is the  $q$ -resolution.

**Q-RESOLUTION** A high  $q$ -resolution is essential to resolve sharp features, for instance, intensity minima of form factors, which can be used to determine the polydispersity of a sample. Another example is the broadening of Bragg peaks, which occurs for small crystals. These high instrumental  $q$ -smearing effects make a detailed analysis impossible.

The scattering intensity depends mostly on the incident flux (Equation 3.10) and the resolution is limited by the beam size. So the decision of the X-ray source is the most important one.

**X-RAY SOURCE** As the anode material of the X-ray tube is responsible for the resulting X-ray energy; it has to be chosen according to the desired application. Furthermore, the type of X-ray tube is crucial because it determines the beam size, the flux, and the reliability. It can be a rotating anode or static anode with line focus or microfocus. Within the time of this thesis, a new type of source came into play: the liquid metal anode.

The complexity of the sample environment limits the use of completely evacuated beam paths, which are favorable for decreasing the background. Consequently, the sample environment represents a critical criterion for an X-ray setup.

**SAMPLE ENVIRONMENT** If only solution based SAXS without heating and cooling is needed, a fully evacuated beam path will be comparably easy to achieve. If the variety of samples is higher and more complex samples environments like humidity chambers are needed, an evacuated sample area will be hard to achieve or even impossible.

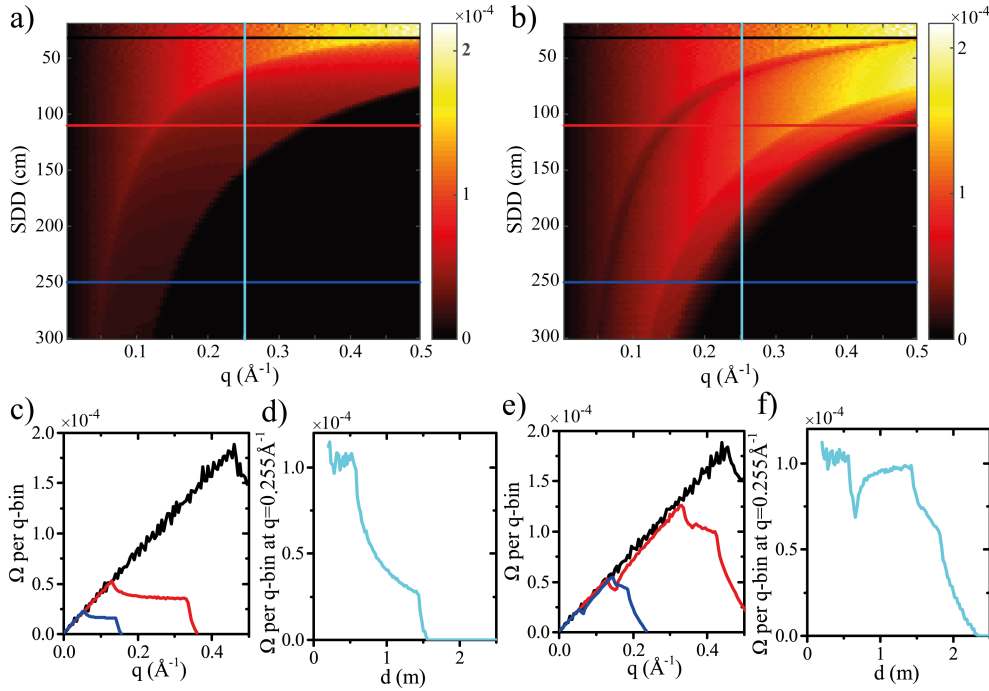


Figure 4.1: Geometries for different SDDs for an X-ray wavelength of  $0.71 \text{ \AA}^{-1}$ . Covered solid angle for a  $q$ -bin of  $5 \cdot 10^{-3} \text{ \AA}^{-1}$  with different distances dependent on  $q$  for a centered beam with a) Pilatus 100K and b) Pilatus 300K detector. c) and e) horizontal cuts of a) and b) at standard SDDs of the X-ray setup. d) and f) vertical cut of a) and b) at  $q=0.255 \text{ \AA}^{-1}$ .

The detector is another key component of a SAXS setup because it determines the detection area, the resolution given by the pixel size and the efficiency of measuring the scattered X-ray photons.

## 4.2 Q-RANGE

The  $q$ -range covered by an X-ray setup depends on the X-ray energy, the SDD and the beam size or rather the beam stop size.

First, the maximal accessible  $q$  value is considered. A lower X-ray energy shifts the accessible  $q$ -range for a constant SDD to lower values and thus limits the maximally achievable  $q$ -value because  $q$  is inversely proportional to the X-ray wavelength (Equation 3.9). Due to the inverse proportionality of  $q$  with  $\lambda$ , the same scattering angle range of  $2\theta$  comprises a larger  $q$ -range for a higher X-ray energy. The measured intensity has to be binned with a lower limit being the pixel size. The bins have to be chosen wide enough in order to avoid oversampling, but also low enough to resolve sharp features. The solid angle per  $q$ -bin rises with decreasing the X-ray energy. For a fixed X-ray energy, the SDD can tune the  $q$ -range. The covered solid angle is shown in Figure 4.1 in dependency on the SDD for  $q$ -values of up to  $0.5 \text{ \AA}^{-1}$  for two state of the art detectors with different active areas (Pilatus 100K and Pilatus 300K, Dectris, Switzerland) at an X-ray energy of  $17.4 \text{ keV}$ . More details on the detectors are given in section 4.5. A shift of the maximal  $q$ -value

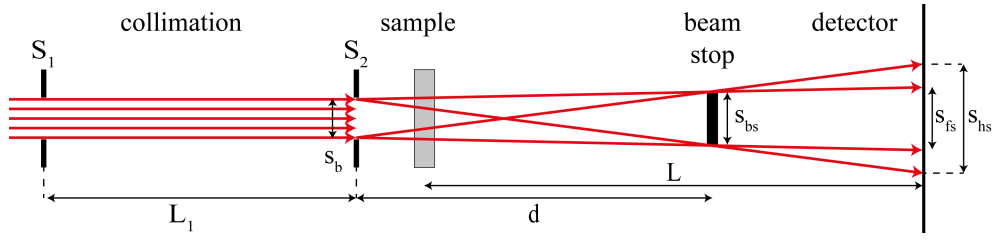


Figure 4.2: Scheme of collimation and beamstop shadow with important geometrical sizes for the calculation of a minimal  $q$ -value.

to lower values for increasing SDDs can be seen. For example, for a distance of 1.1 m it is  $0.36 \text{ \AA}^{-1}$ , but for 2.5 m it is only  $0.155 \text{ \AA}^{-1}$  with a Pilatus 100K. Also, the complete radial angle is only covered up to  $0.13 \text{ \AA}^{-1}$  and  $0.055 \text{ \AA}^{-1}$  for 1.1 m and 2.5 m, respectively. The solid angle enters the scattering intensity linearly (Equation 3.10). The coverage is significantly improved for the Pilatus 300K, for which at SDDs of 1.1 m and 2.5 m the whole solid angle is covered up to  $0.33 \text{ \AA}^{-1}$  and  $0.145 \text{ \AA}^{-1}$ , respectively. For low  $q$ -values, it does not change, but for a feature at  $q=0.255 \text{ \AA}^{-1}$  the scattering intensity increases by a factor of 2.6 for a SDD of 1.1 m by exchanging the Pilatus 100k with a Pilatus 300k. As an example, this aspect becomes very important regarding the study of the inner structure of DNA origami described in section 6.1.1. Another possibility to increase the solid angle per  $q$ -bin is to use a lower X-ray energy but for the same SDD the maximum  $q$ -value as well as highest  $q$ -value with the full coverage of the solid angle decreases. This can be overcome by using a shorter SDD, but this results in a reduced  $q$ -resolution (section 4.3) and a smaller minimal  $q$ -value.

So far only the solid angle, as well as the maximum  $q$ -value, have been considered. Particularly with regard to SAXS the minimal attainable  $q$ -value is an important parameter. The beam size and beamstop size are the crucial criteria, but still, the SDD plays a significant role. Besides the SDD, now denoted by  $L$ , the position of the beamstop  $d$ , with respect to the sample position, has a considerable impact on the minimal  $q$ -value due to shadow effects. The setup geometry for the evaluation of the correct position of the beamstop is sketched in Figure 4.2. The full shadow size of the beamstop  $s_{fs}$  can be easily calculated in the following way:

$$s_{fs} = s_b + \frac{s_{bs} - s_b}{d} L \quad (4.1)$$

with the beam size  $s_b$  and the beamstop size  $s_{bs}$ . The beamstop size must be equal or greater than the beam size because the intensity of the direct beam is too high for the detector:  $s_{bs} \geq s_b$ . If the beamstop is not in close proximity to the detector, the half shade  $s_{hs}$  will be able to have a significant influence on the scattering signal. The size of the half shade can be calculated in the following way:

$$s_{hs} = s_{bs} + (s_b + s_{bs}) \frac{L - d}{d} \quad (4.2)$$

Both Equations 4.1 and 4.2 depend only on geometrical considerations and parameters like the divergence of the X-ray beam are neglected.

The minimal attainable q-value is limited by the full shadow of the beamstop. The data can be corrected for the half shade with a calibrant like glassy carbon [55]. Therefore, the minimal q-value is determined by

$$q_{min} = \frac{4\pi}{\lambda} \sin\left(\frac{1}{2} \arctan\left(\frac{s_{fs}}{2L}\right)\right) \approx \frac{\pi s_{fs}}{\lambda L}. \quad (4.3)$$

By Equation 4.1 the minimal q-value is primarily limited by the beam size, which is the lower limit for the beamstop size. The collimation, the beam divergence and the natural size of the beam at the source are the crucial parameters. The natural beam size and its divergence dependent on the type of source and can be in the  $\mu\text{m}$  and  $\mu\text{rad}$  regime for synchrotron sources, respectively. For microfocus in-house sources, the natural beam size typically ranges around 1 mm and the divergence of the beam is in the 0.1 mrad regime. Since the beam shape of the source is not perfect, a collimation is needed, which can also be used to decrease the beam size. Commonly, a collimation consists of three slits [41]. The first two slits define the beam size as well as the maximal opening angle. In addition, a third slit serves as a guard slit for the parasitic scattering of the second slit. Due to recent technical advance, the three slit collimation can be replaced by only two scatterless slits [53], which produce almost no parasitic scattering.

From only geometrical considerations regarding the slit aperture sizes and positions, the beam size at the beamstop position  $s_{b,g}$  is

$$s_{b,g} = S_2 + (S_1 + S_2) \frac{d}{L_1}. \quad (4.4)$$

Here the slit aperture sizes are described by  $S_1$  and  $S_2$ , the collimation length by  $L_1$  and the distance from slit 2 to the beamstop by  $d$ . This relation expresses the upper limit of the beam size at the beamstop position and is also valid for a beam with a high divergence. For determining the corresponding lower limit, only the divergence of the beam is taken into account. In this case, the beam size at the beamstop position is:

$$s_{b,d} = S_2 + \tan(\Delta 2\theta)d, \quad (4.5)$$

with the divergence of the beam  $\Delta 2\theta$ . Both the upper and lower beam size limit set the boundaries for the minimal beam stop size and therefore the minimal q-value (Equation 4.1 and 4.3).

A typical configuration of the setup build within this thesis has a SDD of  $L=1.1$  m, a beamstop position  $d=1$  m and a collimation length  $L_1=0.82$  m. The divergence of the beam is around 0.15 mrad and the slit aperture sizes  $S_1$  and  $S_2$  are about 0.9 mm. This leads to a beam size in between  $s_{b,g}=3.09$  mm and  $s_{b,d}=1.05$  mm. The beam stop used in the setup has a diameter of 3 mm and therefore it is clearly larger than the divergent beam size  $s_{b,d}$ . If only the collimation is considered, the beamstop has approximately the size of the beam. With Equation 4.1 this leads to a full shade of 3.21 mm on the detector

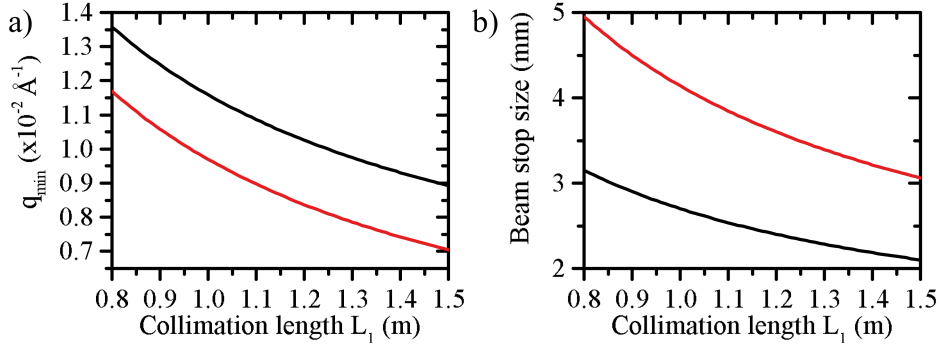


Figure 4.3: The minimal attainable  $q$ -value (a) with corresponding optimal beam-stop sizes (b) in dependency on the collimation length for two SDDs: (black)  $d=1$  m and  $L=1.1$  m, (red)  $d=1.8$  m and  $L=2.3$  m.

where the beam size is taken to be  $s_b = 0.9$  mm defined by  $S_2$ . The resulting minimal  $q$ -value for an X-ray energy of 17.4 keV is  $1.29 \cdot 10^{-2} \text{ \AA}^{-1}$ , which is in agreement with the measurements. The exact same setup employing a Cu anode instead of a Mo anode would result in a minimal  $q$ -value of  $5.9 \cdot 10^{-3} \text{ \AA}^{-1}$ . This points out that especially for high energies a long SDD is needed to obtain a low  $q_{min}$  value. However, a long SDD will only help if the collimation and the divergence are good enough. Therefore, increasing the collimation length can be beneficial for a significant reduction of the minimal attainable  $q$ -value. In Figure 4.3 the dependency of  $q_{min}$  on the collimation length  $L_1$  is shown as well as the necessary beamstop diameter. The SDDs are chosen at the values which are used in the current setup (see section 4.5). An extended collimation length is of particular advantage for the longer SDD. For a collimation length of 1.27 m a minimal  $q$  value of  $8 \cdot 10^{-3} \text{ \AA}^{-1}$  could be obtained.

### 4.3 Q-RESOLUTION

Besides the  $q$ -range, the resolution in  $q$  is another essential parameter for an X-ray setup. Often the  $q$ -resolution of an X-ray setup is called the  $q$ -smearing of the instrument. Basically five parameters limit the  $q$ -resolution: polychromaticity  $\lambda_{\alpha 1/\alpha 2}$ , sample thickness  $t$ , beam size  $b$ , beam divergence  $\Delta 2\theta$  and pixel size  $p$ . Figure 4.4 a) sketches all mentioned parameters with a dashed line as variance to the exact behavior. Figure 4.4 b) shows their respective  $q$ -dependency. The total  $q$ -resolution can be calculated as the square root of the sum of each parameter squared.

For an X-ray tube based setup the polychromaticity is given by the splitting of the two  $K_\alpha$  lines ( $\lambda_{\alpha 1}, \lambda_{\alpha 2}$ ):

$$\Delta q_{poly} = 4\pi \sin \theta \left( \frac{1}{\lambda_{\alpha 1}} - \frac{1}{\lambda_{\alpha 2}} \right) \quad (4.6)$$

For low  $q$ -values the effect is negligible, yet for the WAXS regime it is significantly more distinct. Since both  $K_\alpha$  lines are very narrow and their positions are known, the influence of polychromaticity can be easily considered within

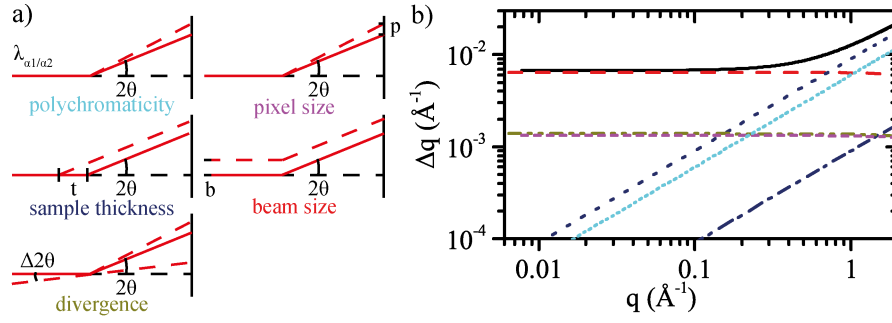


Figure 4.4: Contributions to the  $q$ -resolution  $\Delta q$ : a) schemes and b)  $q$ -dependency for polychromaticity due to  $K_{\alpha}$  splitting (dotted cyan), for a beam size of 0.9 mm (dashed red line), a sample thickness of 1 mm (dashed dotted dark blue) and 10 mm (dotted dark blue), a pixel size of  $172 \mu\text{m}$  (short dashed purple), a beam divergence of 0.15 mrad (dashed double dotted dark yellow) and the square root of the sum of all contributions squared (solid black line). The values are calculated for the Molybdenum  $K_{\alpha}$  line and a SDD of 1.1 m.

data analysis.

The effect of finite sample thickness, too, is low for forward scattering, but significant for WAXS.

$$\Delta q_{\text{sample}} = \frac{4\pi}{\lambda} \left( \sin \theta - \sin \left( \frac{\arctan \frac{\tan(2\theta)(L-t)}{L}}{2} \right) \right) \quad (4.7)$$

As Figure 4.4 b) depicts, for a small sample thickness of 1 mm the entire  $q$ -range remains almost unaffected (dashed dotted dark blue line). Therefore, a small sample thickness is highly recommended for WAXS measurements, but for SAXS even a 10 mm thick sample (dotted dark blue line) has no major impact.

In contrast to polychromaticity and sample thickness, the divergence of the beam has only a very small  $q$ -dependency. The  $q$ -resolution due to the beam divergence  $\Delta 2\theta$  is given by:

$$\Delta q_{\text{divergence}} = \frac{4\pi}{\lambda} \left( \sin \theta - \sin \left( \frac{\arctan (\tan(2\theta) - \tan(\Delta 2\theta))}{2} \right) \right) \quad (4.8)$$

For a highly collimated beam, e. g.  $\Delta 2\theta = 0.15$  mrad, the divergence has usually no effect on the  $q$ -resolution.

Another limiting factor is the the detector pixel size.

$$\Delta q_{\text{pixel}} = \frac{4\pi}{\lambda} \left( \sin \theta - \sin \left( \frac{\arctan \left( \frac{L \tan(2\theta - p)}{L} \right)}{2} \right) \right) \quad (4.9)$$

Apparent from Figure 4.4 the pixel size and the divergence show the same  $q$ -dependency and a pixel size of  $172 \mu\text{m}$  (short dashed purple line) has almost the same effect as a divergence of  $\Delta 2\theta = 0.15$  mrad (dashed double dotted dark yellow line). Therefore, an improvement of the beam divergence would

not increase the q-resolution. The most important contribution for in-house setups is the beam size because the natural beam size remains in the 1 mm regime even for microfocus X-ray tubes. At third generation synchrotron sources, the beam size can be considerably smaller and often the pixel size is the limiting factor. In a simplified way the q-resolution due to the beam size can be estimated by:

$$\Delta q_{beam} = \frac{4\pi}{\lambda} \left( \sin \theta - \sin \left( \frac{\arctan \left( \frac{L \tan(2\theta) - b}{L} \right)}{2} \right) \right) \quad (4.10)$$

This formula assumes a rectangular beam shape with the width  $b$ . This is not the case for a typical beam as Figure 4.14 shows. Although the measurement was not performed at the sample position, the assumption of a rectangular beam shape is obviously wrong. Therefore, typically a Gaussian profile is used for the resolution function of the instrument and convoluted with the model of the scattering intensity [56].

All contributions to the q resolution have an inverse proportionality to the X-ray wavelength (Equations 4.6-4.10). Accordingly, all parameters are about twice as good for Cu than for Mo. The q-dependency does not change with the X-ray energy, only the scale in Figure 4.4 b) changes by the quotient of the X-ray wavelengths.

Pedersen et al. give a detailed description of the q-resolution and how to implement it into model fitting [56, 57]. Brian Pauw provides an overview of SAXS measurements in general and also refers to several papers concerning the q-resolution [58].

#### 4.4 SIGNAL-TO-BACKGROUND

##### 4.4.1 Parameters of Scattering Intensity

The fundamental parameter with respect to data quality is the signal-to-background (S/B) ratio. There are two possible ways to optimize this ratio, either by increasing the signal of the sample or by minimizing the background.

The Equations 3.10, 3.12 and 3.30 express the scattering intensity. There are eight parameters for the signal intensity, four dependent on the setup and four are sample-dependent. Table 4.1 summarizes these quantities with their specific X-ray energy dependency. All parameters are explained in detail below.

##### *Primary beam intensity*

The primary beam intensity is fixed by the anode material of the X-ray tube. Commonly used materials are chromium ( $K_{\alpha} = 5.41 \text{ keV}$ ), copper ( $K_{\alpha} = 8.04 \text{ keV}$ ), molybdenum ( $K_{\alpha} = 17.44 \text{ keV}$ ) or silver (Ag) ( $K_{\alpha} = 22.11 \text{ keV}$ ) [59].

Parameter	Change with increasing X-ray energy
Primary intensity	Decreasing
Detector efficiency	Decreasing
Beam size	Independent
Solid angle per q-bin	Decreasing
Optimal sample thickness	Increasing (Optimum for $H_2O$ : Mo $K_\alpha \approx 10$ mm, Cu $K_\alpha \approx 1$ mm)
Sample concentration	Independent
Size of particles	Independent
Scattering contrast	Material dependent

Table 4.1: Scattering intensity parameters for SAXS measurements and their dependency on the X-ray energy.

The high binding energies of K-shell electrons for atoms with higher atomic number leads to less efficient X-ray generation [60]. At synchrotron sources, there is a similar trend that the primary beam intensity decreases for higher energies, but this depends on many parameters such as the storage ring energy (see section 3.1). Nowadays, there are beamlines which are specialized for high energies, e. g. Po7 at Deutsches Elektronen-Synchrotron (DESY), Hamburg.

#### *Detector efficiency*

The lower absorption of X-rays for higher energies leads to a less efficient detection with rising energy. However, the recently developed single-photon counting detectors achieve high quantum efficiency (76 %) even for a high energy of 17.4 keV. This comparably high efficiency is achieved by using an enlarged silicon sensor thickness of 1 mm compared to 0.32 mm used for Cu radiation, for which the efficiency is 97 %. By replacing silicon with cadmium telluride (CdTe) the efficiency for an energy of Mo is further increased (>90 %) [61]. Detectors with CdTe are commercially available, but until now the costs remain high compared to the silicon version.

#### *Beam size*

The beam size is determined by the multilayer mirror, which monochromatizes and collimates the beam. It is also called Göbel mirror after its inventor [62]. It has a parabolic shape with the X-ray target in its focus and consists of a multilayer which has a repeating distance of two alternating materials so that the Bragg condition is only fulfilled for the characteristic wavelength of the anode material. By increasing the acceptance angle of the mirror, the intensity of the beam is enhanced, but in the same way the beam size increases. Therefore, the natural beam size without slits is given by the multilayer mirror.

At synchrotron sources, the beam size is given by the used wiggler or undulator. For undulators, it is usually smaller than for in-house source beams. Because of the high coherence at third generation synchrotron sources, the beam can be focused with Fresnel lenses even into the nanometer regime. However, in this case, the divergence of the beam increases according to the focusing angle.

#### *Solid angle per q-bin*

In section 4.2 the dependence of the solid angle per q-bin on the type of detector and the SDD was already shown. These arguments are true for all X-ray energies, but the q-range shifts to lower or higher q-values by lowering or increasing the X-ray energy, respectively. In the examples of Cu- and Mo- $K_\alpha$  radiation, the q-range and q-resolution will be the same, if the following relation holds for the SDDs:

$$L_{Mo} = \frac{\lambda_{Cu}}{\lambda_{Mo}} L_{Cu} \quad (4.11)$$

Using the wavelengths  $\lambda_{Cu} = 1.54 \text{ \AA}^{-1}$  and  $\lambda_{Mo} = 0.71 \text{ \AA}^{-1}$ , the Mo setup has an increased SDD of  $L_{Mo} = 2.169 \cdot L_{Cu}$ . The solid angle is

$$\Omega = \frac{A_{det}}{L^2} \quad (4.12)$$

with the detector area  $A_{det}$ . Therefore, the solid angle decreases by a factor of  $1/4.7 \approx 0.213$  for Mo compared to Cu.

#### *Optimal sample thickness*

The scattering intensity is proportional to the transmission  $T$  and sample thickness  $t$  (Equation 3.10). The transmission follows the Beer-Lambert law  $T = e^{-\mu t}$  with the attenuation coefficient  $\mu$  and is thus also dependent on the sample thickness  $t$ . The maximum scattering intensity will, therefore, be reached if the following product is maximized:

$$\max(te^{-\mu t}) \Rightarrow t = 1/\mu \quad (4.13)$$

In this case the transmission is  $e^{-1} \approx 0.368$ . The optimal sample thickness is material dependent and in particular energy dependent. The attenuation coefficient is determined by the interaction of the X-ray photons in the material. In the X-ray regime of 5-30 keV, the relevant interaction processes are the photoelectric effect, and Compton scattering, which are both inelastic and Rayleigh scattering, which is elastic. Figure 4.5 a) shows these interactions for the example of water because it represents a typical medium for SAXS samples. The low energy regime is dominated by the photoelectric effect. Starting from an X-ray energy of 17.5 keV the contribution of the Compton scattering cannot be neglected. The Rayleigh scattering is about two orders of magnitude lower throughout the entire energy regime. Hence, only the two inelastic processes matter for the transmission. The resulting attenua-

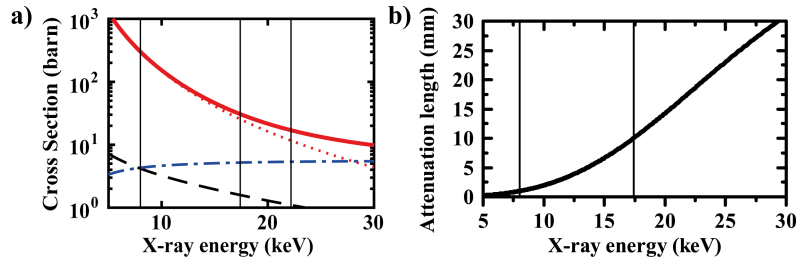


Figure 4.5: a) X-ray scattering cross sections of water in dependence of the X-ray energy: Compton scattering (dashed dotted blue line), photoelectric effect (red dotted line), sum of both (solid red line), Rayleigh scattering (black dashed line), b) attenuation length of water for an energy range of 5-30 keV. Vertical lines show X-ray energies of Cu (left) and Mo (right).

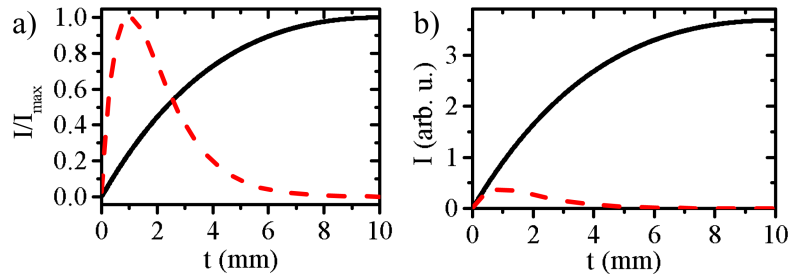


Figure 4.6: a) normalized scattering intensity in dependency on the sample thickness for an X-ray energy of Cu  $K_{\alpha}$  line (red dashed line) and Mo  $K_{\alpha}$  line (solid black line), b) same plot in absolute values with  $I \propto te^{-\mu t}$ .

tion length  $1/\mu$ , which equals the optimal sample thickness, is shown in Figure 4.5 b) for water. For example, it is 1 mm for a Cu source and 10 mm for Mo. As a consequence, the scattering intensity can be increased by a factor of 10 for Mo compared to Cu, if the optimal sample thickness is used. For both energies, the scattering intensity dependency on the sample thickness is shown in Figure 4.6. For Cu the scattering intensity has a rather sharp peak around the optimum of 1 mm thickness and for a 2 mm it is only 74 %. Since the typical beam size is around 1 mm, a 2 mm capillary is often used [55]. For Mo the scattering intensity maximum is broader and for a sample thickness of 2 mm still about 45 % of the maximum scattering intensity is reached. As the Figure 4.6 b) shows, the scattering intensity for a 2 mm thick sample is, therefore, a factor of 6 larger, due to the higher transmission for Mo than for Cu. This will be especially important if the sample is only available with a low amount and for this reason the sample volume has to be kept small. In 2 mm capillaries a volume of  $10 \mu\text{l}$  (3 mm filling level) can be already sufficient, but for a 10 mm thick chamber, at least  $50 \mu\text{l}$  (diameter=2.5 mm,  $t=10$  mm) are necessary. Beside the effect on the sample volume a smaller sample thickness results in a higher q-resolution (see section 4.3).

#### Other sample parameters

The further sample parameters entering the scattering intensity are the concentration of particles  $c$ , the scattering contrast between the particle and

medium  $\Delta\rho$  and the particle size  $V_P$ , see Equation 3.30. These three quantities are energy-independent and can improve the scattering intensity.

The scattering intensity scales linearly with the concentration and so a high concentration is the easiest way to intensify the signal. If the concentration exceeds a certain level, however, effects like inter-particle interaction or multiple scattering will emerge [63]. For highly concentrated samples, it is important to measure diluted samples in order to check for inter-particle interaction. This interaction appears in the low  $q$ -region, where the scattering intensity remains high even for lower concentrations.

The scattering intensity scales with the scattering contrast squared. Therefore, lead (Pb) containing samples like perovskites (see chapter 5) or AuNPs can be studied at an in-house setup with a very low concentration in the nanomolar regime.

The volume of the particle also enters the scattering intensity with a power of two. For large objects like DNA origami (see chapter 6), it is therefore possible to measure at in-house setups even though the scattering contrast of DNA in a buffer solution is less than the one of Pb or AuNP.

#### 4.4.2 Background

Besides the scattering intensity of the sample, a key factor for the data quality is the background of the setup. The intensity of the instrumental background  $I_{bg}$  of an X-ray setup has three contributing sources: scattering by air (a), window material (w) and natural background  $bg_{nat}$ .

$$I_{bg} = I_0 \cdot \epsilon \cdot \Omega \left( t_a T_a \frac{d\Sigma}{d\Omega_a} + t_w T_w \frac{d\Sigma}{d\Omega_w} \right) + bg_{nat} \quad (4.14)$$

The first part of the air and window scattering scales with the primary beam intensity  $I_0$ , while the natural background is a constant, which scales with detector sensor thickness.

Within this thesis two similarly equipped SAXS setups were compared, one employing a Mo- and one a Cu-anode. The setup with the Mo-anode was built during this thesis and is described in high detail in section 4.5. The setup with the Cu-anode is located in Santa Barbara (USA) at the Materials Research Laboratory (MRL) in the group of Prof. Safinya. Both setups are composed of the same key components like the type of X-ray source, multi-layer optic, slits, and detector. The only constructional difference is that the detector of the Cu-setup uses a  $320 \mu\text{m}$  thick sensor instead of a 1 mm thick sensor for Mo. Both setups have air gaps starting at the collimation path exit, around the sample area up to the flight tube entrance.

Figure 4.7 shows the different sources of the background and a typical buffer signal. The natural background for the Mo-setup is  $9.8 \pm 0.9 \cdot 10^{-5}$  ct/s and for the Cu-setup it is  $4.5 \pm 1.5 \cdot 10^{-5}$  ct/s. Thus, the Mo-setup has a factor of 2.2 higher natural background than the Cu setup, which is expected according to the difference in sensor thickness. The scattering data in Figure 4.7 of the air (solid blue line) is corrected for the transmission of the buffer sample

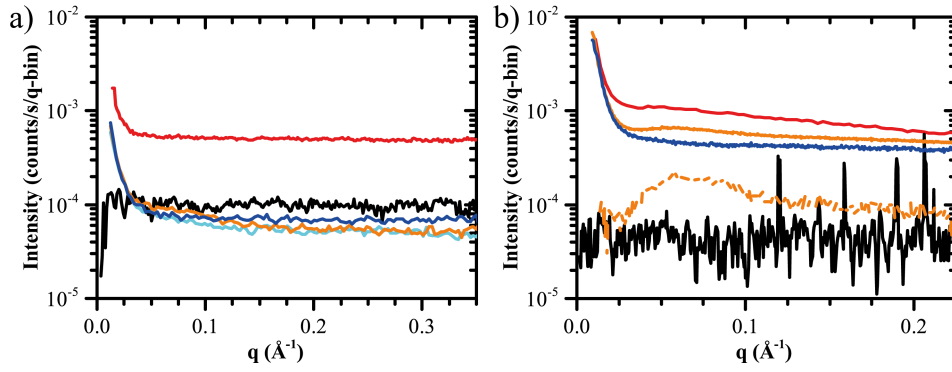


Figure 4.7: Background contributions and scattering of a buffer solution of a) the Mo-setup and b) Cu-setup. Buffer background without corrections (red), natural background measured with detector without beam (black), air scattering (blue), scattering of Kapton (orange) and potassium aluminosilicate (cyan) windows with correction of transmission of the buffer. Scattering of Kapton with transmission correction and subtraction of air scattering (orange dashed) in b).  $q$ -binning of data is  $3 \cdot 10^{-3} \text{ \AA}^{-1}$ .

and the natural background constant is subtracted.

For the Mo-setup, the contribution of the air is below the natural background for  $q$ -values above  $0.03 \text{ \AA}^{-1}$ . The window measurements were carried out with empty sample chambers which have two windows of each  $25 \mu\text{m}$  thickness. The data of Kapton (solid orange line) and potassium aluminosilicate (muscovite mica, solid cyan line) are also corrected for the transmission of the buffer sample because lower transmission causes less air scattering. Additionally, the natural background constant is subtracted. Both window scattering intensities show a similar behavior as the air scattering. However, they are below the air scattering signal, which cannot be explained by the additional absorption of the foils and remains unclear. For Kapton a known broad peak at  $0.07 \text{ \AA}^{-1}$  is only slightly visible for the Mo-setup [64]. For the most of the  $q$ -range, the background signal is dominated by natural background and only the air scattering adds additional signal because there is no difference between the sum of the window and air scattering and the air scattering alone. For Kapton a strong second peak appears at around  $0.4 \text{ \AA}^{-1}$  [64], which is not covered by the data in Figure 4.7. This peak shows up in other measurements and is above the natural background level.

The primary cause of background can also be determined by variation of the SDD for a test sample. For that purpose Equation 4.14 is used because the natural background is constant while the window and air scattering scale with the solid angle  $\Omega$ . In this case, cytochrome *c* was used as a test sample, which is well characterized by previous SAXS measurements [65–67]. The measurements were performed with a concentration of  $8 \text{ mg/ml}$  at SDDs of  $1.1 \text{ m}$  and  $2.5 \text{ m}$  at the Mo setup. Figure 4.8 shows the data on absolute scale (section 3.3.3). Hence, the data is scaled in the way that samples with the same concentration have the same scattering intensity for low  $q$ -values and the background level can change according to the data quality. For  $q$ -values up to  $0.1 \text{ \AA}^{-1}$  the data of both distances are similar to each other and well

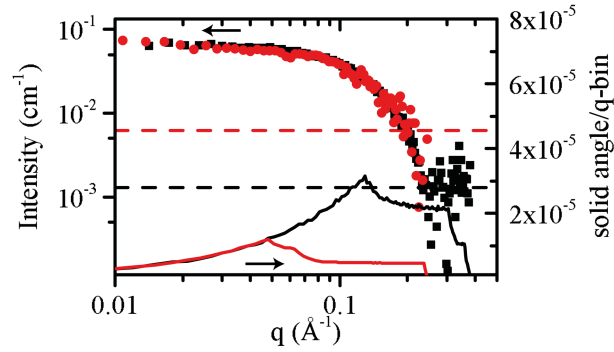


Figure 4.8: Buffer-subtracted scattering intensity of cytochrome *c* measured with Mo setup for SDDs of 1.1 m (black squares) and 2.5 m (red circles). The estimated background level is shown by horizontal dashed lines and is for the short SDD  $1.3 \cdot 10^{-3} \text{ cm}^{-1}$  and for the long SDD  $6.2 \cdot 10^{-3} \text{ cm}^{-1}$ . The solid angle per q-bin is shown with solid lines on the right axis. q-binning of data is  $3 \cdot 10^{-3} \text{ \AA}^{-1}$ .

above the background level. For the shorter distance, the background level is at about  $1.3 \cdot 10^{-3} \text{ cm}^{-1}$ . Figure 4.8 also displays the solid angle per q-bin for both SDDs. For high  $q$ -values ( $0.2 \text{ \AA}^{-1}$  and higher) it is about a factor of 4.8 smaller for the long SDD than for the shorter one. As a consequence, the scattering signal of the sample is lowered by this factor for the long distance, whereas the background remains the same for both SDDs. After scaling to absolute intensity, the background level of the long SDD (red dashed line) is thus 4.8 times higher than the one of the shorter distance (black dashed line).

In summary, it can be stated that the Mo background is dictated by the natural background and only for low  $q$ -values the air scattering might matter. However, the signal could also originate from parasitic scattering around the beamstop. In contrast, for the Cu setup the air scattering is considerably above the natural background level. The window scattering of Kapton is above the air scattering and the air scattering subtracted Kapton signal is also above the natural background level. The reason for this is that the primary beam intensity ( $I_0$ ) is by a factor of 8 higher, the detection ( $\epsilon$ ) shows 21 % greater efficiency and the solid angle per q-bin ( $\Omega$ ) is by a factor of 4.7 higher for the Cu- than for Mo-setup. The scattering intensity of the air and windows is proportional to these three mentioned terms (compare Equation 4.14). As a consequence, the broad peak at  $0.07 \text{ \AA}^{-1}$  is more distinct than in the Mo data.

The high contribution of air scattering to the background is well known [68–70]. Especially for high primary beam intensities at synchrotrons, the background can be improved significantly by evacuation of the entire beam path. The example of the Cu-setup shows the air scattering problem can also be of great importance for in-house setups. This applies in particular for lower energies due to the increased solid angle and the higher accessible primary beam intensities.

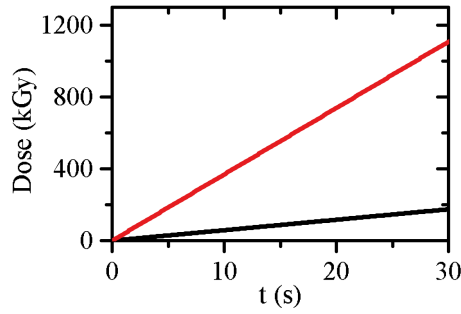


Figure 4.9: Time dependent dose at beamline Po8 (DESY, Hamburg) for 8.4 keV (red) and 18.8 keV (black). The calculated flux is  $5 \cdot 10^{13}$  counts/s for 8.4 keV and  $3.75 \cdot 10^{13}$  counts/s for 18.8 keV with a beam size of  $0.4 \times 0.1 \text{ mm}^2$  [73].

#### 4.4.3 Radiation Damage

The S/B ratio will be able to be enhanced by extending the exposure time if the scattering of the sample exceeds the background level. The exposure time is limited by the effect of radiation damage, by the stability of the sample and the access time to a setup. The maximum exposure time due to radiation damage is given by

$$t_{max} = \frac{X_c \cdot \gamma \cdot t \cdot A}{I_0 \cdot (1 - T) \cdot E} \quad (4.15)$$

It depends on the critical dose  $X_c$ , which differs significantly for different types of samples [71].  $\gamma$  is the density of the sample and  $t$  is the sample thickness,  $A$  the beam size,  $I_0$  the primary beam intensity,  $T$  the transmission and  $E$  the X-ray energy per photon. The maximum exposure time for the utilized setups is about 15 h for Cu and about 528 h for Mo assuming a maximal dose of 1.1 kGy for cytochrome *c* without additives [72] and using the optimal path length for water (density  $\gamma = 1 \text{ g/cm}^3$ ). The characteristics of both setups, primary beam intensity and beam size, were used for the calculation. The reason for the lower maximum exposure time of Cu compared to Mo is the by a factor of 8 higher primary beam intensity along with the 10 times lower sample thickness. For in-house setups the instrument time and not the radiation damage is usually the limiting factor. However, for synchrotron radiation the primary beam intensity is so immense that beam damage occurs within seconds for biological samples. Therefore, the following part should serve as a guideline what the optimal choice of X-ray energy for solution-based SAXS is.

Figure 4.9 illustrates the calculated dose for different energies by using a modified version of Equation 4.15 with the dose  $X$  and time  $t$  instead of  $X_c$  and  $t_{max}$ , respectively. Considering a high energy of 18.8 keV (black) the absorbed dose rate is 6 kGy/s. For 8.4 keV (red), however, it is roughly by a factor of 6 higher (37 kGy/s). In this case, radiation damage for cytochrome *c* occurs after 183 ms and 30 ms for 18.8 keV and 8.4 keV, respectively. For high energies the radiation damage can be decreased significantly, which is mainly a consequence of the increased optimal sample thickness, which dis-

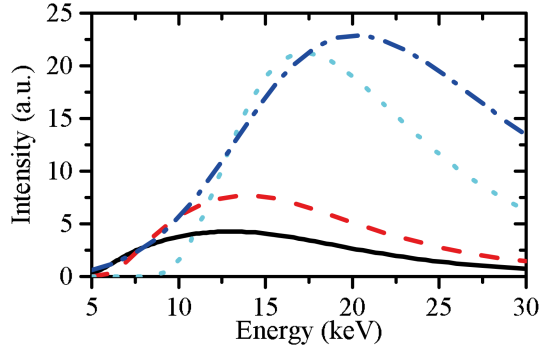


Figure 4.10: Maximal measured intensity for radiation damage-limited measurements in dependence of X-ray energy for a optimal sample thickness (dashed dotted blue line) by using the energy dependent absorption coefficient of water as well as for a sample thickness of 10 mm (dotted cyan), 2 mm (dashed red) and 1 mm (solid black).

tributes the dose over a larger volume (see section 4.4.1). If the measurement is limited by radiation damage, the optimal X-ray energy for maximal measured intensity will be able to be determined by taking the product of the intensity (Equation 3.10) and the maximum exposure time due to radiation damage (Equation 4.15).

$$I_{meas} = I_0 \cdot t_{max} = \frac{X_c A \gamma t^2 T \epsilon \Omega}{(1 - T) E} \frac{d\Sigma}{d\Omega} \quad (4.16)$$

$I_0$  is a intensity in Ph/s as in Equation 3.10 and  $I_{meas}$  is the integrated number of photons on the detector over the time  $t_{max}$ . For further analysis, it is assumed that the critical dose  $X_c$ , the beam size  $A$  and  $\frac{d\Sigma}{d\Omega}$  are energy independent. Interestingly, the primary beam intensity is canceled out. The dependency of the measured intensity on the X-ray energy is shown in Figure 4.10 according to Equation 4.16. The solid angle ( $\Omega$ ) is normalized to the one at 5 keV:  $\Omega \propto (\lambda_2/\lambda_1)^2$  with  $\lambda_1$  the wavelength of 5 keV and  $\lambda_2$  the wavelength of the energy of interest according to Equations 4.11 and 4.12. The detector efficiency ( $\epsilon$ ) was estimated with a silicon sensor thickness  $t_S=1$  mm. The sample thickness  $t$  is the most important variable because it enters in Equation 4.16 with the power of two and with  $e^{-\mu t}$  in the transmission. Figure 4.10 displays the behavior of the measured intensity plotted against the X-ray energy for several fixed sample thicknesses (10 mm, 2 mm and 1 mm) with the transmission according to the water absorption coefficient. For 10 mm the maximum intensity is reached at the optimal sample thickness for an X-ray energy of 17.4 keV (see section 4.4.1). In contrast, for sample thicknesses of 2 mm and 1 mm a shift occurs towards higher energies. The highest intensity is attained for 13.9 keV and 12.9 keV for 2 mm and 1 mm sample thickness, respectively, and not 10.1 and 8.0 keV for which the sample thicknesses would be optimal. These results show that the use of higher energies is beneficial in the case of radiation damage-limited samples. The potential intensity benefit with the optimal energy for a given sample thickness is immense. This can be illustrated by the example of 8 keV and

18 keV, which are close to the  $K_\alpha$  lines of Cu and Mo, respectively. For a sample thickness of 10 mm for 18 keV and 1 mm for 8 keV, the measured intensity gains a factor of roughly 7 for the higher energy. Even if the optimal sample thickness of 8 keV (1 mm) is utilized for both energies, the maximal intensity will be slightly higher for 18 keV than for 8 keV.

If the sample thickness and energy can be freely chosen, the absorption coefficient  $\mu$  of water will be used to determine the sample thickness (dashed dotted blue line). In this case, the highest scattering intensity is reached at about 20 keV with an optimal sample thickness of 14.3 mm. For higher energies than 20 keV, the decreased solid angle ( $\propto \lambda^2$ ) and the lower detector efficiency  $\epsilon = 1 - e^{-t\mu_{Si}}$ ,  $\mu_{Si}$  being the absorption of silicon, exceed the effect of increased sample thickness  $t$  and higher transmission  $T$  and the intensity declines.

There is one important remark to these considerations. The results will be only true if the maximum exposure time is used (Equation 4.15). Particularly for samples with low radiation damage or for time-resolved measurements, this might not be fulfilled.

#### 4.4.4 Conclusion

The best choice of the X-ray energy used for an experiment is complex and strongly depends on the sample type. First, if the sample is in solution, the penetration depth will be important. With a higher X-ray energy the optimal sample thickness increases and with it the maximal accessible scattering intensity. This can be beneficial in spite of less primary beam intensity because the background is also lower with less beam intensity and therefore the S/B can be higher. However, if the sample is not in solution, the primary beam intensity will be more important because the advantage of a higher penetration depth for higher X-ray energies is not or only partly true. Secondly, for solution-based SAXS radiation damage is an issue, especially for biological samples. Usually, this is not the case for microfocus-based setups, but with rotating anodes or liquid metal jet sources this might be different due to the increased beam intensity of a factor of up to 13. At synchrotrons, radiation damage is always a concern and it was demonstrated in section 4.4.3 that the optimal X-ray energy will be independent of the primary beam intensity if the exposure time is radiation damage limited. Furthermore, the results show that an X-ray energy of 20 keV will be the optimal choice if a sufficient amount of sample material is available.

## 4.5 DETAILED DESCRIPTION OF COMPONENTS

A detailed workflow diagram of the SAXS setup built within this thesis and all its components is given in Figure 4.11. It is divided into four blocks: The user of the setup, the main computer with its programs, external devices and units which are in the actual setup. A detailed explanation of the used hard-

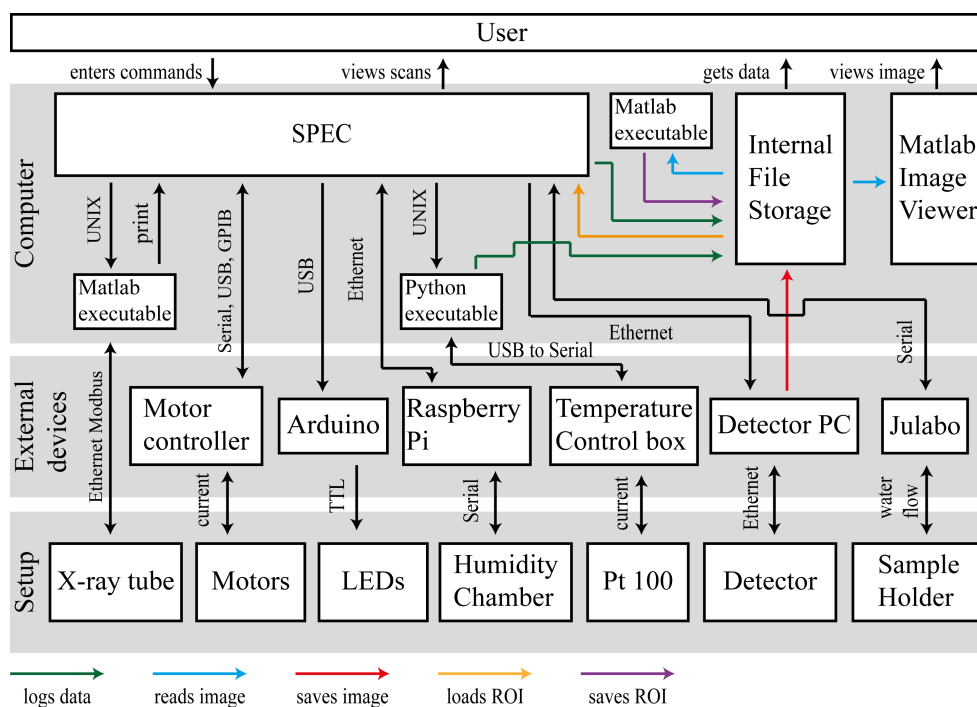


Figure 4.11: Workflow diagram of the setup. The diagram is divided into four blocks: the user of the setup, the main computer with its programs and external devices, and components within the setup. Black arrows indicate the direction of communication and the used interface. Arrows with other colors are explained below the diagram.

ware elements (external devices and setup units) is followed by an overview of the software which is used.

#### 4.5.1 Hardware

The main components of the setup can be split into three parts: X-ray source with collimation, sample area and detector positioning with beamstop. Two schemes of the setup configurations are shown in Figure 4.12 and 4.19.

##### *X-ray source and collimation*

The X-ray source is a Mo-anode based microfocus tube with a focus of  $50\ \mu\text{m}$  in diameter and a maximal power of  $50\ \text{W}$  ( $50\ \text{kV}$  and  $1\ \text{mA}$ ). The beam is monochromatized and collimated with a single reflection multilayer optic and has a horizontal divergence of  $0.12\ \text{mrad}$  and a vertical divergence of  $0.16\ \text{mrad}$  with a flux of  $5.7 \cdot 10^6\ \text{Ph/s}$  without slits. Both components are from Xenocs SA (Sassenage, France) and the product name is *GeniX 3D Mo ultra low divergence*. The used optic is called *FOX 2D*. The collimation path is  $82\ \text{cm}$  long, closed by a  $25\ \mu\text{m}$  thick Kapton foil (DuPont, USA) at the end and consists of two scatterless slits. Each slit is a rectangular single crystal of germanium which is bonded to a metal base substrate with a large tapering angle away from the beam. This configuration reduces parasitic scattering

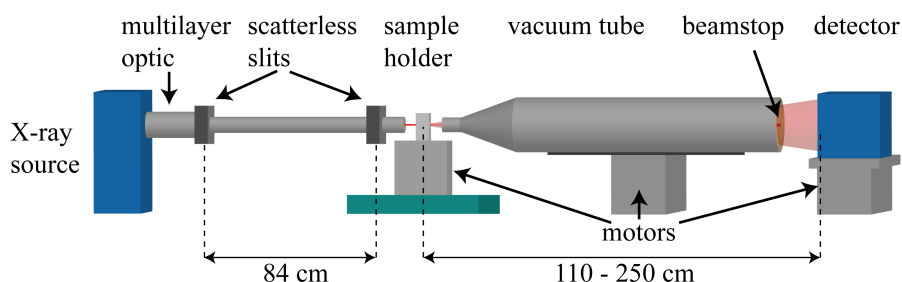


Figure 4.12: Scheme of SAXS setup. The X-ray source with multilayer optic and a collimation consisting of two motorized scatterless slits, the motorized sample stage, where the sample is mounted, and the evacuated flight tube with beamstop and detector.

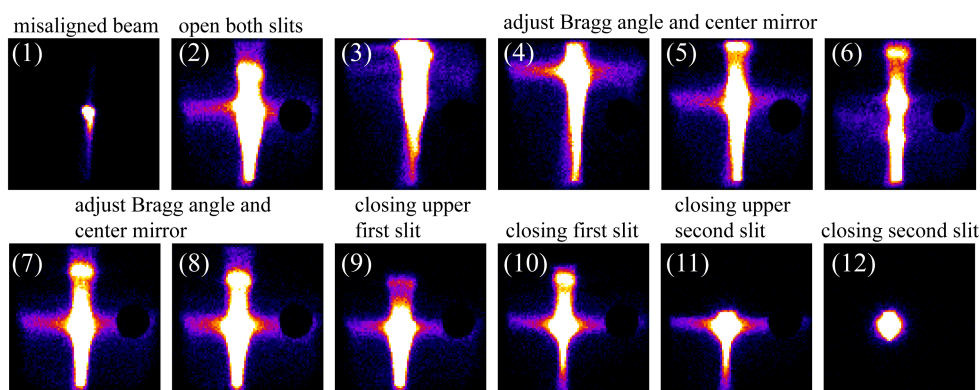


Figure 4.13: Beam adjustment in three steps: The z-position (up and down) is adjusted for the Bragg angle, the x-position (left and right) to center the mirror and the slit positions are adapted to the beam. The procedure is explained in more detail in the text. The color code ranges from 1 (black) to 100 counts/s/pixel or above (white).

significantly and enhances resolution compared to conventional X-ray apertures [53]. Both scatterless slits are fully motorized and are controlled by a *MDrive23* (Schneider Electric Motion, former: IMS, USA) motor controller via a serial to universal serial bus (USB) connection. The beam size can be reduced, but at the expense of flux at the sample. Typically, the flux is  $1.6 \times 10^6$  Ph/s with a beam size of about  $0.9 \times 0.9 \text{ mm}^2$  at the sample position. The size is defined in such a way that the count rate is zero outside and not by the typical size measure of the FWHM.

The multilayer mirror is mounted directly to the X-ray source and its position can be adapted with two screws in x- and z-direction. A typical adjustment of the beam is shown in Figure 4.13. First, a strongly misaligned beam with low intensity and anisotropic shape is shown (1). For the alignment both slits are opened and a cross like intensity with a peak above the beam appears. This peak can be attributed to the direct beam of the source, which is not collimated by the mirror. Both screws are used to center the mirror and to find the position which fulfills the Bragg condition of the mirror (3)-(7). Even when the mirror is aligned the cross shape of the beam is still present

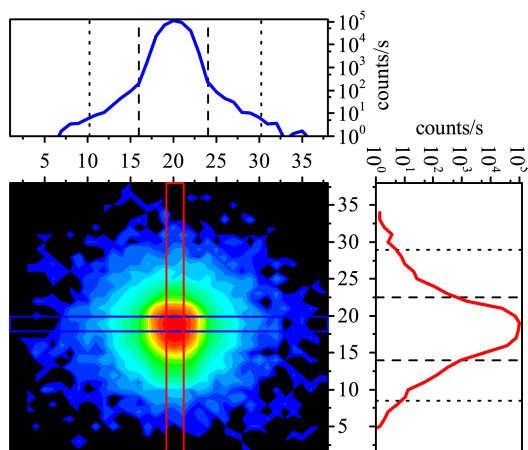


Figure 4.14: Contour plot of the direct beam with horizontal and vertical profile in units of detector pixel (pixel=0.172 mm). Both profiles are integrated over 3 pixels, which is shown by blue and red lines, respectively. The dashed lines in profiles indicate the area of high intensity, which are 8 pixels and 8.5 pixels wide for the horizontal and vertical profile, respectively. The dotted lines are 20.5 pixels (3.53 mm) apart.

due to parasitic scattering of the mirror, see Figure 4.13 (8). The color code is adjusted to low intensities and therefore it is not visible that the center of the beam has several orders of magnitude higher intensity, see Figure 4.14. In the next step, both slits are positioned. By closing the upper first slit (9), the intensity in the upper part of the beam decreases, but the direct beam is not completely absorbed and therefore still visible as a peak. When the first slit is closed it cuts only slightly into the beam and the cross shape of the beam persists (10). Once the second slit is also closed, a well-defined beam is obtained (12).

Figure 4.14 shows the beam in more detail with horizontal and vertical profiles. The beam exhibits a high intensity at its center, which is marked with dashed lines in the profiles. The width is about 8 pixels, which corresponds to a size of 1.38 mm. It appears slightly broader than the calculated value of 1.09 mm at the detector position due to the divergence with a distance from slit to detector of 1.2 m (see section 4.2). The dotted lines indicate the width of the calculated beam size of 3.53 mm as a result of the collimation according to Equation 4.4. This highlights that even for collimated beams, a sufficient long collimation length is crucial to remove the parasitic scattering of the mirror. In section 4.2 it was shown that a longer collimation length can significantly decrease the minimal  $q$ -value. Here, the experiment illustrates the two contributions of the collimated and uncollimated part of the beam. Therefore, an increased collimation length would lead to a smaller  $q_{min}$  without significant loss of primary beam intensity, as most of the intensity is in the inner part of the beam (dashed lines in Figure 4.14).

Another possibility to reach a lower  $q_{min}$  is to close the slits. However, this is at the expense of beam intensity. Figure 4.15 shows the count rate of the beam in dependence on the second slit size. The first slit was adjusted to the

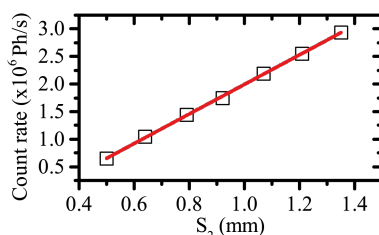


Figure 4.15: Count rate dependence on the size of the second slit. The first slit size is fixed and only cuts slightly into the beam.

beam and with completely open second slit a count rate of  $4.1 \cdot 10^6$  Ph/s was reached. For the measured range of second slit size a linear behavior can be observed. The gradient is  $2.68 \cdot 10^6$  Ph/s per millimeter opening of the slit. The fit has an offset of  $-0.69 \cdot 10^6$  Ph/s because this linear behavior is only present in the beam center, where the slit edge is still in the intensity plateau of the beam. The beam size can be changed easily due to fully motorized slits and the scatterless slit technique. The slits do not introduce parasitic scattering even if the slit is significantly in the beam. If no low minimal  $q$ -value and no high  $q$ -resolution are needed, the second slit can be opened to increase the beam intensity. At the cost of a lower intensity a smaller slit size can be important to obtain a lower minimal  $q$ -value because the scattering intensity of a typical sample is usually the highest at low  $q$ -values. The standard setting of a slit opening of 0.9 mm is a compromise between intensity and minimal  $q$ -value.

#### *Sample environment*

The sample stage is positioned 5 cm in front of the collimation path exit and consists of a  $10 \times 10$  cm<sup>2</sup> platform with high precision mechanics (Huber, Germany). The stage is equipped with six stepper motors and allows to translate the sample in all directions as well as to rotate it around all three axes. All motors are controlled by two motor controllers *IXE* (Phytron, Germany) which are connected to the PC via GPIB and serial to USB. The precision is 5  $\mu$ m in horizontal direction and 0.1  $\mu$ m in vertical direction. For the rotations a precision of 0.005° is reached. This sample stage can host a variety of sample chambers or more complex sample environments for application in transmission as well as reflection or grazing incidence mode. Holders for standard sample chambers like quartz capillaries or silicon wafers exist, but this section focuses on more specialized types of sample environments for SAXS or WAXS and a controlled environment with a humidity chamber.

**SAXS SAMPLE CHAMBERS** Within this thesis two different sample chamber types for SAXS measurements were developed. This was a consequence of the increased optimal sample thickness of Mo compared to Cu (section 4.4.1) because standard sample holders such as quartz capillaries have a maximal diameter of 5 mm. These capillaries use the sample volume inefficiently because the beam is perpendicular to the capillary and therefore only a small

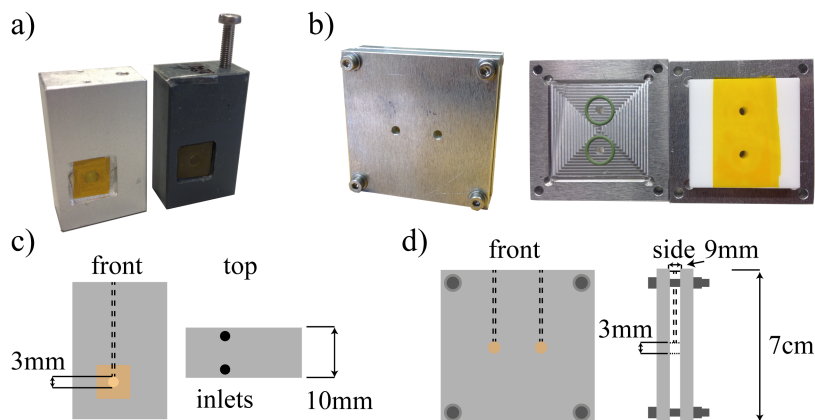


Figure 4.16: Two types of sample chambers for SAXS measurements with photographs in a) and b) and corresponding schemes in c) and d).

area of the volume is illuminated. Photographs of both chambers with their schemes are shown in Figure 4.16.

One approach uses chambers made of plastic or aluminum with a 3 mm hole and a thickness between 2-10 mm depending on the available sample. The holes are glued with windows of 25  $\mu\text{m}$  thick Kapton or potassium aluminosilicate (muscovite mica) sheets (Goodfellows Cambridge Ltd., UK). On the top two small inlets with a diameter of about 0.6 mm are used to fill the sample chamber. The inlet holes are as close as possible to the edges in order to avoid the formation of air bubbles within in sample cell. It turned out that increasing the length of the inlets helps to prevent the formation of air bubbles during the measurement, even if the holes are closed with adhesive tape. This is the reason for the long inlet length of 2 cm. The calculated volume of the sample chamber with a thickness of 10 mm is about 70  $\mu\text{l}$  and the inlets have a volume of about 6  $\mu\text{l}$ , which is in total 82  $\mu\text{l}$ . However, it turned out that is practical to have 90  $\mu\text{l}$  of the sample because the thickness of the sample chamber increases slightly due to the flexibility of the Kapton foils and the holes vary in size due to the machining.

The second type of chamber uses a spacer made of Teflon and the windows are clamped in an aluminum frame with O-rings. The advantage of this type of chamber is that the thickness can be varied by using different thicknesses of the Teflon spacer. Furthermore, the amount of work is less because the windows are clamped and no gluing is necessary. This facilitates cleaning the chamber after usage. The windows can be disposed of and the Teflon block can be cleaned with almost any solvent in a sonic bath cleaner. One drawback is the temperature being harder to control because the chamber is bigger and does not fit in the standard sample holder. However, the size of the chamber can easily be decreased and a suitable sample holder can be built.

The aluminum chambers of the first sample chamber type are suitable for temperature sensitive measurements due to a higher heat transfer of the material in comparison to plastic. On the other hand, a disadvantageous attribute of aluminum is the higher chemical reactivity as opposed to plastic.

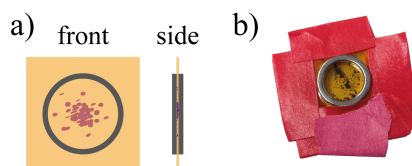


Figure 4.17: Sample holder for powder diffraction measurements. a) sketch of the holder with Kapton foil (orange) and two ring magnets and b) photograph of a sample with additional tape for fixation.

The chamber with Teflon spacer and aluminum frame proves to be a reasonable compromise. The Teflon and the Kapton are resistive to most chemicals and have a low reactivity. The aluminum frame ensures an adequate heat transfer from the sample holder to the sample. The sample holder itself is made of aluminum with a steady flow of water through its frame. The temperature of the water is controlled by a refrigerated-heating circulator (F12-MA, Julabo, Germany), which is connected to the PC via a serial connection. A home made temperature control box measures the temperature at the sample with a PT100 or PT1000 resistor. This box is connected via a serial to USB connection and a self-written Python script can read the current temperature and log it to a file.

**WAXS SAMPLE CHAMBERS** The same chambers as for SAXS can be used for solution-based WAXS, but a smaller sample thickness is required in order to keep a sufficient resolution in  $q$  (section 4.3). Often powders are utilized for WAXS measurements, which need a different sample chamber, as sketched in Figure 4.17. Powder samples are prepared in the following way: First, the powder is put on a 25  $\mu\text{m}$  thick Kapton foil. Since the Kapton foil is electrostatic, the powder sticks to the foil and complicate the handling. Secondly, another Kapton foil is placed on top of the powder. Afterwards ring magnets (inner diameter 9 mm) are carefully positioned on both sides, which fix the powder between the two foils. It is easier to place the magnets when the foils are already in their right location, which can be done by fixing them with tape like in Figure 4.17 b). At this setup WAXS was only measured in the transmission geometry and therefore no preparation for reflection is needed.

The material lanthanum hexaboride ( $\text{LaB}_6$ ) is certified by the National Institute of Standards and Technology (NIST) as a standard material for peak shape analysis. The crystal size and quality of  $\text{LaB}_6$  is sufficiently high that the peak width is only limited by the instrument. Therefore, it was used as a reference material for crystal size analysis with the Scherrer equation and the determination of the SDD for WAXS measurements.

**HUMIDITY CHAMBER** One example for a complex sample environment, which was developed within this thesis, is the temperature controlled humidity chamber. It can be used to study lipid phases in dependency on water content and temperature [74]. Figure 4.18 gives a schematic overview

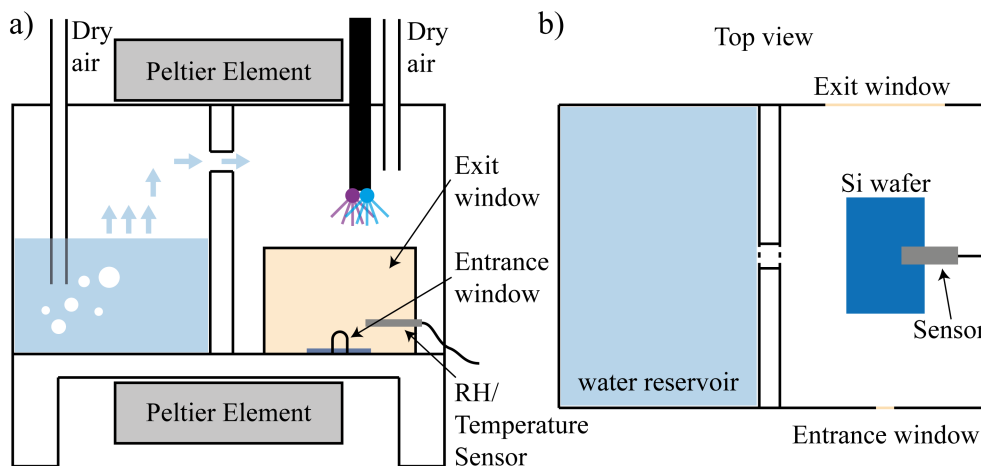


Figure 4.18: Scheme of temperature controlled humidity chamber: a) side view and b) view from top. Dried air is either pressed through a water bath or directly into the chamber. This way the RH can be adjusted. Peltier elements are mounted on top and at the bottom of the chamber to control the temperature. A glass fiber with coupled LEDs can be positioned above the sample. The RH and temperature sensor is mounted directly above the sample.

of the chamber. The humidity is regulated via two mass flow controllers (MF1, MKS, USA), which handle the flow of dry air either directly into the chamber or through a water reservoir producing moist air. The compressed air is cleaned with filters and dried with an active carbon and a membrane filter (Festo, Germany). A Peltier controller and two corresponding Peltier elements, one on top and one at the bottom of the chamber, regulate the temperature. This way the whole chamber is evenly heated or cooled and the water is leveled with the temperature, which prevents condensation. A combined sensor for humidity and temperature (SHT75, Sensirion, Switzerland) is placed above the sample. It has a high accuracy with a RH error of  $\pm 1.8\%$ . In between 10-90%RH at 25 °C the error is even below  $\pm 0.5\%$ . The error of the temperature is  $\pm 0.3\text{ }^\circ\text{C}$ . A Raspberry Pi with a self-written Python script regulates the temperature and RH. The sensor values are used for the regulation with a PID controller.

An optical fiber with two different fibers can be placed above the sample in order to correlate structural changes with illumination. High power LEDs (Prizmatix, Israel) are coupled into the optical fibers. The LEDs have wavelengths of 365 nm with a FWHM of 12 nm and 460 nm with a FWHM of 26 nm. Therefore, they are suited for photo-switching of azobenzene molecules (chapter 7). The intensity can be regulated and depends on the distance between fiber exit and sample because the light is divergent exiting the glass fiber. At a typical distance of 1 cm for the measurements, the intensity can be tuned from  $0.06\text{ mW/mm}^2$  to  $0.35\text{ mW/mm}^2$  for the LED with 365 nm and from  $0.10\text{ mW/mm}^2$  to  $0.53\text{ mW/mm}^2$  for the LED with 460 nm. The optical fibers can also be used without the chamber and the LEDs are controlled via transistor–transistor logic (TTL) signals. The switching of the LEDs with

the TTL signal is done with an Arduino, which is connected to the central computer via a USB connection.

#### *Flight path and detector*

The setup has three different standard configurations, which differ in SDD in order to cover a wide  $q$ -range. The medium (110 cm) and the long (250 cm) SDD only differ in the length of the vacuum tube. For the short distance of 32 cm the vacuum tube has to be removed and a frame with Kapton with a glued beamstop of Pb is placed as close as possible to the sample in order to avoid air scattering. Figure 4.19 depicts a scheme of the setup in the WAXS mode.

All beamstops use adhesive Pb foil tape (3M, USA) with a Pb thickness of  $120\ \mu\text{m}$ , which leads to a calculated transmission of  $10^{-7}$  for  $K_{\alpha}$ -radiation of Mo. Therefore, the beamstops are semi-transparent and the transmitted direct beam can be used, e. g. for normalization. The beamstops are round and 4 mm in diameter for the shortest and longest SDD and 3 mm for the intermediate one. They are punched out of the tape, which sticks to Kapton window of the vacuum tube or the Kapton frame for WAXS. Therefore, no extra beamstop holder is necessary and entire scattering signal around the beamstop can be used for evaluation.

Two different vacuum tubes can be mounted into the setup, one with a total length of 95 cm and the other with 175 cm. Both tubes have the same geometry: An entrance window of 24 mm in diameter with a clamped  $25\ \mu\text{m}$  thick Kapton foil, a conical extension to a 50 mm diameter tube of 14 cm length with a connection for the vacuum pump, followed by a conical extension to a 102 mm tube in diameter, which is either 70 or 150 cm long. The exit window is a  $50\ \mu\text{m}$  thick Kapton foil, which is clamped in a CF flange and supported by rubber. The vacuum tube is mounted on a rail. In order to adjust the beamstop, the whole tube can be moved by two stepper motors in  $x$ - and  $z$ -direction.

A Pilatus 100K (Dectris, Switzerland) serves as the detector with  $487 \times 195$  pixels with a size of  $172\ \mu\text{m}$ , which leads to an active area of  $83.8 \times 33.5\ \text{mm}^2$ .

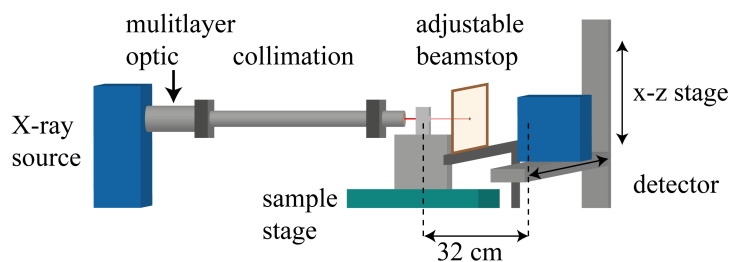


Figure 4.19: Scheme of Setup in configuration for WAXS measurements. The collimation and sample area is unchanged to the SAXS configuration in Figure 4.12. The beamstop is glued to a frame with Kapton foil, which is mounted close to sample and can be adjusted by micrometer screws. The detector is on a  $x$ - $z$  stage and the area can be scanned.

This hybrid pixel detector enables single photon counting and has an efficiency of 76 % for  $K_{\alpha}$ -radiation of Mo due to a silicon sensor thickness of 1 mm. The detector is air-cooled and can easily be moved for the three different configurations of the setup. It has a Linux based PC with an Ethernet connection, which is used for the communication to the detector. An upgrade to the Pilatus 300K is planned. It has three of the sensor elements of the Pilatus 100K, which are on top of each other with gaps of 17 pixels to a size a  $83.8 \times 106.5 \text{ mm}^2$  stacked. With a centered beam this detector covers  $360^{\circ}$  of scattering signal for a wide q-range due to its almost square shape, see Figure 4.1.

#### 4.5.2 *Software*

The used software can be divided into one used directly at the setup and another one for post processing and data analysis.

##### *Setup*

The main program is spec (certified scientific software, USA), which coordinates all hardware and handles the measured data. The software controls all stepping motors and allows to do scans, for instance, for sample alignment. Furthermore, it is possible to implement small macros and define functions in order to automate routines, for example, doing calibration measurements or temperature control of the sample. However, the software cannot directly communicate with all hardware components or perform analysis tasks like evaluating the region of interest (ROI) of a detector image.

For these tasks, several small MATLAB (MathWorks, USA) or Python programs are used. All MATLAB programs are compiled and do not need a license of MATLAB, but the MATLAB Runtime version 7.17 has to be installed. MATLAB scripts for the control of the X-ray generator were provided from Xenocs. These scripts were adapted to spec and compiled. The communication uses a Modbus TCP protocol. Another MATLAB script implements the function of a ROI. It reads the recent detector image, which is always copied via secure copy (SCP) to the computer as "temp.tif". It sums the counts of all pixels within the ROI, which can be entered in spec, and saves the value on the hard drive in a file "temp.dat". This file can be read by spec and used as a counter. The communication with the temperature readout box is done by a Python script, which can read the temperatures and save them to a log file in a defined time period. For the visualization of detector images a MATLAB program with a graphical user interface (GUI) is used. It reads the most recent image "temp.tif" and displays it. The scale of the color code can be easily varied and horizontal and vertical cuts of the ROI can be made.

##### *Post processing and data analysis*

A self-written MATLAB function allows for stitching detector images with shifted acquisition positions which are done for WAXS measurements in

order to increase the solid angle and to reach a higher maximal  $q$ -value. With ImageJ [75] high-intensity peaks of alpha decay can be removed. This can be done by taking the median of at least three detector images or by using the macro "Removing outliers". The data reduction of the 2D image is done by Nika [76], a plugin for Igor Pro (WaveMetrics, USA). In the same software the SDD can be determined with standard calibration materials like silver behenate (AgBE) or LaB<sub>6</sub>. The 2D data can be radially integrated with a given number of bins and is saved versus scattering angles or  $q$ -values. Intensity uncertainty and  $q$ -resolution are saved with the data.

For the analysis of the data, SasView [77] has proven to be a valuable tool. The software has already many form factors included and takes care of polydispersity and  $q$ -smearing. If a model is not already embedded, it can be written in Python or C. One significant advantage for more complex models is that the calculation can be made on the graphics processing unit (GPU). The model must be written in C. Especially the included Differential Evolution Adaptive Metropolis (DREAM) fit algorithm [78] is very robust and provides a detailed error with the dependency of the fitting parameters on each other.



## PEROVSKITE NANOPATELETS

---

*The work described in this section has been partly published [3].*

The first description of a perovskite, which is a calcium titanium oxide, was already in 1839 [79] and the name of the crystal structure originates in this mineral. The organometal version of the crystal structure perovskite is known since the 1970s [80]. In 2009, the first organometal perovskite-based solar cells with an efficiency of 3.8% appeared, followed by a fast increase in efficiency [81]. In 2012, perovskite solar cells gained high attention because a solar cell with 10.9% efficiency was built from a solution of organometal halide perovskites [82]. This attention is mirrored in the number of publications related to the topic "perovskite", which increased dramatically after 2012 like shown in Figure 5.1. The high technical potential is caused by the easy fine tuning of absorption and emission with constituent ions and creation of mixtures [83–85]. Furthermore, small perovskite crystals or nanocrystals exhibit interesting physical properties compared to bulk 3D perovskites like higher exciton binding energy, lower fluorescence decay times, higher absorption or optical nonlinearity. Quasi-two-dimensional structures are also referred to as nanoplatelets which consist of only a few layers of unit cells in one direction. These properties open up a wide application field in optoelectronics [86, 87]. For example, perovskites are suited as photo detector material, for photovoltaics or LEDs. Especially as photo detector for hard X-rays, perovskites are of interest due to the high absorption of X-ray photons by lead [88]. The reason that perovskites only came into focus recently is linked with the development of new instrumentation for the characterization of morphology in shape, size, and thickness. The crystal structure of nanocrystals has always been crucial for understanding their morphology-

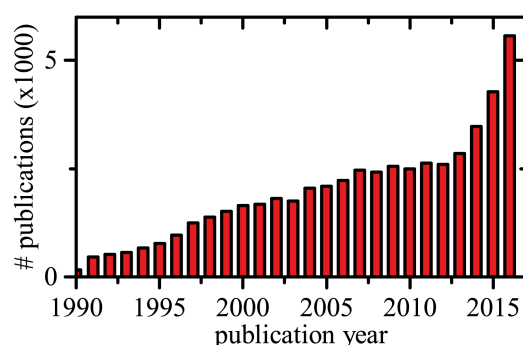


Figure 5.1: Number of publications per year with the topic 'perovskite' [source: Thomas Reuters (Web of Science)].

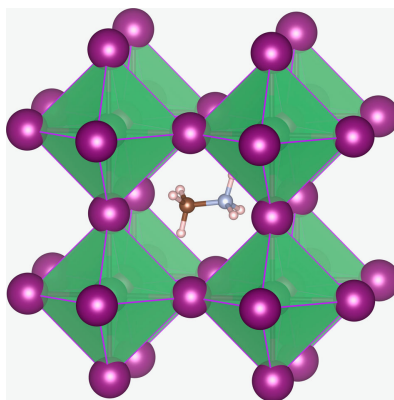


Figure 5.2: Perovskite unit cell structure of  $\text{CH}_3\text{NH}_3\text{PbBr}_3$ . MA occupies the central A site surrounded by 12 nearest-neighbor bromide ions in corner-sharing  $\text{PbBr}_6$  octahedra. Figure is licensed under CC BY 4.0 [95].

and structure-dependent properties. The advances in scientific instrumentation over the years have made the characterization of nanomaterials relatively easy and accurate [87]. The combination of TEM, SEM, AFM and X-rays make a complete understanding of the structure possible. Therefore, the research on perovskites is still ongoing, which the title of a recent short review shows: "Low-Dimensional-Networked Metal Halide Perovskites: The next big thing" (2017) [89].

The unit cell of a typical perovskite used for solar cells is given in Figure 5.2. The usual stoichiometry of perovskites is  $\text{ABX}_3$ . It consists of octahedra with Pb (B) in each center and, in our case, bromide (X) at its corners. Other typical compounds are iodide or chloride. An organic cation is located between the octahedra (A), in our case methylammonium (MA) ( $\text{CH}_3\text{NH}_3$ ). Mixing MA bromide with lead bromide will result in a macroscopic perovskite crystal ( $\text{MAPbBr}_3$ ). In order to control the crystal growth of the perovskite, an additional organic cation can be mixed into the solution. The idea is that it replaces the MA and binds to the octahedra. If the size of the molecule, which replaces MA, is too voluminous to be incorporated into the crystal structure, the growth in the direction of the binding of this molecule will stop. Here, we used octylammonium (OA) ( $\text{C}_8\text{H}_{17}\text{NH}_3$ ), which has the same ammonium group as MA, but it has a carbon chain of eight atoms attached instead of only one.

The crystal structure of  $\text{MAPbBr}_3$  is well known and it is a cubic crystal structure with the space group  $\text{Pm}\bar{3}\text{m}$  at room temperature. However, the lattice constant is not completely consistent in literature and varies between 5.901-5.933 Å [80, 90-94].

For the synthesis of the perovskites the OA to MA concentration was varied from 0-100%. For 0% extended perovskite lattices are expected because no growth limiting OA is in the solution. In contrast, for 100% concentration of OA there is no possibility for 3D growth and only lead bromide octahedra

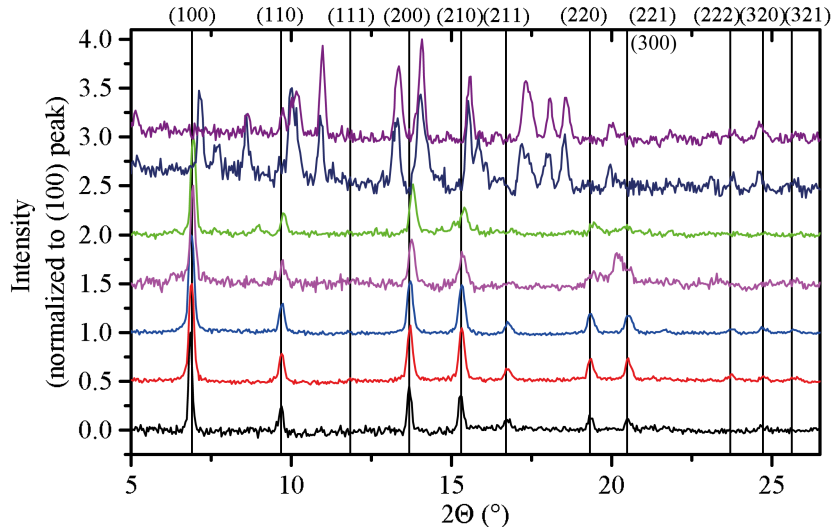


Figure 5.3: Perovskite powder XRD measurements with OA concentration from 0-100% in 20% steps and the precursor  $\text{PbBr}_2$  (bottom to top). The Miller indices (hkl) are indicated with vertical lines for a perovskite with  $\text{Pm}\bar{3}\text{m}$  space group and unit cell parameter  $a=5.988 \text{ \AA}$ . The data is normalized to the highest peak intensity and each data set is shifted by 0.5 for clarity. Mo- $\text{K}_\alpha$  radiation of the setup described in section 4.5 was used.

can grow and form a 2D layer. Absorption and PL measurements on the resulting perovskites showed a blue shift for increasing OA concentration, which can be explained by the theory of quantum confinement. It can be observed once the size of a material is of the same magnitude as the de Broglie wavelength of an electron. Additionally, SEM and TEM images support the theory of a crystal thickness down to one layer. The SEM and TEM images, the absorption and PL measurements, and a theory of quantum confinement are described in high detail in [3]. Here, the focus is on the X-ray analysis to determine the crystal structure and it is tried to estimate the platelet thickness.

## 5.1 PEROVSKITE POWDER

X-ray powder diffraction (XRD) measurements were carried out to confirm the successful crystalline growth of the perovskite with different OA concentrations. The concentration of the perovskites in toluene solution was too low to observe Bragg peaks. Therefore, the solution was dried on a Kapton foil and the resulting powder was fixed with a second Kapton foil and two ring magnets as introduced in section 4.5.1. The sample-to-detector distance was 22 cm, which was calibrated with  $\text{LaB}_6$ . In order to obtain high order Bragg peaks, two images with different x-positions of the detector were made for 300 s each. These two images were stitched with a self-written Matlab code and radially integrated.

The XRD data of the perovskites with different OA concentration and the precursor  $\text{PbBr}_2$  are shown in Figure 5.3. The thickness of the powder var-

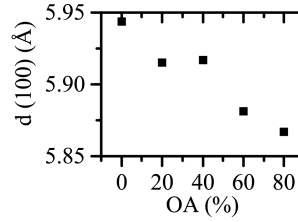


Figure 5.4: Lattice spacing  $d_{(100)}$  for different OA concentrations.

ied, so for better comparison the intensity is normalized to the highest peak intensity, which is the (100) peak for all perovskites. The crystal structure was determined with the sample of 20% OA because it was the thickest sample and therefore showed the highest S/B. The data were analyzed with the GSAS-2 software [96] and confirmed a cubic perovskite structure with a unit cell parameter of  $a=5.988 \text{ \AA}$ . This value is slightly higher than the literature values. A fit of the (100) peak for 0%-80% OA concentration shows a higher agreement with the literature values of the bulk perovskite, which are given in Figure 5.4. The data suggests a tendency of a decreasing lattice constant for increasing OA concentration, but it is only in the sub  $\text{\AA}$  regime. In the literature, the opposite effect of an increasing unit cell was reported for CsPbBr<sub>3</sub> [97]. They attributed the difference to the interaction of the OA. Interaction with OA is also likely to be responsible for the decreasing lattice spacing in our case. For a 100% OA concentration, hence in the absence of MA, no perovskite formation can be observed. Only the Bragg peaks of the precursor PbBr<sub>2</sub> remain. Due to the arrangement of the lead and the bromide, some peak intensities are suppressed, for example, the (111) peak, which is not visible in the data in Figure 5.3.

In order to increase the quality of the data, the 20% OA sample was measured with a different setup geometry, which had an increased SDD, a higher covered solid angle and a longer integration time. This measurement and the one with 20% OA concentration of Figure 5.3 are compared in Figure 5.5. For both measurements, uniform rings appear indicating that the powder consists of many crystallites with isotropically distributed orientations. At first glance, the integrated data is very similar and no significant difference between both measurements can be observed. A closer look allows the finding of a noisier background with the shorter integration time. The improved background of the long measurement is low enough to separate the low-intensity peaks of the (111) and (130) peaks from the background. The observation of these low-intensity peaks corroborates correct perovskite formation. This example of the two different measurements shows that most information can already be gained within minutes if the sample consists of scatterers with high contrast like Pb and/or an extended crystal exists. In this case, more details could be observed by increasing integration time. For a fast scan of several compositions like in this study, a short scan is sufficient because all relevant information is present in the data. The data quality will be crucial, however, if a refinement of the lattice constant is of interest.

The width of a Bragg peak can be used for the determination of the crystallite

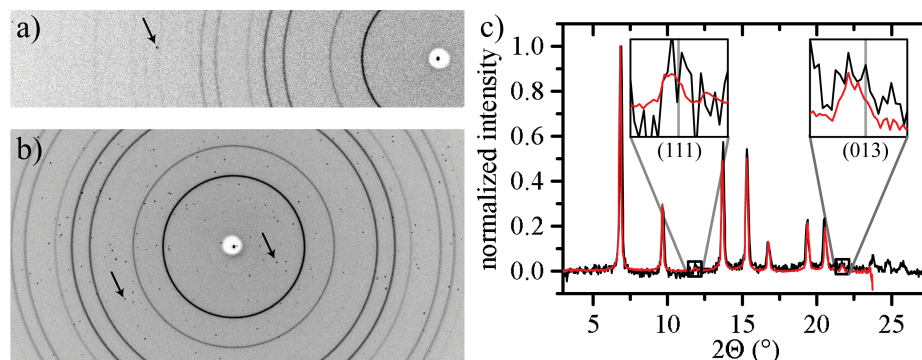


Figure 5.5: Two different XRD measurements of the same perovskite sample with 20% OA concentration. a) two stitched detector images with an integration time of 300 s each (intensity scale 1-30 counts, dark is high intensity) at a SDD of 22 cm, b) twelve stitched detector images with an integration time of 1 h each (intensity scale 1-100 counts) at a SDD of 32 cm. c) radially integrated data of a) (black) and b) (red). The high-intensity peaks (some marked with an arrow) in a) and b) are natural background and were masked for integration in c). Zoom-ins show positions of the weak Bragg peaks (111) and (130). The calculated peak positions ( $a=5.988 \text{ \AA}$ ) are shown as vertical gray lines. The data is normalized to the (100) peak.

size with the Scherrer Equation (Equation 3.38). In this case, the peak broadening due to finite crystallite size is hard to observe because the  $q$ -resolution is low, since a short SDD of 22 cm was used. More details on  $q$ -resolution can be found in section 4.3. In general, for anisotropic particles with a cubic unit cell, the Scherrer Equation is not suited. For example, the (100) peak has a multiplicity of 6. If the crystal is limited in one axis, but the other two are still extended, the Bragg peak is broad with a multiplicity of two, but a sharp Bragg peak with a multiplicity of four is still present. Hence, the peak width is dominated by the sharp peaks and no crystalline size can be extracted. If the (100) peak differs from (010) and (001) due to a non-cubic unit cell, a modified Scherrer Equation can be used [98].

The quality of the data shown in Figure 5.3 worsen with higher OA concentration. The quality loss originates from less sample material and consequently fewer crystallites in the X-ray beam. This little material is mainly owed to the design of the WAXS sample holder. An improvement of the chamber would lead to better data quality with few material and would make the data more comparable. This improvement could be accomplished for instance by having a smaller magnetic ring with a diameter of 2 mm in order keep the powder in a defined region.

## 5.2 CRYSTAL SIZE EVALUATION BY X-RAY BRAGG PEAK ANALYSIS

As mentioned in the previous section a size evaluation of the crystallites with a cubic unit cell is not possible by the Scherrer Equation because the

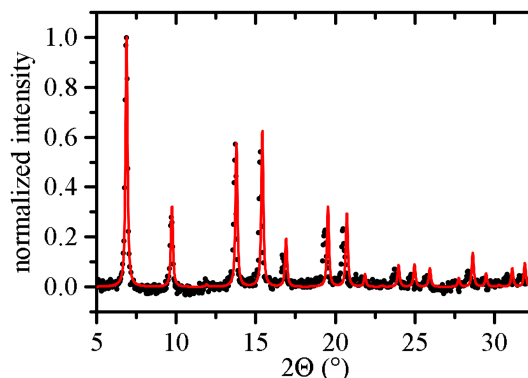


Figure 5.6: XRD data at 20% OA concentration (black circles) and simulated intensity of crystal structure of  $\text{MaPbBr}_3$  from literature (red line) [93]. Both data and simulated intensity is normalized to the (100) peak.

instrument resolution is low and more importantly the particles of interest are anisotropic.

In order to check the quality of the data, it was compared with simulated data reported in literature [93], shown in Figure 5.6. A slight mismatch in the lattice constant can be observed, which is better visible for higher order Bragg peaks. The relative intensities, however, are in good agreement, although the measured intensities tend to decrease with increasing scattering angle  $2\theta$ .

The TEM images have shown that the crystals have a platelet shape and the following analysis takes this into account. Since the domain size cannot be evaluated by the peak width, the idea is to estimate the thickness of the nanoplatelet by the normalized Bragg peak intensities. For example, the (100) peak has a multiplicity of six, but for a 2-dimensional lattice the intensities along only four of the corresponding directions are high and the thickness has nearly no contribution. The measured intensity should be about two-thirds of the simulated intensity. The (111) direction only probes the space diagonal, which is not present in a 2-dimensional sample; and therefore the peak should vanish completely in the limit of a single layer. Unfortunately, the intensity of the (111) peak is strongly suppressed already in the bulk perovskite like shown in Figure 5.5. However, a difference in peak height in the data of long integrated measurements can be observed between 20% and 80% OA concentration, which is shown in Figure 5.7. Some additional small peaks appear in the 80% sample, which can be attributed to residues of the precursor. They are indicated by small arrows in Figure 5.7. In the zoom, the (111) peak is shown, which is present in 20% OA sample but in the 80% it already vanished. This missing peak for 80% OA indicates that the confinement by increasing OA concentration in one growth direction works. Additionally, the intensities of peaks like (211) and (210) decrease strongly. The (200) peak, in contrast, has the same intensity, which is expected since the intensity is normalized to the (100) peak.

In order to support the idea that the decreased intensity is due to finite thickness, the peak intensities of peaks with the highest intensity were eval-

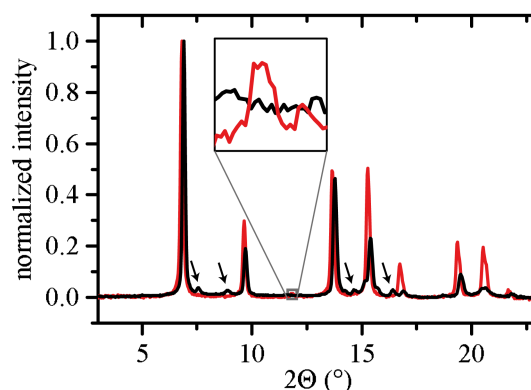


Figure 5.7: XRD data at 20% (red) and 80% (black) OA concentration with zoom to the (111) peak position. For both samples 12 images with 1 h integration time were taken like shown in Figure 5.5 b). The data is normalized to the (100) peak.

uated. The behavior of the normalized intensities with OA concentration is shown in Figure 5.8. A decrease in intensity can be observed for all peaks except (200).

The peak intensities were simulated with the lattice sum in Equation 3.32 and a function for the instrumentation. If the peak is very broad, only a part of it is measured with the instrument and this is taken into account. Furthermore, only the lead and bromide atoms were considered in the simulation because the scattering signal is dominated by these heavy atoms compared to the organic MA. The scaling of the intensities with a prefactor is complicated because many parameters like the Lorentz factor, the polarization and the instrument function contribute. In order to have a good estimation of the prefactor, the simulation was run with an extended crystal in all three dimensions. The result was compared to the output of the software "Diamond" [99] with a cif file containing the lattice parameters. The ratio of both simulations was used as prefactor for the peak intensities shown in Figure 5.8. For the final calculation, the number of unit cells of the nanoplatelet in  $x$  and  $y$  direction was fixed to  $N_x = N_y = 700$ , which corresponds to the mean size observed in TEM images. The thickness of the platelet was varied from  $N_z = 300$  down to one to describe the trend in the data. The result of the peak intensities depending on the nanoplatelet thickness is shown in Figure 5.8 on a second axis with logarithmic scale as solid lines. The trend of the relative intensities with decreasing platelet thickness and increasing OA concentration is well reproduced by the simulation. However, it is difficult to extract more detailed information. The exact dependency of the thickness with OA concentration remains unclear, although the simulation in Figure 5.8 suggests rather a logarithmic rather than a linear behavior. Definitely, for increasing OA concentration the nanoplatelet thickness decreases. Furthermore, polydispersity of the nanoplatelets in lateral direction as well as in thickness is not included in the simulation, but is likely to occur especially for the lateral sizes.

Nevertheless, PL measurements show a strong blue shift for a OA concen-

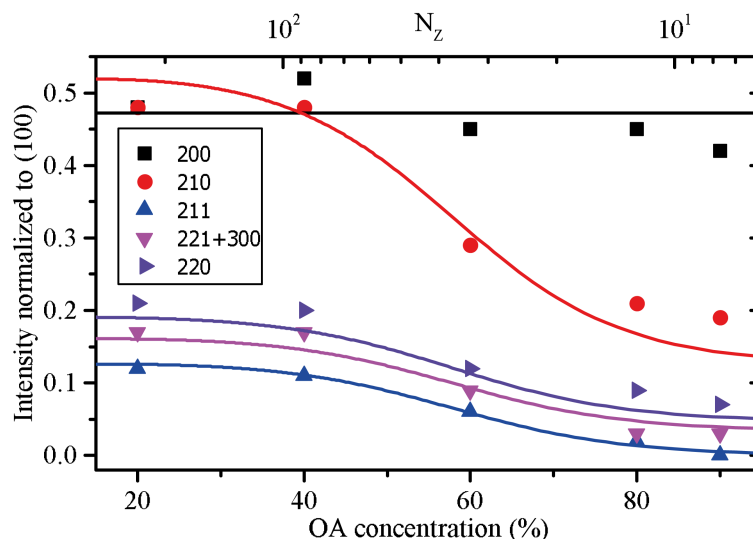


Figure 5.8: Measured intensities of selected Bragg peaks (dots, see legend) as a function of OA concentration. The data is normalized to the (100) peak intensity. Calculated Bragg peak intensities (lines) from  $N_x = N_y = 700$  unit cells in x and y direction with and decreasing  $N_z$  from 300 to 1 and are given in the upper axis. Note the logarithmic scale.

tration of 60% and higher. In the X-ray data, the thickness limited peak intensity decrease also starts with a OA concentration of 60%. Therefore, both measurements are in excellent agreement. Furthermore, TEM images of nanoplatelet clusters suggest thicknesses of down to a single layer and high polydispersity in the lateral dimension [3].

In conclusion, the X-ray data agree with the findings from photoluminescence measurements and corresponding calculations of quantum confinement as well as with TEM images. Only by the combination of these different techniques a complete understanding of the sample becomes possible.

## DNA ORIGAMI

---

DNA is one of the four major types of macromolecules that are essential for known life beside proteins, lipids, and complex carbohydrates. It carries the genetic information of an organism. The structure is known in high detail. A scheme of DNA is shown in Figure 6.1 a). DNA is a polynucleotide composed of nucleotides, which consist of a sugar-phosphate backbone and covalently bound nucleobases: cytosine (C), guanine (G), adenine (A) and thymine (T). The nucleobases bind via hydrogen bonds to form a double helix, which is called base pairing. The scheme in Figure 6.1 shows the double-helical structure of B-DNA with a resulting major and minor groove as well as the base pairs (bps). Watson and Crick suggested the double helix structure of DNA in 1953 [21] and were awarded the Nobel prize in Medicine in 1962 "for their discoveries concerning the molecular structure of nucleic acids and its significance for information transfer in living material" [100]. The double helix structure was proven with the famous X-ray diffraction image 'Photo 51' (Figure 6.1 b)) of Rosalind Franklin in the same issue as the Watson and Crick paper [20]. With this important X-ray image the bp stacking distance could be determined to 3.4 Å [20, 21]. Furthermore, the distance from the center of the DNA to the phosphorus in the backbone was figured out to be 1 nm [20, 21].

In 1982, Nadrian Seeman laid the theoretical framework for DNA nanotechnology [101]. He suggested to use DNA as the building block for 3D lattices using the Watson-Crick base pairing and so-called Holliday junctions, which describes the crossing of four DNA single strands [102]. He was trained in X-ray crystallography and he intended to use this 3D lattice to "(...) alleviate a major problem in the co-crystallization of protein-nucleic acid complexes." [101]. He used DNA in the construction of increasingly complex shapes and lattices [103–106]. In 2004, William Shih and co-workers were able to build an octahedron from a synthetic 1.7-kilobase single stranded-DNA [107]. One big challenge was to find a long DNA strand, which can be duplicated via polymerase chain reaction (PCR).

In 2006, Paul W. K. Rothemund developed the technique of DNA origami [108]. "The design for a desired shape is made by raster-filling the shape with a 7-kilobase single-stranded scaffold and by choosing over 200 short oligonucleotide 'staple strands' to hold the scaffold in place." [108]. This approach had the advantage that the scaffold strand can be extracted from a virus and the short 'staple strands' are easy to synthesize. Furthermore, it allows for a wide variety of structures and functionalization, for example with gold nanoparticle (AuNP) [109, 110]. The first structures Rothemund built are shown in Figure 6.2. They already show the possible variety of simple rectangular shapes (a,b), stars (c), triangles with a hole (e,f) or even

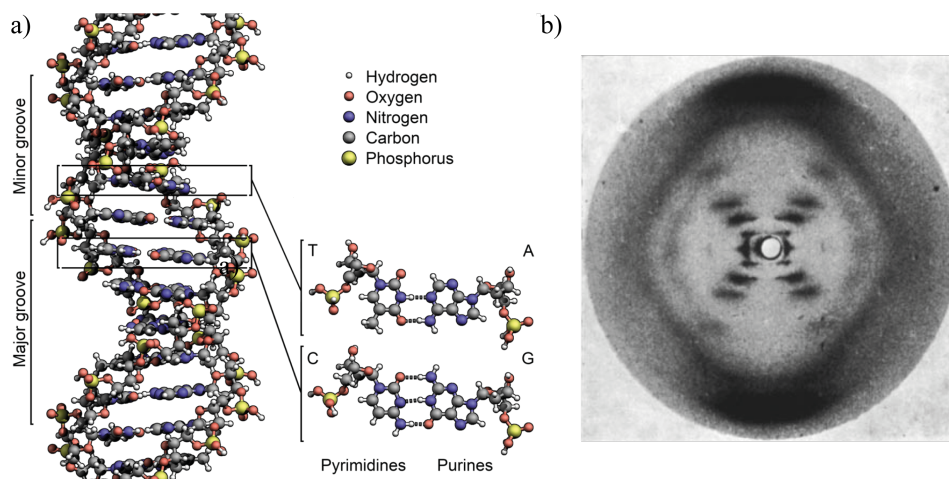


Figure 6.1: a) The molecular structure of B-DNA and in detail the four bases: adenine, cytosine, guanine, and thymine. The location of the major and minor groove is indicated. [source: Zephyris is licensed under CC BY SA 3.0] b) The "Photo 51" of Rosalind Franklin shows the X-ray diffraction of a B-DNA double helix structure. [20] © Nature Publishing Group; reproduced with permission.

smiley faces (d). However, all these structures only consist of a single DNA layer and therefore are 2-dimensional. In 2009, the principle of DNA origami was extended to solid 3D structures [111]. The underlying design principle, explained in Figure 6.3, is based on a honeycomb lattice of DNA double helices. In the same year, it was also shown that it is feasible to build solid 3D structures with a square lattice within the DNA origami [112]. Other groundbreaking advances in the same year were, first, the introduction of twist in DNA origami structures, which allows for curvature within a DNA origami or, for example, ring formation [113]. Also, second, the development of the userfriendly computer program caDNAno facilitated the creation of DNA origami for a broad community [114].

Another approach to form 3D structures was to connect 2D DNA origami by DNA single strands to form a box with a lid [115]. The interesting feature of this box is a programmable opening for cargo delivery, for example. Furthermore, it was the first DNA origami structure to be studied with SAXS in order to measure the size of the box.

At the same time, techniques to form higher order structures out of DNA were developed. The formation of supramolecular structures like polyhedra from smaller subunits of DNA via self-assembly was shown in 2008 [116]. Nadrian Seeman showed the possibility to form extended 3D lattices in the range of  $250\ \mu\text{m}$  out of DNA in 2009 [117]. He used a tensegrity triangle structure as a building block [118]. The over-under motif of the triangle enabled 3D growth. The building block was resolved with  $4\ \text{\AA}$  resolution by X-ray diffraction. However, the maximum cavity size of these structures is about  $1000\ \text{nm}^3$ , which is too small to co-crystallize proteins for example. In 2015, Oleg Gang and co-workers built AuNP-DNA linear chains and 2D square lattices by using octahedral DNA origami with bound AuNP as build-

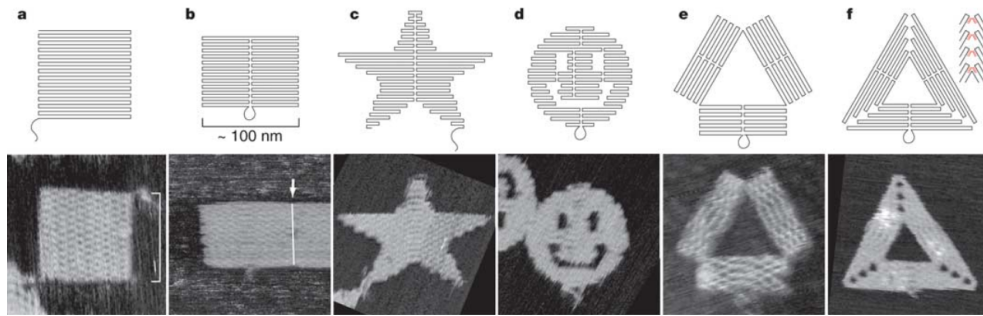


Figure 6.2: DNA origami shapes. Top row, folding paths. a) square; b) rectangle; c) star; d) disk with three holes; e) triangle with rectangular domains; f) sharp triangle with trapezoidal domains and bridges between them (red lines in inset). Dangling curves and loops represent an unfolded sequence. Bottom row, AFM images. All images and panels without scale bars are the same size, 165 nm times 165 nm. [108] © Nature Publishing Group; reproduced with permission.

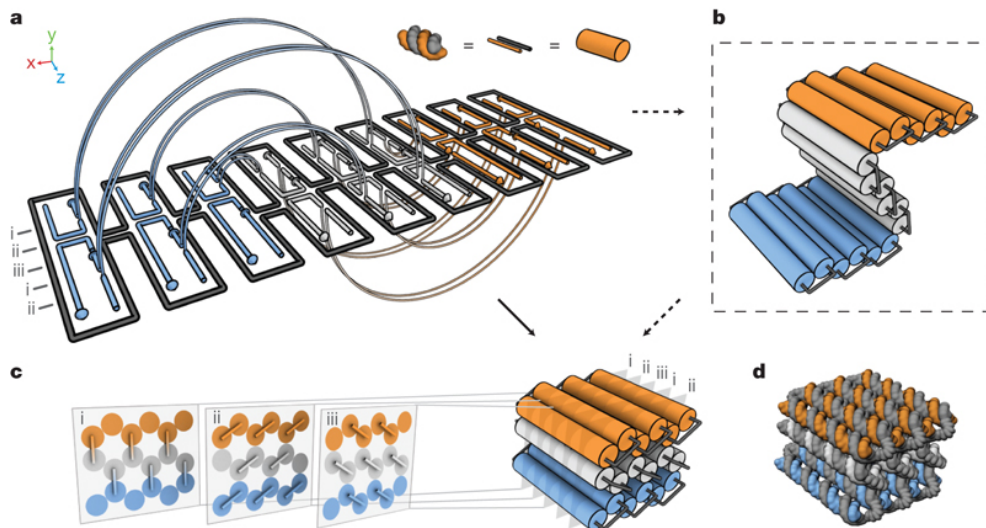


Figure 6.3: Design of three-dimensional DNA origami. a) Double helices comprised of scaffold (gray) and staple strands (orange, white, blue) run parallel to the z-axis to form an unrolled two-dimensional schematic of the target shape. Phosphate linkages form cross-overs between adjacent helices, with staple cross-overs bridging different layers shown as semicircular arcs. b) Cylinder model of a half-rolled conceptual intermediate. Cylinders represent double helices, with loops of unpaired scaffold strand linking the ends of adjacent helices. c) Cylinder model of the folded target shape. The honeycomb arrangement of parallel helices is shown in cross-sectional slices (i-iii) parallel to the x-y plane, spaced apart at seven bp intervals that repeat every 21 bps. All potential staple cross-overs are shown for each cross-section. d) Atomistic DNA model of shape from c). [111] © Nature Publishing Group; reproduced with permission.

ing blocks [119]. They further achieved to create 3D superlattices of AuNP with different lattices (e. g. simple cubic (SC), face centered cubic (FCC)) using polyhedral frames of DNA [120]. The edge length is around 60 nm and therefore large enough for hosting proteins, but the crystal can only grow with the AuNP as a building block. Therefore, the lattice is not suitable for X-ray diffraction of the host proteins due to the dominant scattering of the gold.

Aside from measuring the crystal structures, X-ray scattering had not been used to understand the structure of 3D DNA origami shapes. However, by probing DNA origami in their natural solution conditions it can clarify the structure in buffers of different ionic strength, with temperature as well as probe structural dynamics with high detail. In 2016, the groups of Hendrik Dietz and Jan Lipfert showed that SAXS on 3D DNA origami can resolve dynamics [121]. At the same time, the structure of DNA origami could be determined with high resolution and, for example, the mean inter-helical distance within the object was measured. Furthermore, the response to ionic strength and temperature was tested [5]. These results are presented in the next section.

The group of Tim Liedl achieved to build a pure DNA origami 3D lattice inspired by Seeman's tensegrity triangle. This lattice can host AuNPs of different sizes. SAXS measurements with a detailed analysis of the structure are part of this thesis and are presented in section 6.2.

## 6.1 SINGLE DNA ORIGAMI OBJECTS

*The work described in this section has been partly published [5].*

The structural control of DNA origami is routinely done with AFM and TEM. In some cases, if high resolution is needed, super-resolution microscopy or cryo-EM will be used. All these techniques are explained in chapter 2 with their advantages and disadvantages. Here, SAXS is used to study the different geometric shapes of DNA origami. This technique profits from the possibility to directly measure in a buffer solution and therefore test the structure with different ionic strength as well as temperature. Most of the data shown in this section were measured at the synchrotron (Po8, DESY, Hamburg) because of the increased data quality compared to in-house data. However, most of the measurements were done before at the setup described in section 4.5 where most features were already accessible.

### 6.1.1 Scattering of Different Shapes

#### 6.1.1.1 Design of shapes

Three different DNA origami shapes were studied: a flat sheet, also called one layer sheet (1-LS) because it consists of only one layer of DNA helices, a block shaped structure, which consists of three layers and is therefore called three layer sheet (3-LS) and a cylinder shaped object, which has 24 helices



Figure 6.4: Schematic DNA origami shapes: a) 24HB, b) 3-LS and c) 1-LS. Each solid cylinder represents a DNA double helix (zoom in a)). In this scheme cross-over between different DNA helices are not respected.

and is called 24 helix bundle (24HB). These rather simple shapes were chosen because they exhibit textbook-like structures, which are rather simple to model. All three structures are schematically shown in Figure 6.4. The 1-LS and 3-LS have a square lattice arrangement of DNA double helices, while the 24HB has a honeycomb packing motif. In Figure 6.5 the front view of the models of Figure 6.4 is shown with the defining parameters of height  $A$ , width  $B$ , radius  $R$  and inter-helical distance  $a$ . The length  $L$  of the 24HB and the depth  $C$  of the other two structures are not presented.

The dimensions of the DNA origami structures are given in Table 6.1 in units of number of helices and number of bps as well as in Å under considerations of the known values of DNA.

#### 6.1.1.2 Theoretical X-ray Scattering of Geometric Shapes

For the scattering analysis of the DNA origami shapes above introduced, three different models are applied. Firstly, the form factor (section 3.2) of the geometric shapes of the whole DNA origami is used, i.e. cuboid and cylinder. Secondly, each DNA double helix is modeled by a solid rigid cylinder and arranged as designed, shown in Figure 6.4. Thirdly, both ideas are combined and an additional peak is added to the geometric form factor of the whole structure, which represents the inner arrangement of the DNA helices.

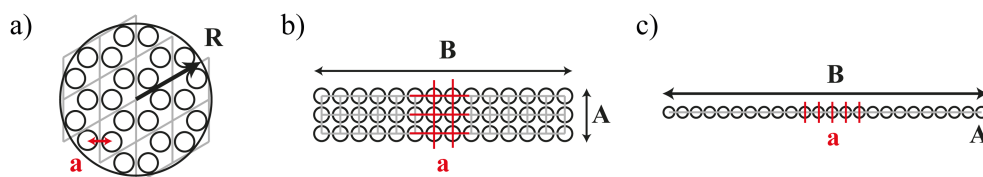


Figure 6.5: Schematic front view of DNA origami shapes: a) 24HB, b) 3-LS and c) 1-LS. The inter-helical distance is called  $a$  for all three structures, the height of the 1-LS and 3-LS is  $A$  and the width  $B$  and for the 24HB the radius of the cylinder is  $R$ . Light gray lines indicate the unit cells of the packing motif.

Shape	A [#helices]	B [#helices]	C [#bp]	R	L [#bp]
24HB	-	-	-	$\sqrt{7}a + r_{DNA}$	284-298
3-LS	3	14	168	-	-
1-LS	1	24	224	-	-
Shape	A [Å]	B [Å]	C [Å]	R [Å]	L [Å]
24HB	-	-	-	79	966-1013
3-LS	72	358	571	-	-
1-LS	20	618	762	-	-

Table 6.1: Design values of DNA origami structures in units of helices and bps and in Å (rounded). The values in Å are calculated with the assumption of a bp to bp distance of 3.4 Å, an inter-helical distance  $a$  of 2.6 nm and a radius of the DNA double helix  $r_{DNA}$  of 1 nm. The double helices of the 24HB are shifted to each other, which causes the difference in length.

**GEOMETRIC MODELS** In order to describe the 24HB, the form factor of a solid cylinder is used, which is given by Fournet and Guinier [41]:

$$F_{Cyl}(q) = 2(\Delta\rho)V \frac{\sin(\frac{1}{2}qL \cos(\alpha))}{\frac{1}{2}qL \cos \alpha} \frac{J_1(qR \sin(\alpha))}{qR \sin(\alpha)} \quad (6.1)$$

where  $\Delta\rho = \rho_{DNA} - \rho_{buffer}$  is the scattering contrast between the DNA origami and the buffer solution,  $V = \pi R^2 L$  is the volume,  $L$  the length, and  $R$  the radius of the cylinder. The angle  $\alpha$  is in between the axis of the cylinder and the vector  $\vec{q}$  and  $J_1$  denotes the first order Bessel function of first kind. The DNA origami structures are dissolved in a buffer and therefore a random orientation between  $\vec{q}$  and the axis of the cylinder can be considered. Hence, the squared form factor must be integrated over all angles in between  $0^\circ$  to  $90^\circ$  to obtain the orientationally averaged intensity.

$$I(q) = \frac{scale}{V} \int_0^{\pi/2} F_{Cyl}^2(q, \alpha) \sin(\alpha) d\alpha + background \quad (6.2)$$

The resulting intensity  $I(q)$  is in absolute units [ $cm^{-1}$ ]. Therefore, the *scale* factor is the volume fraction of the sample, if the data is calibrated to absolute scale (section 3.3.3). Additionally, a *background* can be added, which is in our case a Debye background [122].

$$I_{DebyeBg}(q) = scale_{bg} \cdot \frac{2(e^{-x} + x - 1)}{x^2} \quad (6.3)$$

$$x = (qR_g)^2$$

This model is used for Gaussian coils with a radius of gyration  $R_g$  and represents unfolded single stranded DNA in the solution. It was already successfully used in a previous study of DNA origami with SAXS [115]. The contribution to the scattering intensity can be varied with the *scale<sub>bg</sub>* parameter.

For the 1-LS and the 3-LS the form factor of a cuboid is used. This model assumes that  $a = A/B < 1$ ,  $b = B/B = 1$ , and  $c = C/B > 1$  with the definitions of  $A, B$ , and  $C$  in section 6.1.1.1. The averaged form factor over all orientations is given by Mittelbach and Porod [123]:

$$P_{cub}(q) = \left\langle \int_0^1 \phi_Q(\mu\sqrt{1-\sigma^2}, a) [\text{sinc}(\mu c \sigma / 2)]^2 d\sigma \right\rangle \quad (6.4)$$

with

$$\phi_Q(\mu, a) = \int_0^1 \left\{ \text{sinc} \left[ \frac{\mu}{2} \cos \left( \frac{\pi}{2} u \right) \right] \text{sinc} \left[ \frac{\mu a}{2} \sin \left( \frac{\pi}{2} u \right) \right] \right\}^2 du$$

$$\text{sinc}(x) = \frac{\sin x}{x}$$

$$\mu = qB$$

The averaging over all orientations is denoted with  $\langle \dots \rangle$ . Again, the structures are freely distributed. So the scattering intensity depends only on the magnitude of the scattering vector  $q = |\vec{q}|$ .

$$I(q) = \frac{\text{scale}}{V} (\Delta\rho V)^2 P_{cub}(q) + \text{background} \quad (6.5)$$

The *background* used is a Debye background (Eq. 6.3) and the *scale* factor is the volume fraction of the cuboid.

**ARRANGED MODEL** All coordinates of the DNA helices can be described in  $(x, y)$  pairs and dependent on the inter-helical distance  $a$ . Using the lattice sum (Equation 3.32) for all  $(x, y)$  pairs and spherical coordinates for  $q$ , the orientationally averaged scattering intensity results in:

$$I(q) = \int_0^\pi \int_0^{\frac{\pi}{2}} \left| F(q) e^{iq(x \sin(\alpha) \cos(\phi) + y \sin(\alpha) \sin(\phi))} \right|^2 \sin(\alpha) d\alpha d\phi \quad (6.6)$$

The integral limits depend on the symmetry of the object, e. g. for the 24HB an integration of  $\phi$  up to  $\frac{\pi}{3}$  is sufficient. For the form factor  $F$  a solid cylinder (Equation 6.1) was used as sketched in Figure 6.4. In this model the form factor can be exchanged and also alternative form factors were tested, e. g. a hollow cylinder, a infinitely long continuous helix or a double helix [124].

**GEOMETRIC MODEL AND ADDED INNER STRUCTURE** In the third model, the geometric model from above was used and a peak was added, which represents the helix arrangement within the DNA origami structures. For the peak shape Gaussian and Lorentzian were tested. The Lorentzian matched the data better. The shape of the peak can be influenced by the instrument as well as the sample [125], but here no further analysis was made. The intensity for this model is

$$I(q) = \frac{\text{scale}_1}{V} \int_0^{\pi/2} F_{Cyl}^2(q, \alpha) \sin(\alpha) d\alpha + \frac{\text{scale}_2}{1 + \left(\frac{q - q_0}{B}\right)^2} + \text{background} \quad (6.7)$$

*The form factors are included in SasView [77] and more details are given in its manual.*

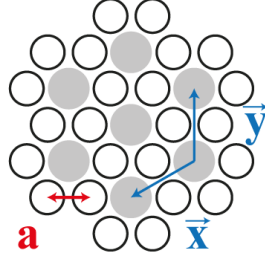


Figure 6.6: Detailed front view of 24HB with inter-helical distance  $a$  and unit cell vectors  $\vec{x}$  and  $\vec{y}$ .

with  $q_0$  the peak center and  $B$  the half-width half-maximum (HWHM) of the Lorentzian peak. The other parameters are the same as in Equation 6.2. The background is also modeled with a Debye background (Equation 6.3). The peak position  $q_0$  is given by the lattice of the DNA origami, which has hexagonal or square packing motifs. Therefore, the position of the fitted peak can be used for determining the inter-helical distance. The spacings  $d$  within a lattice are related to the peak position  $q_0$  by

$$d = \frac{2\pi}{q_0} \quad (6.8)$$

For the square lattice (1-LS and 3-LS) the spacing  $d$  is the same as the inter-helical distance  $a$  (Figure 6.5). The spacings in a 2D square lattice are given by:

$$d = \frac{a}{\sqrt{h^2 + k^2}} \quad (6.9)$$

with the Miller indices  $h$  and  $k$  for a 2D lattice. The first peak appears for  $h=1$  and  $k=0$  or vice versa and if Equation 6.8 and 6.9 are combined, this results in a peak position of

$$q_{(10)} = \frac{2\pi}{a} \quad (6.10)$$

For the honeycomb lattice (24HB) the relation is different. Figure 6.6 shows the cross section of the 24HB with a hexagonal pattern shown by gray circles in the voids between DNA helices and the corresponding unit cell vectors  $\vec{x}$  and  $\vec{y}$ . Both vectors have the same length  $|\vec{x}| = |\vec{y}| = l = \sqrt{3}a$ . The spacings in a 2D hexagonal lattice are given by

$$d = \sqrt{\frac{3}{4}} \frac{l}{\sqrt{h^2 + hk + k^2}} \quad (6.11)$$

For the hexagonal lattice the first peak also appears for  $h=1$  and  $k=0$  or vice versa. Therefore, the first peak of the internal structure of the DNA origami is at

$$q_{(10)} = \sqrt{\frac{4}{9}} \cdot \frac{2\pi}{a} = \frac{4\pi}{3a} \quad (6.12)$$

The next higher order peak (11) should appear at  $q_{(11)} = \frac{4\pi}{\sqrt{3}a}$ , but since the lattice of the 24HB has only about 10 unit cells the peaks are low in intensity and broad. Therefore, higher order peaks could not be observed.

The form factors of the geometric models, the Lorentzian peak function, and the Debye background are implemented in the SasView Software [77]. The arranged model is based on a self-written Matlab code.

### 6.1.1.3 Data with Fitted Models

If the structure of a sample is unknown, the analysis typically starts with standard analysis techniques. However, Guinier analysis and PDDF (section 3.3) cannot be applied to the data because the lowest measured  $q$ -value is not low enough for the dimensions of the DNA origami. Furthermore, these analysis techniques give good estimates about shapes and sizes but do not allow for detailed information. Since DNA origami are designed structures, approximate values are not of interest. In contrast, analytical models like those presented in section 6.1.1.2 can provide highly detailed information.

**GEOMETRIC MODELS** The scattering profile of the 24HB is presented in Figure 6.7 a) and b) with a geometric model fit. The quality of all samples was checked with TEM and a representative image is shown in the inset of the figure. The lowest measured  $q$ -value is  $0.0109 \text{ \AA}^{-1}$ , which corresponds to a length of about 58 nm. Since the calculated length of the cylinder is about 100 nm (Table 6.1), it was fixed to this value for the fitting procedure. The scattering signal shows the typical behavior of a Bessel function as expected (Equation 6.1) and the corresponding radius could be fitted with  $R = 78.7 \pm 0.2 \text{ \AA}$ , which perfectly matches the design value of  $79 \text{ \AA}$  (Table 6.1). The depth of the minima in the scattering signal at around  $0.05 \text{ \AA}^{-1}$  and  $0.09 \text{ \AA}^{-1}$  are limited by the Debye background due to the excess oligonucleotides in the solution. The depth of these minima can be used to determine the polydispersity of the radius, which is in this case limited by the background. This behavior indicates a very low polydispersity in the radius of the 24HB. The fit is in excellent agreement with the data for a wide  $q$ -range, but it does not resolve the peak between  $0.13 \text{ \AA}^{-1}$  and  $0.21 \text{ \AA}^{-1}$ . This  $q$ -range corresponds to shorter length scales of 30 to 48  $\text{\AA}$ , which is within the DNA origami.

For the 3-LS the scattering signal is shown in Figure 6.7 c) and d). It is easily distinguishable from the scattering of the 24HB and the geometric fit with the Debye background matches the data for a wide range of  $q$ -values. Three different slopes can be seen, which link to the three different edge lengths of the cuboid. With a lower background minima as for the 24HB would appear in the signal. The fitted values are for the length  $C = 627 \pm 5 \text{ \AA}$ , the width  $B = 379 \pm 2 \text{ \AA}$ , and the thickness  $A = 76.6 \pm 0.2 \text{ \AA}$ . All values are above the design values given in Table 6.1. For  $C$  the  $q$ -range is already at the limit and therefore the fitted value is not very reliable. However, the estimation of the size in Table 6.1 is oversimplified because the distance between helices

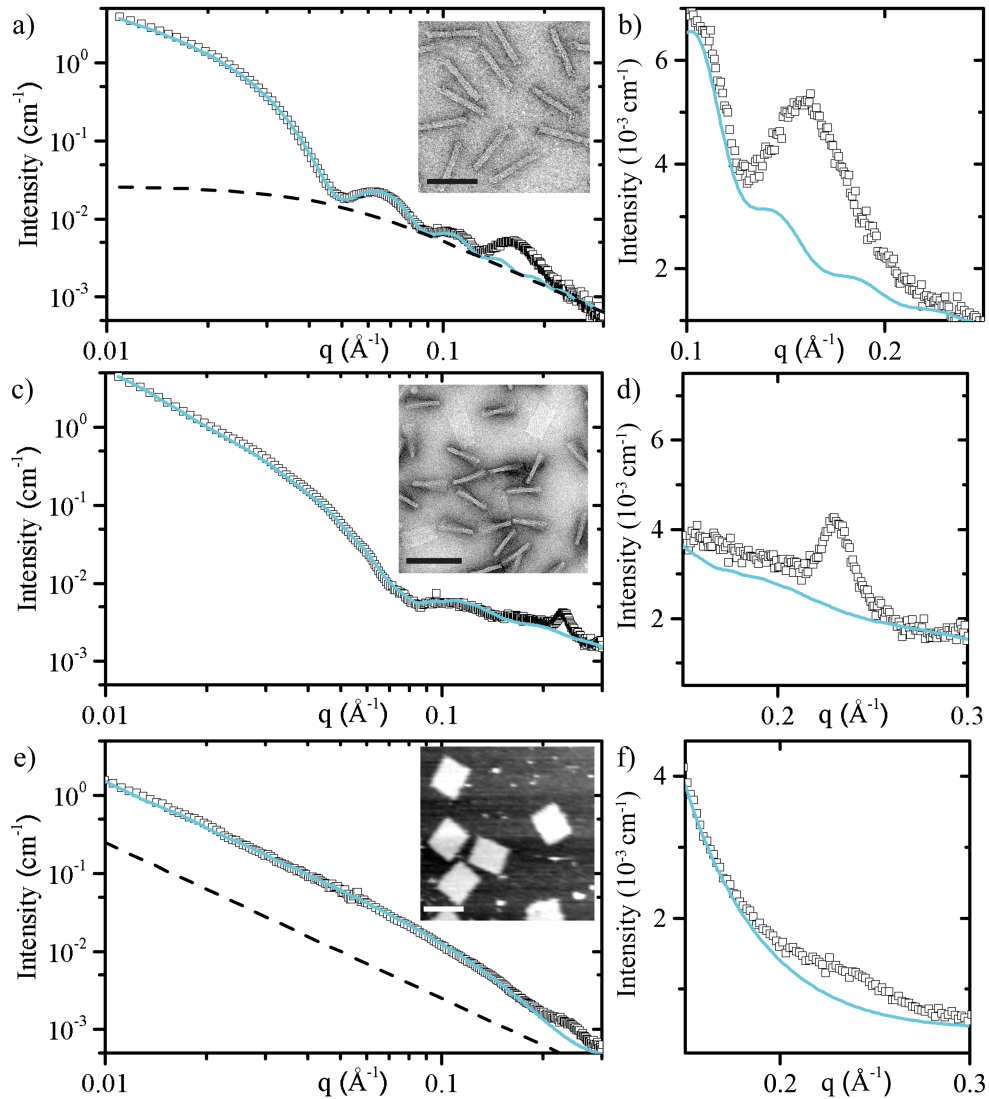


Figure 6.7: a) 24HB scattering profile with the geometric model fit (cyan) and Debye background (dashed line). Inset: TEM image of stained sample, b) zoom to  $q$ -range from  $0.1$  to  $0.25 \text{ \AA}^{-1}$  with linear scale. c) 3-LS scattering profile with the geometric model fit. Inset: TEM image of stained sample, d) zoom to  $q$ -range from  $0.15$  to  $0.3 \text{ \AA}^{-1}$  with linear scale. e) 1-LS scattering profile with the geometric model fit. The dashed line has a behavior of  $q^{-2}$ . Inset: AFM image of sample, f) zoom to  $q$ -range from  $0.15$  to  $0.3 \text{ \AA}^{-1}$  with linear scale. All scale bars are 100 nm.

varies due to the chicken-wire-like design of DNA origami (Figure 6.2). In 3D DNA origami with a square lattice, the repulsion between the negative charges of the DNA leads to an increase in size because the cross-over density is lower than for the honeycomb lattice [112]. As for the 24HB a peak at about  $0.23 \text{ \AA}^{-1}$  is not covered in this model (Figure 6.7 d)).

For the 1-LS the geometric model also matches most of the scattering signal, shown in Figure 6.7 e) and f). For the fit of the data, the length of the long axis was fixed to the design value because it is out of the accessible  $q$ -range. The fit value of the width  $B = 610 \pm 60 \text{ \AA}$  matches the design value perfectly. The thickness of  $A = 21.5 \pm 0.3 \text{ \AA}$  is slightly above the assumed diameter of the DNA double helix of 2 nm. This might be attributed to the fact the structure is rather flexible in solution, which computer simulation with CanDo show [126], and therefore might appear thicker on average. Also in this structure, a peak appears which is not covered by the model. In this case, it is lower and broader than for the 24HB and especially the 3-LS. The dashed line in Figure 6.7 e) indicates a  $q^{-2}$  behavior. This Porod exponent is typical for 2D structures like discs, which was introduced in section 3.3.1. For low  $q$ -values, the 1-LS matches this dependency and therefore can be considered as a 2D object.

Overall, the DNA origami exhibit textbook-like scattering of geometric objects and the structure with all length scales can be already explained by these simple models. However, for DNA origami with more complex shapes like a robot [127], this simple approach will probably fail.

**MODELS TAKING INNER STRUCTURE INTO ACCOUNT** In the next step, the DNA origami were modeled with their inner structure because all three DNA origami showed a feature at a  $q$ -value within the structure. The model uses a solid cylinder for each DNA double helix ordered in the designed way (section 6.1.1.2). Therefore, it is referred to as the arranged model. The result for all three DNA origami is shown in the Figure 6.8 with a solid blue line. This model reproduces the scattering at low  $q$ -values for all designs with high precision. Additionally, a peak appears at the measured position. The intensity of the peak, however, is overestimated by the model (Figure 6.8 b), d) and f)). Nevertheless, the appearance of the peak in the model, while maintaining the scattering of the overall structure, proves that its origin is the arrangement of the DNA within the DNA origami. The overestimation of the intensity is no surprise because the model is a strong simplification. Firstly, the form factor of a solid cylinder is only in first order a good approximation for a DNA double helix. Since the scattering is dominated by the phosphate group in the backbone of the DNA, a hollow cylinder was tested with slightly improved results for the 24HB. Furthermore, a helix and double helix model were applied. The intensity of the peak could be improved for some parameters, but at higher  $q$ -values new strong peaks appeared, which were not present in the data. Secondly, it is well known that the DNA origami has a chicken-wire-like structure due to the cross-overs, which can be seen in Figure 6.2 a) for example. These cross-overs are

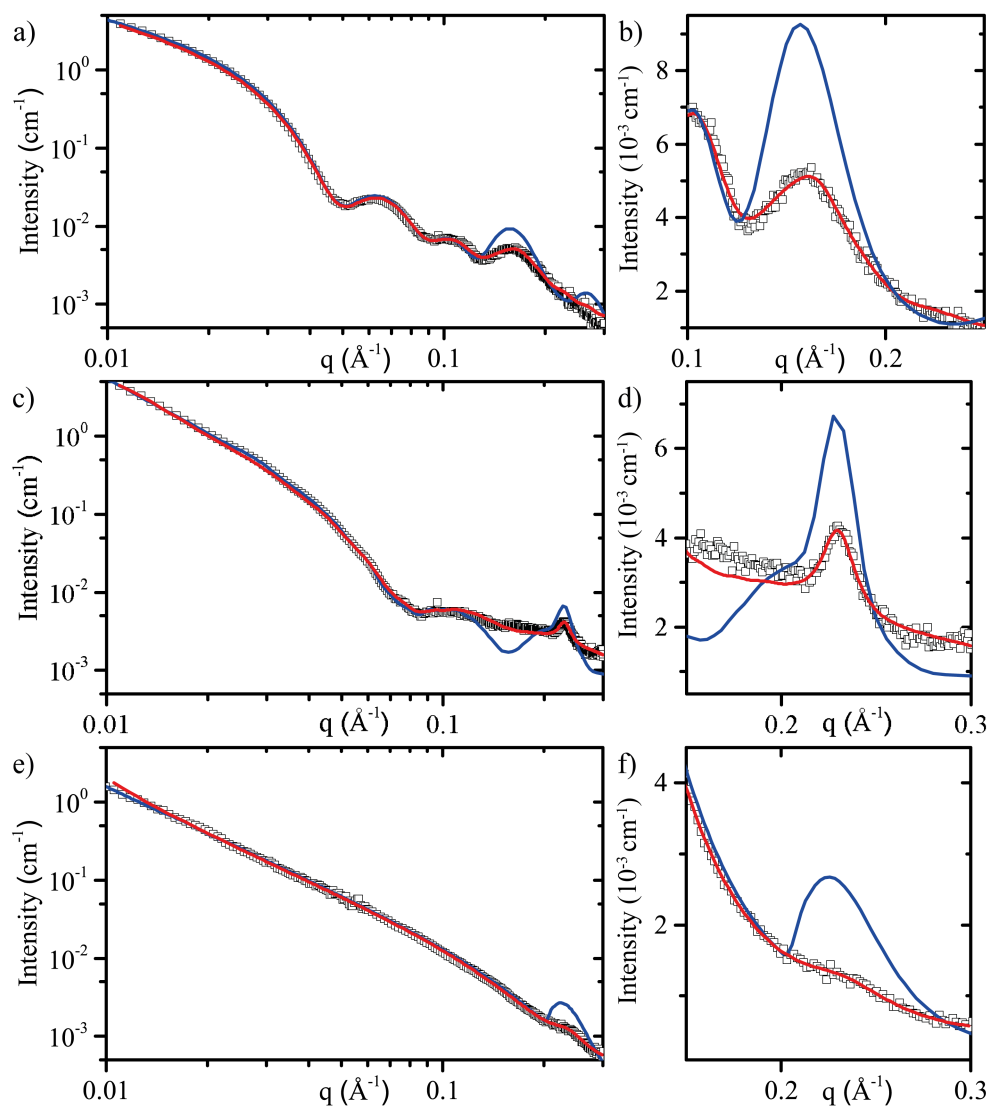


Figure 6.8: Scattering profiles with arranged model (blue line) and geometric model with added inner structure (red line) for a) 24HB, c) 3-LS and e) 1-LS. b) zoom to  $q$ -range from 0.1 to  $0.25 \text{\AA}^{-1}$  and d), f) zoom to  $q$ -range from 0.15 to  $0.3 \text{\AA}^{-1}$  with linear scale.

completely neglected in the model. Thirdly, the model assumes a perfect arrangement without any fluctuations. On the one hand, the perfect alignment of the helices is not true because of the mentioned cross-overs and on the other hand the system has thermal fluctuations and the helices will fluctuate around the mean position. A fluctuation around a well-defined lattice position is a well-known phenomenon in X-ray diffraction and is described by the theory of Debye-Waller, which was introduced in section 3.4. The result of the theory is a reduced intensity of Bragg peaks, but the width and the position are conserved.

Another approach uses the geometric model and adds a peak, which represents the Bragg peak of the inner arrangement. In this way, the mean inter-helix distance can be extracted as well as the overall size. The resulting fits are shown as a red line in the Figure 6.8 for all three DNA origami. All fits match the data over the whole measured  $q$ -range. The peak position was evaluated like explained in section 6.1.1.2. For the 24HB this leads to a mean inter-helical distance of  $a = 25.36 \pm 0.03 \text{ \AA}$  by using Equation 6.12. The inter-helical distance of the flat 1-LS is already increased with  $a = 26.9 \pm 0.2 \text{ \AA}$  and for the 3D square lattice structure of the 3-LS it is highest with  $a = 27.32 \pm 0.02 \text{ \AA}$ . This validates the assumption that the mean inter-helical distance is higher in the square than honeycomb lattices due to a combination of electrostatic repulsion and lower cross-over density. The overall size of the DNA origami is not altered compared to the fit with the geometric model. The inter-helical distances can be checked for consistency by comparing them to the size of the overall structures. With the measured mean inter-helical of the 24HB the radius of the 24HB results in  $77.10 \text{ \AA}$  by using the relation in Table 6.1 and is therefore only slightly smaller compared to the design. For the 3-LS the side lengths are calculated to  $A = 74.64 \pm 0.06 \text{ \AA}$  and  $B = 375.2 \pm 0.3 \text{ \AA}$  and are a bit smaller than the geometric model emphasizes. This difference could have several reasons: First, the assumption of DNA radius of  $10 \text{ \AA}$  is too small because it is the distance from the center of the DNA to phosphorus backbone and no hydration shell is considered. Second, the X-ray measurement for the overall shape also probes an increased ion concentration around the DNA origami, which leads to an increased measured size. Third, the geometric model is an oversimplification at the edges and the mean size is increased due to the repulsion of the DNA helices. Nevertheless, the values of the inter-helical distance and the overall shape are still in agreement. Especially the peak position can be determined to a high precision, which leads to very low errors, especially for the 3-LS.

A peak width evaluation with the Scherrer Equation (3.38) leads to a size of  $\approx 16 \text{ nm}$  for the 24HB and for the 3-LS to  $\approx 32 \text{ nm}$ . The sharper peak due to the larger cross-section of the 3-LS than of the 24HB is already clearly visible in the Figure 6.8. Both values are also in perfect agreement with the values measured for the shape. In contrast, the peak of the 1-LS in Figure 6.8 f) appears very broad and leads to an size of only  $\approx 10 \text{ nm}$ . This small value can be attributed to the low stiffness of the 1-LS due to its small thickness.

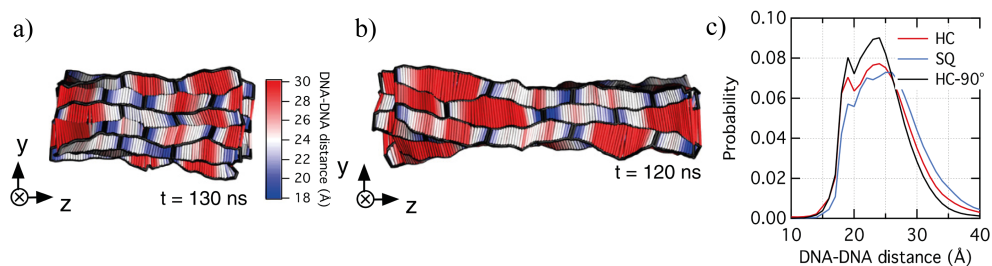


Figure 6.9: MD simulation of DNA origami with a) hexagonal lattice after 130 ns and b) square lattice after 120 ns relaxation time. The inter-helical distance is color coded from 18 Å (blue) to 30 Å (red). c) The distribution of inter-helical distances within the hexagonal lattice (red) and the square lattice (blue) of a) and b). The black line is for a bend DNA origami structure, which was not studied in this thesis. Figure is extracted from [130] and reprinted with permission.

Therefore, the 1-LS will bend in solution and the domains, which coherently scatter, will appear smaller than they are.

#### 6.1.1.4 Comparison of Results to Literature and Simulations

Typically only the correct folding of the DNA origami is controlled by TEM or AFM [108, 128, 129], but it is impossible to study, for example, the inter-helical distance with high detail. One approach to gain more insight into the DNA origami organization is to use computer based simulation. Yoo and Aksimentiev carried out MD simulations of all-atom models of different DNA origami assemblies [130]. They used two rather small squared shaped structures with hexagonal ( $16.5 \times 16.5 \times 32.5 \text{ nm}^3$ ) and square lattice ( $14.0 \times 14.0 \times 47.0 \text{ nm}^3$ ) with about 1 million atoms. The initial structure was relaxed for about 100 ns with a  $\text{Mg}^{2+}$  ion concentration of 10 mM, after which the DNA origami reached a stable configuration. The relaxed structures are shown in Figure 6.9 with a color coded inter-helical distance. The cross-over positions within the DNA origami are visible with an inter-helical distance of about 18 Å. In the distribution of distances in Figure 6.9 c) a small peak for the cross-overs is visible and a rather broad distribution of the other distances peaking at about 24 Å for the hexagonal lattice and about 25 Å for the square lattice. In the broad distribution also distances over 30 Å are present and will shift the mean value to higher values. These values are in good agreement with the SAXS measurements of the previous section and also show a higher mean inter-helical distance of square compared to hexagonal lattices. The cross-over density will influence the result and in another theoretical work it has been demonstrated that a higher cross-over density leads to smaller inter-helical distances [131].

An experimental technique which can provide high resolution is cryo-EM. Bai et al. performed cryo-EM measurements on a square lattice DNA origami [14]. A part of the cryo-EM density map of the structure is shown in Figure 6.10 a) together with a fitted pseudoatomic model of the DNA. The chicken-wire-like pattern is resolved with this technique and parameters like the

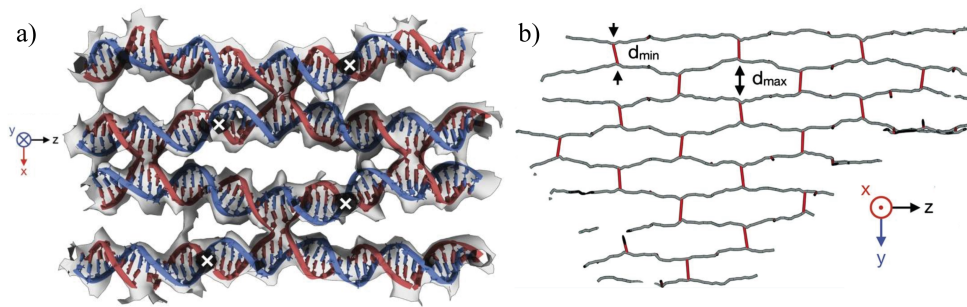


Figure 6.10: a) Cryo-EM density map (transparent gray) and the fitted pseudoatomic model as ribbon/slab model. b) schematic representation of the 3D chickenwire-like pattern found in the structure, depicting double stranded DNA helical stretches in gray and cross-overs in red. The pattern was computed using the coordinates of bp midpoints in the pseudoatomic model. The midpoints of neighboring double stranded DNA helices move on average from a minimum distance  $18.5 \text{ \AA}$  at the cross-over to a maximum distance of  $36 \text{ \AA}$  away from each other. Figure is extracted from [14] and reprinted with permission.

inter-helical distance can be extracted. The minimum distance at cross-overs was found to be  $18.5 \text{ \AA}$  and the maximum distance is  $36 \text{ \AA}$ . Assuming that the distances are symmetrically distributed between these two values, the mean inter-helical distance is  $27.25 \text{ \AA}$ , which is very close to the value of  $27.32 \pm 0.02 \text{ \AA}$  measured for the 3-LS. However, this is a very rough estimation and the mean distance depends on the structure, for example, due to the cross-over density. Nevertheless, the cryo-EM data and the SAXS data are in agreement.

Another approach to evaluate the results of the measurements is simulating the scattering signal of the models of the DNA origami. The software CRY SOL creates from pdb files containing the atomic coordinates a scattering signal of macromolecules in solution [27]. The pdb file was either generated directly from the design of caDNAno [132] or with CanDo [126, 133] by using the default parameters, which are given in Table 6.2. The only parameter which was varied is the diameter of the DNA. The simulation for the 24HB is displayed in Figure 6.11 and for the 3-LS in Figure 6.12. The DNA diameter has a strong influence on the simulated scattering signal. The  $2 \text{ nm}$  diameter, which is the measured one of pure double stranded DNA [20, 21], shows a scattering signal for both a too small structure and too small inter-helical distance. The dip of the form factor and the inter-helical peak are shifted to higher  $q$ -values. For the direct conversion of the caDNAno file [132] the exact parameters are unknown, but the simulation of the shape is good although the inter-helical peak is slightly shifted. The best result was achieved by using  $2.45 \text{ nm}$  DNA diameter with CanDo. All features of the scattering signal are matched. Interestingly, the inter-helical peak intensity is underestimated, although the visualization of the pdb file with visual molecular dynamics (VMD) [134] shows aligned DNA double helices without cross-overs. This alignment should lead to an overestimation of the peak

Parameter geometry	Default value
Axial rise per bp	0.34 nm
Helix diameter	1.85 nm
Cross-over spacing	10.5 bp
Inter-helical angle	60°
Parameter mechanical properties	Default value
Axial stiffness	1100 pN
Bending stiffness	230 pN·nm <sup>2</sup>
Torsional stiffness	460 pN·nm <sup>2</sup>
Nick stiffness factor	0.01
Junction twist angle stiffness	135.3 pN·nm·rad <sup>-1</sup>

Table 6.2: Default values of the software CanDo [126, 133].

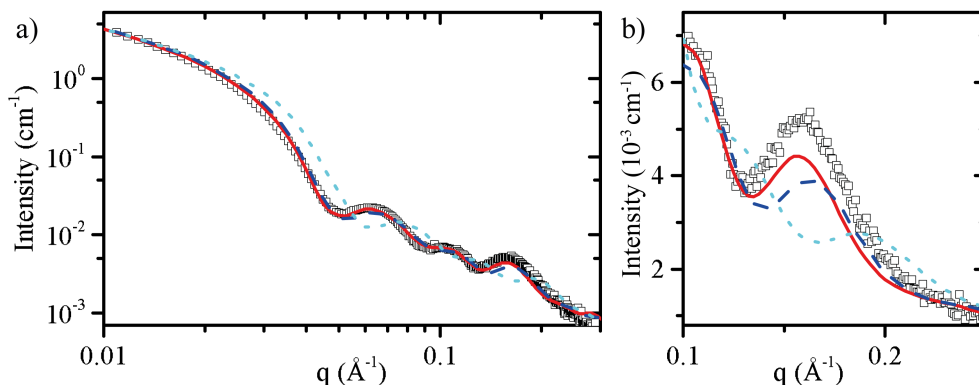


Figure 6.11: Simulated data of 24HB with CRY SOL with added Debye background for a) the whole  $q$ -range and b) zoom on the inter-helical peak. Shown simulations are based on pdb files of CanDo with 2.45 nm (solid red) and 2 nm DNA diameter (dotted cyan) and of caDNANO (dashed blue).

intensity as for the arranged model (section 6.1.1.2). There, the usage of a double helix as form factor already improved the intensity. Therefore, the form factor might play an important role in the peak intensity.

A similar behavior is observed for the 3-LS, which is shown in Figure 6.12. The overall shape shifts to a smaller size with decreasing DNA diameter and the inter-helical peak appears according to Equation 6.8. For a DNA diameter of 2.75 nm the simulation matches the data best. A better match could be achieved by adjusting the Debye background to the simulated scattering signal. However, the scattering intensity at higher  $q$ -values as well as the inter-helical peak are underestimated, which is surprising for the same reasons as for the 24HB. The simulations show that the DNA diameters, which are close to mean inter-helical distance determined in section 6.1.1.3, represent the data best. This suggests that the pdb file generation by the programs is insufficient because the inter-helical distance corresponds to the DNA diameter and the bending of the helices and the cross-overs of the DNA origami

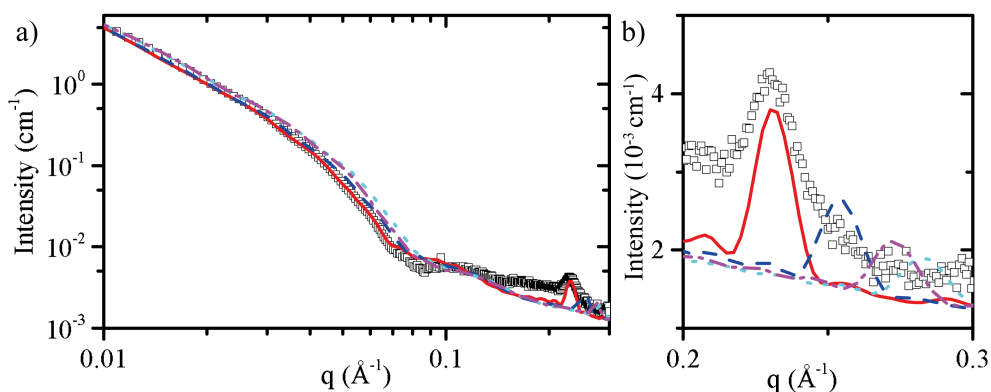


Figure 6.12: Simulated data of 3-LS with CRYSOLE with added Debye background for a) the whole  $q$ -range and b) zoom on inter-helical peak. Shown simulations are based on pdb files of CanDo with 2.75 nm (solid red), 2.5 nm (dashed blue) and 2.25 nm DNA diameter (dotted cyan) and of caDNAo (dashed dotted purple).

are not included. Nevertheless, the results of the simulations are very close to the measured signal. Overall, the scattering signal of the shape of the DNA origami could be found by the simulation, but details in the size range of the inter-helical distance are not well reproduced. The same result with deviations for high  $q$ -values ( $>0.1 \text{ \AA}^{-1}$ ) was also found for a different DNA origami structure [121].

### 6.1.2 Influence of Ionic Strength

The measurements in previous sections were carried out at buffer conditions that favor DNA origami stability that is below  $30^\circ\text{C}$  and above  $10 \text{ mM Mg}^{2+}$  concentration. Here, the stability and the structural change of 24HB are checked with a change of ionic strength by varying the  $\text{Mg}^{2+}$  concentration at room temperature. Therefore, six samples were prepared with the same protocol, but in the end a buffer exchange with a varying  $\text{Mg}^{2+}$  concentration was made. A detailed protocol can be found in the supporting information of [5]. All six samples were measured separately with TEM and SAXS. The results are shown in Figure 6.13. The scattering signal of the different samples show the same features, but the minima of the form factor and the height of the inter-helical peak are less pronounced with decreasing  $\text{Mg}^{2+}$  concentration. The minima and inter-helical peak position both shift to lower  $q$ -values, which indicates a swelling for lower  $\text{Mg}^{2+}$  concentration. Furthermore, the intensity at low  $q$ -values drops with decreasing  $\text{Mg}^{2+}$ . Since the intensity at low  $q$  is an indicator for the concentration, it points to less intact assembled DNA origami. The Debye background stays at the same level and therefore the features are less pronounced. Below  $2 \text{ mM Mg}^{2+}$  the typical scattering intensity of correctly folded 24HB disappears, but it can be fitted by the sum of Debye background terms. The second term has a radius of gyration of  $20 \text{ nm}$  and might occur due to disassembled DNA origami, which form blobs in the TEM images (Figure 6.13 b)). In general, the TEM

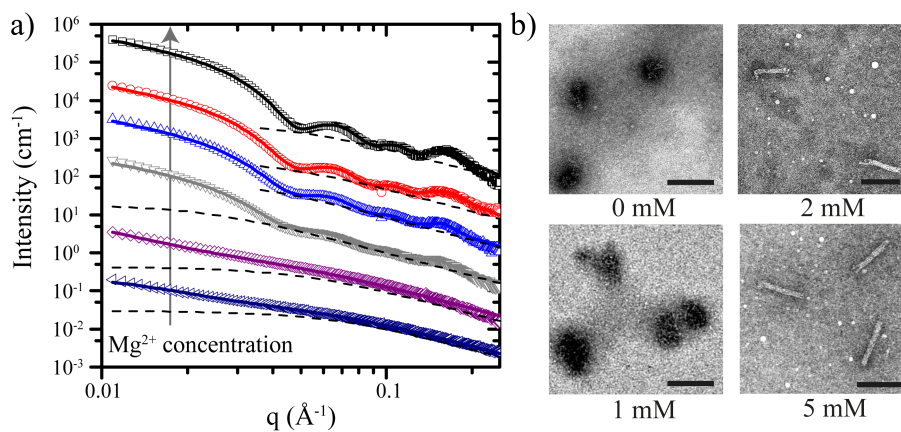


Figure 6.13: a) Scattering intensities of 24HB at varying Mg<sup>2+</sup> concentrations (11 mM, 5 mM, 3 mM, 2 mM, 1 mM, and 0 mM from top to bottom, each data set is shifted by a factor 10 for clarity) with added Debye background (dashed line) and b) TEM images of 24HB at selected Mg<sup>2+</sup> concentrations. Scale bars are 100 nm.

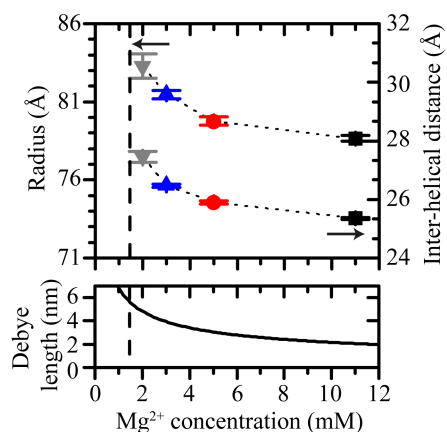


Figure 6.14: (top) Fit values of radius and inter-helical distance of 24HB depending on Mg<sup>2+</sup> concentration, (bottom) the corresponding Debye length for MgCl<sub>2</sub>.

images support the SAXS qualitatively.

In order to quantify the changes in structure, the form factor and the peak position were evaluated. The fitted values for the radius of the 24HB and the inter-helical distance are shown in Figure 6.14. Both increase when the Mg<sup>2+</sup> concentration decreases. Furthermore, they expand in the same way for all Mg<sup>2+</sup> concentrations. This means that the calculated radius by using the inter-helical distance of the 24HB results in the same value as the fitted radius. This same swelling behavior ensures that it is real and no fitting artifact due to the decreased scattering intensity as two different scattering features are considered.

In electrolytes the Debye length is a measure of the electrostatic effect in

solution, and how far this electrostatic effect persists. It is defined as

$$\lambda_D = \frac{\epsilon_0 \epsilon_r k_B T}{2 N_A e^2 I} \quad (6.13)$$

with the physical constants of the vacuum permittivity  $\epsilon_0$ , the Boltzmann constant  $k_B$ , Avogadro's constant  $N_A$  and the elementary charge  $e$ . Furthermore, the relative permittivity  $\epsilon_r$  of the solvent, the temperature  $T$  and the ion strength  $I$  of the electrolyte contribute. As shown in Figure 6.14 the Debye length for  $\text{Mg}^{2+}$  at room temperature has the same trend as the radius and inter-helical distance of the DNA origami. This same tendency indicates that the  $\text{Mg}^{2+}$  ions act as a screening potential within the DNA origami and do not have a specific effect such as ion bridging for free DNA [135, 136]. This is the result of the fixed arrangement of the DNA within the DNA origami as the DNA cannot orient in the way that a bridging is possible [131]. Nevertheless, the ions may play an important role at the Holliday junctions. The electrostatic interaction between double stranded DNA has been the subject of experimental and theoretical work. A summary with an extensive bibliography can be found for example in [137].

### 6.1.3 Influence of Temperature

The second interesting parameter for DNA origami stability is the temperature. Here, the structure of the DNA origami was monitored via SAXS during cooling and heating.

First, DNA scaffold in a concentration of 30 nM and 100 nM of each staple oligonucleotide were pipetted into a typical SAXS sample chamber, shown in Figure 4.16 a). The whole chamber was heated to 65°C and cooled stepwise in the SAXS setup described in section 4.5. A detailed protocol of the cooling process can be found in the supporting information of [5]. For each degree in the cooling ramp, an X-ray image was taken. Due to the low intensity of the sample, five successive images with an integration time of 5 minutes were stacked with ImageJ and the median intensity was used for evaluation. The integrated scattering intensities are shown in Figure 6.15 a). For high temperatures down to 50°C the scattering intensity shows the typical Debye background. Starting from 49°C the intensity at low q-values starts to increase and at the same time, the intensity decreases between 0.04-0.05 Å<sup>-1</sup> which is the position of the first minimum of the form factor of the 24HB. At 44°C and below no significant difference can be observed, which suggests that the folding takes place in between 49 and 45°C. After the cooling ramp, a long measurement for superior statistics was made as well as a buffer measurement for background subtraction. The scattering intensity is shown in Figure 6.15 b) with a geometric fit of the cylinder. The measurement confirms a correct folding of the structure. The corresponding TEM image of the sample also shows intact folded 24HBs. In the SAXS data, however, the Debye background remains high because the excess staples are still in the solution. In the measurements shown previously, the samples were concentrated and purified from excess staples via PEG precipitation [138].

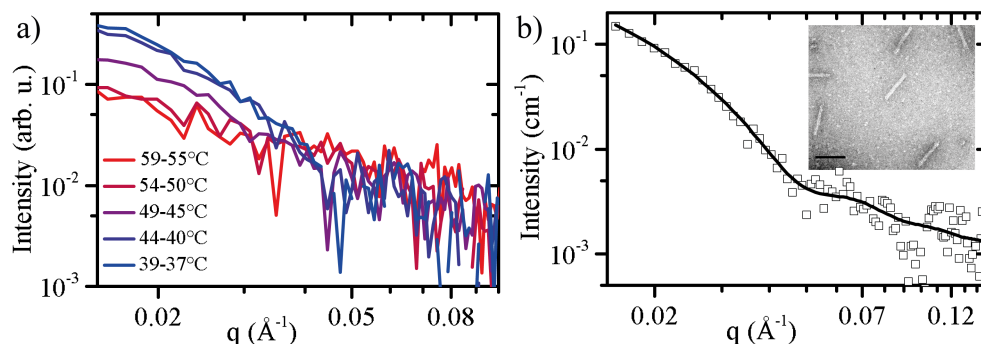


Figure 6.15: In-situ SAXS measurements during cooling of 24HB. a) Temperature dependent scattering intensity during the cooling of scaffold and staple strands of a 24HB. The curves are color coded and the temperatures are in the legend. The data is not buffer subtracted. b) Scattering intensity after folding process with longer integration time and buffer subtraction. Solid black line is a geometric model fit with Debye background. (inset) TEM image of correctly folded structures after cooling, scalebar is 100 nm.

Secondly, a prefolded and concentrated 24HB sample was loaded into the sample chamber and the sample was heated stepwise. Three images with an integration time of 15 minutes were taken for each temperature step. In between the measurement was interrupted for 2 minutes in order to reach the desired temperature in the sample chamber. The corresponding integrated scattering intensities are shown in Figure 6.16 a). At low temperatures the intensity at low  $q$ -values is high and the first minimum and maximum of the form factor of the cylinder are well resolved. At around  $50^\circ\text{C}$  the intensity at low  $q$ -values decreases and the maximum and minimum of the form factor vanish. A similar measurement was performed at the beamline ID01 at the ESRF. Due to the high flux, the exposure time per temperature step was only one second, which also helps to prevent radiation damage (section 4.4.3). Between each measurement, the temperature in the sample was equilibrated for 5 minutes. The beam was focused and therefore had a considerably high divergence and a short SDD, which limits the minimal  $q$ -value. This is why the data start at  $0.07\text{ \AA}^{-1}$ , but the inter-helical peak is well resolved (Figure 6.16 b)). For the evaluation of the parameter of the inter-helical peak intensity, a background was fitted around the peak like shown with dashed lines in Figure 6.16 b) and subtracted from the data. This subtraction was necessary because the peak is close to the background level, which increases with temperature due to a rise of unbound DNA in the solution. The inter-helical peak vanishes approximately at the same temperature as the scattering intensity at low  $q$ -values. Interestingly, there is no change in the position of the form factor minimum as well as in the position of the inter-helical peak. This behavior suggests an abrupt melting of the structure without any expansion before. In contrast, the electrostatically induced disassembly exhibited a continuous lattice expansion at low ionic strengths, indicating that the microscopic mechanism for thermal melting

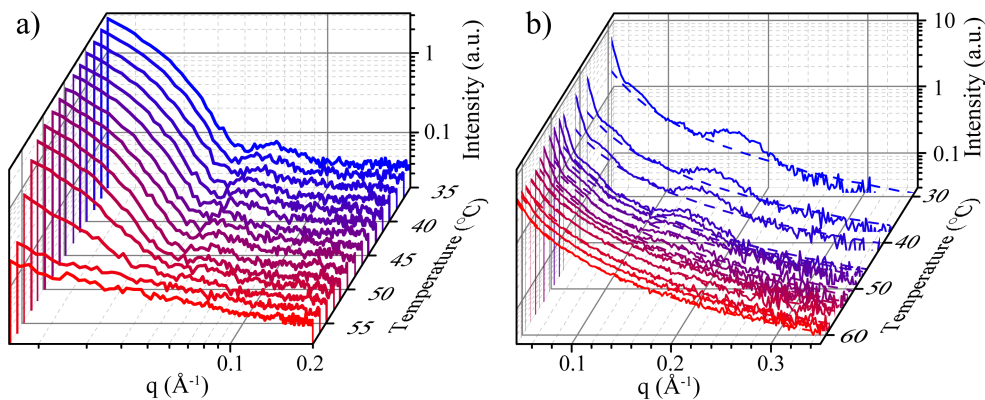


Figure 6.16: In-situ SAXS measurements during heating of 24HB. a) Scattering intensity of a prefolded 24HB structure at the in-house setup, which is heated from 36.5 °C to 58 °C. The curves are not buffer subtracted. b) Scattering intensity of a prefolded 24HB structure at ID01 (ESRF) with superior S/B. The dashed line is an interpolation between the values next to the peak in order to determine the height of the peak. The experiment was done for temperatures from 29 °C to 62 °C. The curves are color coded and the temperatures are at the axis.

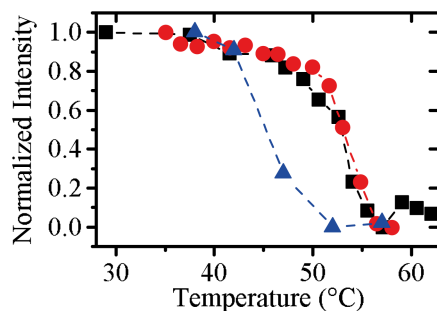


Figure 6.17: Scattering intensity at minimal  $q$ -value for the folding (blue triangle) and the melting (red circles) and the inter-helical peak height during the melting (black squares) in dependency on the temperature. The values are normalized to the maximal intensity.

is fundamentally different from electrostatically driven disassembly. These results suggest that the 24HB should be able to act as a rigid framework in the whole physiologically relevant temperature range of up to 50 °C.

In order to quantify and compare the folding and melting temperature, the intensity at the lowest  $q$ -value  $I(0)$  was evaluated, which is also a measure of the concentration of the structure. For the melting, the intensity of the inter-helical peak was also analyzed. The normalized intensities are shown in Figure 6.17. The intensity  $I(0)$  and the intensity of the peak show the same behavior, which corroborates the assumption that the whole structure melts abruptly. A melting temperature of about 53.5 °C can also be extracted. A clear hysteresis between melting and folding is visible. The data suggest a folding temperature of about 45 °C. However, the resolution is poorer than for the melting because the intensity is lower and therefore the data had to be averaged over a broader temperature range. The resolution could be in-

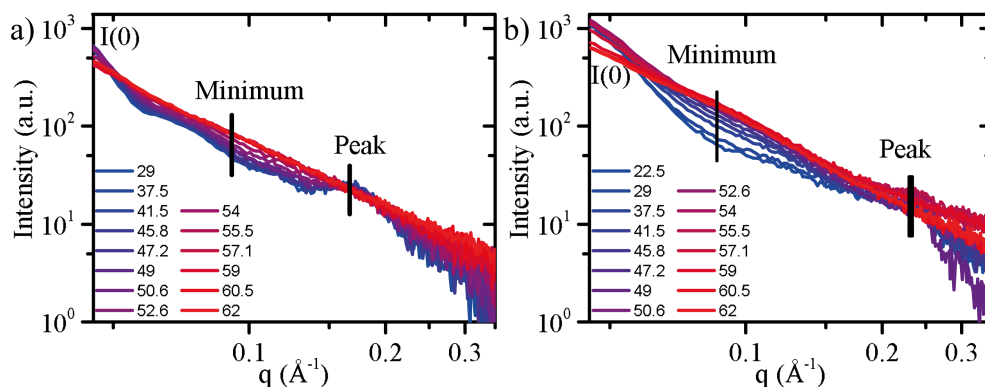


Figure 6.18: Scattering intensity of 24HB and 3-LS during heating. The temperatures are color coded and exact values are in the legend. The three characteristic positions in the scattering curve are indicated:  $I(0)$  at low  $q$ -values, minimum in the form factor of the sample and the inter-helical peak. Data was taken at ID01 (ESRF).

creased by slowing down the cooling ramp.

Similar temperatures and the hysteresis between folding and unfolding are reported in literature [139]. The values were determined by fluorometric measurements. Therefore, small amounts of intercalating dyes are added to the solution and the fluorescence will be enhanced if the dye is intercalated. With this technique it could be shown that the folding takes place at a specific temperature. This helps to speed up the folding process and can improve the design of new DNA origami shapes. However, this technique can only show binding events and gives no detailed information about the structure. In contrast, in-situ SAXS allows to access a wide range of information about the concentration, the inter-helical distance and the shape of the structure during the whole temperature ramp.

To compare the structure evolution during heating to the 24HB, the 3-LS structure was also measured during heating. The scattering intensity versus temperature is shown in Figure 6.18b). The scattering intensity was measured at ID01 at the ESRF and therefore starts at about  $0.04 \text{ \AA}^{-1}$ . At low temperatures the minimum of the form factor and the inter-helical peak can be observed. In order to get a better understanding of what happens during the heating, three parameters were defined characteristic of the scattering intensity of DNA origami, in this case for the 24HB and the 3-LS. The first parameter is the intensity at low  $q$ -values  $I(0)$ , which will be a measure of the concentration of the object, if the object is still intact (Equation 3.30). The second parameter is a characteristic feature of the form factor. In this case, it is the second minimum of the form factor for 24HB and the dip in the form factor of the 3-LS. The inter-helical peak allows to control the internal structure and is the third parameter. These parameters give insight over all length scales, from the volume of the particle down to the internal structure.

The data quality is rather poor because the minimal  $q$ -value is high and the  $q$ -resolution is low due to the divergent beam and the short SDD. Therefore, the condition for a meaningful intensity at  $q$  close to zero is not fulfilled and

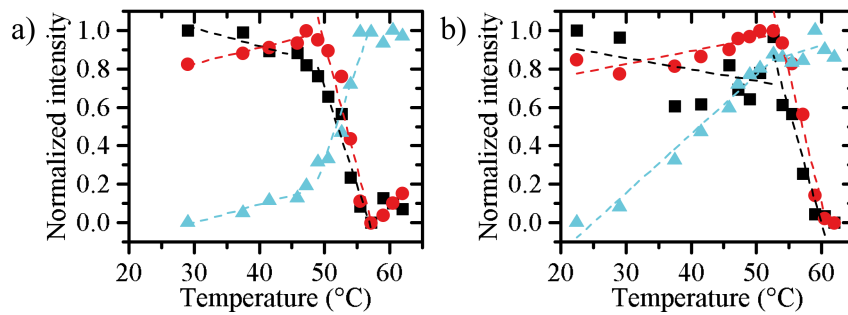


Figure 6.19: The intensity of the three characteristic positions in Figure 6.18 of a) the 24HB and b) the 3-LS during heating. The intensities are given for the low  $q$ -values (red circles), the inter-helical peak (black squares) and the form factor minimum (cyan triangles). The dashed lines are linear fits in different regions and serve as guide to the eye. The values are normalized to the maximal intensity.

the minima of the form factor are smeared due to the instrument. Nevertheless, a difference between both DNA origami with temperature is clearly visible in Figure 6.18.

The different behavior of  $I(o)$  can be seen by comparing the two different data sets of the 24HB in the Figures 6.17 and 6.19 a). The different regimes in the melting curves are fitted with a linear functions which serve as a guide to the eye for the progression of the parameters. For the data in Figure 6.19 a) the intensity increases slightly before it comes to melting of the structure and it drops abruptly. In contrast, with the data in Figure 6.17 at a lower  $q$ -value for  $I(o)$  the intensity behavior is the same as the peak intensity. The same trend for  $I(o)$  as for the 24HB in Figure 6.19 a) can also be observed for the 3-LS in Figure 6.19 b) and can be attributed to a high minimal  $q$ -value for evaluating  $I(o)$ . In order to find differences in the melting behavior of the 24HB and the 3-LS the three defining parameters are shown in Figure 6.19. They show the same curve progression for the  $I(o)$  and the inter-helical peak, but the melting point is slightly increased for the 3-LS to about 57.5 °C. In contrast, the temperature behavior of the intensity at the minimum of both structures shows a different behavior. For the 24HB, it follows the same trend as for the peak intensity, which means that the shape of the 24HB is not altered until the whole structure melts. For the 3-LS, the intensity of minimum increases already from 30 to 40 °C, which is in the physiologically interesting regime. An increase of the intensity at the minimum can be modeled by introducing a polydispersity of the thickness  $A$  of the 3-LS. This means that the 3-LS loses its sharp rectangular shape although polydispersity uses sharp rectangular shapes with different sizes. One possible explanation could be that the 3 layers in the square lattice are less rigid than the 24HB and the temperature introduces a fluctuation in the thickness due to thermal energy. A clear answer can not be given and a more systematic study of this difference would have to take place in order to pinpoint the mechanism. However, this simple example highlights what information can be gained with in-situ SAXS measurements of DNA origami.

#### 6.1.4 Conclusion and Outlook

The previous sections showed that with rather simple geometric models detailed information about DNA origami are gained, which range from the overall shape down to the inter-helical distance. Most of the results can already be achieved at in-house SAXS setups like the one described in section 4.5. For example, the folding of the DNA origami can be monitored. For more detailed analysis of the formation of the inter-helical peak at such low concentrations, synchrotron radiation is still necessary.

In my opinion, more knowledge could be extracted from the existing data by using more complex data analysis methods. As first step, the arranged model introduced in section 6.1.1.2 was written in Matlab and does not support  $q$ -smearing due to the instrument and has no fitting algorithm. Therefore, a significant improvement would be to translate the code to C++ language in order to use it in SasView and make use of the implemented  $q$ -resolution function and the fast and robust fitting routine using a GPU.

Moreover, the arranged model is still incomplete because the chicken-wire like structure of the DNA origami is neglected. One possible approach is to make use of the developed scattering theory of lipid phases by using analytic structure factor for phases with crystallographic symmetry. For example, one could use a hexagonal phase structure factor [140] and combine it with a form factor of a double helix.

The most powerful tool to gain detailed knowledge of SAXS data of DNA origami is a combination of CRY SOL [27] with an atomistic model of the DNA origami, which also takes a  $q$ -dependent background of the excess staple into account. The source code of CRY SOL is not open and a modification is therefore not possible. The included fitting algorithm fails for two reasons. First, a background with  $q$  dependency is not included. For the data shown in section 6.1.1.4 the background was added to the model without any fitting routine. This background issue can be resolved by creating scattering intensities of the DNA origami and the DNA strands with corresponding pdb files with CRY SOL and use them with OLIGOMER [45], which can fit the scattering contributions of multicomponent mixtures by adding the intensities with volume fractions as scaling factor. Second, the existing software, which can create pdb files of DNA origami designs, are not precise enough at the cross-over regions. One approach to overcome this issue would be to determine the scattering intensity of a relaxed DNA origami structure from molecular dynamics simulations with all physical interactions as well as buffer conditions like simulated by Yoo and Aksimentiev [130]. The combination of this molecular dynamics simulation and a fitting algorithm, which takes the scattering signal into account and adjusts the positions of the DNA accordingly to the physical properties, would be the ultimate goal and would also allow for fitting under different environmental conditions. However, the computational demand is still too high to fully simulate all atoms, which are around half a million. Therefore, a simpler model like stack of plates (SOP) model for the DNA within the DNA origami [131] would significantly decrease the

computational effort and might already provide enough information for the exact formation of the DNA within the DNA origami including cross-over formation.

## 6.2 DNA ORIGAMI LATTICE WITH GUEST PARTICLES

*The work described in this section has been partly submitted. The full manuscript (Manuscript 1) is attached in Appendix A.1.*

In this work, the initial idea Nadrian Seeman is fulfilled of building a 3D lattice made of DNA in order to host guest particles. Therefore, his design of the tensegrity triangle [118] is adapted for DNA origami. A detailed description of the design and assembly of the structure can be found in the Ph.D. thesis of Tao Zhang [141] and the attached manuscript in Appendix A.1 and A.1.1.

### 6.2.1 Scattering of Monomers

First, the monomer as a building block of the DNA origami lattice was checked for a correct assembly. A sketch of the monomer is shown in Figure 6.20 in the inset. It consists of three  $14$  helix bundles ( $14$ HBs), which are connected by a common scaffold and form a tensegrity triangle similar to Nadrian Seeman's triangular DNA motif. The packing motif for the  $14$ HB is a honeycomb structure. For the analysis, each  $14$ HB is modeled as a solid rigid cylinder as defined in Equation 6.1. Additionally, the interference in between the cylinders is considered. Therefore, the orientation of the three cylinders to each other is included and only one parameter is used for the fitting of the orientation. This parameter is the separation length of the connecting point of the cylinders with each other as sketched in the inset of Figure 6.20 a). In order to compare the value with the designed value, the radius of the  $14$ HB has to be taken into account because the separation distance depends on the radius of the  $14$ HB.

The scattering intensity of the monomer is shown in Figure 6.20. The geometric model fit, explained above, agrees for  $q$ -values up to  $0.1 \text{ \AA}^{-1}$ . A Debye background is added as for the other DNA origami fits in section 6.1. The fit provides a radius of  $61.8 \pm 0.4 \text{ \AA}$  with a length of  $653 \pm 6 \text{ \AA}$  for each  $14$ HB. The separation length is  $338 \pm 8 \text{ \AA}$  as given in the sketch in Figure 6.20. All these values are in agreement with the design. For example, the connection between the cylinders is made with two connecting DNA strands, which have 3 bps and therefore the separation can vary, but the mean distance is around 100 bps. This leads to a calculated separation length of about  $340 \text{ \AA}$ , which is in perfect agreement with the measured value.

Similar to the  $24$ HB, the whole data can be fitted by taking the geometric model and adding the inner structure with a Lorentzian peak. The peak position is at  $0.148 \pm 0.003 \text{ \AA}^{-1}$ , which leads to an inter-helical distance of

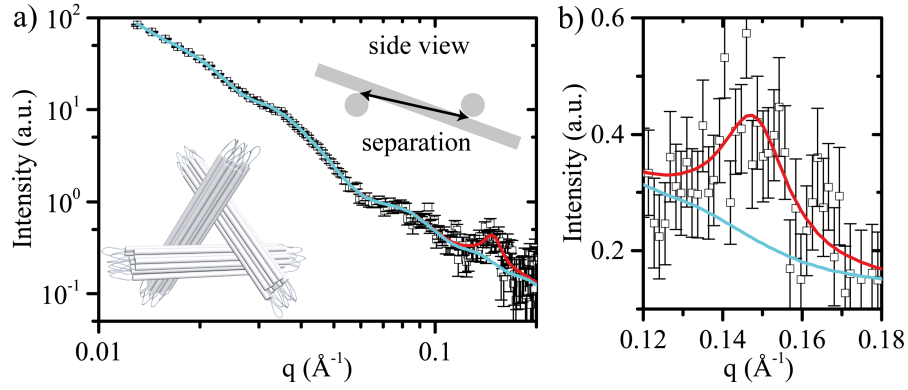


Figure 6.20: a) Scattering intensity of DNA origami lattice monomers with fits of the geometric model (cyan) and geometric model with an added peak (red), (insets) schematic models of monomer. b) Zoom to the inter-helical peak region with both fits in linear scale.

$28.3 \pm 0.6 \text{ \AA}$  with Equation 6.12. This value is larger than the  $25.36 \text{ \AA}$  of the 24HB. The reason for this is not clear. The cross-over density is similar, but the design is more complex. Only a systematic approach of varying the size and the cross-over density would shed light on the origin of the different inter-helical distance. Nevertheless, the analysis provides detailed information of the monomer and proves a correct folding of the design. Moreover, the same models as for the simple shapes of the DNA origami in section 6.1 could also be successfully applied to a more complex DNA origami shape.

### 6.2.2 Scattering of Gold Nanoparticle Lattice

The monomers can be successfully assembled into a 3D lattice, which can be proven by X-ray scattering and is presented in the next section. Additionally, TEM images show large area of DNA lattices, which can be found in the appendix A.1 and A.1.1. Furthermore, the DNA lattice can host AuNPs, which can be seen in TEM images in the appendix. In the case of hosted AuNPs the X-ray scattering signal of the lattice is dominated by the scattering intensity of the AuNPs and the signal of the DNA origami in the lattice can be neglected because the SLD contrast of DNA in water is only  $\Delta\rho \approx 6 \cdot 10^{-6} \text{ \AA}^{-2}$ , which can be calculated with SASSIE Contrast Calculator [142]. In contrast, the SLD contrast of gold in water is  $\Delta\rho = 1.2 \cdot 10^{-4} \text{ \AA}^{-2}$  [143]. The scattering intensity is proportional to  $\Delta\rho^2$  (Equation 3.30) and therefore the scattering intensity of gold is 400 times higher than of DNA.

The AuNP has a spherical shape and the scattering intensity can be modeled with a spherical form factor, which is given in Equation 3.17. The scattering intensity for a lattice with hosted 10 nm diameter AuNPs are presented in Figure 6.21 with a scheme of the unit cell with the AuNPs as red spheres. The scattering intensity is dominated by the scattering of the spheres, shown as a purple dashed line. On top of the form factor some peaks appear. For the fit Equation 3.37 was used with the peak positions of a rhombohedral lattice according to Equation 3.34 and a Debye background like for single DNA

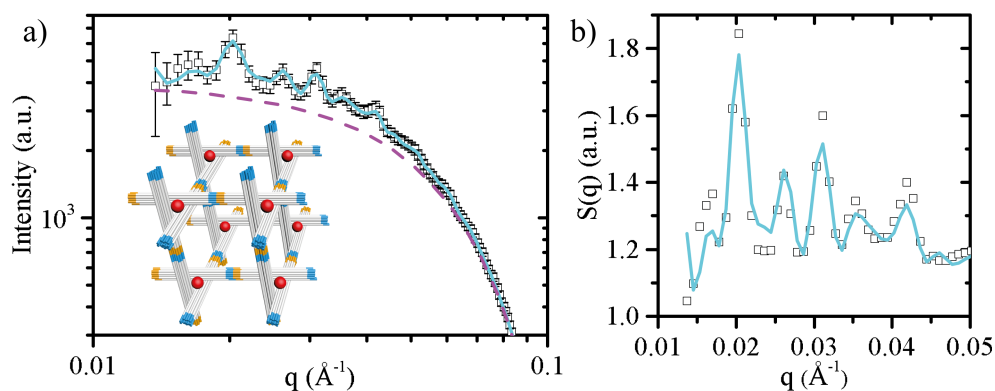


Figure 6.21: Scattering intensity of DNA lattice with 10 nm AuNP. a) Data with the fit of the lattice (cyan) and form factor of AuNP (dashed purple). (inset) scheme of a unit cell of the lattice with AuNP (red). b) Structure factor with fit of lattice (cyan).

origami. Instead of the form factor  $F$  the orientational averaged  $P$  (Equation 3.15) of the sphere can be used because of the high symmetry of the sphere. This symmetry facilitates the calculation because the form and structure factor are separated. All peaks are included in the fit. Their relative intensities are all within the error of the measurement. Here, the fitted lattice constant is  $a = 648 \pm 11 \text{ \AA}$  with an inclination angle of  $\alpha = 108 \pm 2^\circ$ . Due to this high lattice constant, the peaks are at low  $q$ -values and close to each other. Therefore, it is important to include the width of the peak and the  $q$ -smearing due to the instrumental resolution which is treated quantitatively below. Figure 6.21 b) displays the structure factor with the fit. The fitted Debye background was subtracted from the data and the result was divided by the orientational averaged form factor  $P$  of the sphere. In this representation, the Bragg peaks of the lattice appear more clearly and all peaks are included by the fit.

A second sample with 20 nm AuNPs incorporated in the DNA lattice is visible in Figure 6.22. The changed radius of the sphere can be observed with the shift of the first minimum to lower  $q$ -values. The fit of the form factor matches the minimum and maximum perfectly because the fit accounts for the polydispersity of the AuNPs, which is, in this case, 7%. The structure factor is extracted in the same way as for the 10 nm particles and the fit matches the data. The fitted values of the lattice constant and inclination angle are the same within the errors as for 10 nm particles. This shows that the DNA lattice is not altered by the AuNP, even for rather large objects like the 20 nm particles.

For both lattices, the peaks are rather broad, but the peak width is limited by the instrumental  $q$ -resolution. Therefore, only a lower limit of the crystallite size can be estimated with the Scherrer Equation 3.38. The data of the lattice with 10 nm particles have the higher  $q$ -resolution with  $\Delta q = 8.3 \cdot 10^{-4} \text{ \AA}^{-1}$ . This leads to a minimal crystallite size of  $L = 757 \text{ nm}$ , which is about 12 times the lattice constant  $a$ .

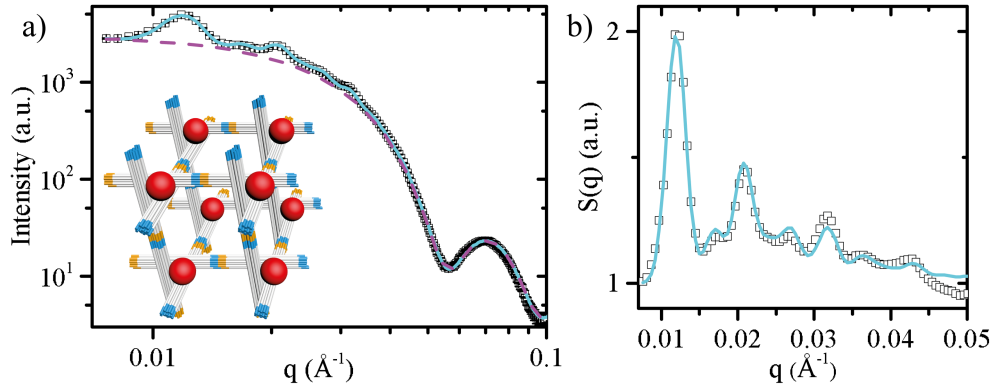


Figure 6.22: Scattering intensity of DNA lattice with 20 nm AuNPs. a) Data with fit of lattice (cyan) and form factor of AuNPs (dashed purple), (inset) scheme of a unit cell of the lattice with AuNPs (red), b) Structure factor with fit of lattice (cyan).

#### *Comparison of Data Quality of Different Instruments*

The data of the 10 and 20 nm gold-decorated lattices appear different because the samples were measured on two different beamlines. The 10 nm AuNPs were measured at Po8 at DESY in Hamburg and the 20 nm particles at the Austrian SAXS beamline at Elettra in Trieste. Both beamlines and the measurement conditions differ significantly. The beamline at Elettra is specialized for SAXS and uses an evacuated flight tube and a flow-through capillary in order to have the same sample thickness for the buffer, which is important for the buffer subtraction. However, the Austrian SAXS beamline uses a wiggler and the storage ring has a ring energy of only 2 GeV. Therefore, it is optimized for lower X-ray energies like 8 keV, which was used for the measurement. In contrast, the PETRA III storage ring of DESY has a ring energy of 6 GeV and the Po8 beamline is equipped with an undulator allowing for higher brilliance. This ring energy allows for higher X-ray energies and the measurement was carried out at an X-ray energy of 20 keV, which helps to prevent radiation damage. The beamline is specialized for high resolution diffraction experiments and therefore no vacuum tube is accessible. A Helium filled tube was used as flight tube instead. A Perkin Elmer flat panel XRD 1621 with  $2048 \times 2048$  pixels of  $200 \mu\text{m}$  size served as detector. The solutions of the sample were loaded in 2 mm quartz capillaries. The SDD was 2434.9 mm, the beam divergence around  $10 \mu\text{rad}$  and the beam size  $0.1 \times 0.4 \text{ mm}^2$ . At the Austrian SAXS beamline, a Dectris Pilatus 3 1M CMOS detector with  $981 \times 1043$  pixels with  $172 \mu\text{m}$  pixel size served as detector. The capillary had 1 mm in diameter, the sample-to-detector distance was 1319.5 mm, the beam divergence  $0.17 \times 1 \text{ mrad}$  and the beam size  $0.5 \times 1.6 \text{ mm}$ .

With the considerations of section 4.3, the  $q$ -resolution is  $8.3 \cdot 10^{-4} \text{ \AA}^{-1}$  for Po8 and is limited by the pixel size. For the Austrian SAXS beamline, the calculation is more complicated because the beam center was positioned at the top of the detector and only a small arc in the vertical direction was

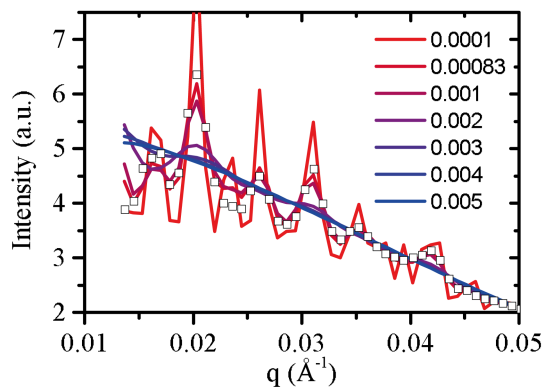


Figure 6.23: Bragg peak intensity depending on  $q$ -resolution for the 10 nm AuNP lattice measured at Po8 (DESY). rectangles: data. lines: fits with different  $q$ -resolution  $\Delta q$  color coded from blue to red with higher resolution as described in the legend. A  $\Delta q = 8.3 \cdot 10^{-4} \text{ \AA}^{-1}$  was used for the fit shown in Figure 6.21.

used for the integration. The reason for this is the high divergence and beam size in the horizontal direction. With the simple calculation of section 4.3 the  $q$ -resolution is  $1.8 \cdot 10^{-3} \text{ \AA}^{-1}$ . This value seems to be overestimated because the peaks of the data were too sharp to be fitted with this value. The beam size is the dominating factor and this contribution is maybe overestimated with the assumed rectangular shape. Therefore, for the fits a  $q$ -resolution of  $0.001 \text{ \AA}^{-1}$  was used because the fits matched the data best.

For a precise determination of the lattice constants and especially the lattice size a high  $q$ -resolution is necessary. The dependency of the data on the  $q$ -resolution is shown in Figure 6.23. The modeled intensity of the 10 nm AuNP lattice was smeared with different  $q$  resolutions. For a  $\Delta q$  of  $0.003 \text{ \AA}^{-1}$  the peaks cannot be distinguished any more. Therefore, a beam with high  $q$ -resolution is necessary to resolve all details of the crystal. In this example, the necessary resolution was achieved in two different ways. In the case of Po8, a high brilliance beamline was used, which has a small beam size and low divergence even for 20 keV X-ray energy. The other beamline has rather high divergence and beam size, but by using an X-ray energy of 8 keV almost the same  $q$ -resolution could be achieved according to the considerations in section 4.3.

The coherence length depicts another important parameter for lattices with a large unit cell. It is the measure of the maximal distance up to which two points can interfere and is limited either by the X-ray energy resolution (longitudinal coherence length) or the beam divergence (transverse coherence length). Estimated values for both beamlines and the setup built in the course of this thesis (section 4.5) are given in Table 6.3. Here, the high brilliance of Po8 at DESY is noticeable with the highest coherence length, although the highest X-ray energy of 20 keV was used. Both types of coherence length are proportional to the X-ray wavelength, compare Equations 3.7 and 3.8. This is also reflected in the transverse coherence length of the in-house setup and the Austrian SAXS beamline. The divergence of both setups is

Coherence length	Po8 (20 keV)	Elettra (8 keV)	In-house (17.4 keV)
Longitudinal	500 nm	150 nm	6 nm
Transverse	3000 nm	450 nm	240 nm

Table 6.3: Estimation of coherence length of Po8 (DESY), Austrian SAXS (Elettra) and in-house SAXS setup. For the longitudinal coherence length (Equation 3.8) of the in-house setup the  $K_\alpha$  line splitting was used and for the transverse coherence length (Equation 3.7) the divergence of the X-ray beam.

almost the same, but due to the lower X-ray energy the coherence length is almost twice as high for the Austrian SAXS beamline as for the in-house setup.

The AuNPs lattice was also measured with the in-house setup, but no peaks were observed. While it remains unclear why, the following might be three possible reasons. Firstly, the sample preparation did not work or the crystal sank to the bottom and could not be measured because the integration time is longer than for synchrotron sources. Secondly, the coherence length is not high enough and therefore no Bragg peaks could be measured. Thirdly, the q-resolution of the setup is too low and the peaks are smeared out due to the instrument.

The coherence length of the setup cannot be further improved, but by increasing the sample-to-detector distance and decreasing the beam size the q-resolution can be significantly improved. In this way, it is possible to find out what the limiting factor is.

### 6.2.3 Scattering of DNA Lattice

This is the first reported lattice of only DNA with a cavity size big enough to host guest particles as AuNP. In contrast to other DNA lattices with AuNP [119, 120], the building block consists only of DNA and therefore enables a wide variety of molecules to bind in the large cavities, for example, for X-ray analysis. The analysis of a lattice of DNA is more complicated than the one with AuNP (section 6.2.2) because the orientation of the monomers in the unit cell has to be taken into account due to their asymmetry compared to the spherical AuNPs. The theory of scattering of crystals with asymmetric particles is summarized in section 3.4. Similar to the form factor intensity of the AuNP which makes up the baseline of the AuNP lattice scattering, the scattering of the triangular DNA monomer underlies the intensity of the DNA crystal, which is shown in Figure 6.24. However, the simple approach of using the orientational averaged form factor  $P$  instead of  $F$  in Equation 3.33 fails because the DNA origami monomer is anisotropic. The resulting fit of the simple approach becomes apparent in Figure 6.25 as a red line. While the first peak is covered by this approach, a look at the structure factor in c) reveals a clear mismatch in peak heights of fit and data. For example at  $0.026 \text{ \AA}^{-1}$  a peak appears, but in the data, there is a minimum in

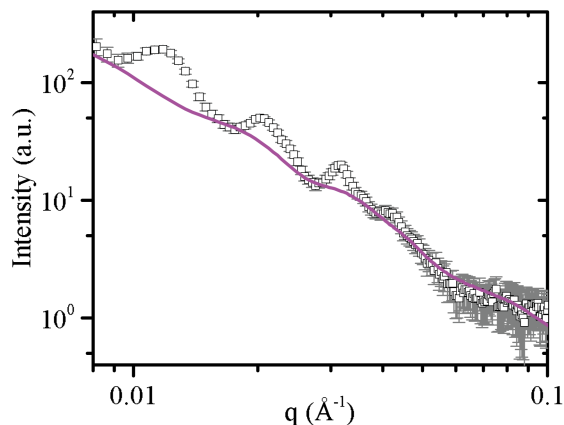


Figure 6.24: Scattering intensity of pure DNA lattice. The fit of the monomer in Figure 6.20 is scaled to the scattering intensity of the lattice and shown in purple.

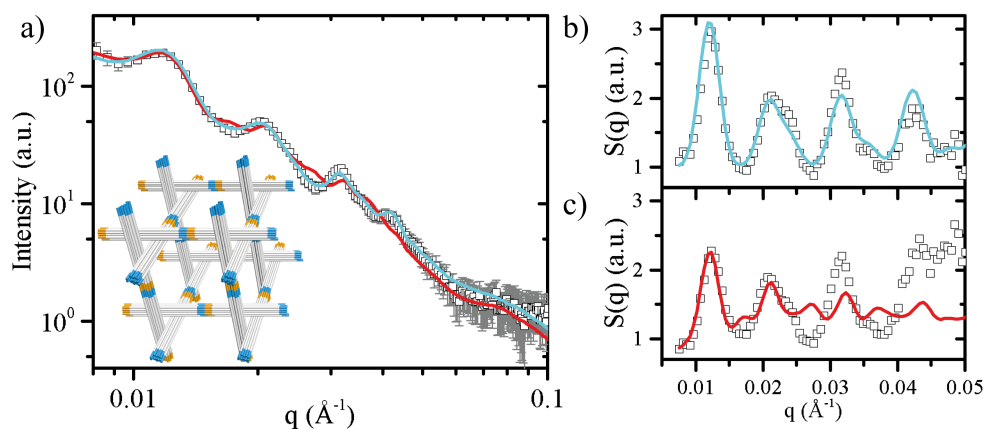


Figure 6.25: a) Scattering intensity of pure DNA lattices with two fits: fit method as for the AuNP lattice, which does not take the orientation of the monomer into account (red), and fit with model which uses the orientation of the monomers (cyan). Inset: model of unit cell of DNA lattice consisting of eight monomers, b) structure factor of oriented monomers and c) structure factor of unoriented model.

the structure factor. In contrast, if the form factor  $F$  of the monomer is used to calculate the structure factor like given in Equation 3.33, the data will be able to be fitted over the whole range. The evaluation of the peak positions of the lattice also becomes more complicated than for the AuNPs lattice. The peak positions were computed by  $\vec{q}_{hkl} = h\vec{b}_1 + k\vec{b}_2 + l\vec{b}_3$  with the reciprocal lattice vectors  $\vec{b}_1$ ,  $\vec{b}_2$  and  $\vec{b}_3$  of the rhombohedral real lattice vectors spanned by the  $14HBs$ . The lattice constant  $a$  is given by the length of the monomer in the fit and the inclination angle  $\alpha$  is given by the separation parameter of the monomer. The fitted values of the monomer in the lattice agree with the values of the dissolved monomer and the calculated lattice constant  $a$  and the inclination angle  $\alpha$  are consistent with the values of the AuNP lattices. These same constants show that the lattice is formed by the DNA monomers and the crystal structure is preserved when AuNPs are attached to the lattice. The development of a DNA based crystal was a long term goal. The easy incorporation of guest molecules via binding to free DNA strands opens a variety of interesting applications. For example, the AuNPs could serve as a photonic crystal. The initial idea by Nadrian Seeman of a DNA lattice for crystallization of proteins is now achievable because the cavity size is about  $184000 \text{ nm}^3$  which is around 115 times larger than in the original design [117]. Of course, new challenges will occur for the hosting of proteins, but the first step is made. In the view of an X-ray crystallographer, the lattice lacks in quality in order to do high-resolution crystallography of binding proteins to the DNA. Therefore, the crystal size, as well as the polydispersity, has to be reduced.

## PHOTO-SWITCHABLE LIPIDS AND FATTY ACIDS

---

The first mention of azobenzene took already place in 1834 and describes the synthesis as well as general chemical properties like melting and evaporation temperature [144]. Also, Alfred Nobel conducted research on this molecule and found an efficient synthesis [145]. This early studies highlight that the molecule is well known and many further studies took place over the years.

The azobenzene group consists of two phenyl rings connected by a nitrogen double bond. The azobenzene group can be incorporated into a wide variety of molecules, which lead to many applications, for example, the controlled bursting of vesicles or the permeability of a lipid membrane [146, 147]. There are many more recent applications in biology and other fields [148–155]. One outstanding property is that the azobenzene undergoes a transition from trans to cis configuration under illumination of UV light. The cis configuration, however, is not stable under ambient conditions and has a thermal relaxation to the trans state. The relaxation time strongly depends on the residual group and the solvent ranges from milliseconds to days [156]. Furthermore, the switching back from cis to trans can be triggered by blue light. Even though the macroscopic collective function is well understood and observed reproducibly, the question remains what happens on the molecular scale. In order to understand the impact of the conformational change of the azobenzene-containing molecules on the collective structure, X-ray studies were conducted on different types of bio-mimicking molecules. Bilayer and multilayer samples were prepared and additional UV-visible (Vis) light measurements were made to understand the number of switched molecules and the speed of the switching progress. The Ph.D. student James Frank of the group of Prof. Trauner at the Ludwig-Maximilians-Universität in Munich provided different molecules with an azobenzene group incorporated in the molecule. One of them is mimicking fatty acids (FAs) and is therefore referred to as azo-FA. The structural formula is depicted in Figure 7.1 a). The second molecule named azo-phosphocholine (PC) relates to a lipid and has a PC head group, shown in Figure 7.1 b). As mentioned above, azobenzene molecules have a trans and a cis state, which both are sketched for the used molecules in Figure 7.1. Azo-PC was studied by fluorescence microscopy and it showed, for example, strong deformation of vesicles under UV illumination [157]. More detailed information about the azo-PC absorption in section 7.3 and bilayer measurements in section 7.4 are provided in the master thesis of Christina Dirscherl [158].

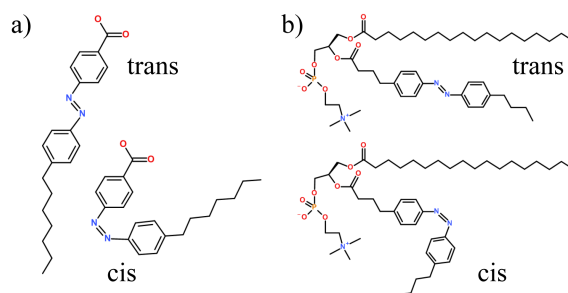


Figure 7.1: Structural formula of azobenzene molecules. a) azo-FA in trans and cis configuration and b) azo-PC in trans and cis configuration.

## 7.1 PREPARATION AND CHARACTERIZATION METHODS

The preparation of lipid multilayers is rather simple, for example, by using the rock-and-roll method [159]. The lipids are pipetted directly on a clean substrate, a silicon wafer, for instance, and while the solvent evaporates, the substrate is rocked and rolled for a uniform distribution of the lipids on the wafer. The multilayer can be hydrated by placing it inside a humidity chamber and phase diagrams can be recorded [160]. Since the sample is on the surface of the solid substrate, SAXS in transmission, as used for the DNA origami in chapter 6, is not feasible. Therefore, the so-called grazing incidence small-angle X-ray scattering (GISAXS) technique is often utilized for substrate-deposited samples. The X-ray beam probes the sample under a grazing angle and the signal is measured with a 2D detector in the same way as for SAXS in transmission. If the grazing angle is below or close to the critical angle of the substrate, the reflectivity will be high and multiple scattering has to be considered, which is covered in the *distorted wave Born approximation* theory [161]. However, the grazing angles for the studies in this chapter are clearly above the critical angle and the reflectivity of the substrate decays with a  $q^{-4}$  dependency [162]. Therefore, the theory of a single scattering event is sufficient.

With the so-called stamping technique, it is possible to prepare lipid bilayer. With this technique, the lipid is deposited on a small surface like the edge of a wafer which is then pressed on a clean substrate resulting in a multilayer of lipids sticking to the surface. The substrate with the lipid multilayer is fixed in the sample chamber. Then, the chamber is filled with a buffer solution, in this case, phosphate-buffered saline (PBS), which has a temperature above the melting temperature of the lipids. The lipids spread over the substrate forming a bilayer. When the entire substrate is covered with a lipid bilayer, the excess lipids are flushed out. For the sample preparation the sample chamber was kept at 65 °C because azo-PC is similar to 1,2-distearoyl-sn-glycero-3-phosphocholine (DSPC), which has a gel to liquid phase transition temperature of 55 °C [163]. For the preparation, a glass substrate was used in order to enable microscopy through the substrate.

The absorption of a sample can be measured with UV-Vis spectroscopy. In this thesis, the sample was illuminated with a wavelength spectrum from

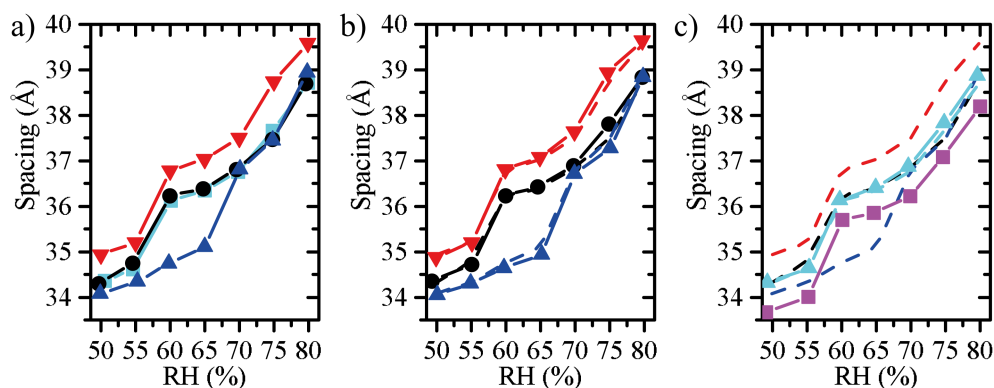


Figure 7.2: Spacing of the multilayer in the direction perpendicular to the surface in lipid phases of DOPE and DOPC with FAs under varying RH and in three illumination conditions: without light, with blue light, and with UV light. a) Pure lipid mixture (black circles), mixture with stearic acid (red downward triangles), mixture with oleic acid (blue upward triangles), and azo-FA mixture (cyan squares) without light. b) Pure lipid mixture (black circles), mixture with stearic acid (red downward triangles), and mixture with oleic acid (blue upward triangles) with UV irradiation. Dashed lines show spacings without illumination. c) azo-FA mixture with UV light (violet squares), and consecutive blue light irradiation (cyan upward triangles). Dashed lines show spacings without illumination for all four samples.

200 to 500 nm and the transmission is evaluated for all wavelengths of the spectrum separately.

## 7.2 STUDY OF LIPID PHASES

First test measurements with mixtures of the lipids 1,2-dioleoyl-sn-glycero-3-phosphoethanolamine (DOPE) and 1,2-dioleoyl-sn-glycero-3-phosphocholine (DOPC) were carried out with 2:1 and 1:1 DOPE:DOPC molecular concentrations because their phase diagrams are well-known [160, 164] and the mixtures exhibit different phases from hexagonal to rhombohedral to lamellar phases within a RH regime of 50-90%. The phase diagram, which was measured with the humidity chamber presented in section 4.5.1, is in agreement with the literature values [160, 164]. During the study, it was found that high-intensity light influences the sensor, and hence, a wrong regulation of temperature and RH can occur. However, at the lowest light intensity for both LEDs (see section 4.5.1) no such effect was observed.

In order to understand the influence of a small amount of azo-FA on the lipid phase of DOPE and DOPC, 8% molecular concentration of azo-FA were mixed with a one-to-one mixture of the lipids. In two control experiments stearic and oleic acid were mixed in the same concentrations with DOPE and DOPC because the molecular structure of those fatty acids is similar to the trans and cis configuration of azo-FA respectively. The spacing of the multilayer in the direction perpendicular to the surface is shown in Figure 7.2.

All samples were tested under three lighting conditions in the following order: without light, with blue, and with UV light. Additionally, the RH varied from 50-80 %. In this RH region all samples have a rhombohedral structure from 50-70 % and at around 75 % a phase transition to a lamellar phase is observed. Figure 7.2 a) shows all four samples without illumination. With increasing RH the spacing increases for all samples because the phase contains more water in between the lipid layers. Between the different samples, there are substantial differences. The presence of stearic acid leads to an increase of the spacing compared to the pure DOPE and DOPC sample for the whole measured RH regime. In contrast, the sample with oleic acid has a significantly decreased spacing for RH up to 65 % and for higher RHs the spacing is the same as for the pure lipid sample. The azo-FA has no significant difference in the lipid sample as long as the molecules are in the trans state. Under illumination with UV light, no significant influence on the spacing can be observed for the three samples without azobenzene, see Figure 7.2 b). In contrast, for azo-FA the spacing decreases over the whole measured RH range, see Figure 7.2 c). The decrease of the spacing is smaller than the one induced by the oleic acid, but the trend is the same. Consecutive blue light illumination induces the same spacings as without illumination which shows that the effect is caused by the molecular switch of azo-FA.

In conclusion, an effect of the switching from trans to cis state of azo-FA can be observed in the lamellar multilayer spacing of the lipid phase. However, the direct analogy with stearic and oleic acid was not confirmed, but the trend in spacing is similar. This result is no surprise because the azobenzene group is large compared to the normal covalent bonds present in conventional FAs and can lead to steric hindrances in the phase. Furthermore, azobenzene is polar in contrast to the nonpolar carbon bonds in the FAs. The cis configuration of azobenzene group has a high dipole moment of 3 Debye, while the trans configuration has none [156].

### 7.3 RATIO OF SWITCHED MOLECULES

For molecules which undergo a conformational change by illumination, an important parameter is the switching ratio, or in other words, how many molecules are in a certain conformation. In the case of azobenzene, this is either the trans or cis configuration. A simple tool to estimate the switching ratio is UV-Vis spectroscopy (see section 7.1). Due to the different conformations of the molecule, the absorption changes. Typical UV-Vis spectra for azo-PC multilayers on a glass substrate are shown in Figure 7.3 a). The spectrum of the sample without illumination is depicted in black and the violet line presents the spectrum of a sample which was illuminated with UV light with a wavelength of 365 nm (section 4.5.1) for ten minutes. This duration is sufficient to have a maximal number of molecules in the cis state, which is demonstrated below. After the UV irradiation, the sample was illuminated with blue light with a wavelength of 460 nm for ten minutes and most molecules switched back to the trans state, blue line in Figure 7.3 a). The change

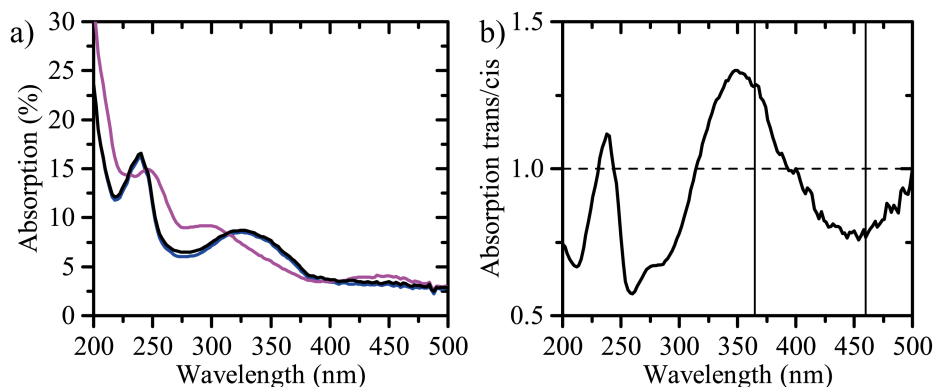


Figure 7.3: Absorption spectra of azo-PC. a) without illumination (black), after 10 min illumination with UV light (violet) and after subsequent 10 min illumination with blue light (blue). b) The quotient of the curve without illumination (trans state) and after UV illumination (cis state). Vertical lines show wavelengths of the light used for illumination.

of conformation of the molecule with different irradiation wavelengths is only possible because the absorption spectra of the states are different. The quotient of the spectra of the trans and cis state is shown in Figure 7.3 b). Wavelengths with a value above one trigger the conformation change towards the cis configuration and vice versa. The used wavelength of 365 nm is displayed in the graph and is close to the maximum for trans-to-cis switching, which is at 348 nm. The same is true for the blue light of 460 nm, which is close to the optimal wavelength in the visible light region for cis-to-trans switching. However, at a wavelength of 260 nm the switch would be more effective. Since the trans state is more stable than the cis state, it is sufficient to use 460 nm instead of 260 nm. This has practical advantages because blue light sources are more common and less dangerous than UV light sources. Overall, with this simple experiment, it was demonstrated that the switch is reversible by using the corresponding wavelengths.

UV-Vis spectroscopy is also capable of determining the kinetics of the switch between the configurations. Single azobenzene molecules in solution switch their conformation within picoseconds [165, 166], but the speed of switching depends on the light intensity [167] and on the environment, e.g. the switching process takes about 0.2 s in liquid crystal of azobenzene upon irradiation with a laser [168]. Here, azo-PC was measured as multilayer on a glass substrate with an illumination intensity of  $0.1 \text{ mW/mm}^2$ . The sample is continuously illuminated with the UV light for a certain time and then the illumination is stopped in order to measure the absorption spectra. These spectra are given in Figure 7.4 a) without background subtraction and as transmission  $T$ , which is simply related to the absorption  $A$  by  $A=1-T$ . The absorption spectra change continuously until one minute after the first exposure. From minute one to two, the absorption does not change, but after three minutes the final state is almost reached. After ten minutes the final state is reached and the transmission does not change with longer illumination. Compared to single molecules in solution the switching process

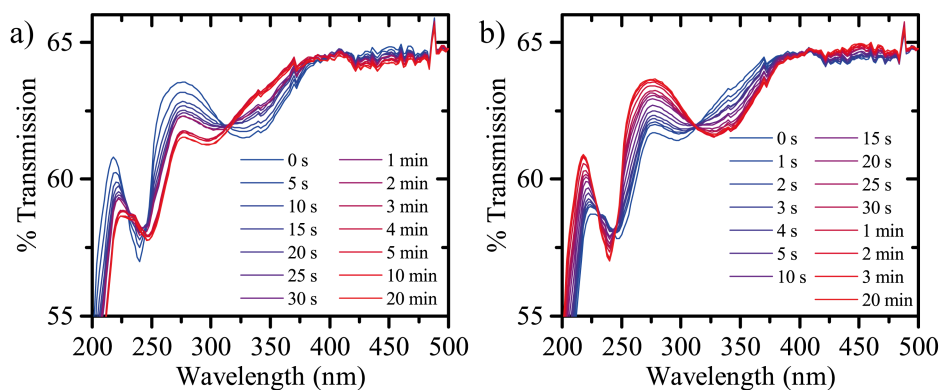


Figure 7.4: Transmission spectra of azo-PC under different durations of illumination with a) UV light and with b) blue light. The data is color coded from blue to red and the time is given in the legend. The data is not corrected for the absorption of the glass slide but scaled to equal transmission of the initial one at 500 nm.

is prolonged, minutes compared to picoseconds. The delay is likely to be caused by steric hindrance in such a close packed system because a similar behavior is also observed for liquid crystals [168]. In that case, the switching time could be decreased to the millisecond regime by using a high light intensity.

The kinetics of the multilayer for the photo-switch back with blue light was also tested under the same conditions as for the UV illumination. First, the sample was irradiated with UV light in order to have a maximum of molecules in the cis configuration. The switching back from cis to trans with blue light is faster than from trans to cis and after one minute almost all molecules have already been switched back, see Figure 7.4 b). The final state is reached in between two and three minutes.

Since the trans state is the thermally stable state, the stability of the cis configuration without illumination was also tested. Until 75 minutes after lighting, the absorption spectra changes only slightly, which is shown in Figure 7.5. After 22 hours most of the molecules have switched back to the trans state. However, an illumination of five minutes with blue light further shifts the absorption spectra indicating that the final state was not fully reached.

For azo-PC, the UV absorption is maximal for the cis state and the blue absorption is maximal for the trans state. Both states have their typical absorption spectrum, which is shown in Figure 7.3. This means that after a characteristic time of illumination the system will end up in a state of photostationary equilibrium (PSE) where no further change in the number of lipids per conformation takes place. The characteristic time depends on the intensity of the illumination and its wavelength. However, processes of switching and back-switching of the azobenzene continue during light irradiation. In the state of PSE not all azo-PC molecules are in the conformation which has the higher absorption for the irradiation wavelength chosen. Only if the absorption for one state is equal to zero, all molecules will have the

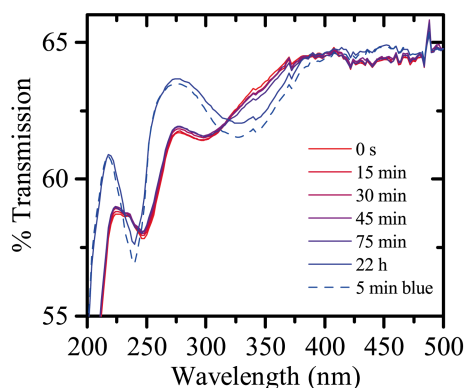


Figure 7.5: Transmission spectra of azo-PC, which was switched to the cis state with UV light and then was stored in the dark. After 22 h storage in the dark the sample is completely switched back to the trans state by an illumination of 5 min with blue light. The data is color coded from red to blue and the time is given in the legend. The data is not corrected for the absorption of the glass slide and scaled to equal transmission of the initial one at 500 nm.

same conformation. Nevertheless, in the state of PSE the number of azo-PC molecules in the state with higher absorption reaches its maximum. The amount of azo-PC molecules in the desired conformation can be changed by choice of the irradiation wavelength.

Now, the ratio of cis and trans states are evaluated for the PSE for the wavelengths of 360 nm and 450 nm which are used in the experiment. The ratios can be calculated from the three absorption spectra in Figure 7.3. The assumption made for the calculation is that in the initial sample without illumination all molecules are in trans configuration. Furthermore, the quantum yield of photoisomerization of azobenzene in water, which can be found in literature [169], is used for the calculation of the transition probability. A detailed derivation and the formula can be consulted in the master thesis of Christina Dirscherl [158]. For the used wavelengths the calculation leads to a percentage of 4.8% azo-PC in trans state and 95.2% in the cis state for blue light irradiation. With UV irradiation, only a percentage of 32.4% molecules reaches the cis state and the majority of 67.6% stay in trans configuration.

#### 7.4 X-RAY REFLECTOMETRY OF BILAYERS

A bilayer of azo-PC with 0.5% Texas Red labeled 1,2-dihexadecanoyl-sn-glycero-3-phosphoethanolamine (DHPE) lipids was prepared with the stamping technique, see section 7.1. Before the X-ray reflectometry (XRR) experiments, the correct spreading of the lipids was checked by fluorescence microscopy with the incorporated Texas Red labeled lipids.

The thickness of the bilayer is determined with XRR. This technique measures the reflectivity of a substrate at an exiting angle equal to the incident angle. Therefore, the  $q$  vector is perpendicular to the surface of the sample and only the  $q_z$  component is measured. The reflected intensity drops with

*A detailed description of X-ray reflectometry can be found in chapter 3 of the book by Als-Nielsen [37].*

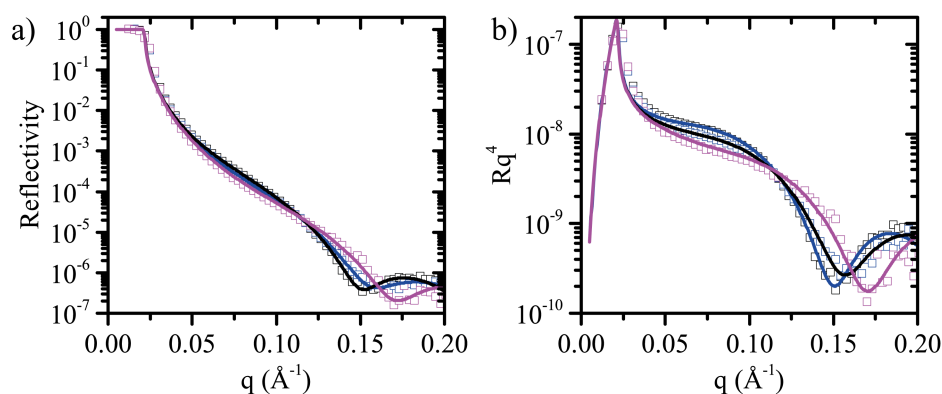


Figure 7.6: XRR of azo-PC bilayer under three different illumination conditions: without light (black), with UV light illumination (violet) and with subsequent blue light illumination (blue). a) semi logarithmic representation, b) reflectivity multiplied with  $q^4$ , which enhances sample features.

$q^{-4}$  for a perfectly flat surface as a result of the Fresnel equations [7]. For rough surfaces, the reflectivity is decreased [162]. Uniform layers cause interference and result in oscillations, which are also called Kiessig-Fringes. Therefore, XRR is used for the study of thin films on substrates. The plugin *Motofit* for *IgorPro* can fit XRR measurements by modeling the scattering length density profile perpendicular to the surface [170]. For the model of lipid bilayer three layers were used, one for both head groups and one for the tail region. All layers have three free parameters: the thickness, the SLD and the roughness. The lipid layers are not completely flat and therefore the roughness is introduced which results in less pronounced features in the X-ray reflectivity compared to totally flat structures. The SLDs of each layer correspond to the electron density and is an indicator of the composition and packing in the layer.

XRR measurements of an azo-PC bilayer are shown in Figure 7.6. In b) the reflectivity is multiplied by  $q^4$ , which highlights the features of the sample because the reflectivity of the substrate drops with  $q^{-4}$ . The bilayer was first measured without irradiation. Next, the UV LED was switched on and the measurement was started ten minutes after the PSE had been reached (see section 7.3). The LED was left on during the whole measurement because a single measurement takes about 21 hours and the UV-Vis measurement showed that most molecules had switched back into the trans state after 22 hours. Finally, the UV illumination was stopped, the blue LED was switched on and a subsequent measurement was started ten minutes afterward. The reflectivity curves in Figure 7.6 show a clear difference with the distinct illumination conditions. The corresponding scattering length profiles of the fits are shown in Figure 7.7. For the UV illumination, the thickness of the tail region of the lipids decreases and its SLD increases compared to no lighting. One possible interpretation is that the molecules in cis configuration move closer together, which increases the electron density in this layer. However, completely different SLD profiles with a similar goodness of fit can be obtained. The fitted thickness values for two exemplary models is given in

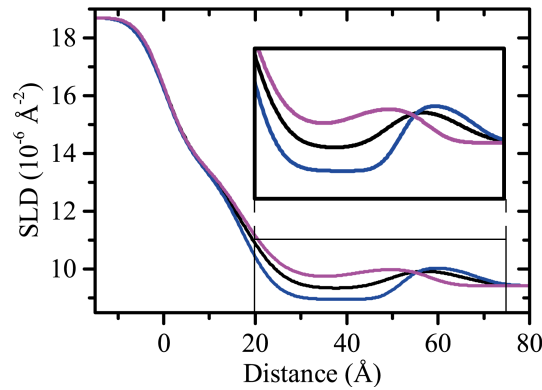


Figure 7.7: SLD profile of azo-PC bilayer of fit in Figure 7.6 with different illumination: without light (black), with UV illumination (violet) and with subsequent blue illumination (blue). Inset: Zoom in bilayer region.

Table 7.1. The first fit, which is shown above, suggests a decrease in thickness in the tail region from no light to UV light. The profile shown in Figure 7.7 has the same behavior for all illumination conditions for the head group at the side of the substrate. The profile has a typical shape for SLD profiles of lipid bilayers although the SLD of the tail region is increased due to the higher electron density of the azobenzene group compared to a hydrocarbon chain [171]. However, the outer head group, which is away from the substrate, appears too big compared to literature value of about  $10 \text{ \AA}$  [172]. The inner head group thickness appears larger due to a small water layer in between the substrate and the lipid head group and thus it seems reasonable. The second fit has more realistic head group thickness for the outer side, but a decreased thickness of all three layers together under UV irradiation is not observed. This results suggest that the reflectivity data quality is not high enough for a clear interpretation because the fit has too many parameters (in total 9) including the thickness, the SLD and the roughness for three layers. The data is above the background level only up to  $0.2 \text{ \AA}^{-1}$  which is not sufficient to determine values in the sub nanometer regime. Furthermore, only about one-third of the molecules change the configuration (see section 7.3). This low change rate makes a system of at least two different thickness profiles probable but also increases the number of free parameters in a fit. In order to find a stringent interpretation, a higher data quality or additional measurements such as the multilayer presented in section 7.5 are necessary.

## 7.5 AZO-PC MULTILAYER

An advantage of a multilayer compared to a bilayer is the increased scattering intensity. The ordered lipid layers exhibit Bragg peaks, which can be measured within seconds, even at in-house setups. The sample of 100 % azo-PC was prepared on a cleaned silicon wafer with the rock-and-roll technique, which is explained in section 7.1. The total amount of azo-PC on the surface

	Model 1			Model 2		
	inner head	tail	outer head	inner head	tail	outer head
off	17.0	34.9	16.2	17.0	36.4	8.1
blue	17.0	32.2	16.0	17.6	36.1	7.1
UV	17.0	24.8	16.3	18.6	32.8	9.9

Table 7.1: Fit values of bilayer thicknesses in Å for two different models with similar quality of fit. Model 1 is shown in Figures 7.6 and 7.7.

is 0.2 mg, but due to the preparation technique, the thickness of the layer is not uniform over the entire substrate area.

### 7.5.1 Multilayer Thickness

First, an XRR measurement was carried out in order to check the quality of the prepared multilayer. With this technique only the  $q_z$  component and therefore the direction perpendicular to the surface is probed. In this way, the thickness of lamellar layers can be measured. The spacing of the multilayer can be evaluated with the Bragg peak position as in Equation 6.8:

$$d_{00l} = \frac{2\pi l}{q_z} \quad (7.1)$$

The peaks are in (ool) direction with  $l$  being the Miller index. The multilayer spacing consists of the thickness of a bilayer of azo-PC and a water layer in between the head groups. The reflectivity data of a multilayer of azo-PC is shown in Figure 7.8. Due to the high intensity of the ordered system, the measurement time was only nine minutes compared to the 21 hours for the bilayer in the previous section. Furthermore, the  $q$ -values go up to  $0.7 \text{ \AA}^{-1}$  and no background subtraction was necessary. A series of Bragg peaks can be observed and are highlighted with dashed lines. The peaks correspond to different orders of  $l$  for the same spacing. Without illumination, thus in trans configuration, the measured spacing of the multilayer is  $d=56.3 \pm 0.4 \text{ \AA}$ . The error is determined with the standard deviation of a Gaussian fit for all peaks. The spacing for the first peak differs with  $d_{001} = 55.3 \text{ \AA}$  because the peak position is shifted due to the background of the X-ray reflectivity. The value of  $56.3 \text{ \AA}$  is below the lowest value measured for the bilayer in section 7.4, even for molecules in cis configuration with a smaller thickness. For the bilayer, the measurement took place at  $65 \text{ }^\circ\text{C}$ . At this temperature, azo-PC is likely to be in the liquid phase. In contrast, the multilayer measurement took place at room temperature ( $\approx 20 \text{ }^\circ\text{C}$ ), at which the multilayer is probably in the gel phase. It is known that the spacing of the gel phase is higher than the liquid phase for DSPC [173]. Therefore, the decreased thickness of the multilayer is surprising. There are two possible reasons. First, the quality of the data in section 7.4 is too poor to receive a reasonable bilayer thickness. Alternatively, second, the reduced water content of the multilayer in air and

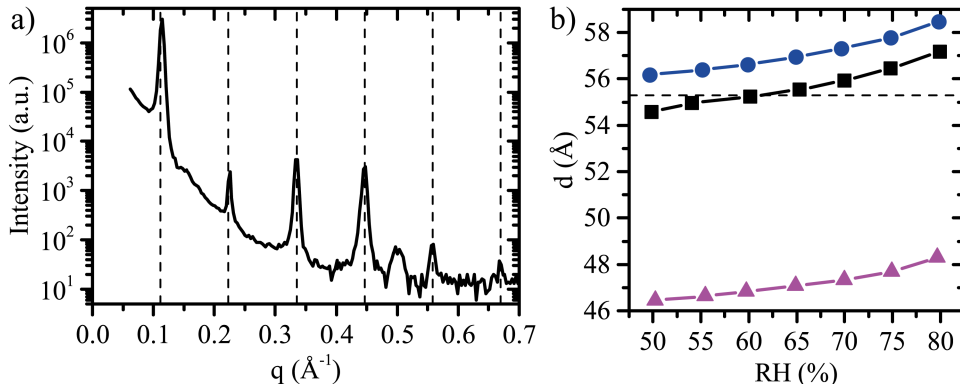


Figure 7.8: a) XRR of an azo-PC multilayer at room temperature. Vertical dashed line correspond to the (001) Bragg peak with a spacing of  $d = 56.3 \pm 0.4$  Å. b) Thickness of multilayer with different RHs at 25 °C and no light (black), illumination with blue light (blue) and UV light (violet) determined with the GISAXS technique. Dashed line is at  $d_{001} = 55.3$  Å of the XRR because thickness was determined by the (001) peak with GISAXS.

the interaction of the layers in the multilayer lead to a decrease of the thickness.

In a second experiment, the azo-PC multilayer was measured in the GISAXS configuration. The incident angle was  $0.2^\circ$  and hence the Bragg condition of the lamellar spacing was not fulfilled. However, the order inside the layer can be determined and a wide  $q$ -range including in-plane scattering of the substrate can be measured by one exposure. Since the order of a lipid multilayer is low compared to crystals, the Bragg peaks are broad and can be observed without perfectly fulfilling the Bragg condition. The RH was changed and the multilayer distance  $d$  was determined with the first Bragg peak position  $q_{(001)}$  using Equation 7.1. The experiment was carried out first without illumination, second with blue light and last with UV light. The resulting spacing  $d$  is shown in Figure 7.8b). For all irradiation conditions, the spacing grows with increasing RH, which is a result of the higher water content in between the layers of azo-PC. The measurement without light is in agreement with the XRR measurement. Interestingly, the spacing increases with the blue light switched on, which can not be explained by the azo-PC switching process because the conformation should not change with blue light illumination. However, the effect is small and in the opposite direction compared to the UV illumination. Here, the difference in spacing is almost one nanometer and is caused by the photo-switch from trans to cis.

The experiment with the multilayer showed that the thickness decreases for UV light illumination. With this information, the SLD profile in Figure 7.7 of the bilayer is more probable. It shows a similar result as for the multilayer, a slight increase in thickness for blue light and a strong decrease for UV light illumination. However, for a proof of the SLD profile, another XRR measurement at a synchrotron should be carried out, which would deliver data up to  $0.5 \text{ \AA}^{-1}$  and would make the solution more definite.

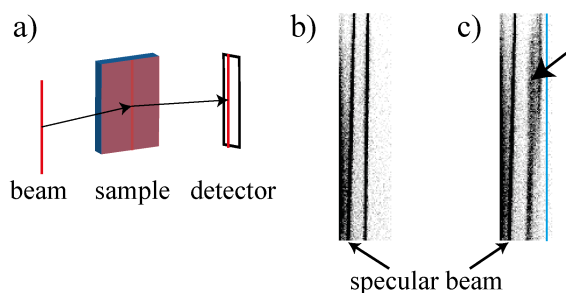


Figure 7.9: Time-resolved XRD measurement geometry. a) Scattering geometry: A line shape beam (red) probes whole sample surface (blue) due to the low incident angle. b) Part of the detector image after blue light illumination and c) part of the detector image after UV illumination. Blue line indicates vertical integration of pixels for each time step.

### 7.5.2 Time-resolved X-ray Measurements

Due to the high scattering intensity for multilayers, time resolved measurements are feasible. They allow finding the time constants of switching. For this experiment, the incident angle of the X-ray beam was chosen in a way to be slightly below the angle of the first order Bragg condition which is  $0.3^\circ$ . Figure 7.9 sketches the measurement geometry and shows two detector images after illumination with blue and UV light respectively. The entire sample surface is probed due to the line shaped beam and the low incident angle. The specular beam appears as a vertical line in the detector images in b) and c). The beam is slightly tilted which decreases the resolution after integration of the detector image. A detector image was taken every second after the start of the illumination with either UV or blue light. In order to analyze the temporal behavior of the peak position each vertical pixel line is integrated and the sum of all pixels is used for the analysis as indicated by the blue line in Figure 7.9 c). The integrated XRD data of azo-PC with first illumination of UV light and subsequent blue light illumination is shown in Figure 7.10. Subfigure a) shows a previously unilluminated multilayer sample with UV illumination. In the beginning, the Bragg peak is at about  $0.114 \text{ \AA}^{-1}$  and shifts to higher  $q$ -values and thus lower spacings which are in agreement with the data of section 7.5.1. The peak splits and one peak reaches a  $q$ -value of about  $0.130 \text{ \AA}^{-1}$  within three minutes which is close to the final state and in agreement with the UV-Vis and the previous multilayer measurements in sections 7.3 and 7.5.1 respectively. The second peak which appears reaches only a  $q$ -value of about  $0.118 \text{ \AA}^{-1}$  after three minutes. These two different contributions could not be observed for the multilayer which was illuminated for 30 min before measuring and more locally probed with a 1 mm beam diameter. The detector image after UV illumination in Figure 7.9 c) reveals that the two peaks originate from different positions of the sample. While the upper part of the image reaches the highest angle (furthest right, indicated by arrow), there is a gradient in the detector image and the lowest part shows the minimum movement of the peak position after an

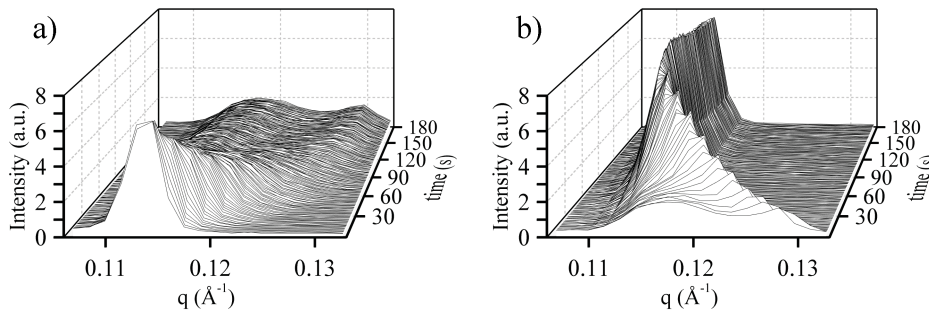


Figure 7.10: Time-resolved XRD of azo-PC multilayer for a) UV and b) blue light illumination. The data of b) can be put behind a) to complete the time axis. The peak is the first order Bragg peak of the multilayer.

illumination of three minutes with UV light. The most probable explanation for this gradient is the illumination of the sample. Divergent light out of a glass fiber was used, which is introduced in section 4.5.1. Since the switching of the azobenzene depends on the light intensity, the cause for the gradient might be a non-uniform illumination resulting in an enhanced switching in the upper part of the sample. Therefore, it is unlikely that two different time constants are present during the switching and it is rather an artifact of the experimental setup. Furthermore, the time scale of the faster-moving peak lies in agreement with the switching of the molecules, which was tested with UV-Vis measurements in section 7.3.

The subsequent measurement with blue light of a previously UV-illuminated wafer shows the inverse process. The peak in Figure 7.9) in the upper part of the detector shifts faster than the second peak in the lower detector area. The switch back to trans configuration is faster than the switch under UV illumination and after about one minute the final state is already reached, which is also in line with the UV-Vis measurement in section 7.3.

A recent experiment measured the transmitted light, which was used for the switching, during the X-ray measurement [174]. The change of the transmission had the same temporal behavior as the change in spacing. The measurement was carried out with a smaller beam size of the setup presented in section 4.5. Therefore, the structural change was probed more locally and only one peak could be observed which is a further indication of an experimental artifact in the presented data in Figure 7.10. In the recent experiment, the shift of the Bragg peak concomitant with the characteristic change in absorption shows that the decreased spacing for azo-PC molecules is indeed caused by the switch by the trans to the cis state.



Part III

CONCLUSION



## SUMMARY

---

Within this thesis, a flexible, versatile X-ray setup was build from scratch, which is explained in detail in chapter 4. The primary focus of the setup is the study of nanomaterials in solution, but it is open to a wide variety of applications. For that, the source was chosen to be a Mo anode with a rather high energy of 17.4 keV. Higher energy will gain penetration depth, which increases the S/B for solution based SAXS, if the sample chamber is adapted to the optimal sample thickness. The background is less for higher energies because the solid angle per q-bin is smaller for higher energies and the available primary beam intensity is typically less than for lower energies. This fewer intensity for higher energies is of course also valid for the scattering of the sample, whose scattering volume has to be increased in order to have a better S/B, otherwise signal and background decrease in the same way. The setup is limited by the natural background and therefore air gaps of a few centimeter do not compromise the quality of the data. This weak dependence on air gaps permits to implement complex sample environments like a humidity chamber without data quality loss.

The setup has three different standard SDDs, which can be changed within few minutes. This provides access to a wide range of q-values and can match the application best. The setup was successfully utilized for a wide range of q-values: DNA origami were measured at low q-values (chapter 6), lipid multilayers with photo-switchable azobenzene groups in the intermediate regime (chapter 7), and wide angle scattering was used for perovskite nanoplatelets (chapter 5). These are also the applications presented in this thesis, but there are many more samples, which have already been measured. For example, *ab initio* reconstructions of a variety of proteins could be made, which are well characterized by SAXS and served as a benchmark for the setup [6]. The thickness of the membrane of lipid vesicles was resolved [175] as well as the structure of lipid ribonucleic acid (RNA) mixtures. Octanol-water mixtures were characterized in high detail with additives, e. g. ketoprofen. The results subvert the concept of the octanol-water partition coefficient, which invokes additive partitioning in two homogeneous solvents. Two different types of nanoparticles were studied, which have a small gap within the particle and thus have low photoluminescence polarization anisotropy [176] or enable control over quantum plasmon resonances [177]. However, the analysis within the master thesis of Fabian Herschel [178] showed that the quality of the data was not high enough for a detailed analysis, which led to a further improvement of the setup at that time. The setup could reveal the size and distribution of a variety of nanoparticles: metal organic frameworks, silver, and gold. Furthermore, other WAXS measurements were conducted. The lattice constants of different calcium phosphate mixtures were deter-

mined and the quality of organic crystals like 6,13-dihydrodiazapentacene (DHDAP) was tested [179]. Moreover, the technique of grazing incidence X-ray diffraction (GIXD) was used for the control of thin films like pentacene and  $C_{60}$ , which are described by Noever et al. [180]. Furthermore, the widely used model system of Poly(3-hexylthiophene-2,5-diyl) (P3HT) and [6,6]-Phenyl  $C_{61}$  butyric acid methyl ester (PCBM) for organic solar cells was determined with the same technique.

In some cases, however, the quality of the data of the setup was not sufficient for a detailed analysis or the demand on sample concentration was too high. For example, the gap size for nanoparticles mentioned above could not be solved and the inter-helical distance of square lattice DNA origami was only observed with the help of third-generation synchrotron radiation. Also, the DNA origami crystal could only be measured with a synchrotron source. The reason is still unclear: either the coherence length of the in-house setup is too low or the measurement time was too long, so the crystal moved out of the beam due to gravity. Nevertheless, the in-house X-ray setup has proven to be a very useful tool for a large variety of applications as pointed out above. For example, the inter-helical peak for honeycomb lattice DNA origami was first observed at the in-house setup.

## CONCLUSION AND OUTLOOK

---

The SAXS setup, which was designed and built within this thesis, is routinely used for many different samples as mentioned in chapter 8. Some highlights were presented in detail in the chapters 5 to 7. It was also mentioned that the data quality is not sufficient for all applications. This lack of data quality can be partly overcome by further development of the setup.

As shown in the sections 4.2 and 4.5, a longer collimation length allows to access lower  $q$ -values. This can be accomplished without extra cost because there is sufficient space in the laboratory for this upgrade. In the same section, it was also made clear that an upgrade to a larger detector like the Pilatus 300K would lead to a substantial increase in coverage of solid angle. Particularly for  $q$ -values of  $0.1 \text{ \AA}^{-1}$  and above, the data quality would be improved substantially by the increased measured intensity due to a larger area detector. This intensity gain could be sufficient in order to observe the inter-helical peak of square lattice DNA origami. The anode material of the source was chosen to be Mo, which has some drawbacks like a significantly lower primary intensity and a lower resolution in  $q$ . These disadvantages can be overcome by using a dual source of Mo and Cu anode microfocus tubes. The collimation is suitable for both X-ray energies and a linear stage could switch the sources. This concept of dual or even triple sources is commercially available from Xenocs in the Xeuss 2.0 system. Of course, an upgrade to a liquid metal source would have an even higher impact on the flux, but the cost of this system remains high compared to microfocus sources.

So far only hardware updates were considered, but there are also potential software upgrades. So far, the handling of the ROI is complicated as introduced in section 4.5. By replacing the MATLAB routine for the ROI with a Python script, for example, the speed of scans at the setup would increase significantly. The data quality would remain unchanged, but complex measurements would be sped up considerably. The following potential upgrade would be more substantial. Due to the rather low intensity of the source, the background intensity caused by window and air scattering is as low as the natural background of cosmic rays and alpha decay, which is shown in section 4.4.2. The natural background has a definite pattern, which can be distinguished from the scattering signal of the sample. Alpha decays, for example, lead to high-intensity rings. These outliers are already eliminated with an ImageJ function or by taking the median of consecutive measurements. Cosmic rays appear as lines in different lengths in the detector image. Thus, an algorithm could correct these intensities with neighboring intensities or mask affected image regions. For this, the time of a single measurement before this correction should be sufficiently short so that cosmic rays are brighter than the intensity originating from the sample. This algorithm

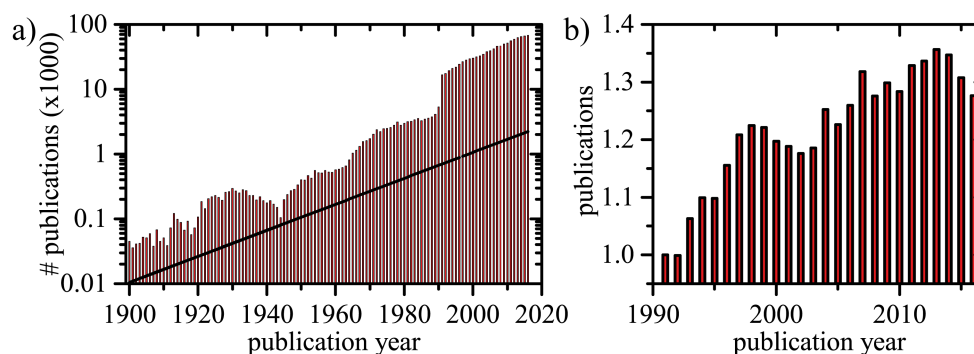


Figure 9.1: Number of publications with the topic 'X-ray' starting from 1900. a) The strong increase in 1990 is due to the start of coverage of conference proceedings in the database. The solid line shows the general growth of scientific publications. Note the logarithmic scale. b) Publications starting from 1991, which are corrected for the general growth of scientific publications and normalized to the number of publications in 1991. [source: Thomas Reuters (Web of Science)]

would lower the background and thus increase the S/B. Possible software implementations are available [181] or described in literature [182].

The advantage of an in-house SAXS setup is the chance to measure many different samples. If the results are not of sufficient quality, at least the preparation for a synchrotron measurement will be optimal. Furthermore, SAXS is a great tool in addition to direct measurement techniques like TEM or AFM. However, the value of SAXS alone is limited because the analysis relies on models, which have to be supported by complementary measurements. If the system is well known, which is the case for DNA origami, highly detailed information with high statistics will be able to be obtained. Furthermore, experiments can be conducted which are impossible with other methods, for example, the heating and cooling during the measurement of DNA origami or the variation of salt concentration. Thus, SAXS being a solution-based method outperforms other techniques as TEM or AFM. X-ray scattering is the most important tool to investigate crystalline materials on the nanoscale with its high sensitivity for lattices due to the appearance of Bragg peaks. With additional techniques like PL measurements and TEM a deep understanding of perovskite nanoplatelets could be achieved. For DNA origami crystals, a 3-dimensional growth could only be proven by X-ray scattering. Furthermore, very small sizes, for example, the thickness of a lipid bilayer, are inaccessible to other techniques and X-ray measurements can provide values down to Ångström resolution.

Even though the concept of X-ray diffraction is over 100 years old, the technique is still established in science and the advancement of X-ray facilities and equipment made new applications possible. This is mirrored in the number of publications on the topic "X-ray" shown in Figure 9.1. Interestingly, the second world war is responsible for the drop in publications during 1935 to

1945 and the upcoming synchrotron radiation in the 1960s fostered an increase of publications in those years. In the 1990s, the development of new X-ray sources by building dedicated synchrotron sources again caused an increase in the number of publications. This new impact highlights that with technology improvement of hard- and software even old techniques find new applications. Therefore, it is crucial to seize the opportunities which come with the development of technology. Modern in-house SAXS setups nowadays have a superior quality to the first synchrotron sources and enable complex experiments. With enhanced computing power, new theories and complex numerical analysis will develop. Furthermore, new fields such as nanotechnology evolved where X-ray scattering is an important technique for structural characterization which is proven by this thesis.





# APPENDIX

---

## A.1 FULL TEXT OF MANUSCRIPT 1

### 3D DNA origami crystals

Tao Zhang, Caroline Hartl, Stefan Fischer, Kilian Frank, Philipp Nickels,  
Amelie Heuer-Jungemann, Bert Nickel, Tim Liedl

Faculty of Physics & Center for NanoScience, LMU Munich, Geschwister-Scholl-  
Platz 1, 80539 München, Germany,

The manuscript is also available online: <https://arxiv.org/abs/1706.06965>

### 3D DNA origami crystals

Tao Zhang, Caroline Hartl, Stefan Fischer, Kilian Frank, Philipp Nickels, Amelie Heuer-Jungemann, Bert Nickel, Tim Liedl\*

Faculty of Physics and Center for Nanoscience (CeNS), Ludwig-Maximilians-Universität, Geschwister-Scholl-Platz 1, 80539 München, Germany

\*Email: tim.liedl@physik.lmu.de

Engineering shape and interactions of nanoscopic building blocks allows for the assembly of rationally designed macroscopic three-dimensional (3D) materials with spatial accuracy inaccessible to top-down fabrication methods<sup>1–3</sup>. Owing to its sequence-specific interaction, DNA is often used as selective binder to connect metallic nanoparticles into highly ordered lattices<sup>1,4–12</sup>. Moreover, 3D crystals assembled entirely from DNA have been proposed and implemented with the declared goal to arrange guest molecules in predefined lattices<sup>3,13</sup>. This requires design schemes that provide high rigidity and sufficiently large open guest space. We here present a DNA origami-based<sup>14,15</sup> “tensegrity triangle” structure<sup>16</sup> that assembles into a 3D rhombohedral crystalline lattice. We site-specifically place 10 nm and 20 nm gold particles within the lattice, demonstrating that our crystals are spacious enough to host e.g. ribosome-sized macromolecules. We validate the accurate assembly of the DNA origami lattice itself as well as the precise incorporation of gold particles by electron microscopy and small angle X-ray scattering (SAXS) experiments. Our results show that it is possible to create DNA building blocks that assemble into lattices with customized geometry. Site-specific hosting of nano objects in the transparent DNA lattice sets the stage for metamaterial and structural biology applications.

The spontaneous self-assembly process of rationally designed molecular building blocks enables the transition from nanoparticle to materials design<sup>17</sup>. One striking example is the programmed assembly of nanoparticles using DNA linkers<sup>1,4</sup>. Typically, spherical gold nanoparticles are modified with DNA oligonucleotides *via* covalent bonds between the gold surface and a terminal thiol residue on the DNA. The sequence-dependent hybridization of the DNA oligonucleotides mediates the formation of densely packed, 3D gold nanoparticle crystals where the connectivity and structural stability of the network is provided by the inorganic core particles. With this method, a variety of nanoparticle lattices with control over the particle-to-particle spacing and the lattice geometry have been implemented.<sup>5–8,10,11,18,19</sup>

An alternative approach for the site-specific positioning of nanoparticles is to use pre-assembled templates that by themselves provide structural rigidity. DNA self-assembly<sup>13,20</sup> allows the rational design of perfectly defined monomeric DNA nanostructures<sup>14,15,21</sup> and the precise tuning of monomer - monomer interaction strengths<sup>15,22,23</sup>. Polymerization of individual DNA motifs can result in designed macroscopic DNA crystals<sup>3,24,25</sup> and in large two dimensional templates that also have been employed for the 2D arrangement of guest molecules with high accuracy<sup>26–32</sup>. We here show the assembly of a crystalline 3D lattice purely based on DNA origami<sup>14,15</sup> building blocks where the lattice geometry is fully determined by the origami monomer design. Note, this approach does not rely on metal colloids and in turn, the lattice is optically transparent and only weakly scattering in the X-ray domain. We demonstrate that this type of construction allows for large unit cells and for the site-specific positioning of nano objects of up to 30 nm diameter.

For our purposes, the DNA origami building block should bear the following features: (i) high structural rigidity, (ii) polymerizability along three axes in space, and (iii) long edges to provide a large unit cell volume to host guest particles. The tensegrity triangle motif introduced by Chengde Mao & Nadrian Seeman *et al.*<sup>3,16</sup> fulfills the first two requirements but lacks space to accommodate large guest objects<sup>33</sup>. We thus built a magnified version of the tensegrity triangle with DNA origami (**Figure 1**)<sup>34</sup>. Each of the three edges is a 14-helix bundle with a designed length of 67 nm and a diameter of 12.5 nm. The three struts are folded from a single-stranded phage-derived scaffolding DNA (8634 nt) together with ~ 235 synthetic oligonucleotides in a temperature

annealing ramp from 65 °C to 4 °C. Scaffold crossovers interconnect all struts in an over-under, over-under fashion (**Supplementary Figure S1**) predetermining the orientation of each bundle towards each other. One of the 14-helix bundles contains a “seam” where the scaffold strand does not continue through the entire edge but is closed by oligonucleotides only (inset in **Figure 1**). By choosing identical cross section, axial orientation, and staggering of the three struts, the origami monomer can polymerize *via* blunt-end stacking into a rhombohedral lattice with the unit cell parameters  $a = b = c = 67$  nm and  $\alpha = \beta = \gamma = 100^\circ (\neq 90^\circ)$  (**Figure 1**). **Supplementary Figure S1** and **S2** show design details and **Supplementary Figure S3** displays different views onto the rhombohedral lattice. Note that all three upper ends (blue) match all lower ends (orange) with similar interaction strength imparting rotational freedom of the triangle around its center point (**Figure 1b**).

First, the monomeric DNA origami structures were thermally annealed starting at 65 °C (for experimental details see **Supplementary Note S1**). To avoid kinetic trapping of the struts in an undesired conformation, the oligonucleotides connecting the seam (**Supplementary Figure S2**) were injected only midway through the folding process at 52 °C. The folded triangles were purified from excess oligonucleotides by PEG precipitation before analysis by transmission electron microscopy (TEM) imaging and polymerization (**Figure 2a**). We observed that the presence of the seam oligonucleotides during the entire folding process leads to the formation of mainly deformed structures, possibly resulting from prematurely closed seams trapping the triangular struts in wrong geometries. Injection of the seam connectors at lower temperatures improved the yield of correctly folded triangles to ~ 60% (**Supplementary Figure S4**). While all misfolded objects featured three edges, they did not exhibit the designed three-fold symmetry (**Figure 2a** asterisk). Note that due to their structural similarity to the targeted design, these defective objects could not be removed during the purification steps but remained in solution during crystal growth.

To initiate the growth of the 3D lattices, “polymerization strands” were added in a ten-fold molar excess over the purified monomers. These oligonucleotides completed the formation of each of the ends of the struts and thus established shape-complementary blunt ends. The sample mix was incubated at a constant temperature of 47 °C for 90 hours and then deposited and dried on TEM grids. SEM images of origami lattices that randomly adsorbed to the grid surface show the morphology of a regular, hexagonal pattern with a center-to-center spacing between the monomers of 64 nm, which deviates slightly from the designed spacing of 67 nm and indicates flattening of the dried 3D objects on the substrate (**Figure 2b - f**). TEM images reveal the same hexagonal pattern and spacing (**Supplementary Figure S5**). Due to the obtuse interaxial angle of the building blocks, the lateral extensions along the [111] plane exceeds those of all other planes. Consequently we predominantly observe hexagonal lattices corresponding to a top view perspective of the [111] plane. For visual comparison **Supplementary Figure S6** shows 3D renderings of the designed crystals at different viewing angles. The magnified inset of the building blocks shown in **Figure 2b** confirms the over-under orientation of the struts and the left-handed chirality of the triangle as designed. Low magnification SEM images reveal the polycrystalline nature of lattice patches that are tens of micrometers in size with single domains spanning several micrometers (**Figure 2d**, **Supplementary Figure S5**). Close-up views display the multiple layers of the lattice and indicate its collapsed state on the dry substrate (**Figure 2e**). Of particular interest is the observation that although the defective triangles are present during the growth process they are not incorporated in the lattice patches but appear only in their periphery (**Figure 2f**). As the defective structures lack the designed symmetry, their overall binding energy does not suffice to stabilize their integration in the lattice at the elevated temperatures during lattice growth. Correctly folded monomers, instead, can replace the defective ones, which permits the self-healing growth of the origami lattices. After growth and at ambient temperatures, however, misfolded triangles can bind to any border of the lattice with just one or two connecting sites. Given the limited yield of correctly folded monomers, the observed assembly of macroscopic origami lattices indicates the effectiveness of the self-correcting processes and an overall robust lattice growth.

To demonstrate the precise placement of guest molecules in our origami lattices, we attached gold particles

of different sizes at the center of each triangular origami monomer (**Figure 3a**). This choice of position preserves the symmetry upon incorporation in the lattice and therefore maintains the rhombohedral lattice type. The particle-bearing building blocks were prepared and purified as described elsewhere<sup>35</sup>. Consecutive lattice growth occurred under equal conditions as for the pure DNA origami lattices. Figure 3B shows again the hexagonal pattern formed by origami triangles but this time with 10 nm or 20 nm gold nanoparticles groupings at the positions expected in this lattice orientation. Here the number of nanoparticles per group indicates the number of origami layers in the lattice. Due to the strong electron scattering properties of the gold particles only a limited penetration depth into the dense samples can be achieved and perfect hexagonal patterns can be observed for not more than a few lattice layers. A different type of nanoparticle pattern – rows of particles – results from adsorption of the lattice in an orientation different from the [111] plane (**Figure 3c, Supplementary Figure S7**). Low magnification TEM images illustrate the high quality of the particle-hosting lattices (**Figure 3d**). When placing gold nanoparticles larger than 10 nm into the monomer building blocks, we observe both in TEM and SEM images the same nanoparticle lattices as for the 10 nm particles. Clear patterns, however, only become visible at the edges of the assemblies due to the even stronger scattering of the larger particles and considerable overlap of the multiple layers (**Figure 3e, Supplementary Figure S8**).

To gain more insight into the native structure of the lattices in solution, we performed small angle X-ray scattering (SAXS) measurements for triangular origami monomers, origami lattices, and origami lattices hosting gold nanoparticles of different sizes. The scattering intensities for all samples are shown in **Figure 4a** and **Supplementary Figure S9**. Using an analytical model of three rigid cylinders each representing the 14-helix-bundles in the triangular structure we found the fitted dimensions (length=65 nm, radius=6.2 nm) to be in very good agreement with the design of the monomer. The extracted inter-helical distance of 2.8 nm matches that of previously published values for multihelical DNA bundles<sup>36</sup> and a constant structure factor indicates the absence of assembly into any structure of higher order. The scattering intensities of the bare origami lattice reproduce the characteristics of the triangular monomer. Additional Bragg peaks confirm the three dimensional assembly as designed. Due to the higher scattering contrast of gold, SAXS intensities of spherical gold nanoparticles placed at predefined positions within the DNA lattices predominantly show Bragg peaks indicating the lattice arrangement on top of the characteristic scattering features of spheres. **Figure 4b** shows the extracted structure factor of the samples in comparison to a model fit<sup>37</sup> representing a rhombohedral lattice with a lattice constant of  $a = 65$  nm and  $\alpha = 110^\circ$  for all three assemblies. More importantly, for both 10 nm and 20 nm gold nanoparticle lattices, the parameters match the ones of the pure origami lattices, which demonstrates the robustness of the lattice formation in the presence of large guest molecules. Individual peak heights and peak positions, however, differ between the pure DNA lattice and the decorated lattices due to the anisotropic nature of the triangular DNA origami monomer compared to the spherical gold particles, which is fully captured by our models (**Supplementary Note S2**). The measured unit cell of our pure DNA lattice has a volume of  $\sim 1.84 \times 10^5$  nm<sup>3</sup>, which is about 100 times larger than for previously reported DNA crystals<sup>3</sup> (**Supplementary Note S3**) and allows hosting guest molecules of the size of the ribosome within the origami lattice template.

In summary, we demonstrated the poly-crystalline assembly of a triangular DNA origami nanostructure into a rhombohedral lattice. With its large and rigid unit cell it can serve as a three dimensional template for the co-crystallisation of guest molecules as demonstrated here with gold nanoparticles. Further improved monomer quality and large-scale screening of crystallization conditions will potentially lead to the formation of DNA origami single-crystals that can host a wide variety of components. Importantly, the use of rigid DNA origami building blocks permits the variable positioning of guest molecules, which would allow different “guest lattices” within the same framework and even dynamically reconfigurable lattices. Combined with the optical transparency of the DNA frameworks, self-assembled metamaterials with precisely, 3D-arranged metamolecules become feasible. Furthermore our DNA lattices are almost invisible under X-ray and electron irradiation, allowing for structural analysis of any incorporated guest molecule. With a view on proteins, their 3D arrangement could open up new

paths to optical super resolution-based structure analysis and CryoEM tomography.<sup>38</sup>

#### References.

1. Mirkin, C. A., Letsinger, R. L., Mucic, R. C., Storhoff, J. J. & others. A DNA-based method for rationally assembling nanoparticles into macroscopic materials. *Nature* **382**, 607–609 (1996).
2. Whitesides, G. M. & Grzybowski, B. Self-assembly at all scales. *Science* **295**, 2418–2421 (2002).
3. Zheng, J. *et al.* From molecular to macroscopic via the rational design of a self-assembled 3D DNA crystal. *Nature* **461**, 74–77 (2009).
4. Alivisatos, A. P. *et al.* Organization of nanocrystal molecules' using DNA. *Nature* **382**, 609–611 (1996).
5. Nykypanchuk, D., Maye, M. M., van der Lelie, D. & Gang, O. DNA-guided crystallization of colloidal nanoparticles. *Nature* **451**, 549–552 (2008).
6. Park, S. Y. *et al.* DNA-programmable nanoparticle crystallization. *Nature* **451**, 553–556 (2008).
7. Macfarlane, R. J. *et al.* Nanoparticle superlattice engineering with DNA. *Science* **334**, 204–208 (2011).
8. Auyeung, E. *et al.* DNA-mediated nanoparticle crystallization into Wulff polyhedra. *Nature* **505**, 73–77 (2014).
9. Tian, Y. *et al.* Prescribed nanoparticle cluster architectures and low-dimensional arrays built using octahedral DNA origami frames. *Nat. Nanotechnol.* **10**, 637–644 (2015).
10. Tian, Y. *et al.* Lattice engineering through nanoparticle-DNA frameworks. *Nat. Mater.* **15**, 654–661 (2016).
11. Liu, W. *et al.* Diamond family of nanoparticle superlattices. *Science* **351**, 582–586 (2016).
12. Jones, M. R., Seeman, N. C. & Mirkin, C. A. Programmable materials and the nature of the DNA bond. *Science* **347**, 1260901 (2015).
13. Seeman, N. C. Nucleic acid junctions and lattices. *J. Theor. Biol.* **99**, 237–247 (1982).
14. Rothmund, P. W. K. Folding DNA to create nanoscale shapes and patterns. *Nature* **440**, 297–302 (2006).
15. Douglas, S. M. *et al.* Self-assembly of DNA into nanoscale three-dimensional shapes. *Nature* **459**, 414–418 (2009).
16. Liu, D., Wang, M., Deng, Z., Walulu, R. & Mao, C. Tensegrity: Construction of Rigid DNA Triangles with Flexible Four-Arm DNA Junctions. *J. Am. Chem. Soc.* **126**, 2324–2325 (2004).
17. Whitesides, G. M. & Boncheva, M. Beyond molecules: Self-assembly of mesoscopic and macroscopic components. *Proc. Natl. Acad. Sci.* **99**, 4769–4774 (2002).
18. Jones, M. R. *et al.* DNA-nanoparticle superlattices formed from anisotropic building blocks. *Nat. Mater.* **9**, 913–917 (2010).
19. Auyeung, E. *et al.* Synthetically programmable nanoparticle superlattices using a hollow three-dimensional spacer approach. *Nat. Nanotechnol.* **7**, 24–28 (2012).
20. Seeman, N. C. DNA in a material world. *Nature* **421**, 427–431 (2003).
21. Fu, T. J. & Seeman, N. C. DNA double-crossover molecules. *Biochemistry* **32**, 3211–3220 (1993).
22. Woo, S. & Rothmund, P. W. K. Programmable molecular recognition based on the geometry of DNA nanostructures. *Nat. Chem.* **3**, 620–627 (2011).
23. Gerling, T. *et al.* Dynamic DNA devices and assemblies formed by shape-complementary, non-base pairing 3D components. *Science* **347**, 1446–1452 (2015).
24. Simmons, C. R. *et al.* Construction and Structure Determination of a Three-Dimensional DNA Crystal. *J. Am. Chem. Soc.* **138**, 10047–10054 (2016).
25. Stahl, E., Praetorius, F., de Oliveira Mann, C. C., Hopfner, K.-P. & Dietz, H. Impact of Heterogeneity and Lattice Bond Strength on DNA Triangle Crystal Growth. *ACS Nano* **10**, 9156–9164 (2016).
26. Winfree, E., Liu, F., Wenzler, L. A. & Seeman, N. C. Design and self-assembly of two-dimensional DNA crystals. *Nature* **394**, 539–544 (1998).
27. Yan, H., Park, S. H., Finkelstein, G., Reif, J. H. & LaBean, T. H. DNA-Templated Self-Assembly of Protein

- Arrays and Highly Conductive Nanowires. *Science* **301**, 1882–1884 (2003).
28. Zheng, J. *et al.* Two-dimensional nanoparticle arrays show the organizational power of robust DNA motifs. *Nano Lett.* **6**, 1502–1504 (2006).
  29. Liu, W., Zhong, H., Wang, R. & Seeman, N. C. Crystalline two-dimensional DNA-origami arrays. *Angew. Chemie Int. Ed.* **123**, 278–281 (2011).
  30. Aghebat Rafat, A., Pirzer, T., Scheible, M. B., Kostina, A. & Simmel, F. C. Surface-Assisted Large-Scale Ordering of DNA Origami Tiles. *Angew. Chemie Int. Ed.* **53**, 7665–7668 (2014).
  31. Ke, Y. *et al.* DNA brick crystals with prescribed depths. *Nat. Chem.* **6**, 994–1002 (2014).
  32. Wang, P. *et al.* Programming Self-Assembly of DNA Origami Honeycomb Two-Dimensional Lattices and Plasmonic Metamaterials. *J. Am. Chem. Soc.* **138**, 7733–7740 (2016).
  33. Hao, Y. *et al.* A device that operates within a self-assembled 3D DNA crystal. *Nat Chem advance on*, (2017).
  34. Douglas, S. M. *et al.* Rapid prototyping of 3D DNA-origami shapes with caDNAo. *Nucleic Acids Res.* **37**, 5001–5006 (2009).
  35. Schreiber, R. *et al.* Hierarchical assembly of metal nanoparticles, quantum dots and organic dyes using DNA origami scaffolds. *Nat. Nanotechnol.* **9**, 74–78 (2014).
  36. Fischer, S. *et al.* Shape and Interhelical Spacing of DNA Origami Nanostructures Studied by Small-Angle X-ray Scattering. *Nano Lett.* **16**, 4282–4287 (2016).
  37. Yager, K. G., Zhang, Y., Lu, F. & Gang, O. Periodic lattices of arbitrary nano-objects: modeling and applications for self-assembled systems. *J. Appl. Crystallogr.* **47**, 118–129 (2014).
  38. Martin, T. G. *et al.* Design of a molecular support for cryo-EM structure determination. *Proc. Natl. Acad. Sci.* **113**, E7456–E7463 (2016).

#### Acknowledgements.

We thank Susanne Kempter for her help on TEM imaging and Philipp Altpeter on SEM imaging. We thank Alexander M. Maier, Iain MacPherson, and Florian Schüder for helpful discussions. We acknowledge support during beam time at DESY (P08, Uta Ruett) and Elettra (Austrian SAXS, Heinz Amenitsch). This work was supported by the Deutsche Forschungsgemeinschaft through the SFB grant 1032 (TPA6 and A7), the Nanosystems Initiative Munich and the European Research Council grant agreement no. 336440 for ORCA (Optical Responses Controlled by DNA Assembly). This work benefitted from SasView software, originally developed by the DANSE project under NSF award DMR-0520547. We confirm no competing financial interests.

#### Author Contributions.

T.Z., B.N. and T.L. designed the research. T.Z., P.N., and T.L. designed the DNA structure. T.Z., C.H., A.H.-J. prepared the assemblies. C.H., S.F., K.F., and B.N. performed the SAXS measurements. S.F., K.F., C.H. and B.N. analyzed the SAXS data. T.Z., S.F., K.F., and C.H. prepared the figures. C.H., T.Z., B.N. and T.L. wrote the manuscript. All authors discussed the results and edited the manuscript.

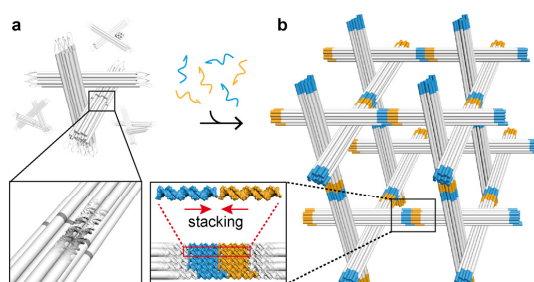


**Figure 1.** Schematic illustration of the triangular DNA origami building block design and assembly. **a**, The three 14-helix bundles of equal lengths are interconnected at defined positions and form a constrained triangular structure. A scaffold seam region is bridged by “connection” oligonucleotides (inset). **b**, Addition of oligonucleotides completing the struts results in the formation of self-matching shape complementary blunt ends. The three-fold symmetry facilitates the polymerization of the triangular monomers into a rhombohedral lattice *via* stacking interactions (inset). Details on the assembly process and additional 3D views are shown in **Supplementary Figure S1 & S2**.

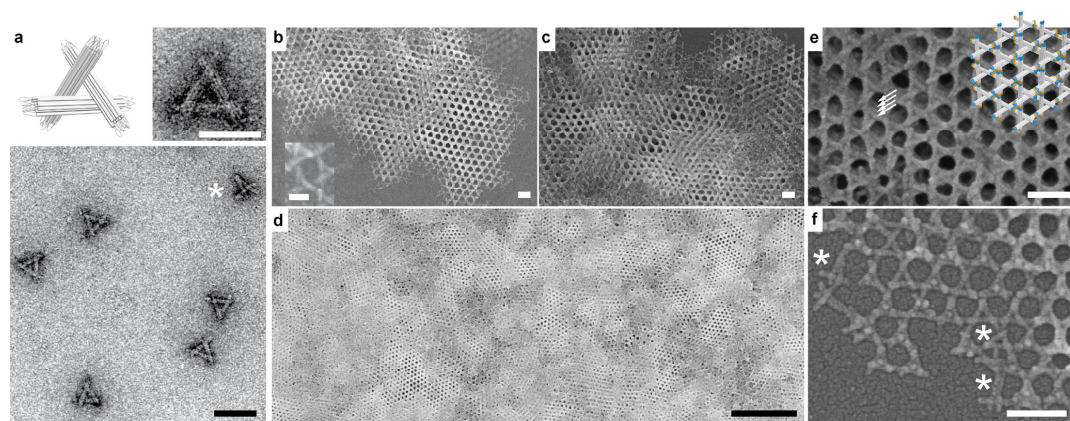


**Figure 2.** DNA origami lattices. **a**, TEM images of purified triangular DNA origami structures after purification and before addition of polymerization oligonucleotides that would initiate lattice growth. The asterisk points out a misfolded monomer. **b-f**, SEM images of DNA origami lattices. The inset in panel **b** exemplifies the left-handed over-under design. Panel **c** reveals the three-dimensionality of the assemblies and their polycrystallinity becomes apparent in the wide-field view shown in panel **d**. Although the lattices collapse on the imaging substrates during drying, the multiple layers and the original geometry can be inferred in a magnified view (white arrows, panel **e**). **f**, SEM image showing the border of a lattice with asterisks indicating defective structures that were expelled from the lattice during the growth process and can only bind later at lower temperatures to the periphery. Scale bars in **a**, **b**, **c**, **e**, and **f**: 100 nm, **d**: 1  $\mu$ m, insets in **a** and **b**: 50 nm.

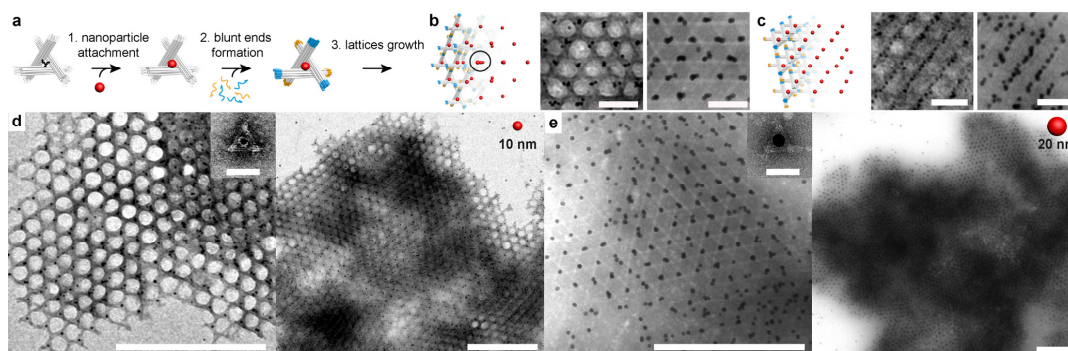


**Figure 3.** Hosting of gold nanoparticles in DNA origami lattices. **a**, Workflow to prepare gold nanoparticle lattices: 1) Folded and purified DNA origami triangles are incubated with gold particles overnight and then purified from excess particles. 2) Addition of the polymerization oligonucleotides to initiate the lattice growth process. 3) Incubation at 47°C for 3-4 days yields assembled host-guest lattices. **b**, **c**, Model views and TEM images of DNA origami lattice hosting 10 (left) or 20 nm (right) gold nanoparticles. The number of particles per grouping indicates the number of lattice layers overlapping at the respective points (black circle in **b**). **d**, **e**, Wide-field TEM images of origami lattices hosting 10 nm (**d**) and 20 nm (**e**) gold nanoparticles. Scale bars in **b** and **c**: 100 nm; **d** and **e** 500 nm, insets: 50 nm.

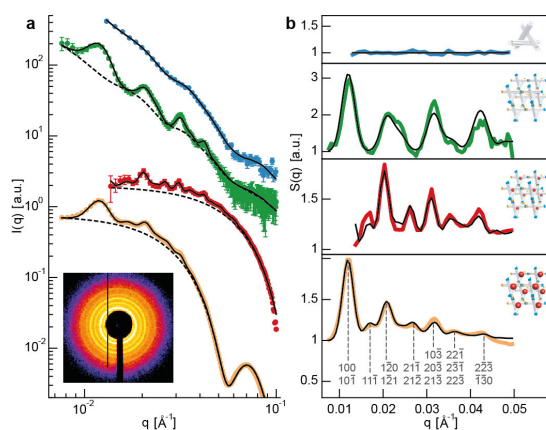


**Figure 4.** **a**, SAXS intensities of triangular DNA origami monomers (blue), origami lattices (green), and origami lattices hosting 10 nm (red) and 20 nm (orange) gold nanoparticles (vertically offset). Solid black lines: Model fits of total intensity. Dotted black lines: Simulated form factor intensities neglecting the lattice structure factors. Inset: SAXS pattern of 10 nm gold-decorated sample. **b**, The monomer SAXS intensity (blue) divided by the fit yields a constant, indicating the absence of a lattice. Lattice structure factors from SAXS data (green, red, yellow) obtained by subtraction of background and division by the form factor intensity (vertically offset). Black lines: Model fits assuming a rhombohedral unit cell ( $a = 65$  nm,  $\alpha = 110^\circ$ ). Dashed lines with Miller indices label selected Bragg peaks.

A.1.1 *Supplementary Information for Manuscript 1*

## Supplementary Information

## 3D DNA origami crystals

Tao Zhang, Caroline Hartl, Stefan Fischer, Kilian Frank, Philipp Nickels,  
Amelie Heuer-Jungemann, Bert Nickel, Tim Liedl

Faculty of Physics & Center for NanoScience, LMU Munich, Geschwister-Scholl-  
Platz 1, 80539 München, Germany,

## Supplementary Notes S1: Materials and Methods

### Design and formation of DNA origami.

*Design.* The triangular tensegrity origami was designed using caDNAo (design schematics in **Supplementary Figure S1, S2**)[1]. The structure consists of three 14 helix bundles (14HBs) packed on a honeycomb lattice with a diameter of about 12.5 nm. These three 14HBs were designed to be of the same length (199 bp) and display self-matching shape complementary blunt ends. The 14HBs were interconnected at selected positions by forced crossovers with three bases of scaffold spacers. In order to avoid topological traps of the struts in undesired geometries, a “seam” was introduced into of the 14HBs. Here the scaffold does not run from one end of the strut to the other but loops back in the middle of the strut for each pair of helices (**Supplementary Figure S1b**). The seam is closed by staple oligonucleotides. Groups of staple strands were divided into “connection” oligonucleotides (closing the seam), “polymerization” oligonucleotides (completing the ends of all struts and thus enabling blunt end stacking), handle oligonucleotides (for capturing the gold nanoparticles) and “core” oligonucleotides (all other strands).

*Folding and Purification.* DNA origami structures were prepared by mixing core and handles staples (100 nM each, MWG Eurofins), and the circular DNA scaffold strand p8634 (12.5 nM, produced in house) in 1x TE-Mg<sup>2+</sup> buffer (10 mM Tris, 1 mM EDTA, 18 mM MgCl<sub>2</sub>). The mixture was thermally annealed from 65 °C to 4 °C over 35 h (15 min at 65 °C, cooling to 58 °C with a cooling rate of -1 °C per 5 min, 58 °C to 35 °C with rate of -1 °C per 1 h, and from 35 °C to 4 °C with rate of -1 °C per 5 min). Connection staples were injected into the folding mixture during the annealing process at 52 °C (**Supplementary Figure S4**). Subsequently the folded DNA nanostructures were purified from excess DNA staples by agarose gel electrophoresis stained with 1x Sybr Safe (1 % agarose in 1x TAE 11 mM MgCl<sub>2</sub> buffer; 6.5 V/cm for 2 h) or by polyethylene glycol (PEG) precipitation([2], [3]). For agarose gel purification, samples were run in 1 % agarose gels containing 1x Tris-acetate buffer (10 mM Tris, 10 mM acetic acid), 11 mM MgCl<sub>2</sub> and 1x SybrSafe (Thermo Fisher Scientific). All gels were cooled in ice water baths. Samples were separated at 6.5 V/cm for 2 h following excision of the bands and recovery of the products by squeezing the band between two glass slides and collecting the resulting liquid droplet with a pipet. For PEG precipitation, equal volumes of 2x PEG buffer (15 % (w/v) PEG-8000, 2x TE, 500 mM NaCl, 20 mM Mg<sup>2+</sup>) and unpurified folding solution were mixed and centrifuged for 30 min at 16,000 rcf. The resulting pellet was re-suspended in 1x TAE, 11 mM MgCl<sub>2</sub> buffer and subsequently shaken at 650 rpm, 30 °C for 24 h in order to re-disperse the origami structures.

### Formation of DNA origami-gold nanoparticle conjugates.

*Functionalization of gold nanoparticles with DNA.* Gold nanoparticles (AuNPs) of 10 nm, 20 nm and 30 nm (BBI International) were functionalized with 5'-thiolated 19T single-stranded DNA (Biomers) following published methods[4]. Briefly, TCEP (tris(2-carboxyethyl)phosphine) treated thiolated DNA was added in excess (200x molar excess for 10 nm AuNPs, 800x for 20 nm AuNPs, and 1800x for 30 nm AuNPs) to AuNPs. The mixture was incubated at room temperature for 24 hours before slowly increasing the salt concentration to 500 mM by addition of 1 M NaCl over a period of 6 h. DNA-modified gold nanoparticles were then purified using Amicon centrifugation filters (100K MW cut-off).

*Conjugation of gold nanoparticles to DNA origami.* Six staple oligonucleotides at the center of the triangular origami structure were extended from the structure with 19A bases serving as handles for attachment of the gold nanoparticles (one nanoparticle per origami nanostructure). An 8x molar excess of DNA-AuNPs was added to the DNA origami structures and incubated overnight. The resulting DNA origami-gold nanoparticle conjugates were purified from excessive gold nanoparticles in 1 % agarose gels containing 1x Tris-acetate, 11 mM MgCl<sub>2</sub> buffer, cooled in an ice-bath. Samples were separated at 7 V/cm for 1.5 h. Bands were excised from the gel and recovered as described previously.

### Polymerization of DNA origami into 3D lattice.

*Polymerization.* Polymerization oligonucleotides were mixed at 10x molar excess with purified bare triangular origami structures or with purified structures carrying gold nanoparticles. The buffer was then brought to 1x TAE and 15 mM MgCl<sub>2</sub>. The polymerization mixture was incubated at a constant temperature of 47 °C for 3-4 days in a thermocycler. Owing to the different purification procedures and varying purification yields, the starting concentration of origami monomer for pure DNA origami lattice growth was ~ 25 nM (PEG purified), while for lattices with gold particles the starting concentration of the gold-carrying nanoparticles ranged between 1 nM and 3 nM (gel purified).

### Characterization techniques.

*TEM.* TEM imaging of DNA origami lattices was carried out using a JEM-1011 transmission electron microscope (JEOL) operating at 80 or 100 kV. For sample preparation 10 µL of polymerized DNA origami structures were deposited on glow-discharged TEM grids (formvar/carbon-coated, 300 mesh Cu; TED Pella, Inc; prod no. 01753 - f) for 1 h. For pure origami lattices and origami lattices containing 10 or 20 nm gold nanoparticles, grids were furthermore quickly washed once with 0.1 % uranyl acetate solution (5 µL) and immediately afterwards stained with 0.1 % uranyl acetate solution (5 µL) for 10 s. For origami lattices hosting 30 nm gold nanoparticles and the lattices for taking SEM images, grids were washed two times with water for 2 s.

*SEM.* The TEM grids were directly used for SEM imaging after 10 s sputtering using an Edwards Sputtercoater S150B 1990. The sputter target contained 60 % gold and 40 % palladium. Process parameters used for sputtering were 7 mbar Ar, 1.1 kV, 35 mA. 10 s sputtering results in the deposition of layer of gold/palladium with a thickness of a few nm. The Au/Pd deposited TEM grids were directly fixed on the sample holder with carbon tape for SEM imaging with a Carl Zeiss LEO DSM 982 GEMINI (containing a source of thermal field emitting (TFE) cathode (1997) and a detector of LEO High Efficiency In-Lense Secondary Electrons). Beam parameters for taking imaging were set as 5 kV acceleration voltage and 30 µm aperture.

*SAXS.* The SAXS data were measured at three different sources. All sample to detector distances and beam centers were calibrated with silver behenate. The scattering data of the monomer was measured at an in-house X-ray source, which is described in detail in the literature[5]. The data of the DNA origami lattice decorated with 10 nm gold nanoparticles and the undecorated DNA origami lattices shown in **Fig. S9** were measured at the beamline P08 at PETRA III (DESY) in Hamburg. A Perkin Elmer flat panel XRD 1621 with 2048 x 2048 pixels with 200 µm size served as detector. The solutions of polymerized sample were loaded in 2 mm quartz capillaries. The measurement was carried out at 20 keV in order to avoid radiation damage of the sample. The data of the DNA origami lattice decorated with 20 nm gold nanoparticles and the undecorated DNA origami lattice shown in Figure 4 were measured at the SAXS beamline at ELETTRA in Trieste. The solutions of polymerized sample were loaded in 1 mm quartz capillaries and measured at 8 keV X-ray energy. A Dectris Pilatus 3 1M CMOS detector with 981 x 1043 pixels with 172 µm pixel size served as detector.

### **Supplementary Notes S2: SAXS data analysis.**

The scattering intensity is shown as a function of scattering vector  $q = \frac{4\pi}{\lambda} \sin \theta$  where  $\lambda$  is the wavelength of the monochromatic X-ray radiation and  $\theta$  is one half of the scattering angle.

The scattering intensity of the DNA origami monomer was modeled as  $I(q) = P(q) + bg(q)$ . To obtain the isotropic form factor intensity  $P(q)$  the analytical expression of the form factor of a rigid cylinder representing a 14 helix bundle was added up once for each bundle. The different axis directions of the bundles inside a monomer were taken into account by a coordinate transform and the spatial offset of their centers by phase factors. Orientational averaging was carried out by numeric integration.

Following the procedure described in *Ref.* [6], the scattering intensities of the lattice assemblies were modeled as

$$I(q) = P(q) \cdot S(q) + bg(q)$$

where  $P(q)$  is the isotropic form factor intensity of the particle in the unit cell. For the origami lattice,  $P(q)$  equals the monomer form factor intensity described above. For the decorated lattices, the gold particle form factor intensity was found to dominate the total intensity due to the higher scattering contrast of gold compared to DNA. Therefore, the isotropic form factor intensity of a sphere was used as  $P(q)$  in these cases.  $S(q)$  is the structure factor and  $bg(q)$  a background contribution consisting of a constant term and a  $q$ -dependent term accounting for excess oligonucleotides in the sample solution. The latter term was modeled by a Debye model representing Gaussian polymer chains.

The structure factor  $S(q)$  was computed as

$$S(q) = \frac{cZ_0(q)}{P(q)}G(q) + 1 - \beta(q)G(q).$$

$c$  is a scaling constant.  $Z_0(q)$  is the lattice factor, representing the structural scattering in terms of Bragg peaks.

$$Z_0(q) = \frac{1}{q^2} \sum_{hkl}^{m_{hkl}} \left| \sum_{\vec{r}_j} F_j(\vec{q}_{hkl}) \cdot e^{-i\vec{q}_{hkl} \cdot \vec{r}_j} \right|^2 \cdot L(q - q_{hkl})$$

$m_{hkl} = 7$  is the maximum absolute value of the Miller indices  $hkl$  which were considered.  $F_j(\vec{q}_{hkl})$  is the form factor of the particle at position  $\vec{r}_j$  in the unit cell, taking into account its orientation.  $L(q - q_{hkl})$  is a Gaussian peak-shape function.  $\vec{q}_{hkl}$  is the scattering vector corresponding to a Bragg peak with Miller indices  $hkl$ . In the case of the origami lattice it was computed as  $\vec{q}_{hkl} = h\vec{b}_1 + k\vec{b}_2 + l\vec{b}_3$  by calculating the reciprocal lattice vectors  $\vec{b}_1, \vec{b}_2, \vec{b}_3$  to the rhombohedral real lattice vectors spanned by the 14 helix bundles. In the case of the gold-decorated lattices the formula

$$q_{hkl} = \frac{2\pi}{a} \sqrt{\frac{(h^2 + k^2 + l^2)\sin^2 \alpha + 2(hk + kl + lh)(\cos^2 \alpha - \cos \alpha)}{1 - 3\cos^2 \alpha + 2\cos^3 \alpha}}$$

for a rhombohedral real space lattice with lattice constant  $a$  and unit cell angle  $\alpha$  was used.

For anisotropic particles the form factor intensity which enters the lattice factor via  $|F(\vec{q}_{hkl})|^2$  differs from the isotropic form factor intensity  $P(q)$ . The orientation of the particle with respect to the unit cell therefore becomes important. This needs to be considered for the origami lattice, where the form factor intensity of the anisotropic triangular monomer enters into the total scattering. This orientation effect on the peak heights of the structure factor is illustrated in **Supplementary Figure S9 c, d** and **e**. The fitted peak heights and positions agree with the measured scattering intensity when taking into account the orientation of the DNA origami monomer in the unit cell. If the orientation is neglected and  $|F(\vec{q}_{hkl})|^2$  is replaced by the isotropic form factor intensity  $P(q)$  the peak heights are not correctly reproduced and additional peaks appear in the simulated curve.

$G(q) = e^{-\sigma_d^2 a^2 q^2}$  models lattice disorder which leads to a damping of higher order peaks and a diffuse baseline in the structure factor.  $\sigma_d$  is the r.m.s. displacement of particle position normalized to the lattice constant  $a$ .  $\beta(q) = e^{-(\sigma_R \cdot R)^2 q^2}$  accounts for particle size polydispersity.  $(\sigma_R \cdot R)$  is the r.m.s. variation of the size of the particles, i.e. the origami monomers in the case of the origami lattice and the gold particles in the case of the decorated lattices.

All models were written as C code in the software package SasView (<http://www.sasview.org/>). Fit parameters for the total scattering intensity  $I(q)$  were obtained by running the software-internal population-based DREAM algorithm. Already during fitting all model intensity curves were smeared with a pinhole function adapted to the respective instrumental resolution of the data.

All experimental structure factors shown were obtained by subtracting the background  $bg(q)$  from the scattering intensity data and dividing the result by the form factor intensity  $P(q)$ . Both  $bg(q)$  and  $P(q)$  as well as the modeled structure factor  $S(q)$  shown for comparison were obtained from one fit to the total scattering intensity  $I(q)$ .

For both undecorated and decorated origami lattices (**Supplementary Figure S9 f-i**) the sharpest and highest Bragg peaks are observed in the samples assembled at 47 °C. Sharp and high peaks indicate the presence of large crystallites and corroborate the observations from TEM images. Therefore this incubation temperature was chosen for all following studies and used for all crystalline samples presented in this work. The Scherrer equation

$$L_c = \frac{2\pi K}{\Delta q}$$

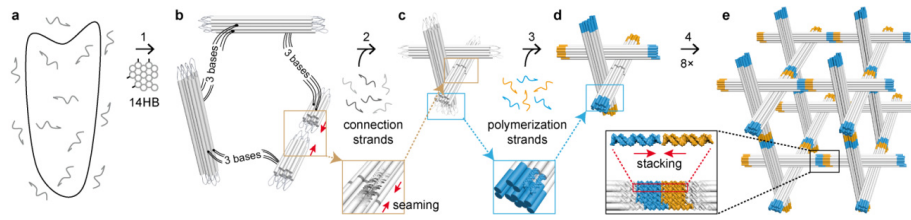
gives an estimate of the crystallite size  $L_c$ , where K is a shape factor of the order of 1 and  $\Delta q$  is the full width at half maximum of a diffraction peak. The dominating contribution to the peak width in all SAXS data shown is from the instrument resolution function  $\Delta q \approx 1 \cdot 10^{-3} \text{ \AA}^{-1}$  which was calculated from the beam size and divergence as well as the detector pixel size. Applying Scherrer equation yields a lower limit to the linear crystallite size of at least  $6300 \text{ \AA} \approx 10$  unit cells.

### Supplementary Notes S3: Cavity size calculation.

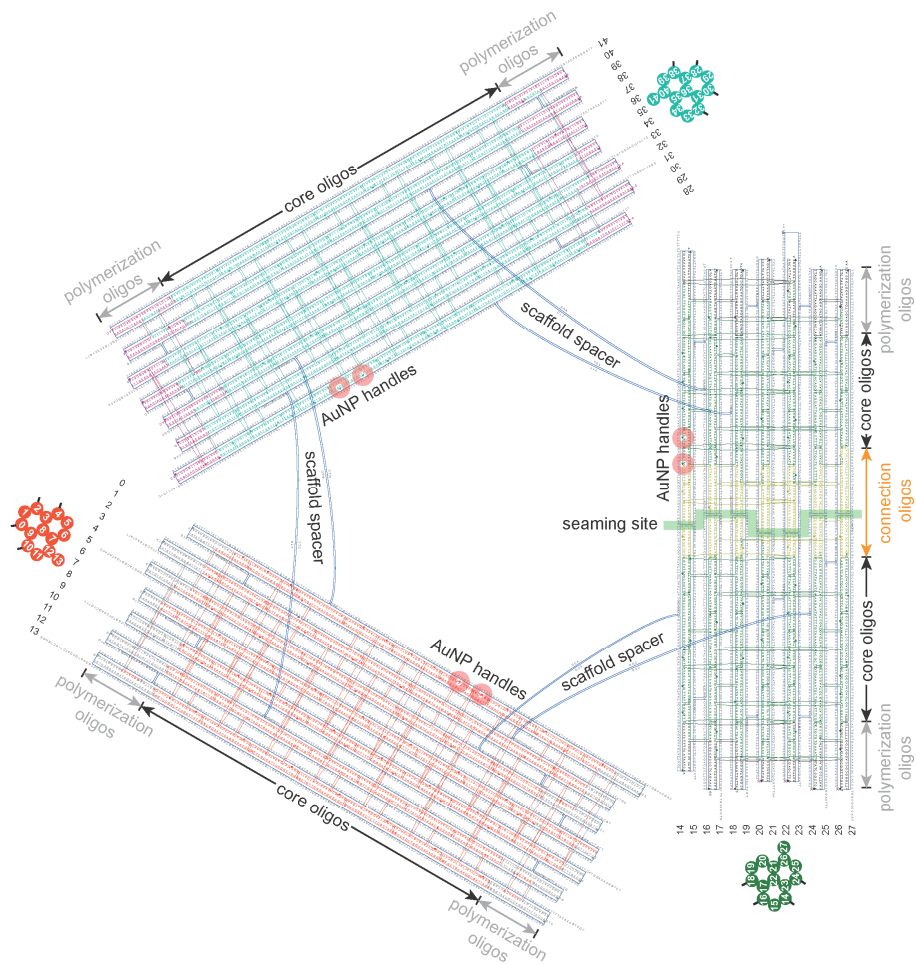
The cavity size of the unit cell should be the unit cell volume minus the bundle volume. We used the formula (E1) for volume calculation. For each 14-helix bundle, it distributes its volume to four neighboring unit cells of a volume given by formula (E2). The cavity size calculated for the triangular DNA origami crystal (bundle radius  $r = 6.2$  nm, rhombohedral unit cell constants  $a = 65$  nm,  $\alpha = 110^\circ$ ) is  $183616 \text{ nm}^3$  which is about 115 times larger than the one previously reported ([7]) for a DNA duplex crystal (duplex radius  $r = 1.25$  nm; rhombohedral unit cell constants  $a = 13.49$  nm,  $\alpha = 110.9^\circ$ ) of  $1584 \text{ nm}^3$ .

$$v = a^3 \sqrt{1 - 3\cos^2\alpha + 2\cos^3\alpha} - \text{bundle volume} \quad (\text{E1})$$

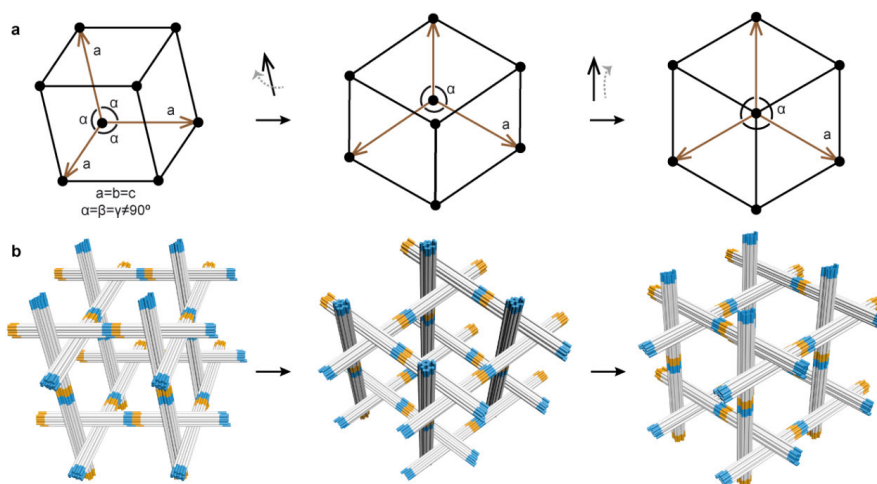
$$\text{bundle volume} = (12 \times \frac{1}{4})(\pi \times r^2) a \quad (\text{E2})$$



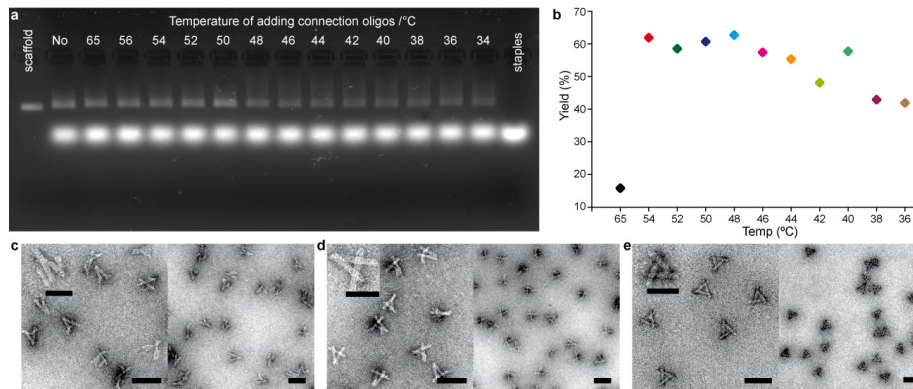
**Supplementary Figure S1.** Structural details of the triangular DNA origami design and the sequential workflow towards DNA origami lattices. **a**, The circular scaffold strand and the core staple strands (without connection oligonucleotides and polymerization oligonucleotides, caDNAno layout in **Supplementary Figure S2**) are annealed in step 1 to form the three 14-helix bundles (14HBs) of the triangular DNA tensegrity structure. The resulting honeycomb design of the 14HBs and the positions where the scaffold crosses over between the struts (black lines) are shown in the cross section image. **b**, Schematic of the 3 nucleotide-long scaffold spacers connecting the three 14HBs. The selected connection positions and the shortness of the scaffold loops results in a structurally self-restricting origami triangle structure. The inset depicts the scaffold seam in one of the 14HBs. This seam is closed in step 2 by the addition of connection strands during the folding cycle. This two-step process favors correct geometries (over-under, over-under arrangement) over misconnected triangles. **c**, Correctly folded DNA origami monomer. The addition of polymerization strands in step 3 results in the completion of the struts' ends and the formation of dsDNA blunt ends (inset). **d**, As the DNA origami monomer displays a three-fold symmetry, any blue end can interact with any orange end (inset). Thus the blunt end stacking of the shape complementary ends leads to polymerization of the monomers in three out-of-plane directions and to the growth of a rhombohedral lattice (step 4). **e**, The resulting unit cell shares eight triangular DNA origami monomers.



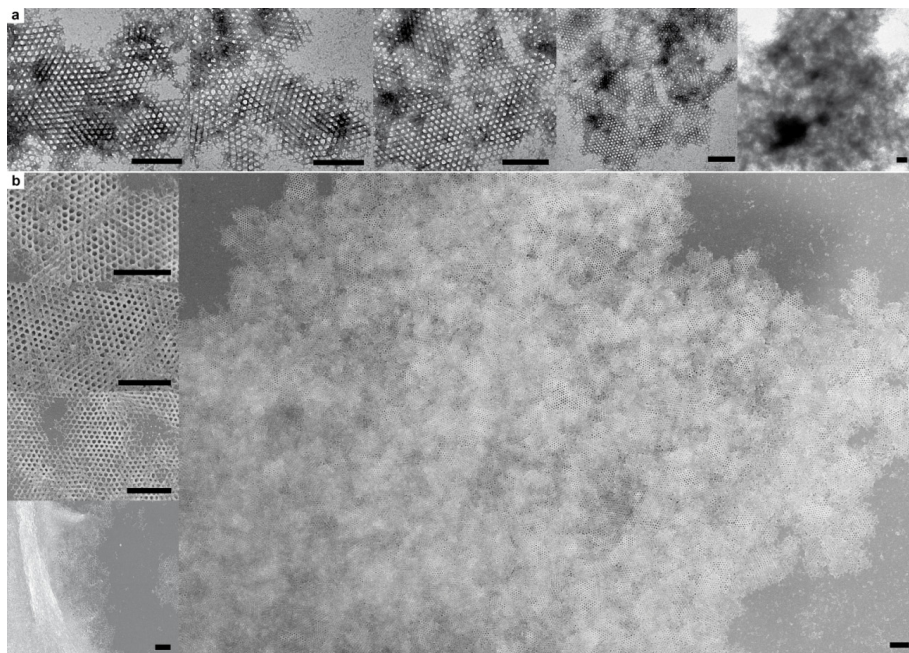
**Supplementary Figure S2.** Rearranged caDNAno layout of the triangular DNA origami monomer. The staple oligonucleotides are sorted into different groups: core oligonucleotides, connection oligonucleotides, polymerization oligonucleotides, and handle oligonucleotides. Six handles (3'-end) for capturing together one gold nanoparticle (AuNP) are highlighted with red circles. The seam is highlighted with a bold green zigzag line.



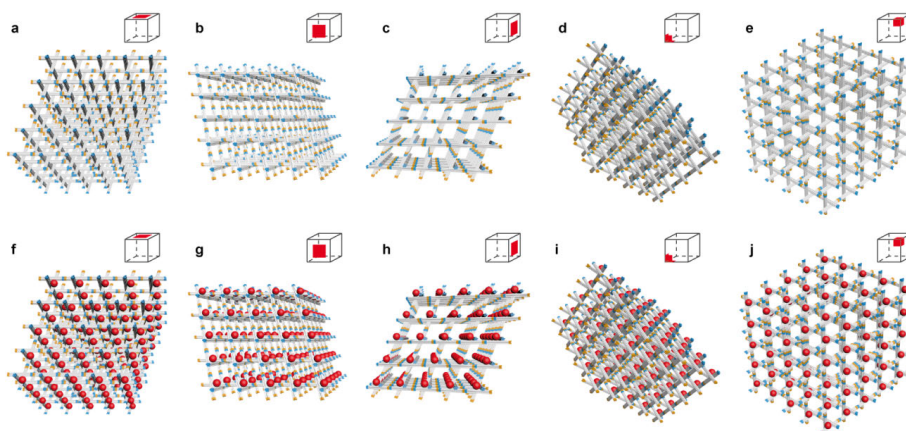
**Supplementary Figure S3. a**, Illustration of the rhombohedral unit cell with lattice constants  $a = b = c = 67 \text{ nm}$  and  $\alpha = \beta = \gamma = 100^\circ (\neq 90^\circ)$ , matching the designed parameters. A step-by-step rotation exemplifies the appearance of a hexagonal pattern ( $\{111\}$  plane) with three-fold symmetry in the unit cell of the rhombohedral lattice. **b**, Schematic of the corresponding rhombohedral lattice unit cell consisting of eight triangular DNA origami structures.



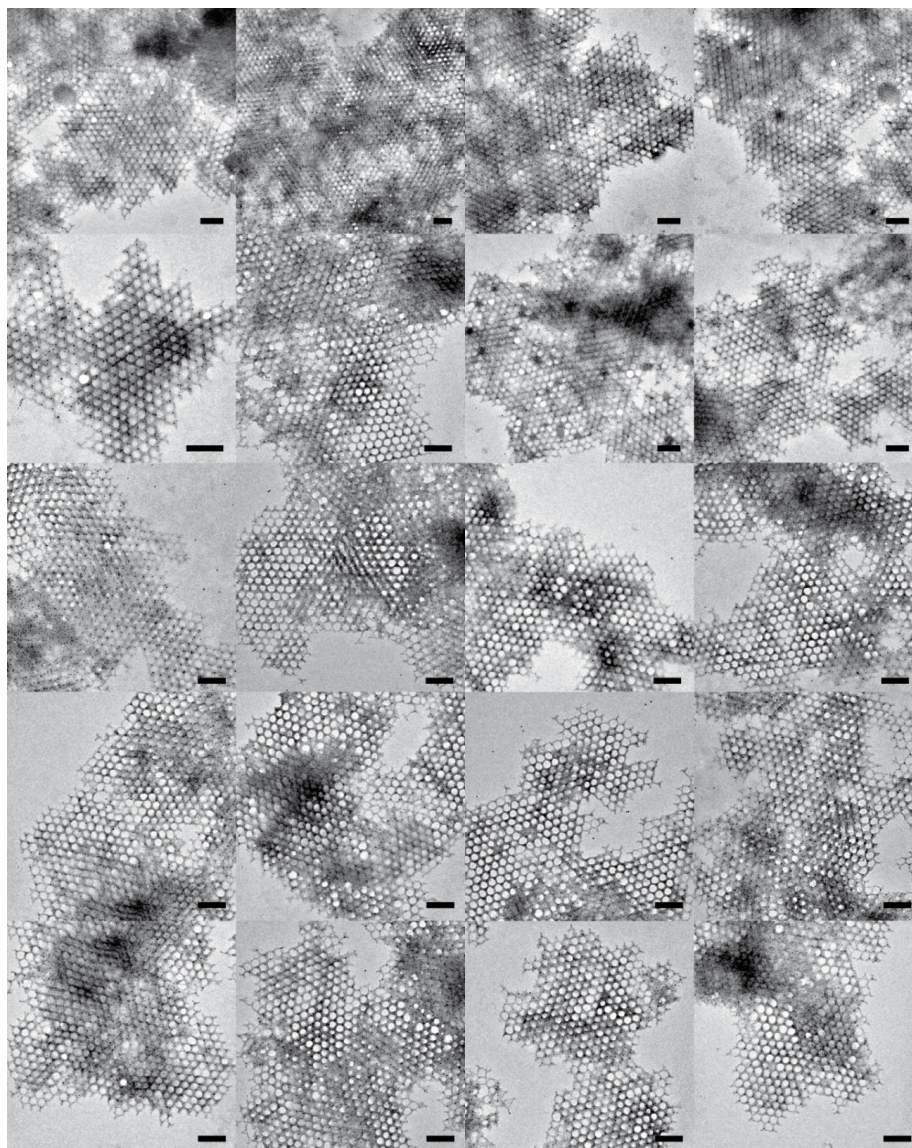
**Supplementary Figure S4. a**, Agarose gel electrophoresis (0.7 %, 11 mM Mg<sup>2+</sup>, 1× TAE pH 8.0) of DNA origami triangles with connection staples added at different temperatures. No: no connection strands added; 65: DNA origami folded with connection oligonucleotides added from the very beginning (one-pot reaction); 56-34: the temperature in °C at which connection strands were added. Correctly folded structures cannot be separated from defective ones *via* agarose gel electrophoresis. **b**, Analysis by TEM imaging revealed that addition of the connection oligonucleotides in a temperature range from 54 to 48 °C resulted in ~ 60% of correctly folded structures. This yield turned out to be sufficient to grow lattices and it is considerably higher than for foldings, where the connection staples were added from the beginning resulting in 15 % correctly folded structures. **c-e**, TEM images of triangular DNA origami structures folded **c**, without connection oligonucleotides, **d**, in a one-pot reaction, and **e**, with connection oligonucleotides added at 52°C. Scale bar of inset: 50 nm, all others: 100 nm.



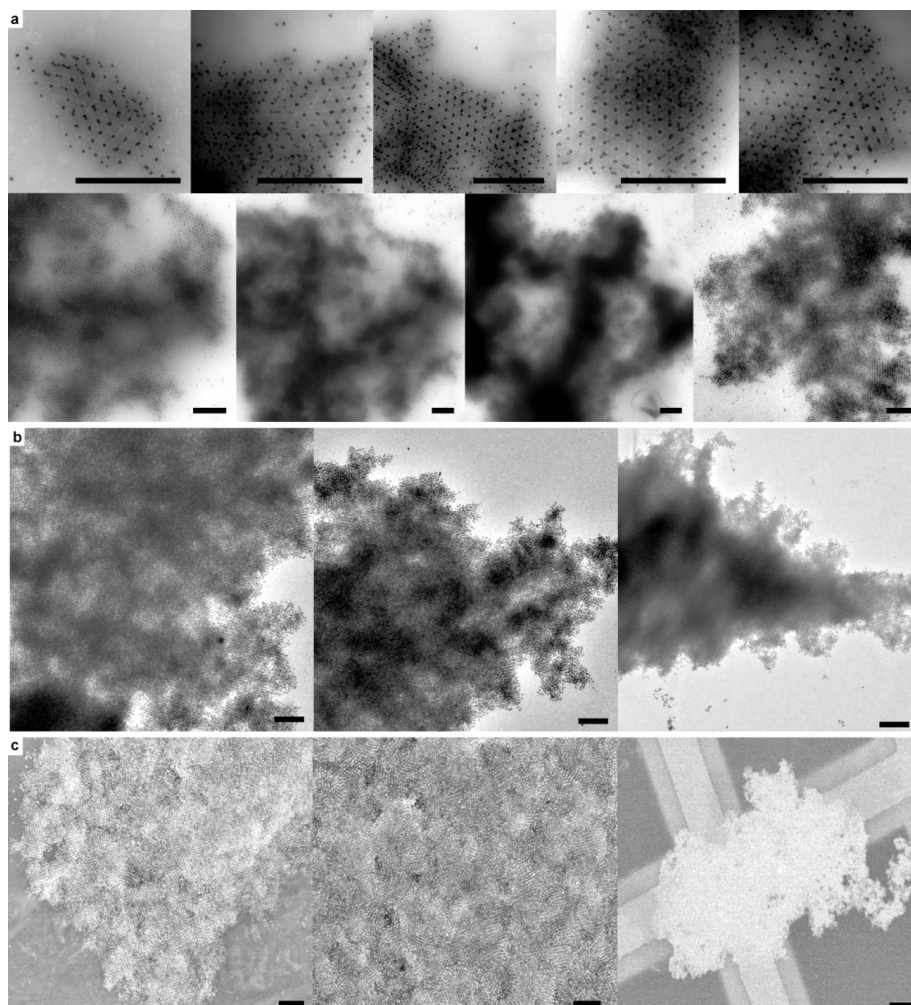
**Supplementary Figure S5.** **a**, TEM images of the DNA origami lattices. The hexagonal pattern characteristic for the view on the [111] plane can be observed particularly well in lattices consisting of only a few layers. Thicker lattices are barely penetrated by the electron beam. **b**, SEM images of the DNA origami lattices displaying the same hexagonal pattern. The lowest small image on the left shows a large lattice patch that buckled during the adsorption on the substrate. The large low magnification SEM image reveals the polycrystalline nature of the DNA origami lattices. Scale bars: 500 nm.



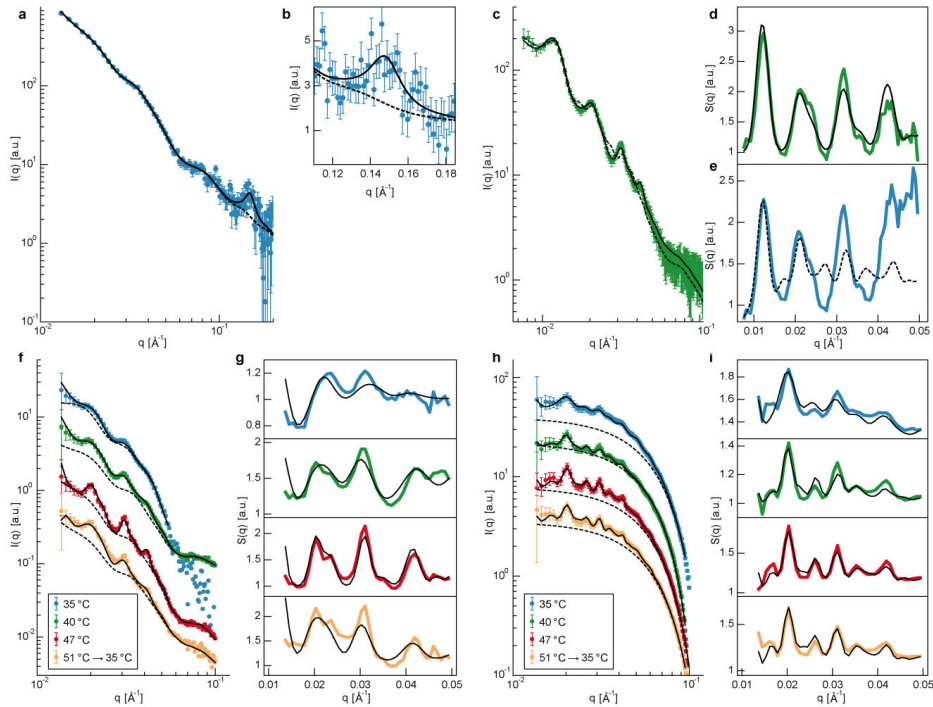
**Supplementary Figure S6.** 3D rendering of the DNA origami lattice (a-e) and the lattice hosting 20 nm gold nanoparticles (f-j) viewed from different perspectives.



**Supplementary Figure S7.** TEM images of the DNA origami lattices hosting 10 nm gold nanoparticles. Scale bars: 200 nm.



**Supplementary Figure S8.** TEM images of DNA origami lattices hosting 20 nm (a) and 30 nm (b) gold nanoparticles. c, SEM images of DNA origami lattices hosting 20 nm gold nanoparticles exhibit the same poly-crystallinity as the templates. Except for the bottom right low magnification image where the scale bar is 10  $\mu\text{m}$  all other scale bars: 500 nm.



**Supplementary Figure S9.** **a**, SAXS intensity of triangular DNA origami monomers dispersed in solution recorded with an in-house source. Model fit to the total intensity including a Lorentzian peak accounting for the regular honeycomb arrangement of DNA double-helical domains inside the 14-helix bundles (solid line) and model fit ignoring this feature (dotted line). **b**, Zoom into the Lorentzian peak. Using the procedure described in *Ref.* [8] we obtain an interhelical distance of 2.8 nm. This is in reasonable agreement with the value of 2.5 nm that was obtained for a honeycomb design in the previous study with an accelerator source. **c**, SAXS intensity of the DNA origami lattices dispersed in solution. Solid line: Complete model fit taking into account the orientation of the triangular monomer with respect to the unit cell. Dashed line: Incomplete model fit neglecting this orientation. **d**, Extracted structure factor from the complete model fit (green line) and model of the complete structure factor assuming a rhombohedral unit cell (black line). Peak positions and heights match. **e**, Extracted structure factor from the incomplete model fit (blue line) and model of the incomplete structure factor assuming a rhombohedral unit cell (black dotted line). Peak heights do not match the data and additional peaks appear where minima are observed in the data. **f-i**, SAXS intensity of origami lattices (**f**) and origami lattices decorated with 10 nm gold particles (**h**) dispersed in solution that were polymerized at different temperatures (blue, green, red) and with an annealing ramp from 51 °C to 35 °C (orange), vertically offset. Solid black lines: Model fits of the total intensity. Dashed black lines: Simulated form factor intensity, neglecting the lattice structure factor. Lattice structure factors from SAXS data (**g** & **i** from **f** & **h** respectively) were obtained by subtraction of the background and division by the form factor intensity. Black lines: Model fits assuming a rhombohedral unit cell.

## References

- [1] S. M. Douglas, A. H. Marblestone, S. Teerapittayanon, A. Vazquez, G. M. Church, and W. M. Shih, "Rapid prototyping of 3D DNA-origami shapes with caDNAno," *Nucleic Acids Res.*, vol. 37, no. 15, pp. 5001–5006, 2009.
- [2] S. M. Douglas, J. J. Chou, and W. M. Shih, "DNA-nanotube-induced alignment of membrane proteins for NMR structure determination," *Proc. Natl. Acad. Sci.*, vol. 104, no. 16, pp. 6644–6648, 2007.
- [3] E. Stahl, F. Praetorius, C. C. de Oliveira Mann, K.-P. Hopfner, and H. Dietz, "Impact of Heterogeneity and Lattice Bond Strength on DNA Triangle Crystal Growth," *ACS Nano*, vol. 10, no. 10, pp. 9156–9164, 2016.
- [4] R. Schreiber *et al.*, "Hierarchical assembly of metal nanoparticles, quantum dots and organic dyes using DNA origami scaffolds," *Nat. Nanotechnol.*, vol. 9, no. 1, pp. 74–78, 2014.
- [5] L. K. Bruetzel, S. Fischer, A. Salditt, S. M. Sedlak, B. Nickel, and J. Lipfert, "A Mo-anode-based in-house source for small-angle X-ray scattering measurements of biological macromolecules," *Rev. Sci. Instrum.*, vol. 87, no. 2, p. 25103, 2016.
- [6] K. G. Yager, Y. Zhang, F. Lu, and O. Gang, "Periodic lattices of arbitrary nano-objects: modeling and applications for self-assembled systems," *J. Appl. Crystallogr.*, vol. 47, no. 1, pp. 118–129, 2014.
- [7] J. Zheng *et al.*, "From molecular to macroscopic via the rational design of a self-assembled 3D DNA crystal," *Nature*, vol. 461, no. 7260, pp. 74–77, 2009.
- [8] S. Fischer, C. Hartl, K. Frank, J. O. Rädler, T. Liedl, and B. Nickel, "Shape and Interhelical Spacing of DNA Origami Nanostructures Studied by Small-Angle X-ray Scattering," *Nano Lett.*, vol. 16, no. 7, pp. 4282–4287, 2016.



## BIBLIOGRAPHY

---

- [1] Peder Olesen Larsen and Markus von Ins. "The rate of growth in scientific publication and the decline in coverage provided by Science Citation Index." In: *Scientometrics* 84.3 (2010), pp. 575–603.
- [2] *The Nobel Prize in Chemistry 2014*. [http://www.nobelprize.org/nobel\\_prizes/chemistry/laureates/2014/press.html](http://www.nobelprize.org/nobel_prizes/chemistry/laureates/2014/press.html). 22 June 2017.
- [3] Jasmina A. Sichert et al. "Quantum Size Effect in Organometal Halide Perovskite Nanoplatelets." In: *Nano Letters* 15.10 (2015), pp. 6521–6527.
- [4] Thomas Reuters. *Web of Science database*. 2017.
- [5] S. Fischer et al. "Shape and Interhelical Spacing of DNA Origami Nanostructures Studied by Small-Angle X-ray Scattering." In: *Nano Letters* 16.7 (2016), pp. 4282–7.
- [6] Linda K. Bruetzel et al. "A Mo-anode-based in-house source for small-angle X-ray scattering measurements of biological macromolecules." In: *Review of Scientific Instruments* 87.2 (2016), p. 025103.
- [7] Wolfgang Zinth and Ursula Zinth. *Optik*. München: Oldenbourg, 2013.
- [8] Jeff W. Lichtman and Jose-Angel Conchello. "Fluorescence microscopy." In: *Nat Meth* 2.12 (2005), pp. 910–919.
- [9] Wolfgang Ott et al. "Single-molecule force spectroscopy on polyproteins and receptor–ligand complexes: The current toolbox." In: *Journal of Structural Biology* 197.1 (2017), pp. 3–12.
- [10] Stephan F. Heucke et al. "Placing Individual Molecules in the Center of Nanoapertures." In: *Nano Letters* 14.2 (2014), pp. 391–395.
- [11] Klinov Dmitry et al. "High-resolution atomic force microscopy of duplex and triplex DNA molecules." In: *Nanotechnology* 18.22 (2007), p. 225102.
- [12] Leo Gross et al. "The Chemical Structure of a Molecule Resolved by Atomic Force Microscopy." In: *Science* 325.5944 (2009), pp. 1110–1114.
- [13] *The Nobel Prize in Physics 1929*. [http://www.nobelprize.org/nobel\\_prizes/physics/laureates/1929/](http://www.nobelprize.org/nobel_prizes/physics/laureates/1929/). 16 May 2017.
- [14] Xiao-chen Bai et al. "Cryo-EM structure of a 3D DNA-origami object." In: *Proceedings of the National Academy of Sciences* 109.49 (2012), pp. 20012–20017.
- [15] Anne Sakdinawat and David Attwood. "Nanoscale X-ray imaging." In: *Nat Photon* 4.12 (2010), pp. 840–848.

- [16] *The Nobel Prize in Physics 1901*. [http://www.nobelprize.org/nobel\\_prizes/physics/laureates/1901/](http://www.nobelprize.org/nobel_prizes/physics/laureates/1901/). 16 May 2017.
- [17] *The Nobel Prize in Physics 1914*. [http://www.nobelprize.org/nobel\\_prizes/physics/laureates/1914/](http://www.nobelprize.org/nobel_prizes/physics/laureates/1914/). 16 May 2017.
- [18] *The Nobel Prize in Physics 1915*. [http://www.nobelprize.org/nobel\\_prizes/physics/laureates/1915/](http://www.nobelprize.org/nobel_prizes/physics/laureates/1915/). 16 May 2017.
- [19] *The Nobel Prize in Physics 1917*. [http://www.nobelprize.org/nobel\\_prizes/physics/laureates/1917/](http://www.nobelprize.org/nobel_prizes/physics/laureates/1917/). 16 May 2017.
- [20] Rosalind E. Franklin and R. G. Gosling. "Molecular Configuration in Sodium Thymonucleate." In: *Nature* 171.4356 (1953), pp. 740–741.
- [21] J. D. Watson and F. H. C. Crick. "Molecular Structure of Nucleic Acids: A Structure for Deoxyribose Nucleic Acid." In: *Nature* 171.4356 (1953), pp. 737–738.
- [22] Paolo Scardi et al. "Celebrating 100 years of the Debye scattering equation." In: *Acta Crystallographica Section A* 72.6 (2016), pp. 589–590.
- [23] André Guinier. "La diffraction des rayons X aux tres petits angles; application a l'etude de phenomenes ultramicroscopiques." In: *Ann. Phys. (Paris)* 12 (1939), pp. 161–237.
- [24] P. Debye and A. M. Bueche. "Scattering by an Inhomogeneous Solid." In: *Journal of Applied Physics* 20.6 (1949), pp. 518–525.
- [25] O. Glatter. "A new method for the evaluation of small-angle scattering data." In: *Journal of Applied Crystallography* 10.5 (1977), pp. 415–421.
- [26] D. Svergun. "Determination of the regularization parameter in indirect-transform methods using perceptual criteria." In: *Journal of Applied Crystallography* 25.4 (1992), pp. 495–503.
- [27] D. Svergun, C. Barberato, and M. H. J. Koch. "CRY SOL - a Program to Evaluate X-ray Solution Scattering of Biological Macromolecules from Atomic Coordinates." In: *Journal of Applied Crystallography* 28.6 (1995), pp. 768–773.
- [28] P. Chacón et al. "Low-Resolution Structures of Proteins in Solution Retrieved from X-Ray Scattering with a Genetic Algorithm." In: *Biophysical Journal* 74.6 (1998), pp. 2760–2775.
- [29] Pablo Chacón et al. "Reconstruction of protein form with X-ray solution scattering and a genetic algorithm." In: *Journal of Molecular Biology* 299.5 (2000), pp. 1289–1302.
- [30] D. I. Svergun. "Restoring Low Resolution Structure of Biological Macromolecules from Solution Scattering Using Simulated Annealing." In: *Biophysical Journal* 76.6 (1999), pp. 2879–2886.
- [31] Dmitri I. Svergun, Maxim V. Petoukhov, and Michel H. J. Koch. "Determination of Domain Structure of Proteins from X-Ray Solution Scattering." In: *Biophysical Journal* 80.6 (2001), pp. 2946–2953.

- [32] Herbert C. Pollock. "The discovery of synchrotron radiation." In: *American Journal of Physics* 51.3 (1983), pp. 278–280.
- [33] C. Rakete et al. "Compact x-ray microradiograph for in situ imaging of solidification processes: Bringing in situ x-ray micro-imaging from the synchrotron to the laboratory." In: *Review of Scientific Instruments* 82.10 (2011), p. 105108.
- [34] O. Hemberg, M. Otendal, and H. M. Hertz. "Liquid-metal-jet anode electron-impact x-ray source." In: *Applied Physics Letters* 83.7 (2003), pp. 1483–1485.
- [35] (Feb 2010) Excillum has successfully shipped the first D1 source prototype to an industrial customer. <http://www.excillum.com/communications/news.html>. 17 May 2017.
- [36] Tadeusz Skarzynski. "Collecting data in the home laboratory: evolution of X-ray sources, detectors and working practices." In: *Acta Crystallographica Section D: Biological Crystallography* 69.Pt 7 (2013), pp. 1283–1288.
- [37] Jens Als-Nielsen and Des McMorrow. *Elements of modern X-ray physics*. John Wiley & Sons, 2011.
- [38] Wilhelmus H. de Jeu. *Basic x-ray scattering for soft matter*. Oxford University Press, 2016.
- [39] A. Guinier. *X-ray Diffraction in Crystals, Imperfect Crystals, and Amorphous Bodies*. Dover Publications, 1994.
- [40] Bertram E. Warren. *X-ray diffraction*. Dover Publications, 1990.
- [41] André Guinier and Gérard Fournet. *Small-angle scattering of x-rays*. Wiley, 1955.
- [42] H Schnablegger and Y Singh. *The SAXS Guide*. Anton Paar GmbH, 2013.
- [43] John David Jackson. *Classical electrodynamics*. Wiley, 2001.
- [44] L Feigin, Dimitrij I Svergun, and George W Taylor. *Structure analysis by small-angle X-ray and neutron scattering*. Springer, 1987.
- [45] Petr V. Konarev et al. "PRIMUS: a Windows PC-based system for small-angle scattering data analysis." In: *Journal of Applied Crystallography* 36.5 (2003), pp. 1277–1282.
- [46] Dina Schneidman-Duhovny et al. "Accurate SAXS Profile Computation and its Assessment by Contrast Variation Experiments." In: *Biophysical Journal* 105.4 (2013), pp. 962–974.
- [47] Nicholas Allec et al. "Small-angle X-ray scattering method to characterize molecular interactions: Proof of concept." In: *Scientific Reports* 5 (2015), p. 12085.
- [48] Cecile A. Dreiss, Kevin S. Jack, and Andrew P. Parker. "On the absolute calibration of bench-top small-angle X-ray scattering instruments: a comparison of different standard methods." In: *Journal of Applied Crystallography* 39.1 (2006), pp. 32–38.

- [49] Doris Orthaber, Alexander Bergmann, and Otto Glatter. "SAXS experiments on absolute scale with Kratky systems using water as a secondary standard." In: *Journal of Applied Crystallography* 33.2 (2000), pp. 218–225.
- [50] Siegfried Hunklinger. *Festkörperphysik*. De Gruyter Oldenbourg, 2014.
- [51] Kevin G. Yager et al. "Periodic lattices of arbitrary nano-objects: modeling and applications for self-assembled systems." In: *Journal of Applied Crystallography* 47.1 (2014), pp. 118–129.
- [52] S. Förster et al. "Scattering curves of ordered mesoscopic materials." In: *Journal of Physical Chemistry B* 109.4 (2005), pp. 1347–1360.
- [53] Y. L. Li et al. "Scatterless hybrid metal-single-crystal slit for small-angle X-ray scattering and high-resolution X-ray diffraction." In: *Journal of Applied Crystallography* 41 (2008), pp. 1134–1139.
- [54] Triple source for the Xeuss 2.0 at the University of Strathclyde. <http://www.xenocs.com/en/news/new-triple-source-for-the-xeuss-2-0-at-the-university-of-strathclyde-39/>. 26 June 2017.
- [55] J. S. Pedersen. "A flux- and background-optimized version of the NanoSTAR small-angle X-ray scattering camera for solution scattering." In: *Journal of Applied Crystallography* 37 (2004), pp. 369–380.
- [56] J. S. Pedersen, D. Posselt, and K. Mortensen. "Analytical treatment of the resolution function for small-angle scattering." In: *Journal of Applied Crystallography* 23.4 (1990), pp. 321–333.
- [57] P. Harris, B. Lebeck, and J. S. Pedersen. "The Three-Dimensional Resolution Function for Small-Angle Scattering and Laue Geometries." In: *Journal of Applied Crystallography* 28.2 (1995), pp. 209–222.
- [58] Brian Richard Pauw. "Everything SAXS: small-angle scattering pattern collection and correction." In: *Journal of Physics: Condensed Matter* 25.38 (2013), p. 383201.
- [59] J. A. Bearden. "X-Ray Wavelengths." In: *Reviews of Modern Physics* 39.1 (1967), pp. 78–124.
- [60] V. Honkimaki, J. Sleight, and P. Suortti. "Characteristic X-ray flux from sealed Cr, Cu, Mo, Ag and W tubes." In: *Journal of Applied Crystallography* 23.5 (1990), pp. 412–417.
- [61] Dectris. *Pilatus CdTe sensor*. <https://www.dectris.com/cdte-sensors.html>. July 2017.
- [62] H. Göbel. "Paper I01." In: *ACA Meeting*. Pittsburgh, 2012.
- [63] J. Schelten and W. Schmatz. "Multiple-scattering treatment for small-angle scattering problems." In: *Journal of Applied Crystallography* 13.4 (1980), pp. 385–390.
- [64] Hiroyasu Masunaga et al. "Accurate measurements of intrinsic scattering from window materials by use of a vacuum camera." In: *Journal of Applied Crystallography* 46.2 (2013), pp. 577–579.

- [65] Shuji Akiyama et al. "Conformational landscape of cytochrome c folding studied by microsecond-resolved small-angle x-ray scattering." In: *Proceedings of the National Academy of Sciences* 99.3 (2002), pp. 1329–1334.
- [66] Daniel J. Segel et al. "Protein Denaturation: A Small-Angle X-ray Scattering Study of the Ensemble of Unfolded States of Cytochrome c." In: *Biochemistry* 37.36 (1998), pp. 12443–12451.
- [67] Jan Lipfert et al. "Sample holder for small-angle x-ray scattering static and flow cell measurements." In: *Review of Scientific Instruments* 77.4 (2006), p. 046108.
- [68] J.-M. Dubuisson, T. Decamps, and P. Vachette. "Improved Signal-to-Background Ratio in Small-Angle X-ray Scattering Experiments with Synchrotron Radiation using an Evacuated Cell for Solutions." In: *Journal of Applied Crystallography* 30.1 (1997), pp. 49–54.
- [69] Manfred W. Roessle et al. "Upgrade of the small-angle X-ray scattering beamline X33 at the European Molecular Biology Laboratory, Hamburg." In: *Journal of Applied Crystallography* 40.s1 (2007), s190–s194.
- [70] M. Knaapila et al. "A new small-angle X-ray scattering set-up on the crystallography beamline I711 at MAX-lab." In: *Journal of Synchrotron Radiation* 16.4 (2009), pp. 498–504.
- [71] Jesse B. Hopkins and Robert E. Thorne. "Quantifying radiation damage in biomolecular small-angle X-ray scattering." In: *Journal of Applied Crystallography* 49.3 (2016), pp. 880–890.
- [72] Cy M. Jeffries et al. "Limiting radiation damage for high-brilliance biological solution scattering: practical experience at the EMBL P12 beamline PETRAIII." In: *Journal of Synchrotron Radiation* 22.2 (2015), pp. 273–279.
- [73] O. H. Seeck et al. "The high-resolution diffraction beamline Po8 at PETRA III." In: *Journal of Synchrotron Radiation* 19.1 (2012), pp. 30–38.
- [74] S. Aeffner et al. "Membrane fusion intermediates and the effect of cholesterol: An in-house X-ray scattering study." In: *European Physical Journal E* 30.2 (2009), pp. 205–214.
- [75] Caroline A. Schneider, Wayne S. Rasband, and Kevin W. Eliceiri. "NIH Image to ImageJ: 25 years of image analysis." In: *Nat Meth* 9.7 (2012), pp. 671–675.
- [76] J. Ilavsky. "Nika: software for two-dimensional data reduction." In: *Journal of Applied Crystallography* 45 (2012), pp. 324–328.
- [77] DANSE. SASView. <http://www.sasview.org/>. 2017.
- [78] Jasper A Vrugt et al. "Accelerating Markov chain Monte Carlo simulation by differential evolution with self-adaptive randomized subspace sampling." In: *International Journal of Nonlinear Sciences and Numerical Simulation* 10.3 (2009), pp. 273–290.

- [79] G. Rose. *De novis quibusdam fossilibus, quae in montibus uraliis inveniuntur, scripsit*. Berlin, 1839.
- [80] Dieter Weber. "CH<sub>3</sub>NH<sub>3</sub>PbX<sub>3</sub>, ein Pb(II)-System mit kubischer Perowskitstruktur / CH<sub>3</sub>NH<sub>3</sub>PbX<sub>3</sub>, a Pb(II)-System with Cubic Perovskite Structure." In: *Zeitschrift für Naturforschung B* 33.12 (1978), p. 1443.
- [81] Robert F. Service. "Turning Up the Light." In: *Science* 342.6160 (2013), pp. 794–797.
- [82] Michael M. Lee et al. "Efficient Hybrid Solar Cells Based on Meso-Structured Organometal Halide Perovskites." In: *Science* 338.6107 (2012), pp. 643–647.
- [83] Feng Zhang et al. "Brightly Luminescent and Color-Tunable Colloidal CH<sub>3</sub>NH<sub>3</sub>PbX<sub>3</sub> (X = Br, I, Cl) Quantum Dots: Potential Alternatives for Display Technology." In: *ACS Nano* 9.4 (2015), pp. 4533–4542.
- [84] Giles E. Eperon et al. "Formamidinium lead trihalide: a broadly tunable perovskite for efficient planar heterojunction solar cells." In: *Energy & Environmental Science* 7.3 (2014), pp. 982–988.
- [85] Constantinos C. Stoumpos, Christos D. Malliakas, and Mercouri G. Kanatzidis. "Semiconducting Tin and Lead Iodide Perovskites with Organic Cations: Phase Transitions, High Mobilities, and Near-Infrared Photoluminescent Properties." In: *Inorganic Chemistry* 52.15 (2013), pp. 9019–9038.
- [86] Jian Zhang et al. "Low-Dimensional Halide Perovskites and Their Advanced Optoelectronic Applications." In: *Nano-Micro Letters* 9.3 (2017), p. 36.
- [87] Lakshminarayana Polavarapu et al. "Advances in Quantum-Confined Perovskite Nanocrystals for Optoelectronics." In: *Advanced Energy Materials* (2017), 1700267–n/a.
- [88] Haotong Wei et al. "Sensitive X-ray detectors made of methylammonium lead tribromide perovskite single crystals." In: *Nature Photonics* 10.5 (2016), pp. 333–339.
- [89] Makhsud I. Saidaminov, Omar F. Mohammed, and Osman M. Bakr. "Low-Dimensional-Networked Metal Halide Perovskites: The Next Big Thing." In: *ACS Energy Letters* 2.4 (2017), pp. 889–896.
- [90] H. Mashiyama, Y. Kurihara, and T. Azetsu. "Disordered cubic perovskite structure of CH<sub>3</sub>NH<sub>3</sub>PbX<sub>3</sub> (X = Cl, Br, I)." In: *Journal of the Korean Physical Society* 32 (1998), pp. 156–158.
- [91] Luciana C. Schmidt et al. "Nontemplate Synthesis of CH<sub>3</sub>NH<sub>3</sub>PbBr<sub>3</sub> Perovskite Nanoparticles." In: *Journal of the American Chemical Society* 136.3 (2014), pp. 850–853.
- [92] Makhsud I. Saidaminov et al. "High-quality bulk hybrid perovskite single crystals within minutes by inverse temperature crystallization." In: *Nature Communications* 6 (2015), p. 7586.

- [93] Giselle A. Elbaz et al. "Unbalanced Hole and Electron Diffusion in Lead Bromide Perovskites." In: *Nano Letters* 17.3 (2017), pp. 1727–1732.
- [94] A. Poglitsch and D. Weber. "Dynamic disorder in methylammoniumtrihalogenoplumbates (II) observed by millimeter-wave spectroscopy." In: *The Journal of Chemical Physics* 87.11 (1987), pp. 6373–6378.
- [95] Christopher Eames et al. "Ionic transport in hybrid lead iodide perovskite solar cells." In: *Nature Communications* 6 (2015), p. 7497.
- [96] Brian H. Toby and Robert B. Von Dreele. "GSAS-II: the genesis of a modern open-source all purpose crystallography software package." In: *Journal of Applied Crystallography* 46.2 (2013), pp. 544–549.
- [97] Quinten A. Akkerman et al. "Solution Synthesis Approach to Colloidal Cesium Lead Halide Perovskite Nanoplatelets with Monolayer-Level Thickness Control." In: *Journal of the American Chemical Society* 138.3 (2016), pp. 1010–1016.
- [98] Yu Wang et al. *XRD anisotropic broadening of nano-crystallites*. Denver X-ray Conference. 2011.
- [99] Crystal Impact. *Diamond: Crystal and Molecular Structure Visualization*. <http://www.crystalimpact.com/diamond/>. 1997–2017.
- [100] *The Nobel Prize in Medicine 1962*. [https://www.nobelprize.org/nobel\\_prizes/medicine/laureates/1962/](https://www.nobelprize.org/nobel_prizes/medicine/laureates/1962/). 21 Dec 2016.
- [101] Nadrian C. Seeman. "Nucleic acid junctions and lattices." In: *Journal of Theoretical Biology* 99.2 (1982), pp. 237–247.
- [102] Robin Holliday. "A mechanism for gene conversion in fungi." In: *Genetical Research* 5.2 (1964), pp. 282–304.
- [103] Junghuei Chen and Nadrian C. Seeman. "Synthesis from DNA of a molecule with the connectivity of a cube." In: *Nature* 350.6319 (1991), pp. 631–633.
- [104] Nadrian C. Seeman. "DNA in a material world." In: *Nature* 421.6921 (2003), pp. 427–431.
- [105] Tsu Ju Fu and Nadrian C. Seeman. "DNA double-crossover molecules." In: *Biochemistry* 32.13 (1993), pp. 3211–3220.
- [106] Xiaojun Li et al. "Antiparallel DNA Double Crossover Molecules As Components for Nanoconstruction." In: *Journal of the American Chemical Society* 118.26 (1996), pp. 6131–6140.
- [107] William M. Shih, Joel D. Quispe, and Gerald F. Joyce. "A 1.7-kilobase single-stranded DNA that folds into a nanoscale octahedron." In: *Nature* 427.6975 (2004), pp. 618–621.
- [108] P. W. K. Rothmund. "Folding DNA to create nanoscale shapes and patterns." In: *Nature* 440.7082 (2006), pp. 297–302.
- [109] Robert Schreiber et al. "Hierarchical assembly of metal nanoparticles, quantum dots and organic dyes using DNA origami scaffolds." In: *Nat Nano* 9.1 (2014), pp. 74–78.

- [110] Vivek V. Thacker et al. "DNA origami based assembly of gold nanoparticle dimers for surface-enhanced Raman scattering." In: *Nature Communications* 5 (2014), p. 3448.
- [111] Shawn M. Douglas et al. "Self-assembly of DNA into nanoscale three-dimensional shapes." In: *Nature* 459.7245 (2009), pp. 414–418.
- [112] Yonggang Ke et al. "Multilayer DNA Origami Packed on a Square Lattice." In: *Journal of the American Chemical Society* 131.43 (2009), pp. 15903–15908.
- [113] Hendrik Dietz, Shawn M. Douglas, and William M. Shih. "Folding DNA into Twisted and Curved Nanoscale Shapes." In: *Science* 325.5941 (2009), pp. 725–730.
- [114] Shawn M. Douglas et al. "Rapid prototyping of 3D DNA-origami shapes with caDNAno." In: *Nucleic Acids Research* 37.15 (2009), pp. 5001–5006.
- [115] E. S. Andersen et al. "Self-assembly of a nanoscale DNA box with a controllable lid." In: *Nature* 459.7243 (2009), pp. 73–75.
- [116] Yu He et al. "Hierarchical self-assembly of DNA into symmetric supramolecular polyhedra." In: *Nature* 452.7184 (2008), pp. 198–201.
- [117] Jianping Zheng et al. "From molecular to macroscopic via the rational design of a self-assembled 3D DNA crystal." In: *Nature* 461.7260 (2009), pp. 74–77.
- [118] Dage Liu et al. "Tensegrity: Construction of Rigid DNA Triangles with Flexible Four-Arm DNA Junctions." In: *Journal of the American Chemical Society* 126.8 (2004), pp. 2324–2325.
- [119] Ye Tian et al. "Prescribed nanoparticle cluster architectures and low-dimensional arrays built using octahedral DNA origami frames." In: *Nat Nano* 10.7 (2015), pp. 637–644.
- [120] Ye Tian et al. "Lattice engineering through nanoparticle-DNA frameworks." In: *Nat Mater* 15.6 (2016), pp. 654–661.
- [121] Linda K. Bruetzel et al. "Conformational Changes and Flexibility of DNA Devices Observed by Small-Angle X-ray Scattering." In: *Nano Letters* 16.8 (2016), pp. 4871–4879.
- [122] P. Debye. "Molecular-weight Determination by Light Scattering." In: *The Journal of Physical and Colloid Chemistry* 51.1 (1947), pp. 18–32.
- [123] P. Mittelbach and G. Porod. "Zur Röntgenkleinwinkelstreuung verdünnter kolloider Systeme." In: *Acta Physica Austriaca* 14 (1961), pp. 185–211.
- [124] Pablo Székely et al. "Solution X-ray Scattering Form Factors of Supramolecular Self-Assembled Structures." In: *Langmuir* 26.16 (2010), pp. 13110–13129.
- [125] R. A. Young and D. B. Wiles. "Profile shape functions in Rietveld refinements." In: *Journal of Applied Crystallography* 15.4 (1982), pp. 430–438.

- [126] Do-Nyun Kim et al. "Quantitative prediction of 3D solution shape and flexibility of nucleic acid nanostructures." In: *Nucleic Acids Research* 40.7 (2012), pp. 2862–2868.
- [127] Carlos Ernesto Castro et al. "A primer to scaffolded DNA origami." In: *Nat Meth* 8.3 (2011), pp. 221–229.
- [128] Philipp C. Nickels et al. "DNA Origami Seesaws as Comparative Binding Assay." In: *ChemBioChem* 17.12 (2016), pp. 1093–1096.
- [129] Samet Kocabey et al. "Membrane-Assisted Growth of DNA Origami Nanostructure Arrays." In: *ACS Nano* 9.4 (2015), pp. 3530–3539.
- [130] Jejoong Yoo and Aleksei Aksimentiev. "In situ structure and dynamics of DNA origami determined through molecular dynamics simulations." In: *Proceedings of the National Academy of Sciences* 110.50 (2013), pp. 20099–20104.
- [131] Jean Michel Arbona, Jean-Pierre Aimé, and Juan Elezgaray. "Modeling the mechanical properties of DNA nanostructures." In: *Physical Review E* 86.5 (2012), p. 051912.
- [132] Jejoong Yoo et al. *cadnano to PDB File Converter*. 2014. URL: <https://nanohub.org/resources/19749>.
- [133] Keyao Pan et al. "Lattice-free prediction of three-dimensional structure of programmed DNA assemblies." In: *Nature Communications* 5 (2014), p. 5578.
- [134] William Humphrey, Andrew Dalke, and Klaus Schulten. "VMD: Visual molecular dynamics." In: *Journal of Molecular Graphics* 14.1 (1996), pp. 33–38.
- [135] Xiangyun Qiu et al. "Inter-DNA Attraction Mediated by Divalent Counterions." In: *Physical Review Letters* 99.3 (2007), p. 038104.
- [136] Binqun Luan and Aleksei Aksimentiev. "DNA Attraction in Monovalent and Divalent Electrolytes." In: *Journal of the American Chemical Society* 130.47 (2008), pp. 15754–15755.
- [137] Alexei A. Kornyshev et al. "Structure and interactions of biological helices." In: *Reviews of Modern Physics* 79.3 (2007), pp. 943–996.
- [138] Evi Stahl et al. "Facile and Scalable Preparation of Pure and Dense DNA Origami Solutions." In: *Angewandte Chemie International Edition* 53.47 (2014), pp. 12735–12740.
- [139] Jean-Philippe J. Sobczak et al. "Rapid Folding of DNA into Nanoscale Shapes at Constant Temperature." In: *Science* 338.6113 (2012), pp. 1458–1461.
- [140] Jonathan V. Selinger and Robijn F. Bruinsma. "Hexagonal and nematic phases of chains. I. Correlation functions." In: *Physical Review A* 43.6 (1991), pp. 2910–2921.
- [141] Tao Zhang. "Assembly of Optically-Active Nano-components with DNA." PhD Thesis. Ludwig-Maximilians-Universität München, 2017.

- [142] Kathryn L. Sarachan, Joseph E. Curtis, and Susan Krueger. "Small-angle scattering contrast calculator for protein and nucleic acid complexes in solution." In: *Journal of Applied Crystallography* 46.6 (2013), pp. 1889–1893.
- [143] NIST Center for Neutron Research. *Neutron activation and scattering calculator*. <https://www.ncnr.nist.gov/resources/activation/>. 05 May 2017.
- [144] E. Mitscherlich. "Ueber das Stickstoffbenzid." In: *Annalen der Physik* 108.15 (1834), pp. 225–227.
- [145] Alfred Nobel. "III. Zur Geschichte des Azobenzols und des Benzidins." In: *Justus Liebigs Annalen der Chemie* 98.2 (1856), pp. 253–256.
- [146] A. Diguët et al. "UV-Induced Bursting of Cell-Sized Multicomponent Lipid Vesicles in a Photosensitive Surfactant Solution." In: *Journal of the American Chemical Society* 134.10 (2012), pp. 4898–4904.
- [147] A. Samanta, M. C. A. Stuart, and B. J. Ravoo. "Photoresponsive Capture and Release of Lectins in Multilamellar Complexes." In: *Journal of the American Chemical Society* 134.48 (2012), pp. 19909–19914.
- [148] A. A. Beharry and G. A. Woolley. "Azobenzene photoswitches for biomolecules." In: *Chemical Society Reviews* 40.8 (2011), pp. 4422–4437.
- [149] S. C. Sebai et al. "Photocontrol of the Translocation of Molecules, Peptides, and Quantum Dots through Cell and Lipid Membranes Doped with Azobenzene Copolymers." In: *Angewandte Chemie-International Edition* 51.9 (2012), pp. 2132–2136.
- [150] T. Liu et al. "Light-controlled ion channels formed by amphiphilic small molecules regulate ion conduction via cis-trans photoisomerization." In: *Chemical Communications* 49.87 (2013), pp. 10311–10313.
- [151] Zhong-Kai Cui et al. "Nonphospholipid fluid liposomes with switchable photocontrolled release." In: *Langmuir* 30.36 (2014).
- [152] Ying Li et al. "Photoresponsive Molecular Switch for Regulating Transmembrane Proton-Transfer Kinetics." In: *Journal of the American Chemical Society* (2015).
- [153] Chiyoung Park et al. "Photoinduced Release of Guest Molecules by Supramolecular Transformation of Self-Assembled Aggregates Derived from Dendrons." In: *Angewandte Chemie* 120.16 (2008), pp. 3001–3005.
- [154] T. Fujii et al. "Molecular dynamics in azobenzene liquid crystal polymer films measured by time-resolved techniques." In: *Physical Chemistry Chemical Physics* 16.22 (2014), pp. 10485–10490.
- [155] Timothy J. White and Dirk J. Broer. "Programmable and adaptive mechanics with liquid crystal polymer networks and elastomers." In: *Nat Mater* 14.11 (2015), pp. 1087–1098.

- [156] Jaume García-Amorós and Dolores Velasco. "Recent advances towards azobenzene-based light-driven real-time information-transmitting materials." In: *Beilstein Journal of Organic Chemistry* 8 (2012), pp. 1003–1017.
- [157] Carla Pernpeintner et al. "Light-Controlled Membrane Mechanics and Shape Transitions of Photoswitchable Lipid Vesicles." In: *Langmuir* (2017).
- [158] Christina Felicitas Dirscherl. "Structural and Dynamic Changes in Light-Switchable Lipid Membranes: A Combined X-Ray and UV-Vis Study." Master Thesis. Ludwig-Maximilians-Universität München, 2016.
- [159] Stephanie A. Tristram-Nagle. "Preparation of Oriented, Fully Hydrated Lipid Samples for Structure Determination Using X-Ray Scattering." In: *Methods in molecular biology (Clifton, N.J.)* 400 (2007), pp. 63–75.
- [160] Sebastian Aeffner. "Stalk Structures in Lipid Bilayer Fusion Studied by X-ray Diffraction." PhD Thesis. Universität Göttingen, 2012.
- [161] Gilles Renaud, Rémi Lazzari, and Frédéric Leroy. "Probing surface and interface morphology with Grazing Incidence Small Angle X-Ray Scattering." In: *Surface Science Reports* 64.8 (2009), pp. 255–380.
- [162] S. K. Sinha et al. "X-ray and neutron scattering from rough surfaces." In: *Physical Review B* 38.4 (1988), pp. 2297–2311.
- [163] Norbert Kučerka, Mu-Ping Nieh, and John Katsaras. "Fluid phase lipid areas and bilayer thicknesses of commonly used phosphatidylcholines as a function of temperature." In: *Biochimica et Biophysica Acta (BBA) - Biomembranes* 1808.11 (2011), pp. 2761–2771.
- [164] Lin Yang, Lai Ding, and Huey W. Huang. "New Phases of Phospholipids and Implications to the Membrane Fusion Problem." In: *Biochemistry* 42.22 (2003), pp. 6631–6635.
- [165] T. Fujino, S. Y. Arzhantsev, and T. Tahara. "Femtosecond time-resolved fluorescence study of photoisomerization of trans-azobenzene." In: *Journal of Physical Chemistry A* 105.35 (2001), pp. 8123–8129.
- [166] T. Fujino and T. Tahara. "Picosecond time-resolved Raman study of trans-azobenzene." In: *Journal of Physical Chemistry A* 104.18 (2000), pp. 4203–4210.
- [167] Sajjan. D. George, V. Subramanyan Namboodiri, and Steffen Hardt. "Laser induced photoswitching of azobenzene incorporated in PDMS films." In: *Proc. SPIE* 7774 (2010). DOI: 10.1117/12.860125.
- [168] Tomiki Ikeda and Osamu Tsutsumi. "Optical Switching and Image Storage by Means of Azobenzene Liquid-Crystal Films." In: *Science* 268.5219 (1995), pp. 1873–1875.
- [169] H. M. Dhammika Bandara and Shawn C. Burdette. "Photoisomerization in different classes of azobenzene." In: *Chemical Society Reviews* 41.5 (2012), pp. 1809–1825.

- [170] Andrew Nelson. "Co-refinement of multiple-contrast neutron/X-ray reflectivity data using MOTOFIT." In: *Journal of Applied Crystallography* 39.2 (2006), pp. 273–276.
- [171] Christian Reich et al. "Asymmetric Structural Features in Single Supported Lipid Bilayers Containing Cholesterol and G(M1) Resolved with Synchrotron X-Ray Reflectivity." In: *Biophysical Journal* 95.2 (2008), pp. 657–668.
- [172] C. E. Miller et al. "Characterization of Biological Thin Films at the Solid-Liquid Interface by X-Ray Reflectivity." In: *Physical Review Letters* 94.23 (2005), p. 238104.
- [173] Rana Ashkar et al. "Tuning Membrane Thickness Fluctuations in Model Lipid Bilayers." In: *Biophysical Journal* 109.1 (2015), pp. 106–112.
- [174] Philipp Reindl. "Röntgenstreuung und optische Transmissionsmessung an photoschaltbaren Lipid-Multilagen." Bachelor Thesis. Ludwig-Maximilians-Universität München, 2017.
- [175] Katinka von Grafenstein. "Messung der Membrandicke uni- und multilamellarer Lipidvesikel mittels Kleinwinkel-Röntgenstreuung." Bachelor Thesis. Ludwig-Maximilians-Universität München, 2017.
- [176] Guohua Jia et al. "Couples of colloidal semiconductor nanorods formed by self-limited assembly." In: *Nat Mater* 13.3 (2014), pp. 301–307.
- [177] Shu Fen Tan et al. "Quantum Plasmon Resonances Controlled by Molecular Tunnel Junctions." In: *Science* 343.6178 (2014), pp. 1496–1499.
- [178] Fabian Herschel. "Kleinwinkelröntgenstreuung an Nanopartikeln in Lösung." Master Thesis. Ludwig-Maximilians-Universität München, 2015.
- [179] Jasmin Moazzami-Fallah. "Charakterisierung der strukturellen und elektrischen Eigenschaften von 6,13-Dihydrodiazapentacen-Dünnschichten." Master Thesis. Ludwig-Maximilians-Universität München, 2016.
- [180] S. J. Noever, S. Fischer, and B. Nickel. "Dual Channel Operation Upon n-Channel Percolation in a Pentacene-C60 Ambipolar Organic Thin Film Transistor." In: *Advanced Materials* 25.15 (2013), pp. 2147–2151.
- [181] S. S. Nielsen et al. "BioXTAS RAW, a software program for high-throughput automated small-angle X-ray scattering data reduction and preliminary analysis." In: *Journal of Applied Crystallography* 42.5 (2009), pp. 959–964.
- [182] S. L. Barna et al. "Calibration procedures for charge-coupled device x-ray detectors." In: *Review of Scientific Instruments* 70.7 (1999), pp. 2927–2934.

## LIST OF FIGURES

---

Figure 1.1	Visualization of length scales . . . . .	4
Figure 1.2	Number of publications per year with topic 'nano' . . .	5
Figure 2.1	STED principle . . . . .	8
Figure 2.2	High-resolution AFM image of pentacene . . . . .	9
Figure 2.3	Evolution of brilliance of synchrotrons and laboratory X-ray sources . . . . .	12
Figure 3.1	Synchrotron radiation . . . . .	16
Figure 3.2	Energy dependency of brilliance . . . . .	17
Figure 4.1	Solid angles in sample-to-detector dependency . . . . .	31
Figure 4.2	Scheme of collimation and beamstop shadow . . . . .	32
Figure 4.3	$q_{min}$ dependency on collimation length . . . . .	34
Figure 4.4	Contributions to the q-resolution $\Delta q$ . . . . .	35
Figure 4.5	Energy scattering cross sections and attenuation length of water . . . . .	39
Figure 4.6	Scattering intensity of sample thickness (X-ray energy dependent) . . . . .	39
Figure 4.7	Background contributions of SAXS setups . . . . .	41
Figure 4.8	SDD dependent scattering of cytochrome <i>c</i> . . . . .	42
Figure 4.9	Dose of beamline Po8 (DESY, Hamburg) . . . . .	43
Figure 4.10	Maximal measured intensity for radiation damage- limited measurements . . . . .	44
Figure 4.11	Workflow diagram of setup . . . . .	46
Figure 4.12	Scheme of SAXS setup . . . . .	47
Figure 4.13	Beam adjustment . . . . .	47
Figure 4.14	Beam shape . . . . .	48
Figure 4.15	Count rate dependence on slit size . . . . .	49
Figure 4.16	Photographs and schemes of sample chambers for SAXS measurements . . . . .	50
Figure 4.17	Sketch and photograph of the sample holder for pow- der measurement . . . . .	51
Figure 4.18	Scheme of temperature controlled humidity chamber .	52
Figure 4.19	Scheme of Setup in WAXS mode . . . . .	53
Figure 5.1	Number of publications with the topic 'perovskite' . .	57
Figure 5.2	Perovskite unit cell structure scheme . . . . .	58
Figure 5.3	Perovskite powder XRD with OA concentration . . . .	59
Figure 5.4	Lattice spacing $d_{(100)}$ . . . . .	60
Figure 5.5	Data quality difference of perovskite XRD measure- ments with 20 % OA concentration . . . . .	61
Figure 5.6	XRD data comparison with literature . . . . .	62
Figure 5.7	Powder XRD at 20 and 80 % OA concentration . . . .	63
Figure 5.8	Bragg peak intensities as a function of OA concentration	64

Figure 6.1	Scheme of DNA and 'Photo 51' . . . . .	66
Figure 6.2	DNA origami shapes . . . . .	67
Figure 6.3	Design of three-dimensional DNA origami . . . . .	67
Figure 6.4	Schematic DNA origami shapes . . . . .	69
Figure 6.5	Schematic front view of DNA origami shapes . . . . .	69
Figure 6.6	Detailed front view of 24HB . . . . .	72
Figure 6.7	DNA origami scattering profiles with geometric model fit . . . . .	74
Figure 6.8	DNA origami scattering profile with the arranged model and geometric model with added inner structure . . . . .	76
Figure 6.9	MD simulation of DNA origami . . . . .	78
Figure 6.10	Cryo-EM density map and schematic representation of the 3D chicken-wire-like pattern . . . . .	79
Figure 6.11	Simulated data of 24HB with CRY SOL . . . . .	80
Figure 6.12	Simulated data of 3-LS with CRY SOL . . . . .	81
Figure 6.13	Scattering of 24HB at different $Mg^{2+}$ concentrations . . . . .	82
Figure 6.14	Size of 24HB at different $Mg^{2+}$ concentrations . . . . .	82
Figure 6.15	In-situ SAXS measurements during cooling of 24HB . . . . .	84
Figure 6.16	In-situ SAXS measurements during heating of 24HB . . . . .	85
Figure 6.17	Temperature dependent scattering intensities . . . . .	85
Figure 6.18	Scattering intensity of 24HB and 3-LS during heating . . . . .	86
Figure 6.19	Parameters of 24HB and 3-LS during heating . . . . .	87
Figure 6.20	Scattering of DNA origami lattice monomer . . . . .	90
Figure 6.21	Scattering of DNA lattice with 10 nm AuNP . . . . .	91
Figure 6.22	Scattering of DNA lattice with 20 nm AuNP . . . . .	92
Figure 6.23	Bragg peak intensity depending on q-resolution for DNA AuNP lattice . . . . .	93
Figure 6.24	Scattering of pure DNA lattices in comparison with monomer . . . . .	95
Figure 6.25	Scattering of pure DNA lattice with two models . . . . .	95
Figure 7.1	Structural formula of azobenzene molecules . . . . .	98
Figure 7.2	Spacing in a multilayer of lipid phases with FAs . . . . .	99
Figure 7.3	Absorption spectra of azo-PC . . . . .	101
Figure 7.4	Transmission spectra under UV and blue light illumination . . . . .	102
Figure 7.5	Transmission spectra of the back switch of cis to trans without light . . . . .	103
Figure 7.6	XRR of azo-PC bilayer . . . . .	104
Figure 7.7	SLD profile of azo-PC bilayer . . . . .	105
Figure 7.8	Thickness of azo-PC multilayer with illumination . . . . .	107
Figure 7.9	Time-resolved XRD measurement geometry . . . . .	108
Figure 7.10	Time-resolved XRD of azo-PC multilayer . . . . .	109
Figure 9.1	Publications with topic 'X-ray' . . . . .	116

## LIST OF TABLES

---

Table 2.1	Brilliance of laboratory X-ray sources [36]. . . . .	13
Table 3.1	Radius of gyration and Porod exponent . . . . .	20
Table 4.1	Intensity parameters in SAXS measurements . . . . .	37
Table 6.1	Design values of DNA origami structures . . . . .	70
Table 6.2	Default values of CanDo . . . . .	80
Table 6.3	Coherence length of setup and beamlines . . . . .	94
Table 7.1	Fit values of Bilayer of two models . . . . .	106



## ACKNOWLEDGMENTS

---

Eine Doktorarbeit wird am Ende immer nur einer Person zugerechnet, aber gerade in der experimentellen Physik gelingt ein erfolgreicher Abschluss nur mit der Unterstützung von vielen.

Daher möchte ich mich zuerst bei meinem Doktorvater, Bert Nickel, für die ausgezeichnete Betreuung dieser Arbeit bedanken. Besonders dankbar bin ich dafür, dass Du immer offen für meine/unsere Vorschläge warst, auch wenn sie sich nicht immer als grandios herausgestellt haben (Käsecke). Deine wertvollen Ideen, Dein Interesse, Dein Spaß am Forschen und Deine Gelassenheit haben es ermöglicht mit viel Freude zu arbeiten. Joachim Rädler danke ich für die Möglichkeit Teil seines Lehrstuhls zu sein, welcher zu Recht bekannt ist für seine besonders nette Atmosphäre. Ich bin fasziniert wie schnell Du die Themen überblickst und immer gute Ideen zu unseren Projekten beisteuern konntest. Des Weiteren bin ich Dir sehr dankbar, dass Du mich bei meinem Auslandsaufenthalt in Santa Barbara unterstützt hast.

Einen ganz großen Dank an die gesamte Nickel Gruppe für die tolle Zeit, ihr ward mehr als einfach nur Kollegen: Simon, der mich vom ersten Tag an, noch als Praktikant, begleitet hat und nicht nur sein Wissen mit mir geteilt hat, sondern auch die Vorzüge eines Feierabendbieres. Unser aller Sonnenschein Philip, der einen mit seiner positiven Einstellung mitreißt. Aber natürlich möchte ich auch die übrigen Doktoranden der Gruppe nicht namentlich unerwähnt lassen: Christian, Ida, Clemens, Franz, Janina und Samira. Vielen Dank für die schöne Zeit und den Spaß mit euch!

Alle meine Bachelor- und Masterstudenten, die ich betreut habe, hatten einen großen Anteil am Erfolg dieser Arbeit. Allen voran muss ich hier Kilian erwähnen. Ich bin sehr glücklich, dass du dich nach der Bachelorarbeit entschieden hast, zur Masterarbeit wieder zurückzukommen. Ohne dich wäre die gesamte Arbeit zu den DNA origami nie so schnell und gut abgeschlossen worden. Des Weiteren war ich immer sehr beeindruckt von der Geschwindigkeit und darüber hinaus noch hohen Qualität deiner Korrekturen zu dieser Arbeit. Josef, ich danke Dir für deine entspannte und gleichzeitig produktive Arbeitsweise. Ich bezweifle stark, dass die Röntgenanlage so schnell ohne dich gestanden hätte und noch viel wichtiger, dass es so viel Spaß gemacht hätte. Auch hier möchte ich alle nicht namentlich unerwähnt lassen: Maximilian, Benjamin, Jonathan, David, Christopher, Katica, Philipp, Christina, Fabian, Tina, Ramon und Anton. Vielen Dank für die gute Zusammenarbeit!

A great thank you to my second group of Cyrus Safinya, Youli Li, Phillip Kohl and Miguel Zepeda-Rosales who made it possible to have an amazing time in Santa Barbara.

Ich hatte während meiner Arbeit zahlreiche Kollaborationen, die nicht nur erfolgreich waren, sondern sich auch durch freundschaftliche Kommunikation ausgezeichnet haben. Vielen Dank an euch: Jan Lipfert, Linda, Tim Liedl, Caro, Tao, Philipp, Amelie, Dirk Trauner, James Frank, Theo Lohmüller, Patrick Urban, Alex Urban, Yu Tong, Carlos Cárdenas-Daw, Verena Hintermayr.

Einen ganz großen Anteil daran, dass der Laden nicht auseinander fällt haben Susi, Charlott, Philipp und Gerlinde. Vielen Dank, dass ihr immer ein offenes Ohr für mich und meine Probleme hattet, aber natürlich auch für die zahlreichen schönen Mittags- und Kaffeepausen. Liebe Gerli, es war mir eine große Freude mit Dir ein Büro teilen zu dürfen und ich freue mich schon auf zukünftige Feierabendbiere.

Stefan Manus danke ich für die häufige Hilfe bei jeder Art von elektrischen Fragestellungen und mindestens genauso wichtig dem häufigen Reparieren der Kaffeemaschinen. Christian Neubert und dem ganzen Team aus der Werkstatt danke ich für so unzählig viele Einzelteile, die in der Röntgenanlage eingesetzt wurden.

Vielen Dank an den gesamten Lehrstuhl für die entspannte Zeit und dem Spaß, wie z.B. bei den legendären Oktoberfestausflügen von unserem Wiesnexperten Felix, aber auch bei unser wöchentlichen Laufgruppe um Jürgen, Carolin, Svenja und Sonja. Diese Liste könnte noch endlos weitergeführt werden... Danke für die tollen Momente mit euch!

Zuletzt möchte ich all meinen Freunden und meiner Familie danken für den Ausgleich neben der Arbeit. Ein ganz großer Dank geht an meine Liebesschwägerin Katja. Ich weiß, es war nicht einfach sich durch mein Englisch zu kämpfen, vor allem wenn es dabei um Röntgenstreuung geht. Ich bin sehr froh einen Bruder wie dich zu haben, Andreas. Ich weiß, ich kann mich jederzeit auf Dich verlassen. Ich bin überglücklich, dass ich durch diese Arbeit Dich kennenlernte durfte, Jasmin, und möchte Dir dafür danken, dass alles mit Dir einfach leichter und schöner ist. Von ganzem Herzen danke ich meinen Eltern. Ihr habt mir das alles ermöglicht und mich immer bedingungslos unterstützt. Zu jeder Zeit habt ihr mit mir gelitten, mit mir gefiebert und euch mit mir gefreut, besonders Mama. Mein Papa hat den entscheidenden Beitrag zum Entstehen dieser Doktorarbeit geleistet, indem er mich mit dem einfachen Satz "Du arbeitest noch lang genug und ein Doktor schadet nie." erst überzeugt hat anzufangen...

Vielen Dank!